STEEL AND GEOSYNTHETIC REINFORCEMENT—SOIL INTERACTION

A Dissertation

by

ANAHITA GOUDARZI

Submitted to the Office of Graduate and Professional Studies of
Texas A&M University
in partial fulfillment of the requirements for the degree of

DOCTOR OF PHILOSOPHY

Chair of Committee,	Jean-Louis Briaud
Committee Members,	Charles P. Aubeny
	Marcelo Sanchez
	Alan B. Palazzolo
Head of Department,	Robin Autenrieth

May 2019

Major Subject: Civil Engineering

ABSTRACT

For the last 50 years, the use of reinforced soil systems has increased significantly. As such it is important to gain an in-depth understanding of the soil-reinforcement interface properties for designing and simulating purposes. The interaction between the soil and the reinforcement can be complicated, depending on the properties of the soil and the reinforcements. The goal of this research is to investigate the soil-reinforcement interaction during pullout tests and during direct shear tests using experimental and numerical modeling. The influence of the rib spacing, soil density, grain size, and confining stress on the interface shear strength and pullout force were evaluated. Furthermore, the contribution of the soil passive resistance due to the ribs to the pull-out force was quantified.

This study focused on the behavior of the smooth and then ribbed steel strips and of the geosynthetic reinforced soil systems. The first step of this research was to undertake an in-depth review of the published literature regarding the reinforcement/soil interaction. Then geotechnical laboratory tests including small and large direct shear tests and large direct, simple shear tests on selected soil materials were conducted. After that, over 200 laboratory tests were conducted including large direct shear tests and pullout tests to investigate the interaction between various reinforcement types and various soil materials. A comparison study utilizing these two types of test was conducted to investigate the underlying mechanism of soil and reinforcement interaction under different condition. The final step of the research was to conduct numerical simulations of the large direct shear

test and pull out test performed in the laboratory by using FLAC3D by Itasca Inc. The numerical simulation was first calibrated by comparing the experimental data and the simulation data including the soil/reinforcement interaction mechanism.

The results showed that the numerical results are in good agreement with the experimental results. The influence of the number of ribs on steel strip reinforcements is more significant at a lower depth of embedment, for dense soils, and soil aggregates with D_{80} lower than the ribs height.

ACKNOWLEDGMENTS

I would first like to thank my advisor, Dr. Jean-Louis Briaud for his supervision, support, guidance, and encouragement through my graduate studies. I am privileged to work with professor Briaud. The lessons I have learned from him is not limited to professional and research skills, but he also teaches me to be a better human being and that happiness is a choice. Many thanks go to my committee members, Dr. Aubeny, Dr. Sanchez, and Dr. Palazzolo, for their guidance and support throughout the course of this research. Also, I would like to highly appreciate the efforts of Dr. Tom Taylor, Vice President and Director of Research and Development at Big R Bridge for his invaluable help and his contribution to my research. Many thanks go to Mr. Augusto Lucarelli, principal engineer at ITASCA, for his guidance, patience, and support through my research.

Thanks also go to my friends and colleagues and the department faculty and staff for making my time at Texas A&M University a great experience.

Finally, an especial thanks go to my family for their encouragement and support.

CONTRIBUTORS AND FUNDING SOURCES

This work was supervised by a dissertation committee consisting of Professor Jean-Louis Briaud, Professor Charles Aubeny and Professor Marcelo Sanchez of the Zachry Department of Civil Engineering and Professor Alan B. Palazzolo of Department of Mechanical Engineering.

Graduate study was supported by a project funded by Texas A&M Transportation Institute, and the Texas A&M Engineering Experiment Station.

TABLE OF CONTENTS

Page

LIST OF FIGURES

Page

LIST OF TABLES

Page

1 INTRODUCTION

Modern soil reinforcement system was initiated by Henri Vidal, who developed the first steel strip reinforcement in the early 1960s. The main function of soil reinforcements is to improve the mechanical properties of soil. The application of soil reinforcement is increasing in use such as Mechanically Stabilized Earth (MSE) walls, pavements, embankments, railroads, and slopes. Layers of reinforcing elements were installed into the soil to provide improved stabilization for the whole structure. Different type of reinforcements has been used to improve the behavior of soils in different structures such as steel strips, geotextile sheets, steel or polymeric grids and steel nails. A various study has been conducted by scholars and engineers on the interaction between soil and reinforcement under pullout mode. However, the interaction between the reinforced elements and soil have not been thoroughly understood due to the complexity of the mechanism depending on the soil and reinforcement properties. This study dedicated to gain a better understanding of reinforcement-soil interface on both fine and coarse aggregates, smooth/ribbed steel strip, geostrap and geogrid with the utilization of both experimental (interface direct shear test and pullout test) and numerical simulation.

The first output of this study will be the shear properties of large aggregate soil specimens (crushed limestone) which is not possible to obtain from standard shear apparatus. The constitutive model for mentioned soil samples will be provided based on the stress-strain curves obtained from the simple shear test, the stress-displacement curve

obtained from the direct shear test, and the simulation of direct shear/simple shear test with FLAC3D software.

To optimize the pullout and shear forces of ribbed steel strip, the F*(the pullout resistance factor) value will be reported for different ribs spacing under pullout and interface shear mode.

1.1 Research Objective

The underlain goal of this research is:

- To understand in depth the mechanism of the interaction between soil and ribbed steel/geosynthetic reinforcement under shear and pullout mode.
- To develop a relationship between the pullout force and the interface shear force of reinforcements.
- To evaluate the influence of rib spacing, soil density, grain size, and confining stress on interface shear and pullout force.
- To evaluate the percent contribution of the passive resistance due to the ribs in the shear force measured.
- To evaluate the contribution of the transverse members in the reinforcements under the pullout and shear mode.
- To obtain the shear properties of large aggregates and provide recommendations for the selection of a proper soil model in simulating the behavior of large aggregate soils.

1.2 Research Approach

The major activities of this research were starting with a review over the previous experimental and numerical efforts on the interaction of soil-reinforcements based on interface direct shear and pullout test. The research approach divided into two categories: experimental work and numerical work.

The experimental work was performed in 7 steps as described below:

Task 1: Perform small direct shear tests on sand (loose and dense)

Task 2: Perform large direct shear tests on sand (loose and dense) and crushed limestone under various normal pressures

Task 3: Perform large simple shear tests on sand (loose and dense) and crushed limestone

Task 4: Perform interface direct shear tests using the modified large direct shear apparatus

Task 5: Perform interface direct shear tests between sand/crushed limestone and smooth/ribbed aluminum plate with different rib spacing and confining pressures

Task 6: Perform interface direct shear tests between sand/crushed limestone and geogrid under various confining pressures

Task 7: Perform pullout tests on smooth/ribbed steel strip reinforcement embedded in dense sand.

The numerical work was performed using FLAC3D and summarized in the following steps:

Task 1: Simulate direct shear test and simple shear test to identify parameters of soil specimen.

Task 2: Numerical simulation of interface direct shear tests.

Task 3: Numerical simulation of pullout test.

1.3 Thesis Organization

Chapter 1 of the dissertation presents the general background information about the mechanism of soil-reinforcement interaction, research approach, objectives, and outline of this dissertation.

Chapter 2 provides a thorough literature review related to the numerical and experimental studies on soil-reinforcement interaction and shear behavior of large aggregates. Chapter 2 is divided into three main parts. The first part presents a review of published experimental results of shear behavior of large aggregates. Second, the previous experimental studies related with the interface direct shear test between soil and reinforcements and pullout test of reinforcements embedded in the soil were presented. The last part reviews previous numerical modeling of these tests and the interface parameters were summarized.

The introduction to the laboratory devices and testing materials are presented in chapter 3. The detail of small/large direct shear, simple shear, and pullout device is

provided. Then, the soil material which is used in this study introduced and the mechanical properties of them presented. Also, the various type of reinforcements used in this study is presented and the mechanical properties of them are described.

Chapter 4 presents the test plan, procedure and test results of direct shear, simple shear, interface direct shear, and pullout tests. This chapter is divided to three sections: tests on soil aggregates, interface direct shear test between soil and smooth/ribbed plate as well as geogrid, and the pullout test on smooth/ribbed steel strip embedded in dense sand. For each series of test, the results were presented and discussed in detail.

Chapter 5 presents numerical simulation of the direct shear test, simple shear test, interface direct shear tests and pullout tests using the FLAC3D by Itasca Inc. This chapter starts with an introduction to FLAC3D. Then, the detail of each model including the geometry, constitutive model, boundary condition, and the loading condition is explained. The results of numerical simulation of tests are discussed and calibrated with experimental results.

Chapter 6 provides a comprehensive analysis of the results obtained from experimental and numerical work. The answers are provided to the objectives of the research and the results are explained more in depth. The interface parameters obtained from both direct shear and pullout test are presented in this chapter. The influence of different parameters including confining pressure, soil type, reinforcement type, soil density, and ribs spacing on pullout and direct shear results are disuced. The contribution

of cross elements in ribbed steel strip in the pullout and shear force is reported using the combination of numerical simulation and laboratory tests.

Chapter 7 presents the main conclusion and discussion of this dissertation. The scope of future work is also suggested.

2 LITERATURE REVIEW

To understand the function of reinforcements in soil an element of cohesionless soil is considered as illustrated in Figure 2-1, if a vertical load is applied to the element, the soil will compress axially and expand laterally. By adding the reinforcement in horizontal layers to the soil elements, the friction or other means provides the adhesion or interaction between reinforcement and soil. The stiff reinforcement will restrain the soil element as if acted a lateral force equivalent to the at-rest pressure ($K_0\sigma_v$). As Figure 2-1 shows, the stress state of soil element for the reinforced condition always lies below the failure curve. This means that failure can happen only when the reinforcements ruptures or the adhesion between the reinforcement and the soil fails (Jones, 2013).

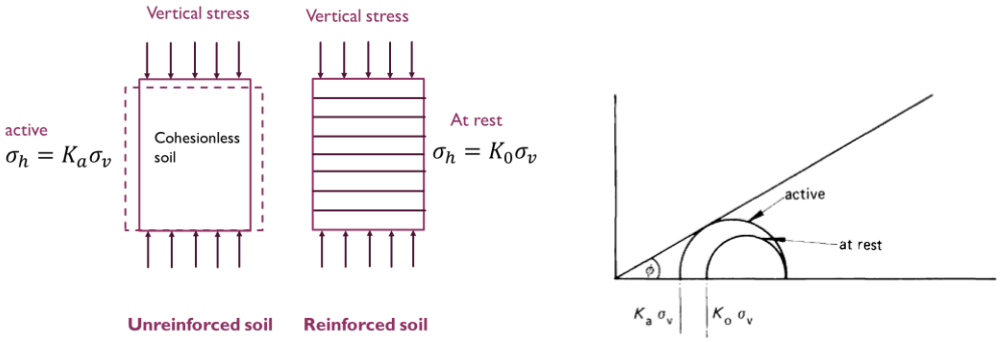

Figure 2-1. Soil-reinforcement mechanism

2.1 Stress Transfer Mechanism

The interaction between soil and reinforcement can be evaluated under shear and pullout mode.

Under direct shear mode, a block of soil slides over a layer of reinforcement. In this case, the reinforcement is located on soil or rigid base in the lower half of the shear box, and the upper half slides over the reinforcement. If the reinforcement has apertures, like geogrid, the lower half of the shear box should be filled up with soil (Lopes, 2010).

The pullout resistance of reinforcement is defined as the tensile load required to generate the outward movement of the reinforcement through the reinforced soil mass. Pullout resistance factor (F*) and scale effect correction factor (α) are recommended by FHWA. These parameters can be obtained from pull out tests and the following equations:

$$P_r = F^* \times \alpha \times \sigma_v' \times L_e \times 2$$

$$F^* \times \alpha = C_i \tan \emptyset$$

In these equations, P_r is the pullout resistance of reinforcement per unit width of reinforcement, σ_v' effective vertical stress, and L_e development length behind failure surface.

The coefficient of interaction or interface efficiency (C_i) is one of the main required parameters in the design of geosynthetics-soil structures and is defines as the ratio of the shear strength at the soil-reinforcement interface to the shear strength of the soil at the same overburden condition. For cohesive soil, can be defined as (Tatlisoz et al., 1998):

$$C_i = \frac{C_a + \sigma_n \tan \delta_a}{C + \sigma_n \tan \phi}$$

Where C_a is apparent adhesion intercept, σ_n confining pressure, δ_a apparent interface friction angle, C cohesion of soil, and ϕ friction angle of soil. If the interaction coefficient is less than 0.5, it means that there is a weak bonding between the soil and the reinforcement. On the contrary, if the interaction coefficient is greater than 1 it means that there is a strong bonding between the soil and the reinforcement (Tatlisoz et al., 1998).

The stress between soil and various reinforcement systems can be transferred with two mechanisms: friction and passive resistance (Figure 2-2). Depending on reinforcement geometry, the stress transfer mechanism can be governed by friction and/or passive resistance. Friction resistance is more dominate in reinforcements such as smooth steel strips, smooth rods, and sheets where relative shear displacement happens between soil and the reinforcement surface. In others, passive resistance occurs through the development of bearing-type stresses on reinforcing elements oriented normal to the direction of movements like welded wire and anchored earth. Both mechanisms are involved in ribbed strips, deformed rods and geogrids (FHWA, 2001, Mitchell and Villet, 1987).

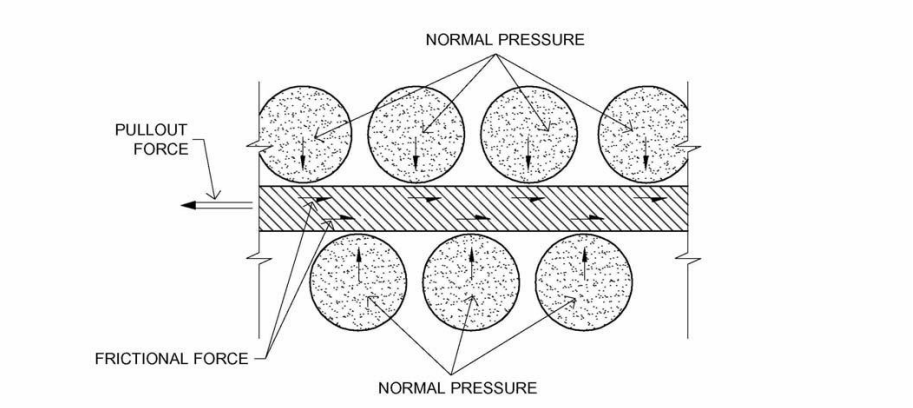

(a)

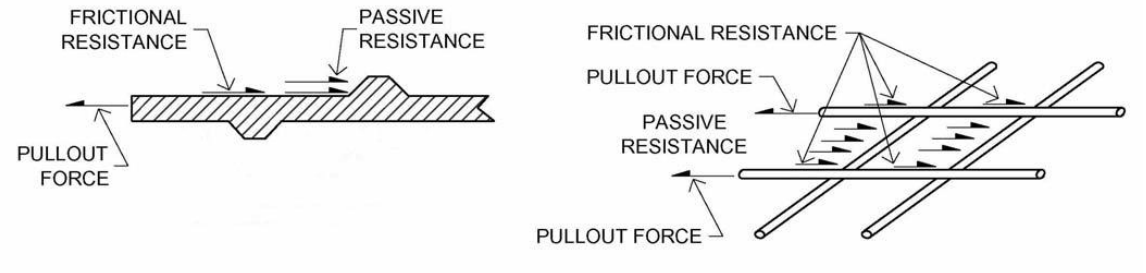

(b)

Figure 2-2. Stress transfer mechanism between soil and reinforcement, a) Friction b) Passive resistance

Bergado et al. (1992) proposed that the total direct shear force can be given as:

$$F_t = F_{s\text{-}s} + F_{s\text{-}g}$$

Where F_t is total direct shear resistance force, $F_{s\text{-}s}$ soil to soil direct shear frictional force, and $F_{s\text{-}g}$ Soil to geosynthetic direct shear frictional force. He suggested the following

equation to calculate the frictional resistance force for the direct shear interaction mechanism on sands:

$$F_t = \sigma_n \times A \times (\alpha_{ds} \times \tan\delta + (1 - \alpha_{ds}) \times \tan\emptyset_{ds})$$

Where:

$\emptyset_{ds}$ = Friction Angle of soil from direct shear test

δ = Interface friction angle

α_{ds}= Ratio of reinforcement shear area to total shear area

σ_n= Normal stress at shear plane (kPa)

A = Total shear area (m^2)

F_t= Direct shear resistance (kN)

Soil to soil direct shear frictional force, and soil to geosynthetic direct shear frictional force defined as follow:

$$F_{s-g} = (C_a + \sigma_n \times \tan\delta_a) \times A_{s-g}$$

$$F_{s-s} = (\mathrm{C} + \sigma_n \times \tan\emptyset) \times A_{s-s}$$

In these equations, C_a is the adhesion between soil and the geosynthetic, δ_a is the interface friction angle, A_{s-g} is the area of the interface friction, C is the cohesion of the soil, $\emptyset$ is the soil friction angle, and A_{s-s} is the area of the soil to soil friction.

Irsyam and Hryciw (1991) presented friction and passive resistance equations for ribbed steel strips with large rib spacing where a full passive zone develops. The total pullout resistance (F) consists of two components:

$$F = F_f + F_p$$

Where F_f is the frictional component and F_p is the passive resistance component.

$$F_f = (s - 2H_r)\sigma_n tan\delta_b$$

In this equation, S is the rib spacing, H_r the rib height, σ_n the effective normal stress, and δ_b the soil-rib friction angle.

$$F_p = P_r H_r \cos\delta_r + P_s H_s \cos\delta_s$$

Where P_r is the pressure along the rib wall, δ_r the rib-wall friction angle, P_s the pressure along the soil wall, H_s the soil wall height, and δ_s the soil wall friction angle.

2.2 Research Outcomes of Interface between Soil and Steel Reinforcements

Irsyam and Hryciw (1991) conducted the pullout tests on Ottawa sand and ribbed plate in a modified direct shear device. The ribs were 2.5 mm high, 2.5 mm wide and spaced 15 mm and 33 mm apart. In order to identify failure surfaces, they used various observation techniques such as, monitoring collared sand grains using video camera through plexiglass walls of the direct shear box and developing a carbowax solidification technique. Their results showed that for small ribs spacing, the failure surface approaches a plane parallel to the plate and a passive zone is developed partially, while for large ribs

spacing, the failure surface exhibits a pronounced curvature initiated above the tops of the ribs, touched the base plate and continues to the rear face of the previous ribs. It is worth mentioning that for 2.5 mm height ribs, they proposed the optimum rib spacing which allows the greatest number of full passive soil zones to develop per length of reinforcement is 25 mm and 33 mm for loose and dense sand, respectively.

Hryciw and Irsyam (1993) evaluated the influence of rib geometry and spacing, soil density, grain shape, grain size, and a number of shearing cycles using the same modified direct shear box which was explained above. Figure 2-3 illustrates the various rib spacing and geometry of tested steel strips. They concluded that the optimum spacing to obtain passive resistance is 10-13 times the ribs height and if the ribs spacing is less than two times the ribs height, the passive resistance will diminish. The strips with 90-degree ribs have greater strengths than strips with trapezoidal shapes because no passive zone can develop for this rib geometry. The trapezoidal ribs act only as rough surfaces and the maximum shear strength obtainable is the soil shear strength.

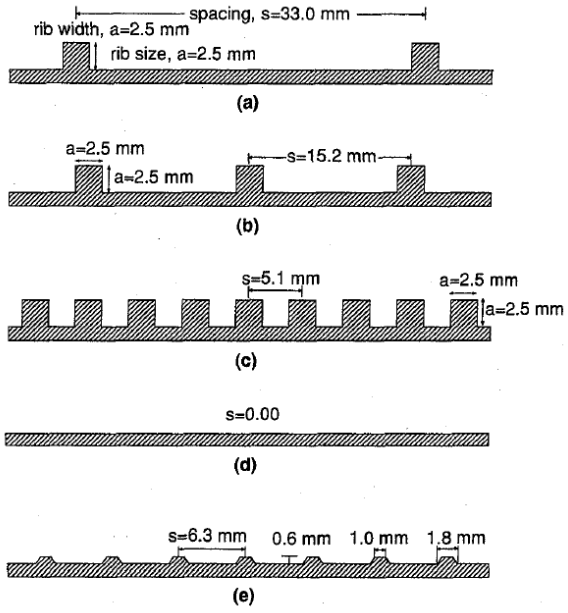

Figure 2-3. Rib spacing and geometries (Hryciw and Irsyam, 1993)

Dove and Jarrett (2002) investigated the influence of surface topography on shear stress and volume change behavior of granular material interface system. They conducted modified the direct shear test and used Ottawa 20/30 Sand as well as 0.5-0.7 mm diameter glass microbead spheres to reduce the influence of grain shape. The lower half of shear box replaced with the machined surface, molded polymer surface, Geomembranes (HDPE) to study the influence of surface hardness. Figure 2-4 shows the topography of surfaces in this study.

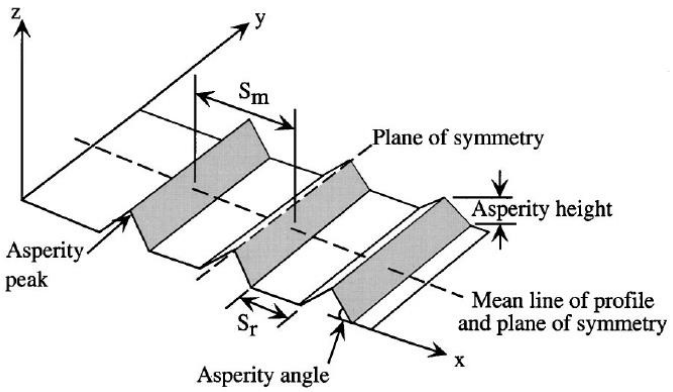

Figure 2-4. Description of the ruled surface (Dove and Jarrett, 2002)

To study the effect of surface roughness and particle size, Lings and Dietz (2005) conducted small direct shear tests by replacing the lower frame with a series of solid steel blocks with various roughness. They concluded that the stress ratio and the rate of dilation will increase with increasing the roughness of the surface.

The modified direct shear test results show that for both glass beads and Ottawa 20/30 sand, the interface efficiency (C_i) varies between nearly zero when interface strength is small to 1.0 if full soil strength is mobilized. Efficiency is a function of ribs height, ribs spacing, and particle diameter. Independent of asperity spacing variable, the efficiency increases with increasing the ratio of ribs height (R_t) over D50 of soil. Regardless of ribs spacing, surfaces with R_t/D_{50} less than 0.9 have efficiencies less than 1. As Figure 2-5 illustrates the maximum efficiency obtained at a S_m/D_{50} ratio of 1.5. The efficiency decreases as S_m/D_{50} increases to about 10, after that efficiency remains almost constant. They concluded that maximum efficiency occurs when the height of the ribs be equal to

the median grain diameter, the ribs spacing be between one and three times the median grain diameter, and ribs angle be on the order of 45+ dilation angle/2.

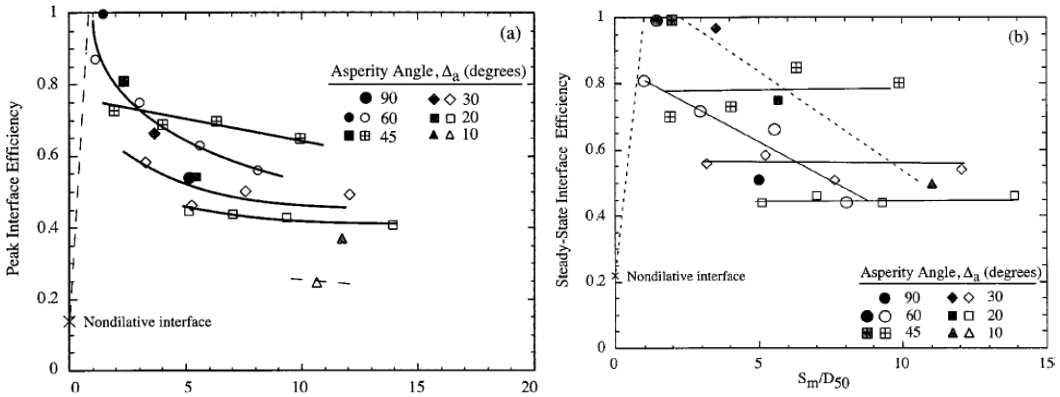

Figure 2-5. Normalized spacing relationships for glass beads: a) Peak state and b) steady-state. Rt /D50=0.9 (open symbols) and 1.0 (shaded symbols) (Lings and Dietz, 2005).

Abdelouhb et. al. (2010) compared the behavior of metallic strap and synthetic strap by conducting laboratory pullout test on fine sands (Hostun RF sand). For the metallic strap, the head and the end mobilize at the same time while for synthetic trap, the tension and displacement mobilize with a delay. The maximum apparent friction coefficient (μ*) obtained from the following equation:

$$\mu^* = \frac{\tau_{max}}{\sigma_{v0}}$$

Where σ_{v0} is the initial vertical stress, and τ_{max} is the maximum shear stress obtained from pullout test. As shown in Figure 2-6 maximum friction coefficient, μ^*, decreases with increasing confinement stress. Due to the shear stress, the volume of the

surrounding zone of the reinforcement increases. Therefore, vertical stress around the reinforcement increases. This phenomenon is called constrained dilatancy. Under lower confining pressure, the constrained dilatancy is higher, and the vertical effective stress increases. Thus, the maximum friction coefficient at the soil/ reinforcement interface decreases as the confinement stress increases on the two types of reinforcement (metallic and synthetic).

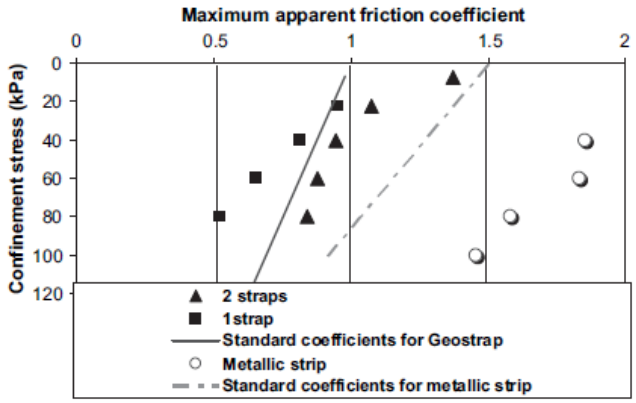

Figure 2-6. Maximum apparent friction coefficient (Abdelouhb et. all., 2010)

Pull- out the test was conducted on the plain strip, strip with ribs on both sides and strip with the shear element by Esfandiari and Selamat (2012). The soil material used in this study was well-graded sand with friction angle of 39 and 45 for a relative density of 60% and 90%, respectively. The height and number of ribs were variable along the 100-cm length of strips (Figure 2-7). They reported that under the normal stress of 100kpa, F* has ranged from 0.377 for the plain strip to 6.329 for the strip with 4 anchorage elements of 8 cm depth each. With increasing the height of the ribs from 2cm to 8 cm, the pullout

force increases too. However, the rate of increase in pullout capacity decreased from 6cm high ribs. The pullout force increased with increasing the number of ribs on the strip. However, the changes in pullout capacity were more sensitive to depth than the number of elements. Furthermore, the percentage of increase in pullout capacity generally rises with increasing count of ribs but reduces with increasing depth of elements.

Esfandiari and Selamat (2012) suggested the following equation for calculating the ratio of pullout capacity over normal force:

$$F/P_{max} = 11.158 \times \left(\left(\frac{n}{h}\right) \times D_{50}\right) + 8.48E - 10 \times \left(\frac{P \times h}{\gamma \times D_{50}^{4}}\right) + 0.032 \times (n \times \frac{h}{D_{50}})$$

Where, F is pullout capacity, P normal force, n number of ribs, and h depth of ribs.

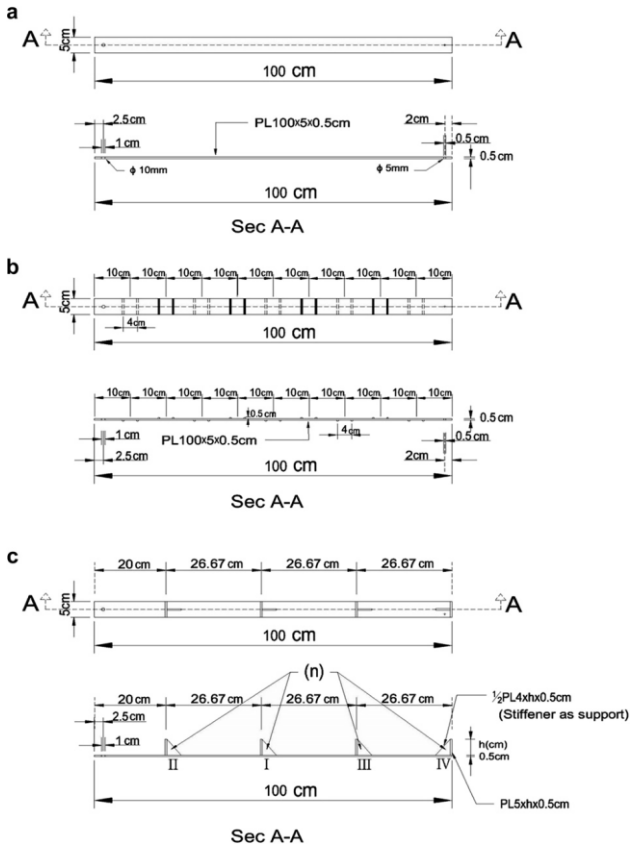

Figure 2-7. Various types of strips; a) plain strip, b) Strip with ribs on both sides, c) Strip with shear elements (Esfandiari and Selamat, 2012)

Khemissa et. al. (2015) performed the experimental and numerical analysis of pullout test on five steel strips with various forms of roughness (Figure 2-8). They used PLAXIS-2D to model pull out tests and simulated the strips as geogrid structural elements characterized by axial rigidity. There was a good agreement between the experimental and numerical results. The surface roughness improves the adhesion and friction angle between sand and strip, an among the rough strips in their study, chain had higher pullout resistance due to the anchorage resistance mobilized by the rings. The apparent friction's

coefficient sand-strips, μ* for various surface roughness and vertical stress is shown in Figure 2-9.

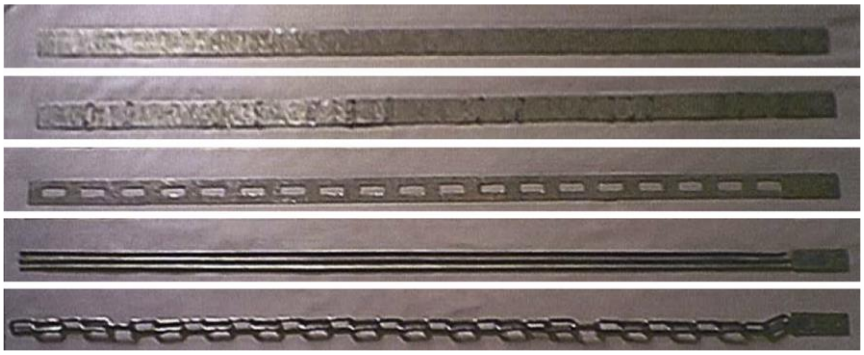

Figure 2-8. Five various steel strips; Smooth, Ribbed, Punched, W-shaped, and chain (Khemissa et. al., 2015)

σ_v (kPa)	Strip									
	Smooth		Ribbed		Punched		W-shaped		Chain	
	F_{ult} (kN)	μ^*	F_{ult} (kN)	μ^*	F_{ult} (kN)	μ^*	F_{ult} (kN)	μ^*	F_{ult} (kN)	μ^*
Experimental results										
25	0.22	1.50	0.50	3.33	0.33	1.81	0.28	2.18	0.65	5.73
50	0.34	2.32	1.09	7.23	0.80	4.40	0.43	3.42	1.24	10.88
75	0.71	4.85	1.50	9.99	1.20	6.60	0.65	5.16	1.70	14.97
Numerical results										
25	0.21	1.43	0.45	2.96	0.30	1.63	0.24	1.94	0.47	4.14
50	0.42	2.87	1.23	8.20	0.59	3.27	0.43	3.42	1.31	11.50
75	0.63	4.32	1.33	8.88	0.89	4.91	0.65	5.13	1.96	17.22

Figure 2-9. Ultimate pulling load and corresponding apparent friction's coefficient sand-strip (Khemissa et. al., 2015)

Stranhler et. al. (2006) conducted a series of laboratory pullout tests on single and multi-ribbed steel strips embedded in the well graded gravelly soil to study the potential for the frictional interface between closely spaced reinforcements. Three various soil type were used in their study: Kanaskat gravel, rounded to sub-rounded, and well-graded sandy gravel. The apparent friction coefficient, F* presented Figure 2-10. In this Figure, isolated

and confined strip referred to single and multi-strip tests. Reduction in the reinforcement spacing increased the available peak resistance but reduces the initial pullout stiffness.

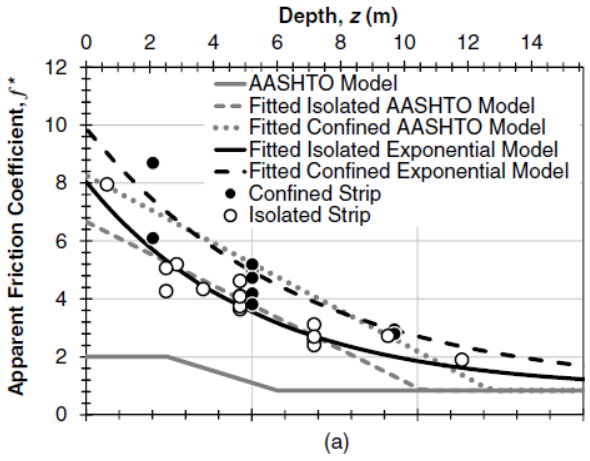

Figure 2-10. Apparent friction coefficient; Single and multi-strip pullout tests using Kanaskat gravel (Stranhler et. al., 2006)

In addition to study the behavior of steel ribbed strips, Chang et. al. (1977), Peterson (1980), and Weldu (2015) performed experimental tests to study the pullout resistance of welded wire mesh reinforcements. The pullout resistance of wire-mesh reinforcements has two components including friction between longitudinal wires and soil particles and anchorage of transverse wires embedded in the soil. The estimated frictional resistance, F_t and anchorage (bearing) resistance for a single longitudinal and transverse wire, respectively, in cohesionless backfills formulated as Peterson (1980):

$$F_t = \sigma_v(\pi dl)tan\delta$$

$$P_b = \sigma_v d N_q$$

Where σ_v= normal stress, δ= backfill-reinforcement friction angle, d = diameter of reinforcement wire, Nq = bearing factor which given as follows:

$$N_q = e^{\pi \tan \emptyset} tan^2(45 + \frac{\emptyset}{2}) \text{ for shear failure}$$

$$N_q = e^{\left(\frac{\pi}{2}+\emptyset\right) \tan \emptyset} tan(45 + \frac{\emptyset}{2}) \text{ for punching shear failure}$$

The interaction mechanism between reinforcement and soil is influenced by both the reinforcement and soil characteristics. For example, the surface roughness, grid aperture of reinforcement, soil grain size, water content and cohesion (FHWA, 2001).

Weldu (2015) reported that pullout resistance of plain bar-mesh reinforcements was about six times more than strip reinforcements with the same surface area in gravelly sand soil.

2.3 Research Outcome of Interface between Soil and Geosynthetic Reinforcements

The soil-geosynthetic interaction can be evaluated by direct shear tests or pullout tests. The shear strength of soil-geosynthetic interfaces has been investigated using direct shear tests by Jarret and Bathurst (1985), Cancelli et al. (1992), Bauer and Zhao (1993), Cazzuffi et al. (1993), Bakeer et al. (1998), and Abu-Farsakh and Coronel (2006). The laboratory and field pullout tests on geosynthetics have been done by Bergado et al. (1992), Cowell and Sprague (1993), Abu-Farsakh et. al. (2006), etc.

Rowe et al. (1985) conducted series of direct shear tests and pullout tests for a number of different geotextiles and geogrids in both granular fill and saw dust. They

studied the soil-geosynthetic interface strength properties of geosynthetics in these materials. For woven and non-woven geotextiles, in both direct shear and pullout tests, the interface friction angle (δ) was the same. On the other hand, for geogrid "Tensar SR2", the interface friction angle (δ) measured by direct shear test was essentially the same as that of the soil (i.e. $\delta = \Phi = 30°$), and the interface friction angle measured by pullout test was considerably lower (i.e. $\delta = 18°$).

Koutsourais et al. (1998) compared the interface friction angle (δ) obtained from pullout and direct shear tests of geosynthetic reinforcement in the marginal cohesive soil. They concluded that the pullout tests provide approximately 13% to 17 % higher soil interaction values at low confining pressures (< 4 psi) and provide essentially the same soil interaction values at higher confining pressures. The total pullout resistance for geotextiles is contributed only by the frictional resistance. Therefore, the shear strength of sand-geogrid interfaces under direct shear mode is significantly higher than that of sand-geotextile interfaces.

Bergado et al. (1992) compared the laboratory and field pullout test results of steel geogrids in weathered clay. They conducted laboratory pullout tests with various conditions including reinforcement sizes, mesh geometry, and compaction conditions of the weathered clay. The results show that the field pullout tests provided higher pullout resistance than the laboratory tests. The total pullout resistance of the geogrids is the combination of the frictional resistance and the passive bearing resistance. Though the tests were conducted with steel geogrids, they provided the effect of cohesive nature of

the soils and provided the necessary formulations for passive bearing resistance for cohesive soils. The passive bearing resistance was related to the bearing capacity factors in the Terzaghi-Buisman bearing capacity equation. Two failure models were adopted to evaluate the bearing capacity factors, namely the bearing capacity failure model (Peterson and Anderson, 1980) and the punching shear failure model (Jewell et al. 1984).

Cowell and Sprague (1993) conducted pullout tests for geogrids and geotextiles in the uniformly fine sand. They compared the differences in the pullout performance for geogrids with and without junctions, and for geogrids and geotextiles with similar stress-strain characteristics. The pullout resistance at 0.75 inches of displacement for the geotextiles tested was 50% to 67% lower than that obtained for geogrids of similar strengths. The removal of the junctions from the geogrid tested reduced the pullout resistance of the geogrids by less than 10%.

Liu et al. (1996) studied the performance of polymeric geogrids in compacted cohesive lateritic soil and complemented the analysis done by Bergado et al. (1992) and presented identical conclusions. They reached similar conclusion that bearing capacity failure and the punching failure modes appeared to be an upper bound and lower bound envelope for the pullout capacities of the polymer grid reinforcements.

Holtz (1977) firstly studied the shear stress distribution along the geosynthetics using pullout test. Ochiai et al. (1996) evaluated the shear stress distribution of geogrids tested in the sand. They both concluded that the maximum shear stress is located at the face of the geo-material while decreasing along the length.

The pullout resistance factors F* (friction-bearing interaction factor) and α (scale correction factor) can be determined using the method introduced in the FHWA 1996 manual (Elias and Christopher, 1996).

Bergado et al. (1993) proposed an equation to obtain the shear strength in a sand-geogrid interface mobilized under direct shear mode:

$$\tau_{sand-geogrid} = \sigma_n \times [(1-\rho)\tan\delta + \rho\tan\Phi_{ds}]$$

where ρ is percent open area of geogrid, δ interface friction angle between sand and geosynthetic, and Φ_{ds} internal friction angle of sand obtained from direthe ct shear test.

Liu et. Al. (2009) proposed an equation to obtain the passive resistance contribution in total shear resistance of sand-geogrid as:

$$\beta = \left[\tau_{sand-geogrid} - (1-\rho)\tau_{sand-geotextile} - \rho\tan\tau_{sand}\right]/\tau_{sand-geogrid}$$

Cancelli et al. (1992) reported interface shear strength coefficients (C_i) ranging from 1.04 to 1.12 for interfaces between HDPE and polypropylene (PP) geogrids against sand; Cazzuffi et al. (1993) stated that interface shear strength coefficient is 0.97 for sathe nd-HDPE geogrid interface, Bakeer et al. (1998) reported interface shear strength coefficient of 0.92 for the light weight aggregrate-HDPE geogrid interface. Cowell et al. (1993) evaluated the soil interaction coefficients of geotextiles and geogrids in the sand, the Ci values ranged from 0.8 to 1.0. However, Koutsourais et al. (1998) evaluated the coefficient of interaction (Ci) of geotextiles and geogrids in clay, and they obtained Ci

values that ranged from 0.5 to 0.9. Tatlisoz et al. (1998) studied the interaction between reinforcing geosynthetics and soil-tire chip mixtures. In their study, they evaluated the coefficient of interaction for different geosynthetics with different soil combinations. The Ci values obtained in the study ranged from 0.3 to 1.5. Abu-Farsakh et. al. (2006) conducted a series of laboratory and field pullout tests with different types of geosynthetic reinforcements in marginal silty clay soil of medium plasticity. They reported that the coefficient of interaction ranged from 0.4 to 0.8 and 0.2 to 0.6 for woven geotextile and unwoven geotextile, respectively. It is worth mentioning that weaker geogrids had higher coefficients of interaction than stronger geogrids. The coefficient of interaction for strong geogrids was about 0.5 while that for weak geogrids ranged from 0.4 to 0.8. The interface shear strength coefficient of sand-geotextile ranges from 0.7 to 0.8 while that of sand-geogrid ranges from 0.9 to 1. (Liu et. al., 2009). According to Tatlisoz et al., 1998, when the interaction coefficient is greater than one, it indicates that there is an efficient bond between the soil and the geosynthetic and that the interface strength between the soil and the reinforcement is greater than the shear strength of the soil. If the interaction coefficient is less than 0.5, it indicates weak bonding between soil and geosynthetic or breakage of the geosynthetic layer.

Chu and Yin (2005) conducted a serious of large direct shear test and laboratory pullout test to study the shear stress-displacement behavior and ultimate shear strength at the interface between the cement grout nail and completely decomposed granite (CDG) well graded clayey gravelly silty sand. The cement grout surface was tested with different

roughness angles including 0, 10, 20, and 30. The apparent coefficient of friction decreases with the increase of the normal stress. The reason for this fact is that wit increasing the normal stress, the confining effect on the reinforcement will increase, and the dilatancy will reduce. The apparent friction coefficient μ* is defined as the ratio of shear strength over effective vertical stress ($\mu * = \frac{\tau_s}{\sigma_v'}$). The pullout test results showed the higher values of the apparent friction coefficient than the interface shear tests because of normal stress concentration on reinforcement in the pullout tests. The difference of the apparent friction coefficient between the pullout tests and the interface shear tests is smaller for large shear displacements. In the pullout tests, a cavity performs at the end of the reinforcement, and causes arching formation in this cavity. Therefore, the volume changes of the surrounding soil are small, and the dilatancy is small.

The displacement for mobilization of pullout resistance is larger for lower normal stress. With increasing the normal stress, the mobilized displacement of pullout resistance decreases (Baykal & Dadasbilge, 2009).

Award and Tanyu (2014) compared the results obtained from direct shear and pullout tests of the frictional connection between geotextile reinforcement and concrete block. They claimed that at lower wall height, sliding of the block over geotextile is the critical while at higher wall height, the pullout mechanism is more critical than sliding.

Liu et. Al. (2009) investigate the contribution from the ribs in the interface shear if soil and geogrid interaction using direct shear test. He found that the yield stress between sand and geogrid is similar to the sand and geotextile interface.

2.4 Research Outcome of Numerical Simulation of Direct shear test

The non-uniform stress and strain distribution of soil sample within the shear box had proven by Saada and Townsend (1981). They explained that the non-uniform stress distribution causes progressive failure inside the soil sample and reduction in the ultimate shear strength of soil. Potts et al. (1987) confirmed the stress non-uniformity of soil; however, they concluded that progressive failure developed during shearing may be insignificant. Dounias and Potts, 1993 pointed out that direct shear tests did not consider non-uniform distribution of stress and progressive failure caused by the side wall boundary condition.

Potts et al. (1987) used perfectly plastic model to analyze direct shear test. He found that the dilation angel and initial stress state of the soil sample will influence the stress-strain behavior significantly.

Ni et al. (2000) performed 3D DEM simulations of direct shear test. Their results showed that the deformation was located to a narrow zone near the mid-height of the specimen.

Masson & Martinez (2001) modeled direct shear test using 2D DEM method on dense and loose sample. It was found that the shear deformation of the dense sample is localized in a layer at the middle of the shear box while no localized shear deformation is observed in the loose sample.

Frydman & Operstein (2001) studied the influence of plant roots on the stability of slopes. The simulation was performed using the finite difference code, FLAC, and two different soil models were used: the hyperbolic model, and a plastic, strain-hardening model. They applied boundary conditions during the consolidation and shearing stage.

Thornton & Zhang (2003) modeled the direct shear test using Two-dimensional DEM. They found that evolution of the stress ratio inside the shear band was very similar to that inferred from boundary force calculations.

Tejchman & Bauer (2005) modeled the direct shear test using finite element method. They found the stress and deformation is non-uniformly distributed in the sample. Dilation is observed in the shear band and it reduced to zero to the boundary.Lobo-Guerrero & Vallejo, (2005) studied the crushing during direct shear test in a simulated granular material. With an increase of normal force, more crushing will be produced.

Zhang and Thorton (2007) simulated two-dimensional model of the direct shear test using the discrete element method (DEM). They study the stress distribution and the porosity changes during the direct shear test. Their results demonstrated that the dilation inside the shear zone is much greater than that deduced from boundary measurements. Also, the stress calculated from the boundary forces is about 10% greater than that calculated in the shear zone. The actual shape of the shear zone is lenticular, and not like the rectangular (Figure 2-11). The approximate shear zone developed in the mid-height of the specimen is about 10D50. It is worth mentioning that the width of the shear band in

the center is wider than that near the edge. An 10% increase of vertical stress is observed during the simulation.

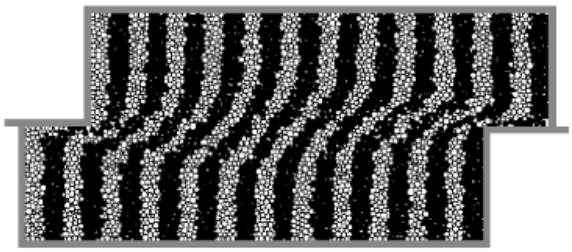

Figure 2-11. DEM model of DST after shear phase (Zhang and Thorton, 2007)

Härt & Ooi, (2011) investigated the influence of particle shape and interparticle friction on the bulk friction of dry granular materials in a direct shear test using the discrete element method (DEM). The PFC3D program used to simulate the direct shear test. Also, they conducted 90 small direct shear tests on the single and paired glass beads. The comparison of the numerical and experimental study showed that DEM is capable of providing proper agreement results with the experimental one.

Ziaie Moayed et. al. (2011) performed a series of 3D numerical simulation of direct shear test under different normal loading using ABAQUS. They investigate the effects of different parameters such as cohesion, friction angle and Young's modulus on the shear strength of sandy clay. El-Emam et. al. (2012) investigate the direct shear test using FLAC. They found that the angle of internal friction at plane strain condition is significantly larger than the direct shear friction angle. In addition, both normal and shear stresses distributions at failure plane are diverted from being uniform at initial conditions to non-uniform during the shearing process and at failure.

3 DEVICES AND MATERIALS

The devices and the test materials which were used in this research are presented in this chapter. The details of the large direct shear test device, large simple shear test device and the pullout test device are provided in this chapter. Furthermore, this section provides the characteristics of tested soil material and the type of steel and geosynthetic reinforcements.

3.1 Small Direct Shear Device

Small direct shear test (SDST) is a laboratory test to determine the consolidated drained shear strength of a soil sample (ASTM D3080). The idea behind this method is to impose a constant strain rate (displacement gradient) on a soil sample until the soil fails. Usually, there are three or more soil samples are tested under different normal loading conditions. With the normal load applying on the sample and the constant strain on one of the shear planes on the apparatus, the Mohr`s circle would be a great method to get the strength properties of the soil sample. However, since a certain height of the sample cannot be determined for a soil sample, stress-strain relationship, Young`s modulus and other shear properties by DST.

There are two terminologies regarding the DST:

- Relative Lateral Displacement: this is the horizontal displacement of the top and the bottom of the shear box halves.

- Failure: the stress level at the failure of a test soil sample. Usually, the failure is defined as the maximum shear stress that is imposed on the sample or the 15 to 20% relative lateral displacement. This means that if we have 15 to 20% of the displacement of the sample with respect to the constant strain exerted by the apparatus on the sample.

There are multiple parts involved in the DST apparatus used at TAMU geotechnical lab, as shown in Figure 3-1:

The shear device is the entire setup of the DST apparatus which is capable of having a normal load to the sample to make sure the drainage through porous stones in the shear box while the sample is submerged and also able to apply a shear force to the specimen in water. The frames that hold the specimen shall be sufficiently rigid to prevent their distortion during shearing. The various parts of the shear device shall be made of a material not subject to corrosion by moisture or substances within the soil, for example, stainless steel, bronze, or aluminum, etc.

Shear box, either circular or square is the made of steel, bronze, or aluminum, with the way to provide drainage for the sample inside. The box has two equally sized halves with the option of having one half moving while the other one is stationary which can simulate the shearing in the sample.

Porous inserts are the drainage tools which allows the water drains out from the sample. The porous stone permeability is significantly greater than the soil sample due to the fact that it has to act as a drainage factor.

Force measure, to measure the normal force exerted on the top of the sample. This is done by either dead weight or a pneumatic device. Also, in the connection of soil sample top and the normal force tip, there is a cap weighting 0.475 kg placed over the sample.

Shearing the specimen device, the device shall be capable of shearing the specimen at a uniform rate of displacement, with less than 65 percent deviation, and should permit adjustment of the rate of displacement from 0.0001 to 0.04 in/min (.0025 to 1.0 mm/min). The rate to be applied depends upon the consolidation characteristics of the soils. In current tests, the strain applied was 0.5 mm/min.

Shear force transducer, this device is connected to the other side of the shear box to measure the resultant force of the shearing of the soil sample.

Figure 3-1. Small Direct Shear Apparatus, TAMU Laboratory

3.2 Large Direct Shear Test Device

The large direct shear test (LDST) is a laboratory test to determine the shear properties of the soil specimens and large aggregates which is not possible to obtain from the standard direct shear apparatus. The large direct shear apparatus can be used to perform a direct shear test on aggregates up to a diameter of 1.2 in. (3 Cm). Figure 3-2 shows the testing device used for both large-scale direct shear and simple shear test. The equipment called ShearTrac-III apparatus was manufactured by Geocomp co. and located at the Soil and Aggregate Laboratory at Texas A&M University. The ShearTrac III system is capable of performing the consolidation and shearing phases of a 305 mm x 305 mm (12 x 12 in. by 200 mm (8.0 in) height direct shear test under automatic control for soils and geosynthetics (geomembrane, geotextile, GCL, geogrid, etc.) as well as for determining the interface frictional properties of soil and geosynthetics, and internal friction of GCLs. The device is capable of performing the following tests:

- Direct shear test on soil and aggregates
- Monotonic direct simple shear test on soil and aggregates
- Cyclic simple shear test on soil and aggregates
- Direct shear testing process has up to 32 independent input parameters and steps
- Interface frictional properties of soil & geosynthetics
- Internal friction of GC
- 1-D incremental consolidation up to 32 steps
- Constant displacement rate control shear

- Constant load control rate shear

As shown in Figure 3-2, the apparatus, ShearTrac-III system consists of three different parts including the Shear Trac-III load frame, test accessories, and computer.

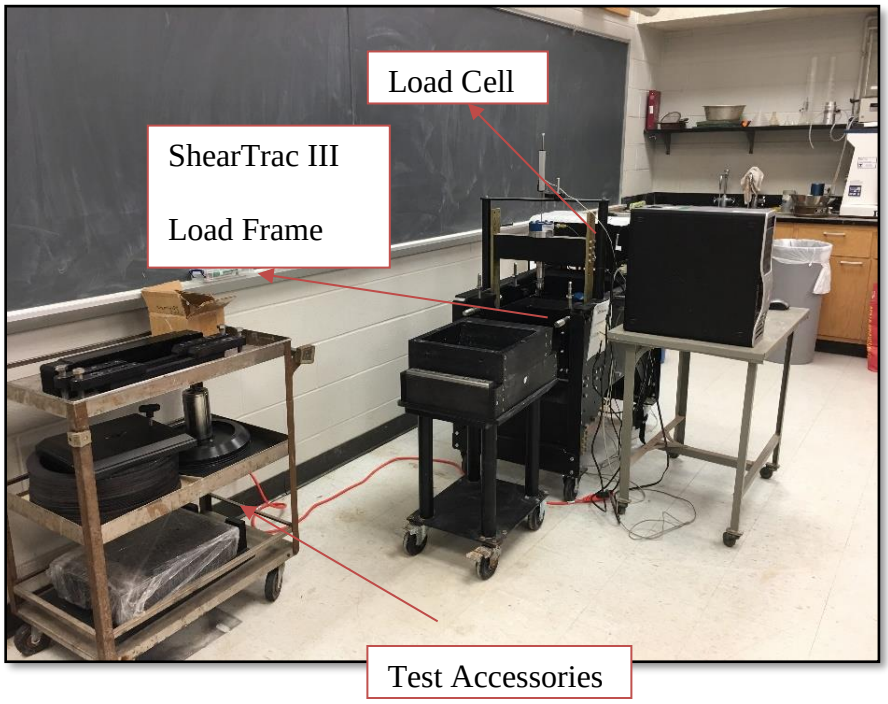

(a)

Figure 3-2. Large Direct Shear and Simple Shear Apparatus, TAMU

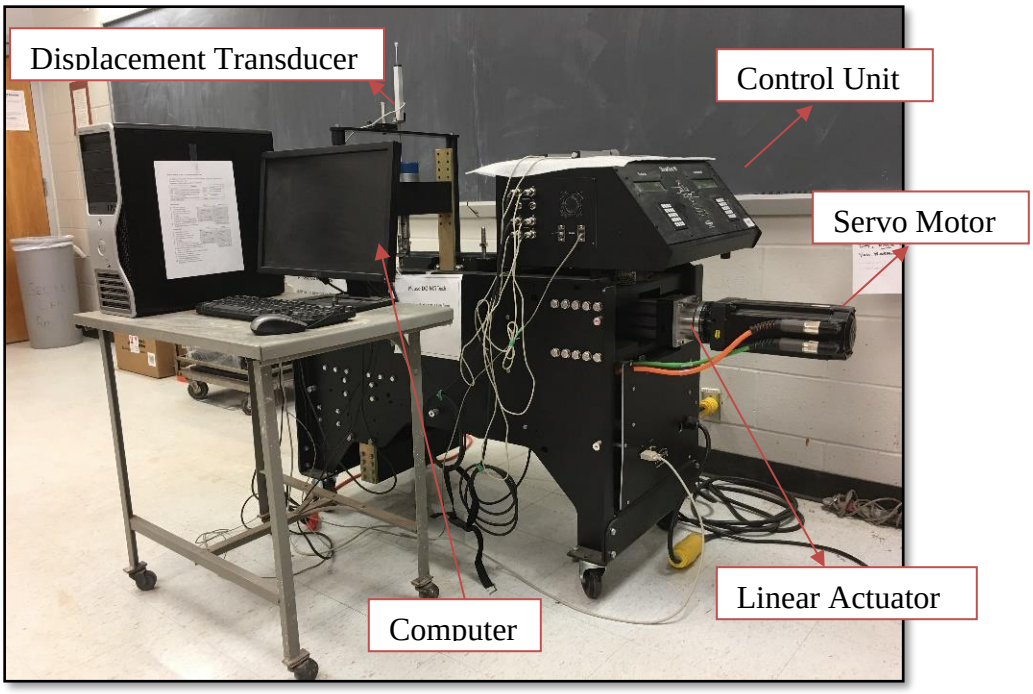

(b)

Figure 3-2. Continued.

ShearTrac-III load frame: The load frame is the main part of the device which includes the control unit, Horizontal and vertical power systems, water bath, and transducers. The device has two independent control systems along the vertical and horizontal directions which are controlled using a control panel as illustrated in Figure 3-3. Figure 3-4 shows the water bath which is the container to place the direct shear or the simple shear box. The movement of the water bath is generated by two geared screw-jack coupled to a high-speed precision micro-stepper motors in both vertical and horizontal directions. The horizontal movement is generated with a 5kW, high-torque low-inertia MPL series model servo motor that is powered by a three-phase Ultra 3000 digital

servo drive. “The servo motor encoder is read at the very high resolution and used with an advanced adaptive control algorithm specifically developed to control monotonic and cyclic horizontal load and displacement application on specimens of different types without loss of control. The vertical axis is controlled by a closed-loop PID controller with feedback either provided by the load cell or the displacement transducer to obtain load or displacement control” (Zehtab, et. All., 2018). The servo motor is attached to a 5:1 ultra-low backlash in-line gearbox that drives a high-velocity low-friction linear actuator. The linear actuator is connected directly to a 22 kN low-profile interface load cell with a resolution of 1.2 N. The bottom steel part of the water bath is placed on a set of six steel rollers which allows the water bath to move bath back and forth. The water bath is supported against vertical movements and unaligned lateral displacements. The water bath can move in the horizontal direction up to 10 cm (4.0 in). The Movement of the water bath is monitored for both tests along the horizontal direction using a displacement transducer with a range of +/- 90 mm (+/-3.5 in.) and resolution of 0.002 mm (0.00008 in.).

The movement of the water bath in the vertical direction is recorded using the vertical load cell which has the capacity of 44 kN with a resolution of 2.4 N and is attached to the vertical frame. The vertical movement can be up to 5 cm (2.0 in.). Figure 3-5 shows the vertical and horizontal load cells.

Test Accessories: As Illustrated in Figure 3-2, the test accessories of the device include the specially designed square direct shear box, shear box spacer, shear box top cap, lifting beams, fixed-end cross beam, rounded shear rings, and simple shear top cap.

Figure 3-6 shows the direct shear box which consists of two parts of the upper and lower half box with the same height of 101.6 mm. The upper part is a square box with an inner dimension of 305 mm × 305 mm. The lower half box is a rectangular box of 305 mm × 405 mm inner dimension. The length of the lower part of the box can be exactly equal to the upper part of the box by placing the spacer in the lower part. For the purpose of performing interface direct shear test on geosynthetics, the shear box spacer as shown in Figure 3-7 is placed in the lower part of the shear box and the geosynthetic is located on top of the shear box spacer. The clamping plates and clamping bolts were designed to hold the geosynthetic reinforcement in place. Figure 3-7 explains the detail of the shear box for geosynthetic interface test. The rigid top cap for the direct shear test is an aluminum plate which is placed on top of the specimen in the shear box and is transfer the applied load from the steel loading piston to the specimen. As described in chapter II, one part of the direct shear box should be fixed along the three directions and the other half of the shear box will move horizontally along the shear axis. In this apparatus, during the shearing phase, the upper half of the box is fixed using the cross beam, and the lower half of the box is moved horizontally by pushing the water bath. Before applying the shear displacement, the specific amount of gap should be created between two parts of the box to prevent sliding the shear box edges on each other. This gap is provided using two lifting beams. More explanation will be provided in the next chapter, test procedure.

Test accessories for monotonic/cyclic simple shear tests including the stack of simple shear rings and simple shear top cap are explained in detail in the next section of this chapter.

Computer: The device is fully automated, and all sensors are connected to the PC. SHEAR software designed by the Geocomp co. is used to control the running of tests, collecting test data, and storing the data in a file while the test is running. Running a direct shear test is performed in two phases including consolidation and shear phase. The first phase of each direct shear test is to apply the normal pressure by entering parameters in the consolidation table that shows how the consolidation of the test will run. The constant load can be applied up to 32 steps on the specimen with various duration of loading depending on the type of the soil and interface properties. For example, Table 3-1. Recommended Duration of Consolidation Phase (Geocomp Co., 2015) describes the recommended values by the manual for the maximum and minimum duration of the consolidation phase. The shear table is used to control the behavior of the shear phase. The two possibilities to control the shear phase are displacement and force. By selecting each of these choices, the constant rate of displacement /force is given to the software. At this table, the maximum horizontal displacement and maximum horizontal force are entered 50.8 mm (2 in.) and 22 kN, respectively. This means that during running the test if the horizontal load cell or the horizontal displacement transducer measurements exceed the threshold, the test will stop automatically (Geocomp Co., 2015).

Figure 3-3. Vertical and Horizontal Control Panel

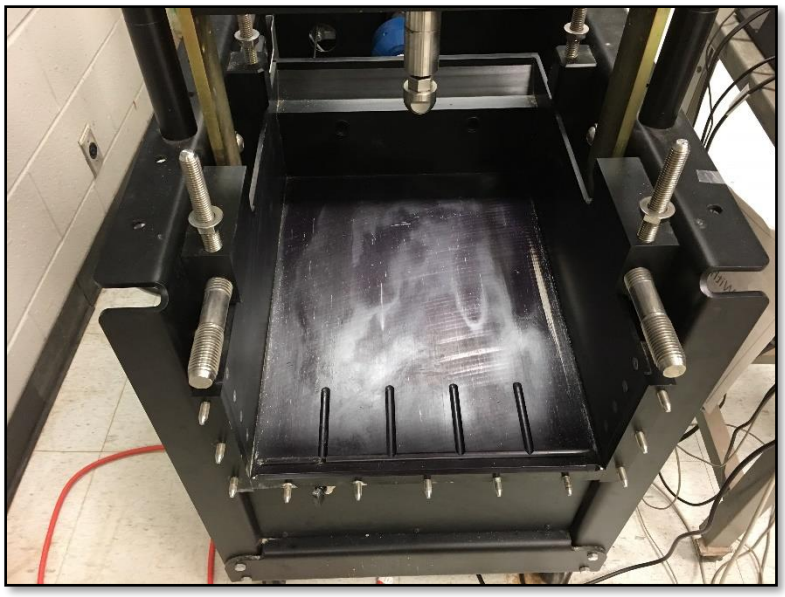

Figure 3-4. Water Bath

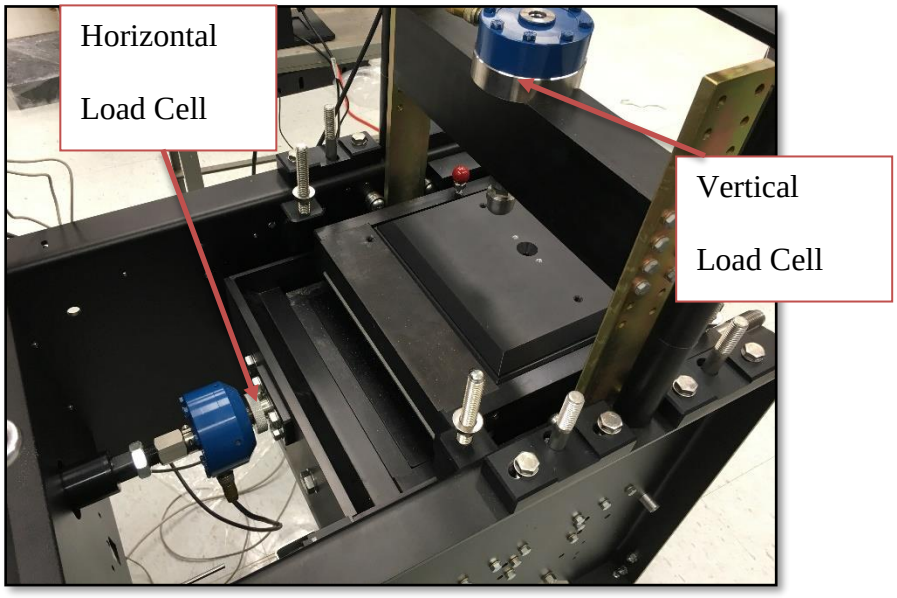

Figure 3-5. Vertical and Horizontal Load Cells

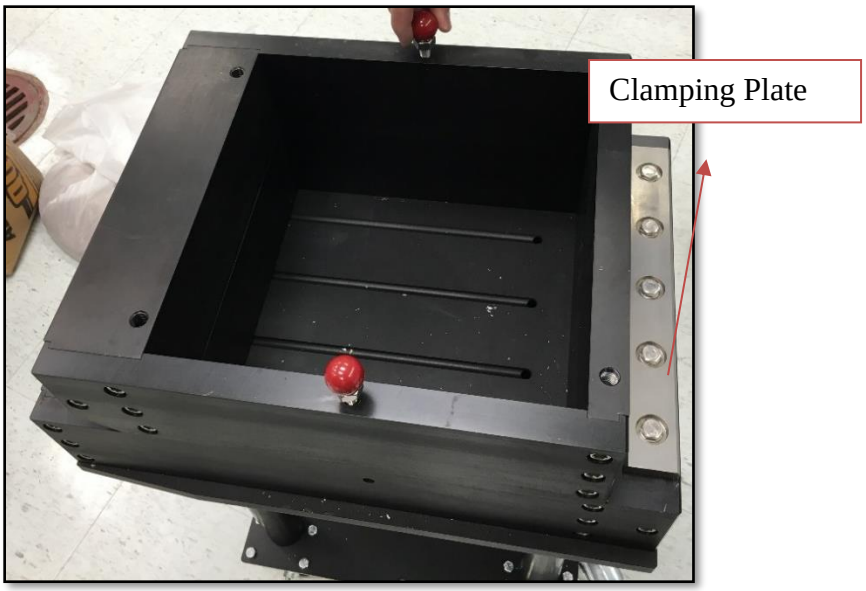

Figure 3-6. The Shear Box

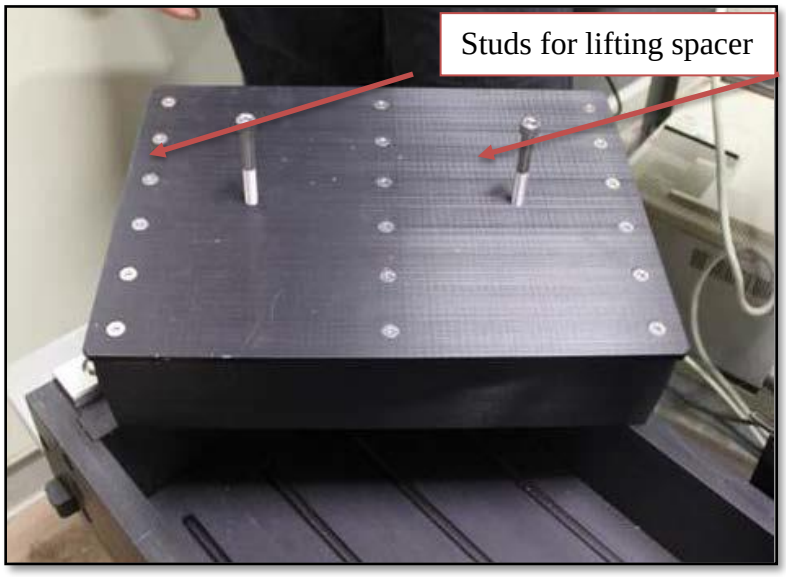

Figure 3-7. Shear Box Spacer

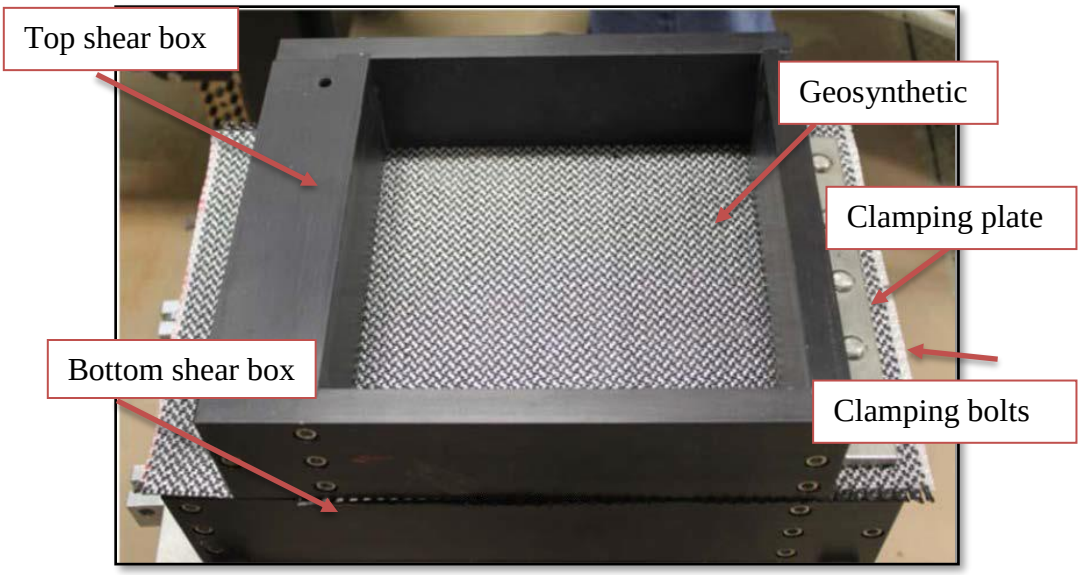

Figure 3-8. Geosynthetic Interface

Table 3-1. Recommended Duration of Consolidation Phase (Geocomp Co., 2015)

Recommended Duration Settings for the Consolidation Phase		
Condition/Soil Type	**Recommended Max. Duration**	**Recommended Min. Duration**
Sandy Silt	1440 min (24 hr)	30 min
Silty Clay	1440 min (24 hr)	60 min
Plastic Clay	1440 min (24 hr)	120 min
Geotextile-Geotextile interface	15 min. (if creep is not significant)	
Geotextile-Geomembrane interface	15 min. (if creep is not significant)	
Geotextile-Clay interface	1 hr.	
Geomembrane-Sand Interface	15 min. (if creep is not significant)	
Geotextile-GCL Interface	24 hr.	
Geomembrane-Clay interface	Measure vertical displacement to get to end of consolidation/swelling	
Geomembrane-GCL interface		
GCL internal		

3.3 Simple Shear Test Device

The before mentioned apparatus allowed us to perform the monotonic direct simple shear test with a cylindrical specimen. The direct shear test setup can be replaced by a simple shear test setup including the rounded base plate and a stack of shear rings. Figure 3-9 describes the detail of the different part of the apparatus for the simple shear test setup. The simple shear sample is prepared inside the shear rings and on the circular base plate. The Teflon-coated aluminum shear rings were fabricated as they have minimum friction during the shearing phase. Therefore, the lateral deformation during shearing is allowed. The inner diameter of the shear ring as illustrated in Figure 3-10 is 300mm, the thickness of each ring is 6.35 mm, and a maximum height of specimen can reach up to 137 mm. Therefore, the minimum ratio of the height to the diameter of the specimen is 0.4 (ASTM D6528-07., 2007). To protect the shear rings from scratching by soil grains, a latex membrane can be used between the inner side of the shear ring and the specimen. The top cap is attached to a rigid steel loading piston and it attached to the vertical load cell. Figure 3-11 shows a sample for simple shear test placed in the water bath box. A rigid steel loading piston is supported by four low-friction steel rollers. Therefore, the movement of the top cap attached to the piston is limited to upward and downward, and the lateral displacement due to the movement of the specimen under the top cap is not allowed (Figure 3-12). The vertical movement of the top cap is measured using three displacement transducers installed on the top of the cap.

The uniform vertical pressure is applied on top of the soil sample using a rigid rounded top cap which is attached to the vertical steel piston. The vertical movement of the top cap is measured by three displacement transducers with 0.002 mm resolution and 90 mm capacity. The displacement rate in both directions can be controlled from 0.00003 to 7.5 mm per minute. The maximum movement of water bath box in the vertical and horizontal direction is up to 5 cm and 10 cm, respectively. The device is capable of performing tests up to a vertical load of 44.5 kN, and 22.5 kN load in the horizontal direction.

The simple shear system is controlled by a software called CDSS3 designed by the Geocomp co. The software runs the test, collect test data, and stores the data in a file while the test is running. Running a simple shear test is performed in two phases including consolidation and shear phase. The first phase of each direct shear test is to apply the normal pressure by entering parameters in the consolidation table that shows how the consolidation of the test will run. Like the direct shear test, the consolidation load can be applied up to 32 steps on the specimen with various duration of loading depending on the type of the soil and interface properties. The shear table is used to control the behavior of the shear phase. The two possibilities to control the shear phase, displacement and force were assigned to the apparatus by selecting the parameters of the shear table. (Geocomp Co., 2015).

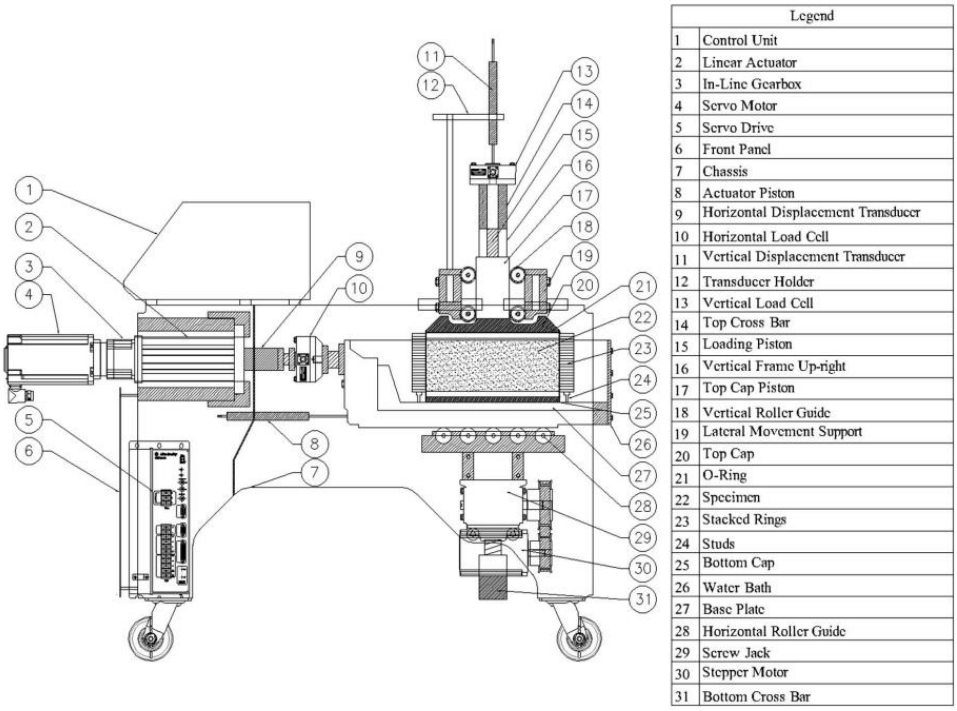

Legend	
1	Control Unit
2	Linear Actuator
3	In-Line Gearbox
4	Servo Motor
5	Servo Drive
6	Front Panel
7	Chassis
8	Actuator Piston
9	Horizontal Displacement Transducer
10	Horizontal Load Cell
11	Vertical Displacement Transducer
12	Transducer Holder
13	Vertical Load Cell
14	Top Cross Bar
15	Loading Piston
16	Vertical Frame Up-right
17	Top Cap Piston
18	Vertical Roller Guide
19	Lateral Movement Support
20	Top Cap
21	O-Ring
22	Specimen
23	Stacked Rings
24	Studs
25	Bottom Cap
26	Water Bath
27	Base Plate
28	Horizontal Roller Guide
29	Screw Jack
30	Stepper Motor
31	Bottom Cross Bar

Figure 3-9. Large Direct Shear and Simple Shear Apparatus (Zehtab et.al., 2018)

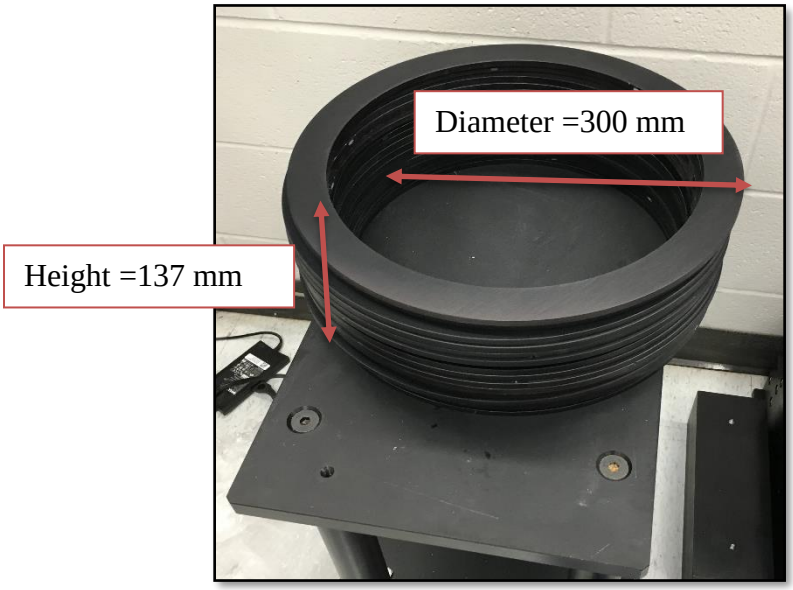

Figure 3-10. Stack of Simple Shear Rings

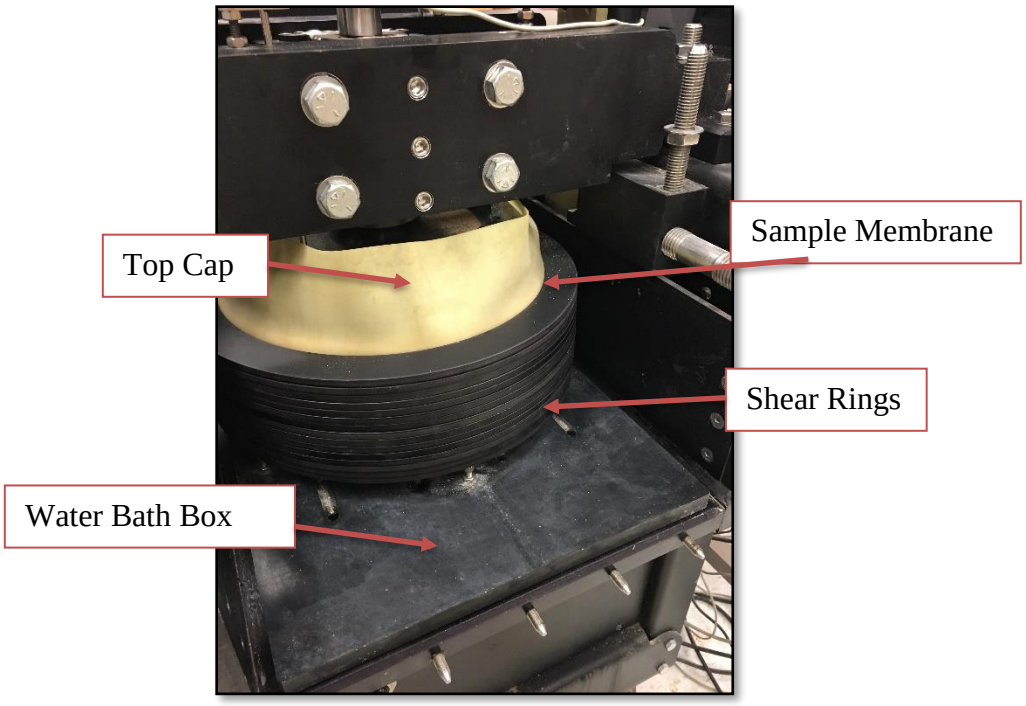

Figure 3-11. Specimen in the Simple Shear Device

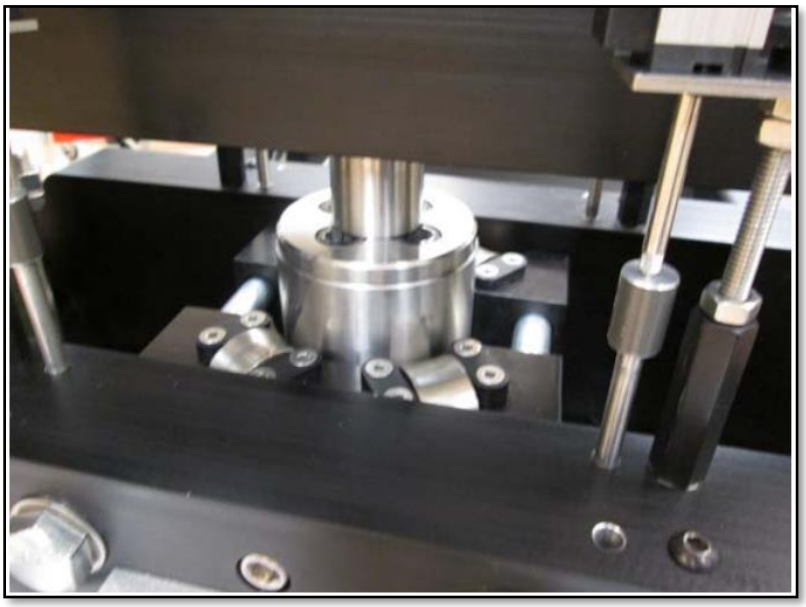

Figure 3-12. Crossbar and Roller Configuration

3.4 Pullout Test Device

Based on FHWA, the soil-interaction, pullout capacity coefficient is a required parameter to design MSE walls and is developed by pullout test. The pullout device used in this study is located at Big R Bridge, Texas (Figure 3-13). The pullout tests for this experimental test program was performed in a state-of-practice pullout apparatus that was specifically developed for the program. The pullout apparatus was fabricated in conformance with the recommendations of the ASTM D 6706, Standard Test Method for Measuring Geosynthetic Pullout Resistance in Soil and modified to remove boundary effects that have been recognized and reported in the literature. The device consists of a pullout soil box, reaction frame, load frame, hydraulic system, instrumentation tools, and the data acquisition system. Each component of the device is briefly described in the following sections and more detailed information regarding this device can be found in Tayler 2018. Figure 3-14 shows different components of the apparatus schematically.

Figure 3-13. Pullout Test Apparatus (Taylor, 2018)

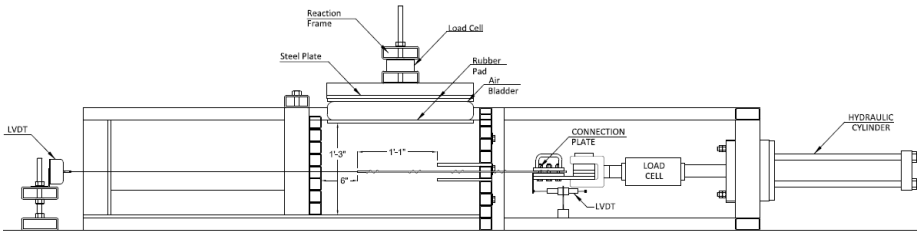

(a)

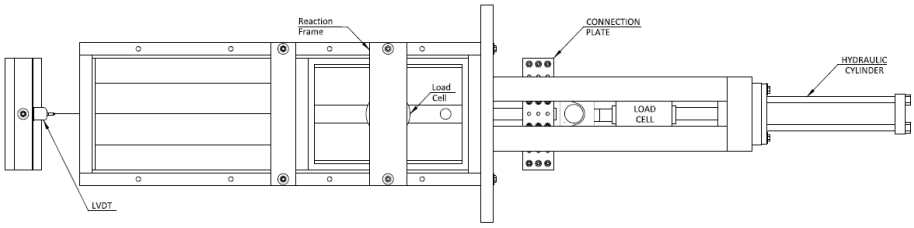

(b)

Figure 3-14. Pullout Device, a) Section View, b) Plan View

3.4.1 Pullout Box

The dimension of the box is to 1.5 m (60 in.) length, 0.45 m (18 in) width, and 0.375 m (18 in.) depth. The box designed as by placing a cross diaphragm inside the box, the length of the box can be varying. The box is used to contain soil and reinforcement to simulate in situ condition. The diaphragm has steel plates with the dimension of the 0.1m × 0.1 m × 0.006m (4 in. × 4 in. × ¼ in.) welded to a 0.05 m × 0.1 m × 0.006 m (2 in. × 4 in. × ¼ in.) cross member. For this research, the tests were performed in both full length of the box and the half-length of the box. A 50 mm high slot is adjusted on the front wall between two 50 mm x 50 mm structural steel tubes. Two 12 mm x 300 mm (½ in. x 6 in.) steel plates were welded to the top and bottom of the slot. These sleeve plates will decrease the arching effect from boundaries during the pullout test. The pullout box, when looking toward the front, is shown in Figure 3-15.

Figure 3-15. Pullout Box (Taylor, 2018)

3.4.2 Vertical Reaction Frame

The pullout soil-box was designed with two different vertical reaction frame concepts: Closed-Mount and Elevated-Mount (Taylor, 2018). The Closed-Mount reaction frame consists of a 12 mm (½ in.) thick structural steel plate that has an area equal to the opening of the soil-box plus 100 mm in all directions. The Closed-Mount reaction frame is shown in Figure 3-16. The rectangular tubes on top of the plate are designed to stiffen the plate. The pneumatic bladder pushes back on the 12 mm (½ in.) thick structural steel plates as well as the surface of the compacted soil when inflated. The pressure inside the

pneumatic bladder dictates the load that is then applied to the surface of the soil inside the soil-box.

Figure 3-16. Pullout Box with Closed-Mount (Taylor, 2018)

The Elevated-Mount consists of structural steel tubing and 19 mm (¾ in.) high strength all-thread rods, washers, and nuts. Two-high strength all-thread rods are attached to the opposing side rails of the soil-box. The structural tubing is placed over the high strength threaded rod, so they bridge over and span between the soil-box side rails. Like the Closed-Mount, the steel plates are placed on top of the pneumatic bladder. The structural steel stiffener tubes are used to distribute the load equally to the surface of the steel plates that are on top of the pneumatic bladder. The pressure inside the pneumatic bladder dictates the load that is applied to the surface of the soil inside the soil-box. The Elevated-Mount system is shown in Figure 3-17.

Figure 3-17. Vertical Elevated Reaction Frame (Taylor, 2018)

3.4.3 Horizontal Load Frame

The horizontal load frame consists of welded 50 mm x 100 mm x 6 mm (2 in. x 4 in. x 1/4 in.) structural steel tubing. The horizontal load frame is used to mount the hydraulic actuator. The load frame with hydraulic actuator is shown in Figure 3-18.

Figure 3-18. Horizontal Load Frame (Taylor, 2018)

3.4.4 Hydraulic Load System

The horizontal load system consists of a two-way hydraulic cylinder (Taylor, 2018). The hydraulic cylinder used in the test program consisted of a body with a 125 mm (5 in.) bore and a 50 mm (2 in.) threaded rod. The maximum extension force of the hydraulic cylinder using 21 MPa (3000 psi) line pressure, is equal to 260 kPa (58,000 lbf). The maximum retraction force of the hydraulic cylinder, using the same line pressure, is equal to 220 kN (50,000 lbf). The maximum stroke of the hydraulic cylinder is 455 mm (18 in.). The cylinder is mounted to the horizontal reaction frame as shown in Figure 3-19.

Figure 3-19. Horizontal Cylinder (Taylor, 2018)

3.4.5 Clamping System

The soil-reinforcing is clamped to the hydraulic actuator using a special compression clamp (Taylor, 2018). The clamping system consists of two opposing harden steel plates. The hardened steel plates are attached to the rod end using the clevis that is attached to the hydraulic cylinder rod-end. The connection is fabricated so the hardened steel plates are free to rotate in all directions. Rotation of the connection components prevents uneven force application and allows the soil-reinforcing to displace freely. The inside surface of the connection plates is fabricated with a series of pointed serrations, like the hardened points that are on a steel file. Each of the steel plates is fabricated with a series of through-bores that allow for the attachments of all-thread bolts. The lower plate through-bores are threaded so all-thread bolts can be attached so they protrude through the top surface and then through the through-bores of the top plate. The soil-reinforcing element is sandwiched between the top and bottom serrated connection plate. A bearing element of the soil-reinforcing is typically positioned at the trailing edge of the top plate. Once the soil-reinforcing is placed in the connection plates the plates are secured and tightened using a series of nuts (Figure 3-20).

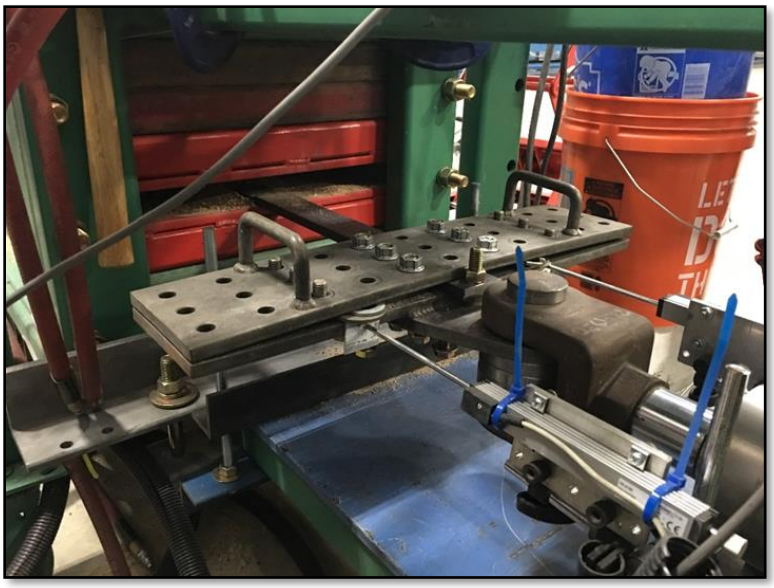

Figure 3-20. Soil-Reinforcing Clamp (Taylor, 2018)

3.4.6 Hydraulic System

The hydraulic system consists of a power unit, flow controls and the hydraulic actuator (Taylor, 2018). The power unit consists of a motor, hydraulic pump, and a reservoir. The hydraulic system is placed in-line with a chiller. The chiller is used to cool the hydraulic fluid that is returned to the system before it is pumped back into the reservoir. The hydraulic unit and chiller are shown in Figure 3-21.

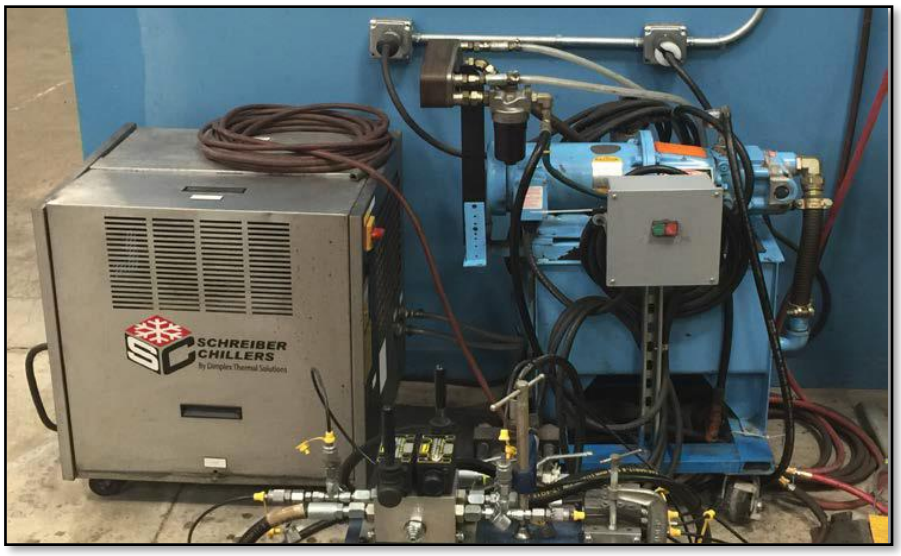

Figure 3-21. Hydraulic Power Unit and Chiller (Taylor, 2018)

The hydraulic flow control consists of a series of directional control valves and flow reducers. The hydraulic system has been designed to allow for manual adjustment of the rate of retraction of the rod-end. The rate of retraction of the rod-end for this experimental test program varied from 1 mm/min to 3 mm/min. The flow control system is shown in Figure 3-22.

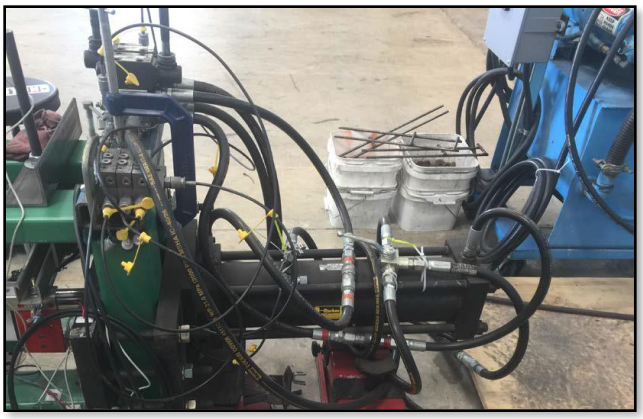

Figure 3-22. Hydraulic Flow Control System (Taylor, 2018)

3.4.7 Load Cells

Two load cells are placed to measure the horizontal and vertical force applied to the soil-reinforcing. One end of the horizontal load cell is attached to the horizontal actuator rod and the other end is attached to a rod extender that is then attached to a clevis. The vertical load cells are placed between the reaction frame and the structural steel beams above the pneumatic bladder. The vertical and horizontal load cells are shown in Figure 3-23.

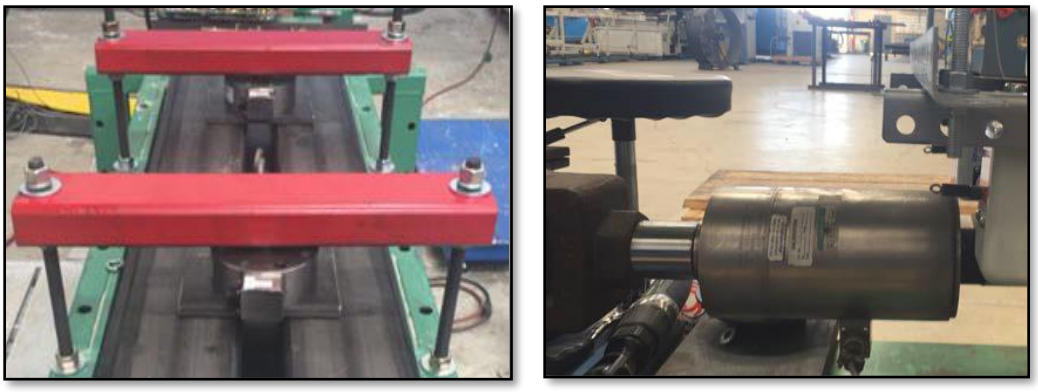

(a) (b)

Figure 3-23. Load Cells, (a) Vertical, (b) Horizontal

3.4.8 Position Sensors

There are two different position transducers used with the pullout soil-box (Taylor, 2018). These include a Linear Variable Differential Transformer (LVDT) and a wire-rope potentiometer. Both transducers are mounted outside the soil-box at strategic locations. The position sensors monitor the displacement of the soil-reinforcing during application of the load. The position sensors are shown in Figure 3-24.

(a) (b)

Figure 3-24. Position Sensors, (a) LVDT – Front of Soil-Box, (b) Wire Rope – Back of Soil-Box

3.4.9 Inflatable Pneumatic Diaphragm

The inflatable pneumatic diaphragm was specifically manufactured for this application (Taylor, 2018). The profile of the inflatable pneumatic diaphragm was 25 mm (1 in.) in length, and width, less than the plan area of the soil-box chamber, i.e. 430 mm x 1500 mm (17 in. x 59 in.). The pneumatic diaphragm was manufactured to be able to provide a simulated overburden of depth of 9 m (30’-0 in.) and 180 kPa (26 psi) of pressure. The pressure in the inflatable pneumatic diaphragm was controlled using a fine thread pressure regulator attached to an Omega general purpose pressure gauge. The inflatable pneumatic diaphragm for the large soil-box is shown in Photograph 3-13. and the inflation control system is shown in Photograph 3-14

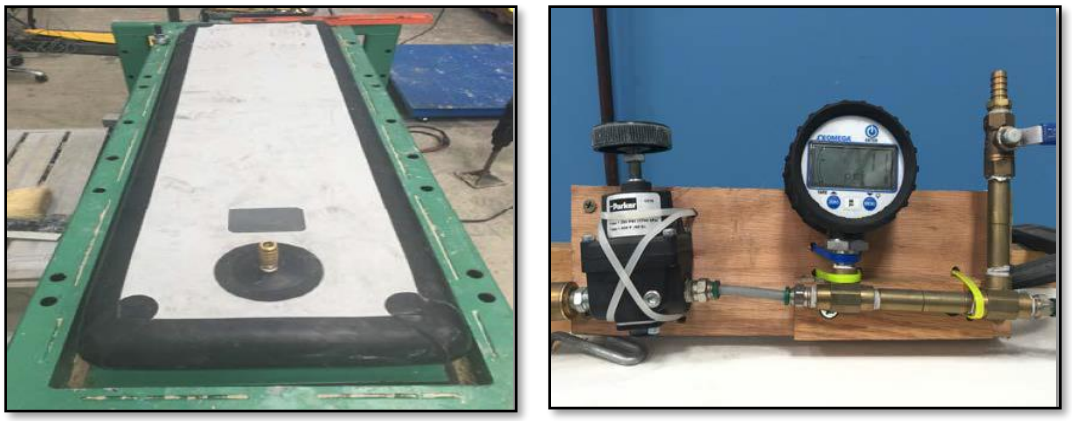

(a) (b)

Figure 3-25. Inflatable Pneumatic Diaphragm, (a) Pneumatic Diaphragm, (b) Pneumatic Control

3.4.10 Data Acquisition System

The data accusation system consists of Campbell Scientific components and software program (Taylor 2018). The datalogger consisted of a CR10X Wiring Panel. The wiring panel provided sensor measurements, timekeeping, data reduction, data/program storage, and control functions. In addition to the CR10X, the AVW4 amplification and signal conditioning system was used to connect to vibrating-wire transducers. To collect the data the Campbell Scientific, PC400 datalogger software was used. The data acquisition system is shown in Figure 3-26.

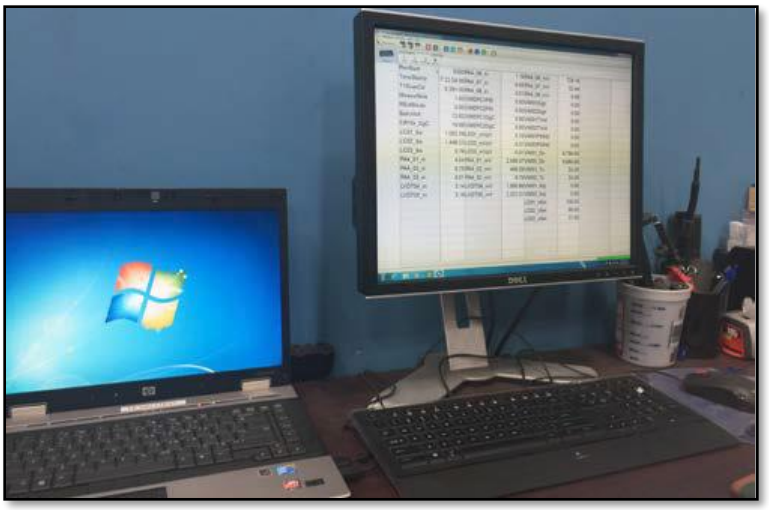

Figure 3-26. Data Acquisition system

3.5 Soil Material

As mentioned in the previous chapter, the purpose of this research is first to study the shear behavior of soil and coarse aggregates that are too large to be tested in a standard direct and simple shear apparatus, second, to evaluate the effect of the grain size, soil density, normal stress, and ribs spacing on the interface shear resistance and pullout resistance of various reinforcements embedded in soil aggregates. Two type of soils were used in this research: loose/dense fine sand and compacted crushed limestone with fines. Sub-rounded dust free play sand was provided to perform fine sand tests. The crushed limestone soil sample was collected from Riverside Campus, TX, USA, and was taken to the soil and aggregate laboratory at Texas A&M University. The soil properties of each soil are characterized by performing particle size analysis (ASTM D 422), Atterberg limits (ASTM D 4318), compaction using standard effort (ASTM D 698), and listed in Table

3-2. The compaction test using standard method was performed on the crushed limes stone with fines passing through a No. 4 (4.7 mm) sieve. Figure 3-28 shows the dry unit weight of soil versus water content of soil obtained from the compaction test. The maximum dry unit weight of soil is 19.8 kN/m^3 and the optimum water content corresponding to the maximum dry unit weight of soil is 9.45%. The soil particles more than 38 mm were removed, and the retained fraction of the sample was classified according to the Unified Soil Classification System (USCS) (ASTM, 2011a). To satisfy this requirement, the soil particles more than 38 mm were removed. Figure 3-27 illustrates the grain size distribution of the soil materials. Based on USCS classification, the soil specimens classified as poorly graded sand (SP) for fine sand, and poorly graded gravel (GP) for crushed limestone with fines. The maximum grain size for fine sand and crushed limestone with fines are 2mm and 23 mm, respectively. For this study, the effect of fine materials on the shear properties of crushed limestone, the DST and DSST were conducted on crushed limestone with 20% fines of low plasticity (PI = 2.8, PL = 12.5).

Table 3-2. Mechanical Properties of Soil Material

Property	**Sand**	**Crushed Limestone with Fines**
D_{10} (mm)	0.147	0.0525
D_{30} (mm)	0.26	0.1427
D_{50} (mm)	0.36	2.8
D_{60} (mm)	0.41	10.192
D_{80} (mm)	0.8	20
Coefficient of uniformity	2.79	194.13
Coefficient of curvature	1.12	0.038
Optimum Water Content (%)	-	9.45
USCS symbol	SP	GP

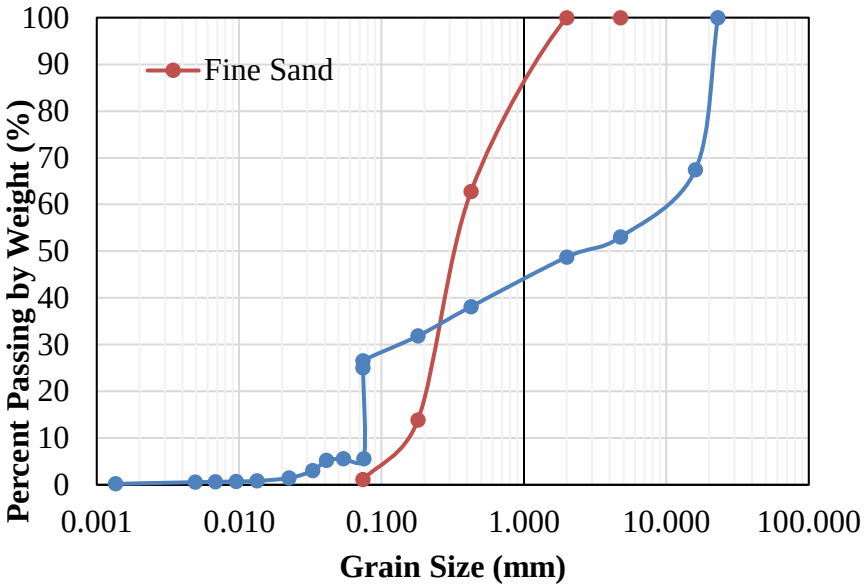

Figure 3-27. Grading Curve of Play Sand and Crushed Limestone with Fines

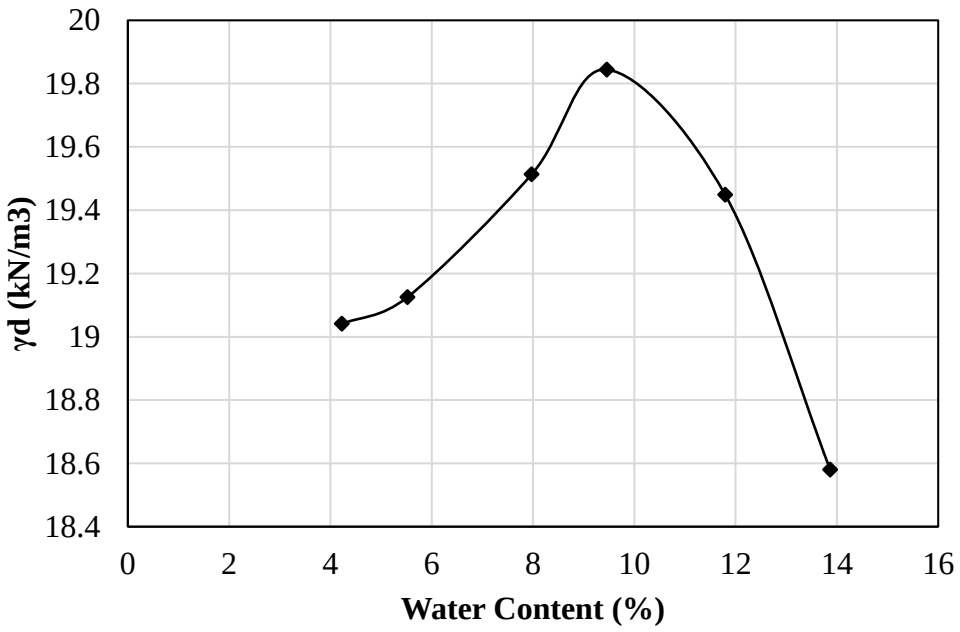

Figure 3-28. Compaction Curve for Limestone

3.6 Reinforcements

This experimental and numerical study was focused on a study the behavior of three kinds of reinforcements including, smooth/ribbed steel strip, Geogrid, and Geostrap using interface direct shear and pullout tests.

3.6.1 Steel Strip Reinforcements

Galvanized ribbed steel strip reinforcements which are manufactured by the Reinforced Earth Company (RECO) was the main focus of this research (Figure 3-29). The strip reinforcement has 50 mm width, 4 mm thickness, and varies length depend on the test type. The reinforcement has ribs 3 mm in height on both sides of the strip. The detail section of the ribs and the spacing of the ribs on the strip are shown in Figure 3-30.

Figure 3-29. RECO Reinforcement

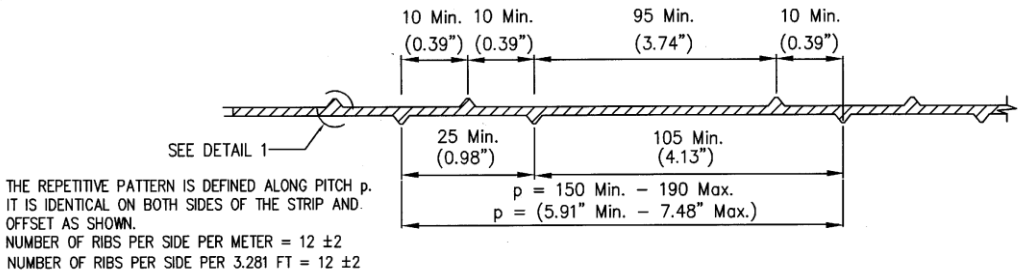

(a)

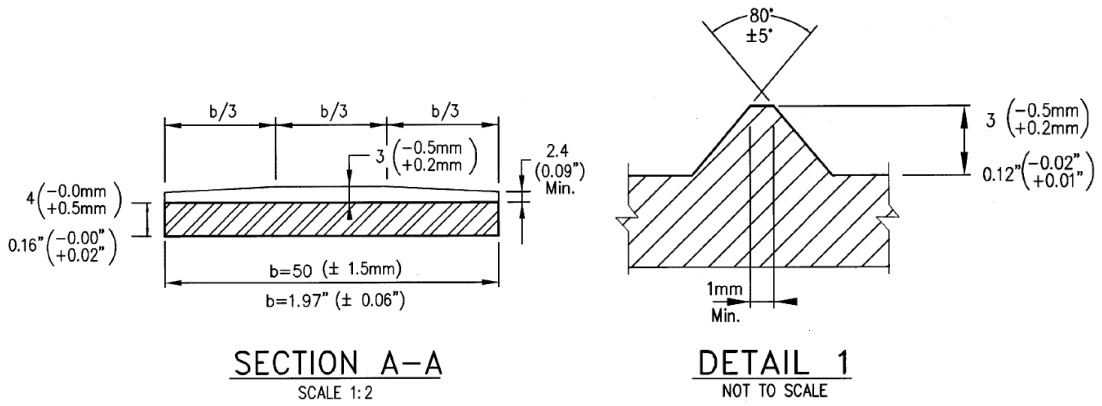

(b) (c)

Figure 3-30. Ribbed Steel Strip, (a) Longitudinal Section, (b) Transverse Section, (c) Detail of Ribs

The main goal of this research is to study the influence of the ribs spacing using both pullout tests and interface direct shear test. For interface direct shear tests, five square aluminum plates with a width of 30.48 cm and a thickness of 0.635 cm were manufactured in a machine shop. The ribs with the exact detail as shown in Figure 3-30 c were carved on this plates with different spaces. The plates were built with no ribs, 2 ribs (ribs space = 10.16 cm), 4 ribs (ribs space = 6.1 cm), 6 ribs (ribs space = 4.06 cm), and 9 ribs (ribs space

= 2.54 cm). Soil reinforcement elements for the interface direct shear tests on smooth/ribbed steel reinforcements are explained in Table 3-4. Figure 3-31 illustrates the cross-section view and the plan view of the aluminum plates with the ribs spacing. The bottom half of the box of the direct shear apparatus was replaced with a play wood spacer and the aluminum plate. The thickness of the spacer and the aluminum plate were designed as they fit in the half of the box, and the ribs stand over the surface of the bottom box.

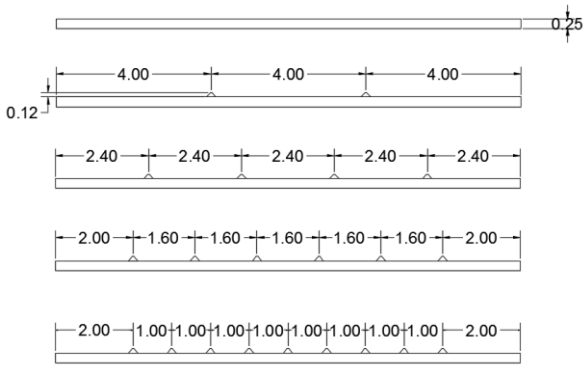

(a)

Figure 3-31. Cross Section of Smooth/Ribbed Aluminum Plate

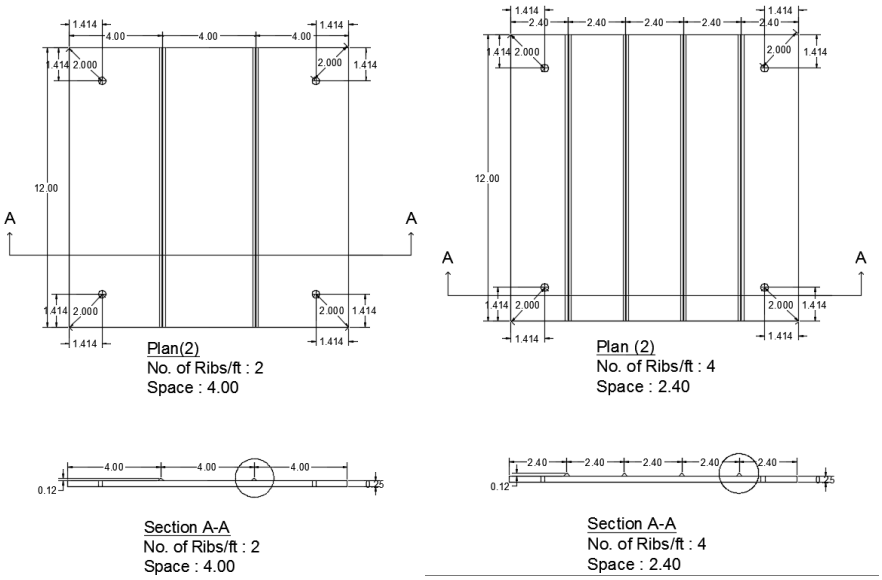

(b) (c)

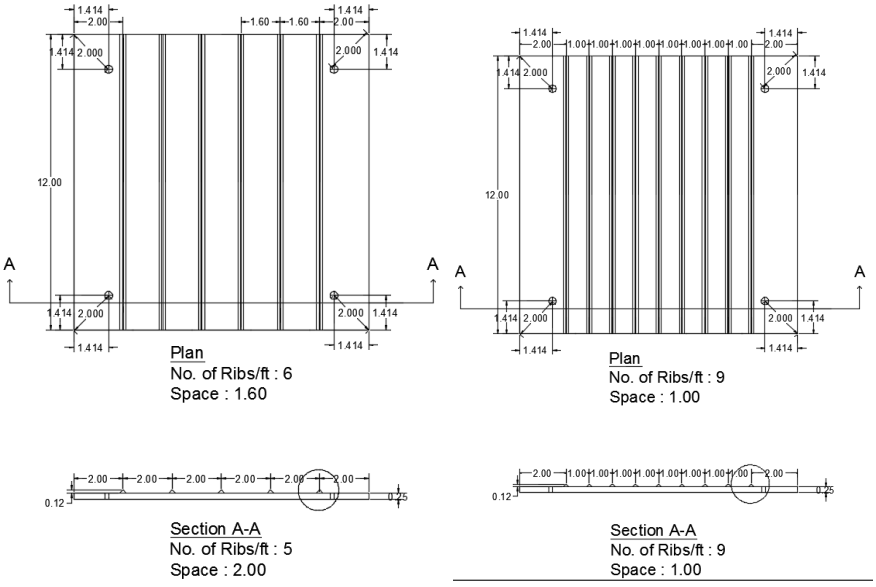

(d) (e)

Figure 3-31. Continued.

Table 3-3. Description of the Steel Reinforcements-Interface Direct Shear Test

Reinforcement No.	No. Of Ribs per ft. per Side	Ribs Spacing mm (in.)	Embedded Length mm (in.)
1	0		304.8 (12)
2	2	101.6 (4)	304.8 (12)
3	4	60.96 (2.4)	304.8 (12)
4	6	40.64 (1.6)	304.8 (12)
5	9	25.4 (1)	304.8 (12)

Figure 3-32 shows the aluminum plate with six ribs on it. As shown in Figure 3-32 the four holes in the corner are built to connect the plate to the wooden spacer. The two holes close to the edges were made to place the stud for lifting the plate easier. More details were presented in the next chapter.

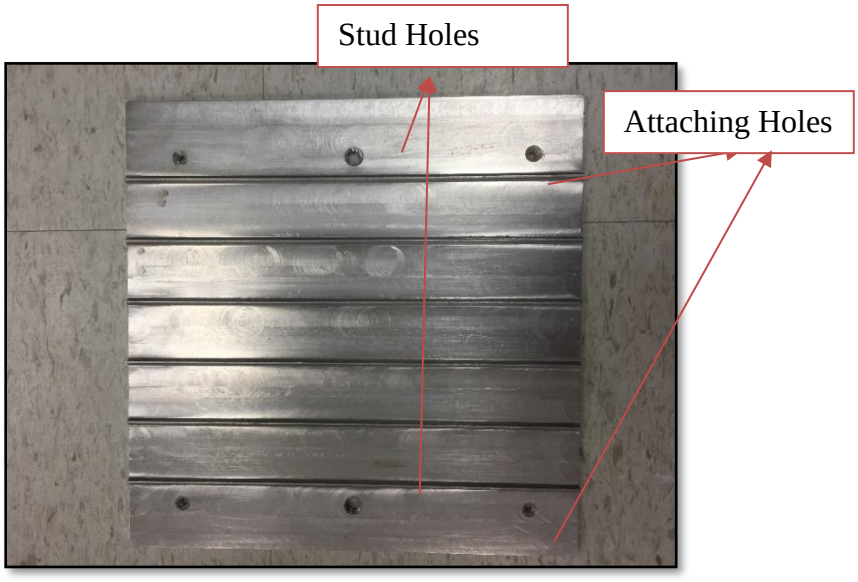

Figure 3-32. Ribbed Aluminum Plate

In order to compare the interface direct shear test results with the pullout test results, three smooth/ribbed steel strips were made with the no ribs, 2 ribs (ribs space = 10.16 Cm), 4 ribs (ribs space = 6.1 Cm), and 9 ribs (ribs space = 2.54 Cm). The rib's dimensions were exactly the same as the RECO strips and the ribs spacing were the same as aluminum plates designed for the interface direct shear test. As mentioned before the pullout box were designed as the length of the box can be variable and tests were designed to be conducted with the half-length of the pullout box. The tests were performed in the half box as the length of the strip to contact with the soil to be 10.48 Cm (12 inches.), the same length of the aluminum plates for IDST. Figure 3-33 shows a drawing of the cross-section of the smooth/ribbed galvanized steel reinforcements to be tested in a half box of the pullout device. As shown in this Figure, 40.64 Cm (16 in.) of the strip reinforcements were made with the thickness of the 1.12 Cm (0.44 in.) which is the part of the strip stays outside of the box at the location of the connection clamp. 50.8 Cm (20 in.) of the strips were located inside the box and 30.48 Cm (12 in.) of the strip reinforcements were in contact with the soil as shown in Figure 3-34. Table 3-4 explains the description of the reinforcement elements were utilized to perform half box pullout tests.

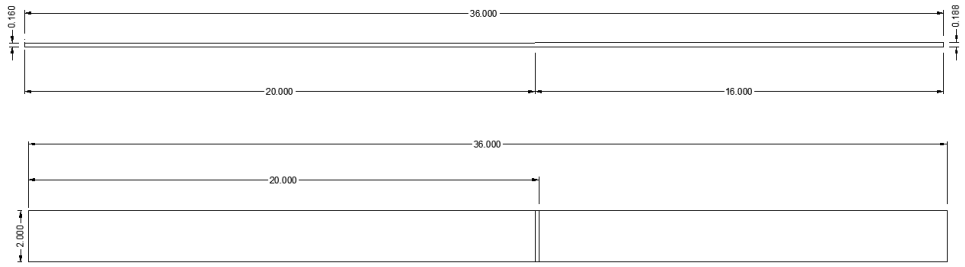

(a)

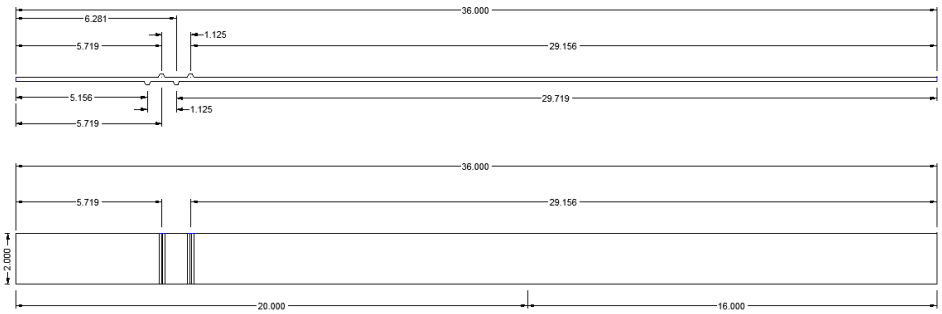

(b)

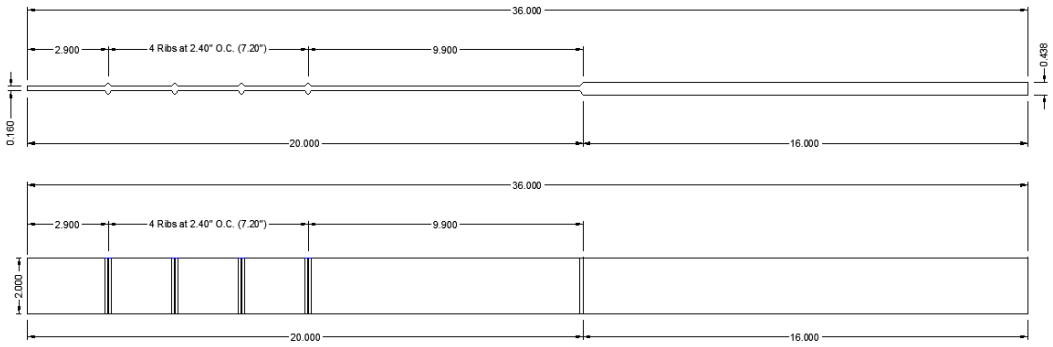

(c)

Figure 3-33. Steel Strip Reinforcements-Half Box Tests, (a) Smooth, (b) 2 Ribs, (c) 4 Ribs, (d) 9 Ribs

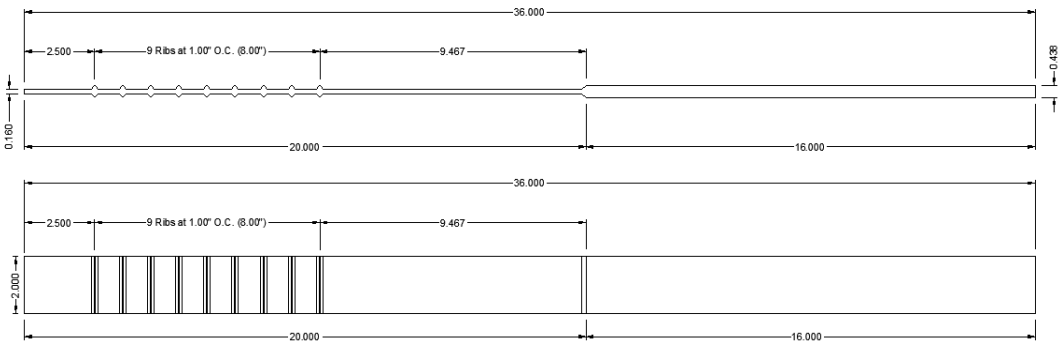

(d)

Figure 3-33. Continued.

Figure 3-34. Plan View of the 9-Ribbed Steel Strip-Half Box

Table 3-4. Description of the Steel Reinforcements-Pullout Test-Half Box

Reinforcement No.	No. Of Ribs per ft. per Side	Ribs Spacing mm (in.)	Embedded Length mm (in.)
1	0		304.8 (12)
2	2	101.6 (4)	304.8 (12)
3	4	60.96 (2.4)	304.8 (12)
4	9	25.4 (1)	304.8 (12)

The reinforcement elements designed for full box pullout tests were RECO strips which are 1.06 m long, 0.0508 m wide, and 0.004 m thick. The detail of the reinforcements is demonstrated in Figure 3-30. To study the influence of the ribs spacing on the pullout force in conformance with the recommendations of the ASTM D6706, four smooth/ ribbed galvanized steel strip reinforcement were manufactured with a various number of ribs per side. Table 3-5 shows the detail explanation of reinforcement elements used for full box pullout tests.

Table 3-5. Description of the Steel Reinforcements-Pullout Test-Full Box

Reinforcement No.	No. Of Ribs per Side	No. Of Ribs per ft. per Side	Ribs Spacing mm (in.)	Embedded Length mm (in.)
1	0	0		1066.8 (42)
2	2	1	259.6 (10.22)	1066.8 (42)
3	4	2	129.8 (5.11)	1066.8 (42)
4	6	4		1066.8 (42)

3.6.2 Geosynthetic Reinforcements

Two types of geosynthetic reinforcements were used in this research including GeoStrap and geogrid reinforcements. The GeoStrap strips are manufactured in Reinforced Earth Co. The strips were manufactured from high tenacity, multifilament polyester yarns placed in tension, then extruded with a polyethylene sheath to form a polymeric strip. The material properties of the GeoStrap are explained in Table 3-6. Figure 3-35 illustrates these GeoStrap materials.

Table 3-6. The Material Properties of GeoStrap

Property	**Test Method**	**Grade**
Mechanical		
Ultimate Tensile Strength (kN)	ASTM D6637	50
Elongation @ Ultimate (average) (%)		11
Polymeric		
Carboxyl End Group (CEG) Count (mmol/kg)	ASTM D 7409	<30
Molecular Weight by Viscosity (g/mol)	ASTM D 4603	>25,000

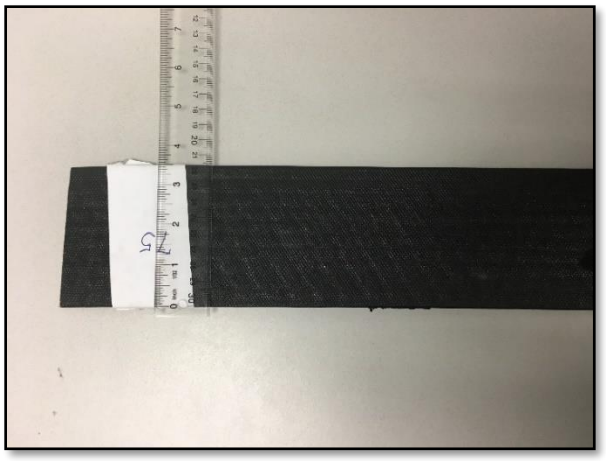

Figure 3-35. GeoStrap Reinforcement

Another geosynthetic reinforcement used in this research is the Geogrid UX1600MSE manufactured in Tensar Co. This Tensar Uniaxial (UX) Geogrid was manufactured from grades of high-density polyethylene (HDPE) resins that are highly oriented and are designed to resist elongation (creep) when subjected to heavy loads for long periods of time. These geogrids are also highly resistant to installation damage as well as long-term chemical or biological degradation. Tensar UX Geogrids have shown no degradation in soils with pH levels measuring as high as 12 and can be used in both dry and wet environments. Given the inert properties of HDPE resins, they can be designed for use with a variety of backfill materials, including on-site soils and recycled concrete. Table 3-7 describes the material properties of the Geogrid UX1600MSE. Each roll of the geogrids has the dimension of the 1.33 m (4.36 ft.) width and 61.0 m (200 ft.) length. Figure 3-36 illustrates the photo of the Geogrid UX1600MSE. As shown in this photo the

spacing between the transverse bars and longitudinal ribs are 2.5 cm and 49.5 cm, respectively. The thickness of the longitudinal and transverse ribs are 4 mm and 22 mm.

Table 3-7. The Material Properties of Geogrid

Index Properties	**Units**	**MD Values**
Tensile Strength @ 5% Strain	kN/m (lb/ft)	58 (3980)
Ultimate Tensile Strength	kN/m (lb/ft)	144 (9870)
Junction Strength	kN/m (lb/ft)	135 (9250)
Flexural Stiffness	mg-cm	6,000,000
Durability		
Resistance to Long-term Degradation	%	100
Resistance to UV Degradation	%	95
Load Capacity		
Maximum Allowable Strength for 120-year Design Life	kN/m (lb/ft)	52.7 (3620)
Recommended Allowable Strength Reduction Factors		
Minimum Reduction Factor for Installation Damage		1.05
Reduction Factor for Creep for 120-year Design Life		2.6
Minimum Reduction Factor for Durability		1

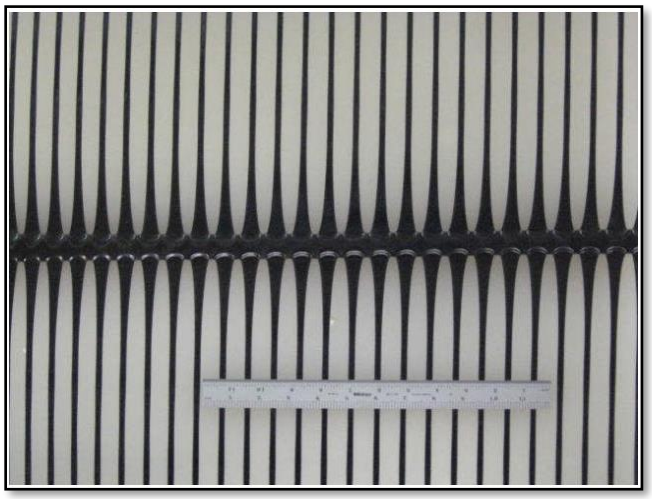

Figure 3-36. UX1600MSE Geogrid Reinforcement

4 TEST PROCEDURE AND RESULTS

A large laboratory campaign (228 tests) was performed including Small Direct Shera test (SDST), Large Direct Shear Test (LDST), Direct Simple Shear Test (DST), Interface Direct Shear Test (IDST), and Pullout Test (PT). This chapter presents the test matrixes, procedure, and results for each before mentioned laboratory tests on fine sand and Crushed Limestone with Fines (CLF). The test plan is presented in Table 4-1 - Table 4-6.

Table 4-1. Test Plan for Small Direct Shear Test- Fine Sand

Test No.	Test Type	Soil Specimen	Soil Density (kg/m3)	Normal Stress (kPa)
1	SDST	Fine Sand	1504	10
2	SDST	Fine Sand	1504	30
3	SDST	Fine Sand	1504	50
4	SDST	Fine Sand	1504	100
5	SDST	Fine Sand	1504	150
6	SDST	Fine Sand	1684	10
7	SDST	Fine Sand	1684	30
8	SDST	Fine Sand	1684	50
9	SDST	Fine Sand	1684	100
10	SDST	Fine Sand	1684	150

Table 4-2. Test Plan for Large Direct Shear Test- Fine Sand

Test No.	Test Type	Soil Specimen	Soil Density (kg/m3)	Normal Stress (kPa)
1	LDST	Fine Sand	1504	10
2	LDST	Fine Sand	1504	30
3	LDST	Fine Sand	1504	50
4	LDST	Fine Sand	1504	100
5	LDST	Fine Sand	1504	150
6	LDST	Fine Sand	1684	10
7	LDST	Fine Sand	1684	30
8	LDST	Fine Sand	1684	50
9	LDST	Fine Sand	1684	100
10	LDST	Fine Sand	1684	150

Table 4-3. Test Plan for Large Direct Shear Test- Crushed Limestone`

Test No.	Test Type	Soil Specimen	Soil Density (kg/m3)	Normal Stress (kPa)
1	LDST	Crushed Limestone With Fines	1768.2	10
2	LDST	Crushed Limestone With Fines	1768.2	10
3	LDST	Crushed Limestone With Fines	1768.2	10
4	LDST	Crushed Limestone With Fines	1768.2	30
5	LDST	Crushed Limestone With Fines	1768.2	50
6	LDST	Crushed Limestone With Fines	1768.2	70
7	LDST	Crushed Limestone With Fines	1768.2	100
8	LDST	Crushed Limestone With Fines	1768.2	150

Table 4-4. Test Plan for Direct Simple Shear Test

Test No.	Test Type	Soil Specimen	Soil Density (kg/m3)	Normal Stress (kPa)
1	DSST	Fine Sand	1504	10
2	DSST	Fine Sand	1504	30
3	DSST	Fine Sand	1504	50
4	DSST	Fine Sand	1504	100
5	DSST	Fine Sand	1504	150
6	DSST	Fine Sand	1684	10
7	DSST	Fine Sand	1684	30
8	DSST	Fine Sand	1684	50
9	DSST	Fine Sand	1684	100
10	DSST	Fine Sand	1684	150
11	DSST	Crushed Limestone With Fines	1768.2	10
12	DSST	Crushed Limestone With Fines	1768.2	30
13	DSST	Crushed Limestone With Fines	1768.2	50
14	DSST	Crushed Limestone With Fines	1768.2	100
15	DSST	Crushed Limestone With Fines	1768.2	150

Table 4-5. Test Plan for Interface Direct Shear Test- Steel Reinforcement

Test No.	Test Type	Reinforcement Type	No. of Ribs/ 30.48 Cm	Rib's Spacing, Cm (inch)	Soil Specimen	Soil Density (kg/m3)	Normal Stress (kPa)
1	IDST	Steel	0		Fine Sand	1504	10
2	IDST	Steel	0		Fine Sand	1504	30
3	IDST	Steel	0		Fine Sand	1504	50
4	IDST	Steel	0		Fine Sand	1504	100
5	IDST	Steel	0		Fine Sand	1504	150
6	IDST	Steel	0		Fine Sand	1684	10
7	IDST	Steel	0		Fine Sand	1684	30
8	IDST	Steel	0		Fine Sand	1684	50
9	IDST	Steel	0		Fine Sand	1684	100
10	IDST	Steel	0		Fine Sand	1684	150
11	IDST	Steel	0		CLF	1768.2	10
12	IDST	Steel	0		CLF	1768.2	30
13	IDST	Steel	0		CLF	1768.2	50
14	IDST	Steel	0		CLF	1768.2	100
15	IDST	Steel	0		CLF	1768.2	150
16	IDST	Steel	2	10.16 (4)	Fine Sand	1504	10
17	IDST	Steel	2	10.16 (4)	Fine Sand	1504	30
18	IDST	Steel	2	10.16 (4)	Fine Sand	1504	50
19	IDST	Steel	2	10.16 (4)	Fine Sand	1504	100
20	IDST	Steel	2	10.16 (4)	Fine Sand	1504	150
21	IDST	Steel	2	10.16 (4)	Fine Sand	1684	10
22	IDST	Steel	2	10.16 (4)	Fine Sand	1684	30
23	IDST	Steel	2	10.16 (4)	Fine Sand	1684	50
24	IDST	Steel	2	10.16 (4)	Fine Sand	1684	100
25	IDST	Steel	2	10.16 (4)	Fine Sand	1684	150

Table 4-5 Continued

Test No.	Test Type	Reinforcement Type	No. of Ribs/ 30.48 Cm	Rib's Spacing, Cm (inch)	Soil Specimen	Soil Density (kg/m3	Normal Stress (kPa
26	IDST	Steel	2	10.16 (4)	CLF	1768.2	10
27	IDST	Steel	2	10.16 (4)	CLF	1768.2	30
28	IDST	Steel	2	10.16 (4)	CLF	1768.2	50
29	IDST	Steel	2	10.16 (4)	CLF	1768.2	100
30	IDST	Steel	2	10.16 (4)	CLF	1768.2	150
31	IDST	Steel	4	6.1(2.4)	Fine Sand	1504	10
32	IDST	Steel	4	6.1(2.4)	Fine Sand	1504	30
33	IDST	Steel	4	6.1(2.4)	Fine Sand	1504	50
34	IDST	Steel	4	6.1(2.4)	Fine Sand	1504	100
35	IDST	Steel	4	6.1(2.4)	Fine Sand	1504	150
36	IDST	Steel	4	6.1(2.4)	Fine Sand	1684	10
37	IDST	Steel	4	6.1(2.4)	Fine Sand	1684	30
38	IDST	Steel	4	6.1(2.4)	Fine Sand	1684	50
39	IDST	Steel	4	6.1(2.4)	Fine Sand	1684	100
40	IDST	Steel	4	6.1(2.4)	Fine Sand	1684	150
41	IDST	Steel	4	6.1(2.4)	CLF	1768.2	10
42	IDST	Steel	4	6.1(2.4)	CLF	1768.2	30
43	IDST	Steel	4	6.1(2.4)	CLF	1768.2	50
44	IDST	Steel	4	6.1(2.4)	CLF	1768.2	100
45	IDST	Steel	4	6.1(2.4)	CLF	1768.2	150
46	IDST	Steel	6	4.06(1.6)	Fine Sand	1504	10
47	IDST	Steel	6	4.06(1.6)	Fine Sand	1504	30
48	IDST	Steel	6	4.06(1.6)	Fine Sand	1504	50
49	IDST	Steel	6	4.06(1.6)	Fine Sand	1504	100
50	IDST	Steel	6	4.06(1.6)	Fine Sand	1504	150
51	IDST	Steel	6	4.06(1.6)	Fine Sand	1684	10

Table 4-5. Continued

Test No.	Test Type	Reinforcement Type	No. of Ribs/ 30.48 Cm	Rib's Spacing, Cm (inch)	Soil Specimen	Soil Density (kg/m3	Normal Stress (kPa
52	IDST	Steel	6	4.06(1.6)	Fine Sand	1684	30
53	IDST	Steel	6	4.06(1.6)	Fine Sand	1684	50
54	IDST	Steel	6	4.06(1.6)	Fine Sand	1684	100
55	IDST	Steel	6	4.06(1.6)	Fine Sand	1684	150
56	IDST	Steel	6	4.06(1.6)	CLF	1768.2	10
57	IDST	Steel	6	4.06(1.6)	CLF	1768.2	30
58	IDST	Steel	6	4.06(1.6)	CLF	1768.2	50
59	IDST	Steel	6	4.06(1.6)	CLF	1768.2	100
60	IDST	Steel	6	4.06(1.6)	CLF	1768.2	150
61	IDST	Steel	9	2.54(1)	Fine Sand	1504	10
62	IDST	Steel	9	2.54(1)	Fine Sand	1504	30
63	IDST	Steel	9	2.54(1)	Fine Sand	1504	50
64	IDST	Steel	9	2.54(1)	Fine Sand	1504	100
65	IDST	Steel	9	2.54(1)	Fine Sand	1504	150
66	IDST	Steel	9	2.54(1)	Fine Sand	1684	10
67	IDST	Steel	9	2.54(1)	Fine Sand	1684	30
68	IDST	Steel	9	2.54(1)	Fine Sand	1684	50
69	IDST	Steel	9	2.54(1)	Fine Sand	1684	100
70	IDST	Steel	9	2.54(1)	Fine Sand	1684	150
71	IDST	Steel	9	2.54(1)	CLF	1768.2	10
72	IDST	Steel	9	2.54(1)	CLF	1768.2	30
73	IDST	Steel	9	2.54(1)	CLF	1768.2	50
74	IDST	Steel	9	2.54(1)	CLF	1768.2	100
75	IDST	Steel	9	2.54(1)	CLF	1768.2	150

Table 4-6. Test Plan for Interface Direct Shear Test- Geosynthetic Reinforcement

Test No.	Test Type	Reinforcement Type	Soil Specimen	Soil Density (kg/m3)	Normal Stress (kPa)
1	IDST	Geogrid	Fine Sand	1504	10
2	IDST	Geogrid	Fine Sand	1504	30
3	IDST	Geogrid	Fine Sand	1504	50
4	IDST	Geogrid	Fine Sand	1504	100
5	IDST	Geogrid	Fine Sand	1504	150
6	IDST	Geogrid	Fine Sand	1684	10
7	IDST	Geogrid	Fine Sand	1684	30
8	IDST	Geogrid	Fine Sand	1684	50
9	IDST	Geogrid	Fine Sand	1684	100
10	IDST	Geogrid	Fine Sand	1684	150
11	IDST	Geogrid	CLF	1768.2	10
12	IDST	Geogrid	CLF	1768.2	30
13	IDST	Geogrid	CLF	1768.2	50
14	IDST	Geogrid	CLF	1768.2	100
15	IDST	Geogrid	CLF	1768.2	150

4.1 Small Direct Shear Test

To compare and validate the shear strengths parameters of the large direct shear tests, the direct shear tests were performed on loose and dense fine sand sample using standard direct shear apparatus.

ASTM standard related to this test can be found in the document ASTM D 3080. In this test, we used the same fine sand which explained in the previous chapter. The sample is poured into the shear box with the bottom cap and sealing plate at the bottom. To obtain comparable results, the required amount of the sand for both cases of loose (1504 kg/m^3) and dense (1684 kg/m^3) were calculated for the small shear box. The sample preparation for loose sand was performed using a small funnel and based on the dry pulviation, or the raining of sand through air method. To prepare the dense sample, the sample was prepared in three layers and compacted by tapping each layer with the plastic hammer. The sand is poured to a height so that the top cap would come out of the circular area of the shear box by its half-height. Then carefully loaded the normal force loading device and adjust the touching groove on the metal hanger with the ball on the top cap, making sure that there would be no miss-alignment between them. Then the shearing device and the data acquisition system are connected to the laptop and test started. This process IS repeated for three different normal loads: 1, 2, and 3 kilograms. For each test, we continued the shearing until the sample failed. This was done by monitoring the variation in voltage readings. The diameter of the specimen for this specific apparatus is 2.5 inches (0.0635 m). The subjected area is then calculated as 0.0031 m^2. Table 4-1 illustrates the test plan for small direct shear test on the loose/dense fine sand. To compare the results of SDST with LDST on fine sand, the results presented in the next section.

4.2 Large Direct Shear Test

A serious of shear tests were performed on fine sand and crushed limestone specimens under various density and vertical stress. Table 4-2 and Table 4-3 describes the test plan of large direct shear tests on selected soil materials. The test procedure for large direct shear test on soil specimens was followed the ASTM D3080, ASTM D-5321, and ASTM D-6243, and is explained as follow:

4.2.1 Test Procedure

Prior to specimen preparation, the test conditions were defined as described in Table 4-2 and Table 4-3. According to the ASTM procedure for a maximum and minimum density for cohesion less soils, D 4253-00, the maximum and minimum dry density of the play sand (the fine sand used in this research) is 1760 kg/m^3 (109.9 pcf) and 1395 kg/m^3 (87 pcf), respectively (Melton & Morgan, 1996). The target dry density of loose and dense fine sand was selected 1760 kg/m^3 and 1395 kg/m^3, respectively. It is worth mentioning that the soil samples were prepared at the air-dry condition.

The first step of the sample preparation is to prepare the required mass of the material to achieve the target density of loose/dense fine sand, and crushed limestone having the dimension of the shear box. Figure 4-1 shows the measured soil specimen. The average water content was determined and recorded using a minimum of three samples of the measured material. Then, the required height of the specimen for each layer was calculated using this equation:

$$h_n = \frac{h_t}{n_t}\left[(n-1) + (1 + \frac{U_n}{100})\right]$$

Where,

h_n is the required height of the specimen at the nth layer, h_t the total height of the specimen, n_t the total number of layers, and U_n the percentage of under compaction for considered layers (Ladd, 1978).

Figure 4-1. Soil Sample Measurements

Next, the bottom half of the shear box was placed on the shear box stand and inside the box were cleaned from the leftover soil samples of the previous test. The rectangular lower half of the box was transferred to the square 305 mm box by placing the small shear

box spacer as shown in Figure 4-2. Now the box is ready to pour the first layer of the soil sample. Since the soil samples were prepared at the air-dry condition, I did not place the porous stone and filter paper at the bottom of the shear box, and the sample was placed directly inside the box.

Depending on the soil type and the density the sample preparation was different. The loose fine sand was prepared inside the shear box using a dry pulviation, or the raining of sand through air method. A funnel was used to pour the sand from very low height to obtain loose density. I poured the sand to the half-height of the lower box. Then, the upper half of the box was placed on top of the bottom box, and the two alignment screws were inserted to fix the top and bottom box during specimen preparation as shown in Figure 4-3. The sample preparation was continued until to a height so that the top cap would come out of the square area of the shear box by its half-height.

Figure 4-2. Lower Shear Box Standing on the Shear Box Stand

Figure 4-3. Placement of Top Shear Box and Alignment Screws

The dense fine sand specimen was compacted in three layers using a vibrator. A different method of compaction was tried to reach the maximum density including the standard compaction as shown in Figure 4-4 an electric vibrator with the speed of 3200 VPM, voltage of 115 VOTLS, and amplitude of 0.5 was attached to a 0.5-inch thickness play wood. After placing the first layer of the fine sand, the sample was compacted using the vibrator plate for 8 minutes. The thickness of the soil layer was measured during the compaction process and compared with the calculated thickness to make sure that the soil

was adequately compacted. After placing and compacting the first layer in the bottom half of the box, the top half of the box was placed on top of the bottom box, and the two alignment screws were inserted to fix the top and bottom box during specimen preparation. The previous steps were repeated until the last layer was in place. Figure 4-5 illustrates the prepared sample in the shear box. After completing the last layer of sample preparation, the top cap was placed carefully on the surface of the specimen, and make sure that the top cap is aligned horizontally as shown in Figure 4-6. To lift the top cap, there are two studs inserted to the top cap and used to lace the top cap on the surface of the specimen.

Figure 4-4. Sample Compaction

The crushed limestone soil sample was compacted in three layers using a rubber hammer. The hammer was hit on a plywood plate which is placed on top of the specimen until reaching the target soil density and the desired thickness.

The exact amount of soil that fit in the shear box and the height of the sample were measured and recorded for each sample. The unit weight of each test was calculated after preparing the soil sample. The average unit weight of loose sand, dense sand, and crushed limestone were equal to 1504 kg/m^3 (93 pcf), 1684kg/m^3 (105.2 pcf), and 1775.5 kg/m^3 (110.4 pcf) respectively.

Figure 4-5. Final Layer of Soil Sample in Direct Shear Box

Figure 4-6. Top Cap Placement

Once the specimen was prepared, the shear box stand was moved in front of the load frame and the specimen was gently slid into the water bath (Figure 4-7 and Figure 4-8). The Bolts were tightened on the back of the container which connects the water bath to the bottom container. Next, the vertical loading piston was initialized using the vertical control panel and jogged down close to the top cap. The alignment screws were removed, and the small sitting load was applied using the Shear software. The apparatus is fully automated and is controlled by the Shear software designed by Geocomp Company. As presented in Figure 4-9 the two lifting beams were placed at each end of the shear box. The lifting beams will provide a gap between two half of the boxes before the shearing

phase started to reduce friction. Next, the fixed-end crossbeam was placed and fixed by tightening the threaded bolts and flange nuts. During the shear phase, the bottom box will move horizontally while the top box stays fixed. The crossbeam is used to prevent the top box from sliding.

Each test was run in two phases, Phase one: applying the normal load (consolidation phase). Phase two: applying the shear displacement at a constant rate (shear phase). Before starting phase two, the gap was provided using the lifting beams.

Starting with the consolidation phase, these series of tests were performed under various normal stresses: 10, 30, 50, 100, and 150 kPa. The higher vertical stress was applied gradually and step by step on the specimen.

When the consolidation phase of the test is completed, a gap was created between the upper and lower halves of the shear box by lifting the top box. This is done to decrease the possibility of metal to metal friction. The ASTM D3080 was followed for the large-scale DST method excluding the gap size. As the ASTM D3080 was established for standard direct shear tests where the maximum gap size is limited to 0.635 mm (0.025 in.). For large scale DST, the size of the gap where selected D85 of the soil specimen, the aggregate size that 85% particles are finer. Therefore, the gap size was selected 0.635 mm to 17.8 mm (0.7 in.) for sand and crushed limestone with fines, respectively. As the tests were performed under the dry condition, the shear rate should not be very slow to dissipate the excess pore water pressure. Therefore, the constant shear rate was selected 0.0001016 m/s. The maximum horizontal displacement was set 50.8 mm (2 in.). The test will stop

when the displacement reaches to this value or the capacity of the load cell (22 kN). The output data of each test for each phase includes vertical displacement, horizontal displacement, vertical load, and horizontal load.

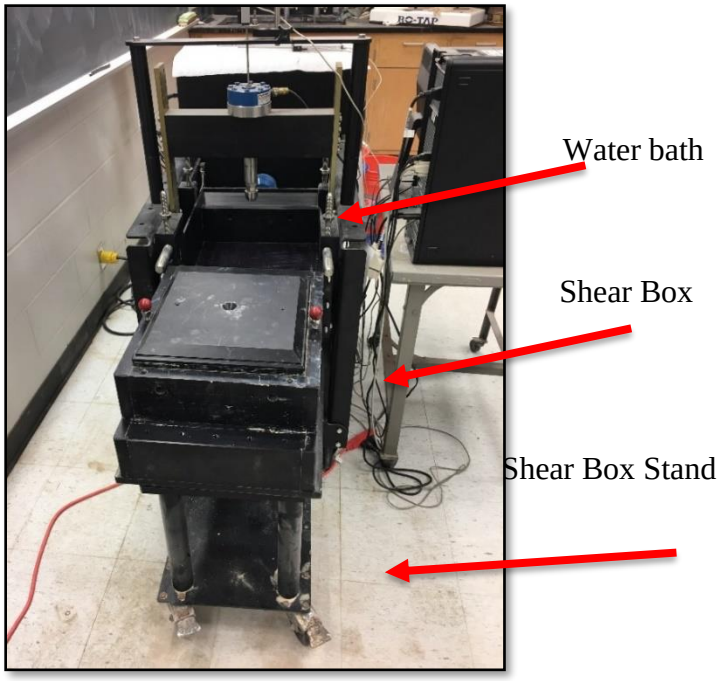

Figure 4-7. Prepared Sample

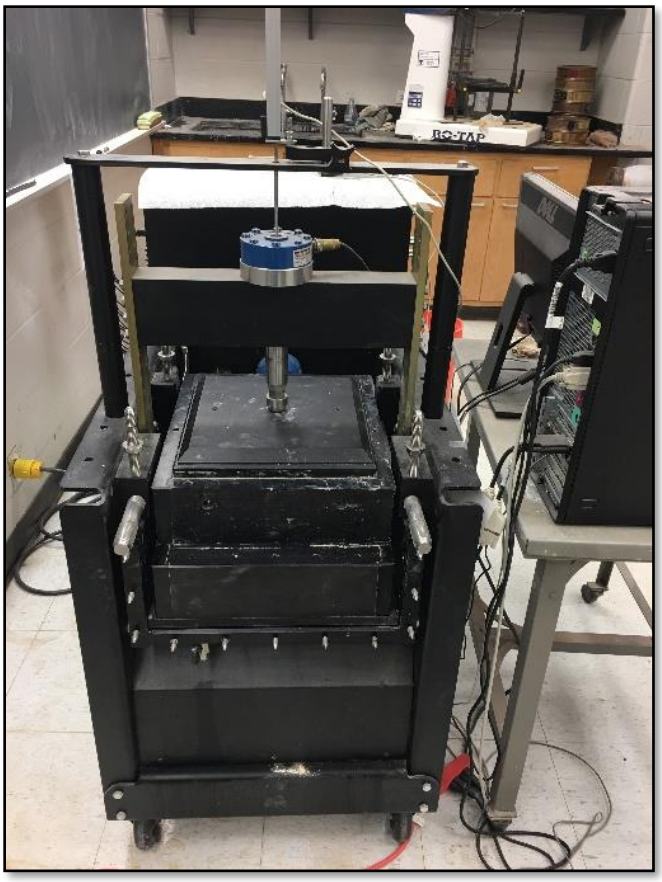

Figure 4-8. Placement of Shear Box in the Water Bath

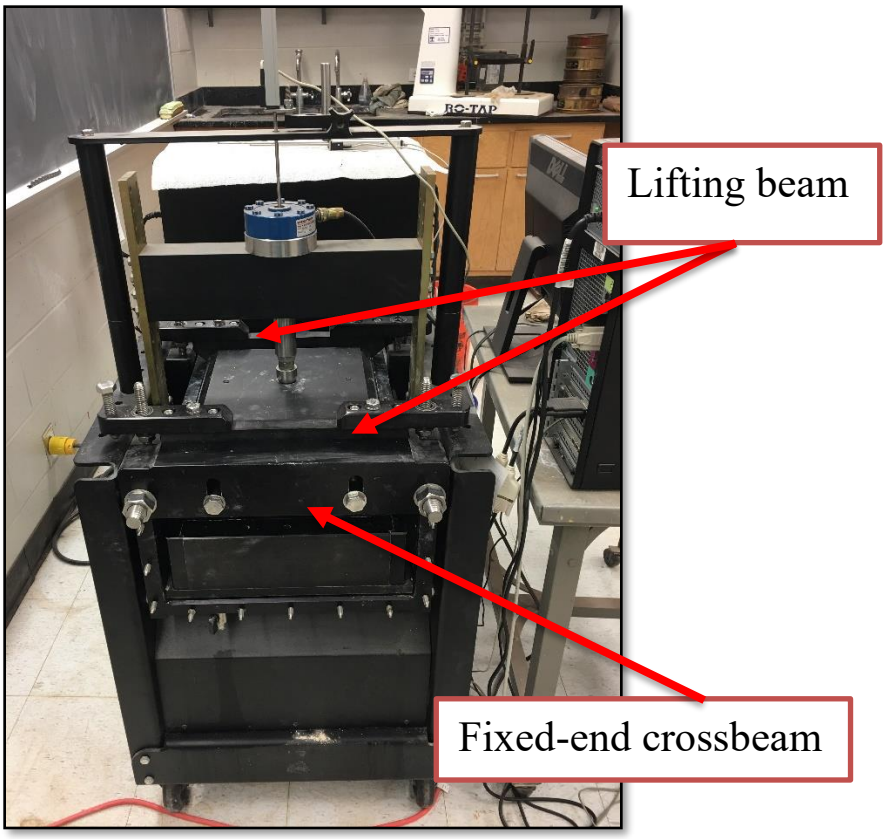

Figure 4-9. Lifting Mechanism and Fixed-End Configuration

4.2.2 Test Results

4.2.2.1 Comparison of Small and Large Direct Shear Test Results

To validate the testing results from large direct shear apparatus, a serious of shear tests were performed on sub-rounded dust free play sand with both small and large direct shear test with the same density and under the same normal stresses. Specimens were prepared to desire density of 1504 kg/m3 and 1685 kg/m3 to present the loose and dense condition, respectively. Tests were performed at an effective normal stress of 12, 32, 52,

102 and 152 kPa according to ASTM D3080. Figure 4-10 shows the shear stress vs. shear displacement curve for loose and dense fine sand. The continues lines represent the results of large direct shear tests and the dash lines show the small direct shear test results. As shown in this figure, the stress-displacement response is nearly identical. The peak value of the shear stress from LDST meets the one from SDST. However, the residual shear stresses obtained from SDST are slightly lower than the LDST. As shown in Figure 4-10(a), for loose sand starting from very low horizontal displacement, the shear stress-horizontal displacement shows a hyperbolic shape of the curve until it reaches the failure. After the failure, the shear stress stays constant with increasing the horizontal displacement. On the other hand, for dense sand, with increasing the horizontal displacement, the shear stress will increase almost linearly to reach the peak value and then decrease to a large-displacement stress (strain-softening). The peak shear strength occurs at the displacement of 0.01-0.02 mm depend on the normal stress. The Mohr-Coulomb failure envelopes for peak and residual loose and dense fine sand are described in Figure 4-11. The envelopes are defined by linear least-squares regression with R^2 ranging from 0.9537 to 0.9999. The apparent cohesion is small for all tests with the range of 0.6-3.7 kPa. It is worth noting that area correction was applied for direct shear test results to calculate the shear stress.

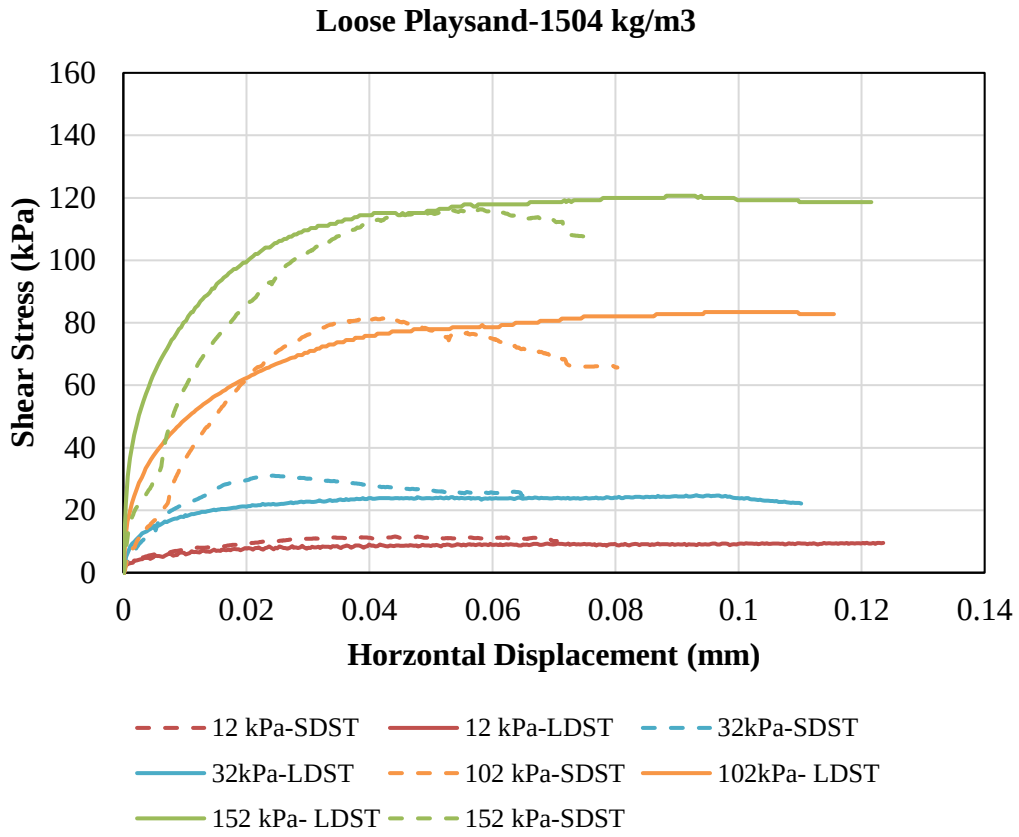

(a)

Figure 4-10. Shear Stress vs. Horizontal Displacement, Large and Small Direct Shear Test, (a) Loose Fine Sand, (b) Dense Fine Sand

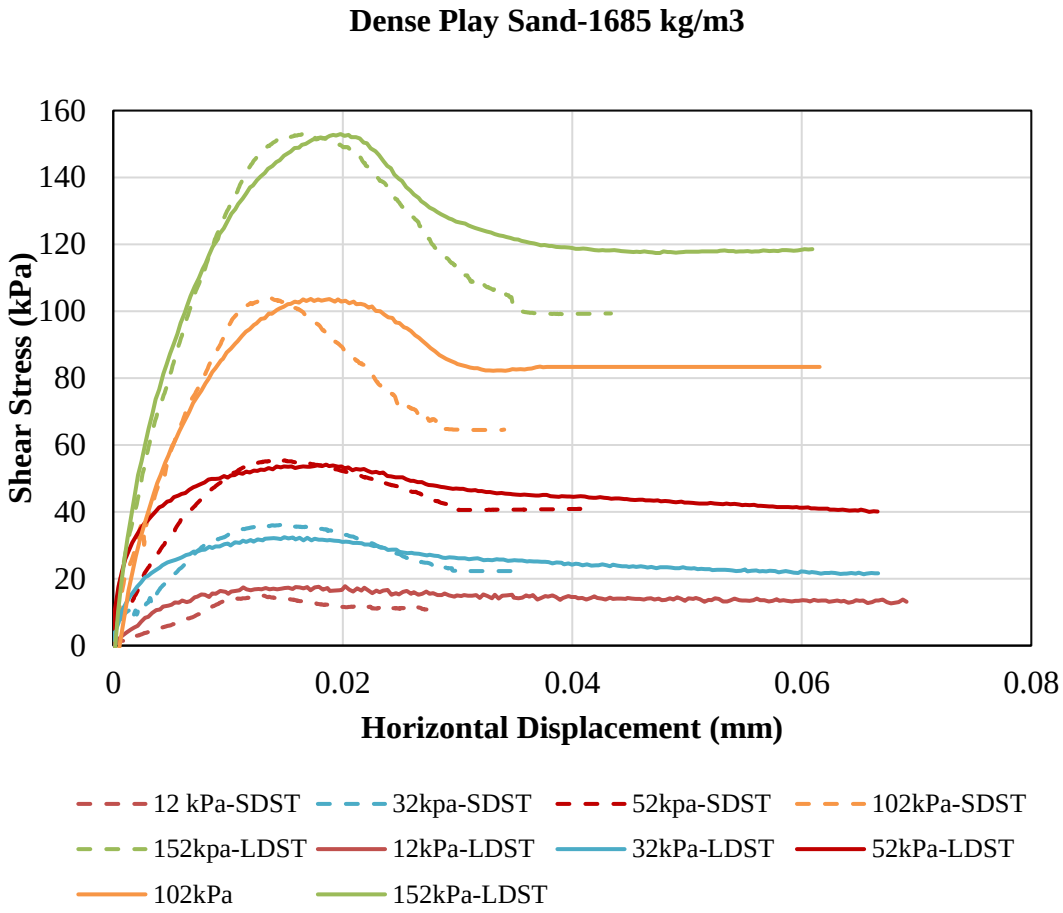

(b)

Figure 4-10. Continued.

The slope of the Mohr-Coulomb failure envelope will provide the friction angle ($\emptyset_s$) of the soil specimen.

$$\emptyset_s = \tan^{-1}\left(\frac{\tau_f}{\sigma_n}\right)$$

A comparison of friction angle obtained from LDST and SDST are shown in Figure 4-11 and Table 6-2. The failure was defined at the maximum shear stress, and the large displacement shear strength was chosen at 0.1 mm for loose fine sand and 0.06 mm for dense fine sand. The peak and residual friction angles of dense sand obtained from LDST is equal to 47° and 42°, respectively. The obtained peak and residual friction angles of dense sand from SDST are calculated at 44.5° and 32°, respectively. This means that the friction angle of dense sand from LDST is 2.5° higher than the SDST. The peak and residual friction angles calculated from the failure envelope of the loose sand are 38° and 37.5° for LDST and 35° and 34° for SDST, respectively. For Loose sand, $\emptyset_{LDST} \approx \emptyset_{SDST}$; the friction angle obtained from LDST is 1° greater than the one from the SDST. It is worth mentioning that at large horizontal displacements, the shear stress increasing slightly compare to the small direct shear tests for both loose and dense sand. This is because the fact which is showing in Figure 4-13; during the shearing phase the dilation occurs at the front of the box and the contraction happens at the back of the box. The numerical simulation of the direct shear test also indicates this fact and will explain more in the next chapter.

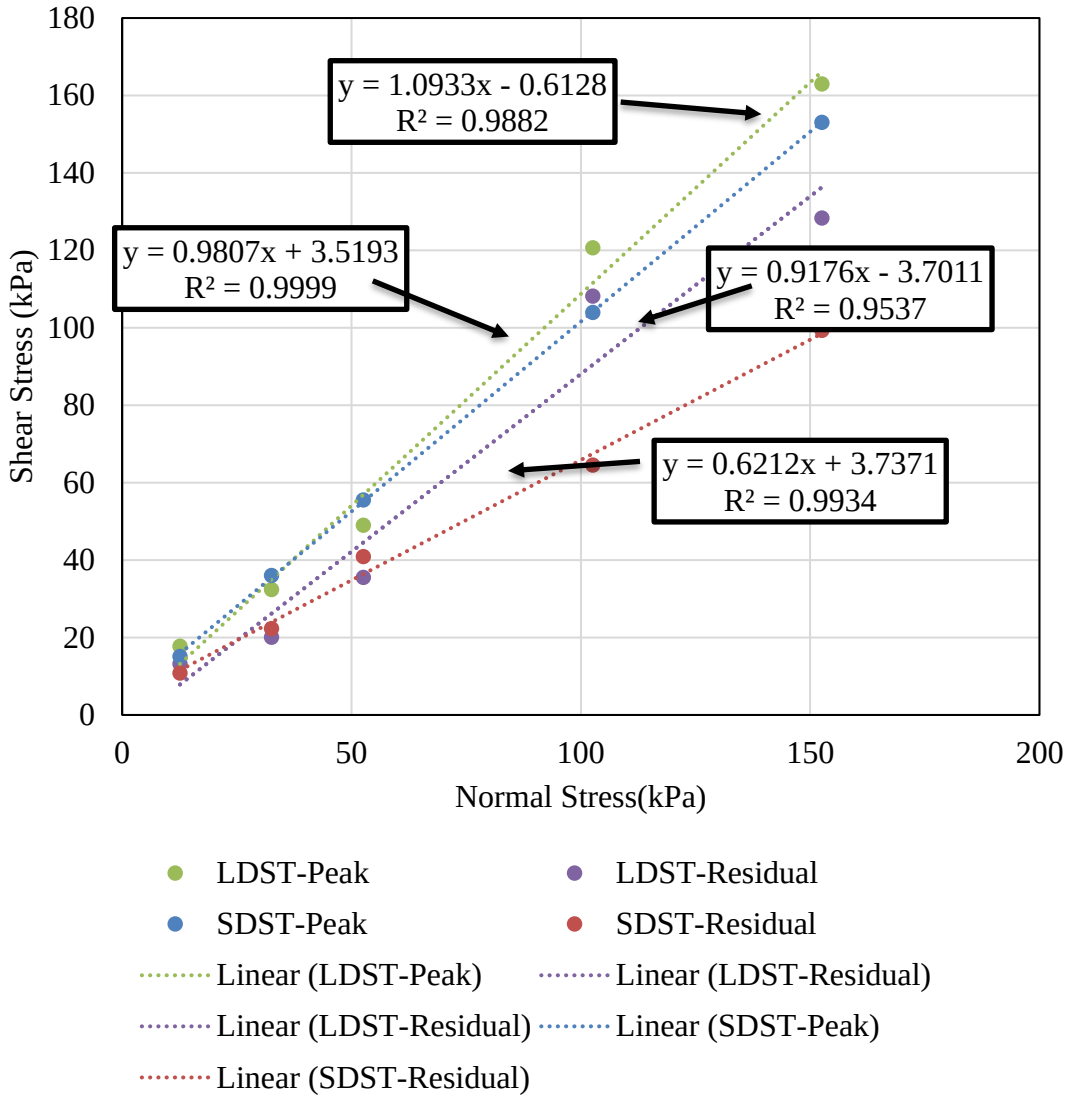

Figure 4-11. Shear Stress vs. Normal Stress of Loose and Dense Fine Sand, Peak and Residual Small Direct Shear Test (SDST), Large Direct Shear Test (LDST)

4.2.2.2 Crushed Limestone Results

Figure 4-12 illustrates the shear behavior of the compacted crushed limestone with fines under six different normal stresses: 10, 30, 50, 70, 100, and 150 kPa. The mass of the top cap and the mass of the soil on top of the shear plane added 2.5 kPa normal stress to the applied normal pressure (ex. 10 kPa+2.5 kPa = 12.5 kPa). To study the repeatability of the test results and test preparation method, three tests were repeated on crushed limestone under 10 kPa normal stresses. As shown in Figure 4-12, the three trials are almost identical and the maximum shear stress for these three tests are obtained at the same horizontal displacement and equal to 33.8, 44, and 25.6 kPa. Considering the grain shape and size of the crushed limestone, the difference of the shear strengths is acceptable. As the poorly graded and the combination of fine and large aggregates will cause the deference for the different test set up. The shear stress vs. horizontal displacement of the crushed limestone shows that with increasing of the effective normal stress, the shear strength of the material is also increasing to an ultimate stress and remain almost constant thereafter. Since there is no softening behavior observed for crushed limestone with fines, the failure is defined the shear stress at the horizontal displacement of 0.03 mm. The shear stress increases slightly at large horizontal displacements because of the reason that explained before for results of sand. The fluctuation of the shear stress-horizontal displacement curve is due to particle breakage during the test and coarse particle rotations among the fine particles.

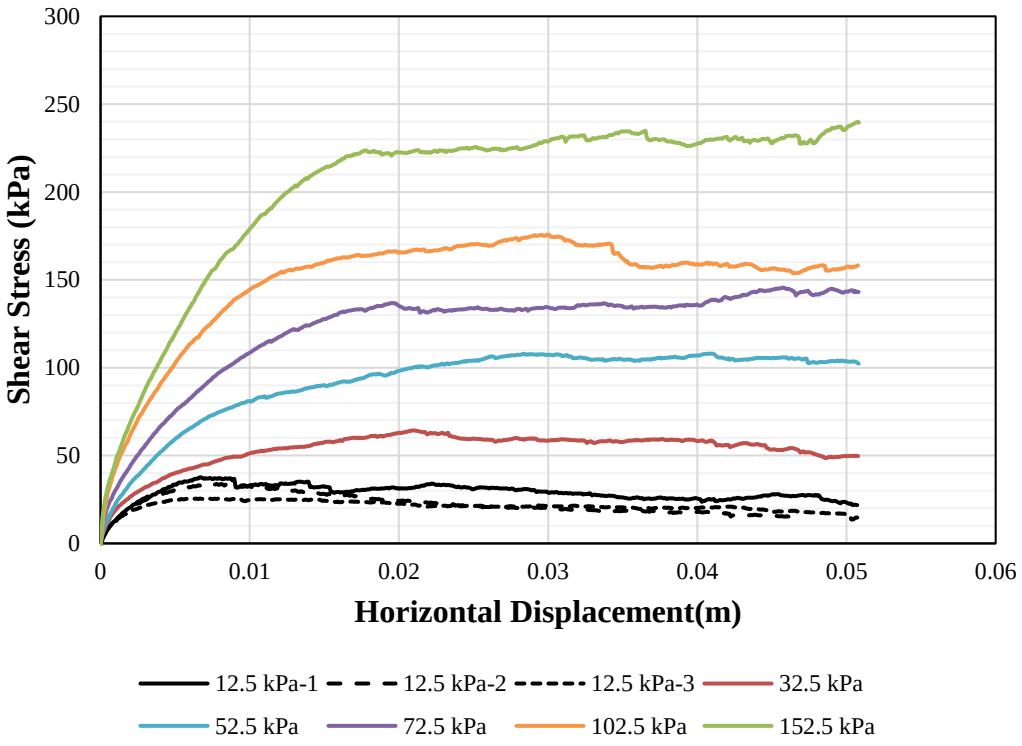

Figure 4-12. Shear Stress vs. Horizontal Displacement (LDST), Crushed Limestone with Fines

Figure 4-13. Top Cap movements during shearing, LDST

Figure 4-14 shows shear stress versus normal stress curve obtained from the LDST on crushed limestone with fines at the horizontal displacement of 0.03 mm. The shear strength parameters are summarized in Table 6-2. The envelopes are linear with the coefficients of determination (R^2) equal to 0.98 for the peak and large displacement envelopes. The friction angle for peak shear stress is 56° and the apparent cohesion is 19.2 kPa. The crushed limestone specimen has 20% fine materials with a low plasticity of PI = 2.8, PL = 12.5. The high value of the obtained cohesion is because of that the shear strength envelope of crushed limestone does not follow the straight line. During shear, the soil

tends to dilate at low confinement level and compress at higher confinement pressures (Figure 4-17). The Mohr coulomb envelope follows the equation below:

$$\tau_f = c' + \sigma' \tan(\varphi' + \psi')$$

Where τ_f is the shear stress, c' is the cohesion, σ' is the normal stress, φ' is the friction angle, and ψ' is the dilation angle. As the ψ' is positive at lower stresses (dilation) and negative at higher stresses (compression), the sum of $\varphi' + \psi'$ is greater at the lower confining pressure than higher normal stresses. Therefore, the shear strength envelope is curved (Briaud, 2013).

The high value of the cohesion can also because of the limestone fine material. The limestone is a sedimentary rock that cement the grains together and it will strengthen the soil. Figure 4-15 illustrates the changes in friction angle corresponding of peak shear stress versus normal stress. As shown in Figure 4-15, the friction angle of crushed limestone with fines decreases with increasing the normal stresses. Because the coarse grain particles break with increasing the normal stresses.

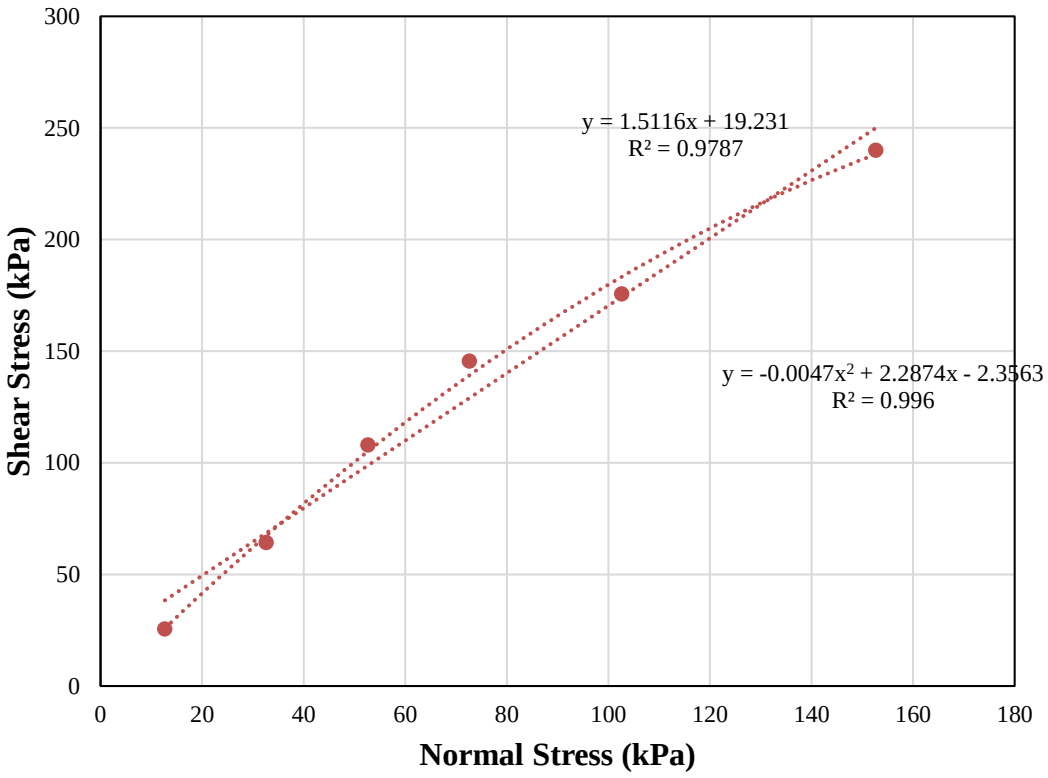

Figure 4-14. Shear Stress vs. Normal Stress for Crushed Limestone with Fines (LDST)

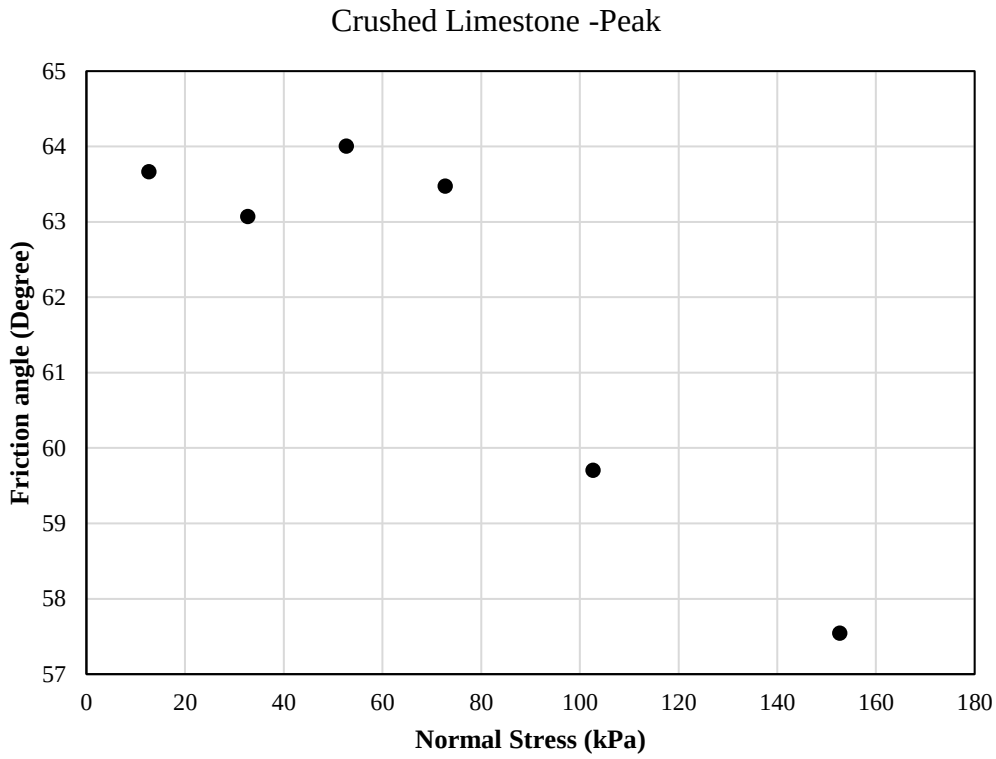

Figure 4-15. Friction angle vs. Normal Stress, Crushed Lime Stone with Fines

Figure 4-16 (a) and (b), show the relationship between the vertical displacement and the horizontal displacement for dense sand and crushed limestone under the normal stresses of 10, 30, 50, 100, and 150 kPa, respectively. It is worth noting that the negative direction of vertical axis shows a contraction and the positive axis shows dilation. No dilative behavior is observed for the loose sand under different normal stresses. Differently, a dilative behavior is observed for dense fine sand. For low normal stresses, 10 to 50 kPa, the dilative behavior is starting from the initial steps of horizontal displacement of shear phase while a small contraction behavior is observed at the initial phase of shearing of dense sand under greater normal stresses. A greater dilation observed

for soil under 10 kPa normal stress, and the lower dilation is observed for higher normal stressed, 100 and 120kPa. For all normal stresses, the soil ends up compressing at large displacement.

The vertical displacement versus horizontal displacement curve of crushed limestone under 10, 30, 50, 100, and 150 kPa normal stresses. A great dilative behavior is observed for low normal stress of 10 kPa starting from the initial horizontal displacement, with increasing the shearing displacement, the dilative vertical displacement increasing, and it reaches to 4.5 mm vertical displacement at 50 mm horizontal displacement. On the other hand, for high normal stress of 150 kPa, the curve shows an initial contraction of 0.6 mm and following by small amount of dilation reach 0.4 mm at 50 mm horizontal displacement. Comparison between dilation of the crushed limestone under 10kPa and 150kPa vertical stress shows that increasing vertical stress on the DST test will reduce dilation by approximately 95%.

In conclusion, for both the dense sand and crushed limestone sample, with increasing the normal stresses, the dilation displacement decreases. The influence of the normal stresses on the amount of dilation is greater for crushed limestone with fines than dense fine sand. As shown in Figure 4-17 the friction angle of the loose sand, dense sand, and crushed limestone with fines are 38°, 47°, and 56°, respectively. The lowest friction angle belongs to loose sand and the highest one is obtained for crushed limestone with fines because the crushed limestone's grains are much greater than sand. Also, the dense sand has higher shear strength and friction angle compare to the loose sand which is

reflected the dilation angle. The influence of normal stresses on the volumetric strain of the CLF (coarse grain soil) is more significant than sand (fine grain soil).

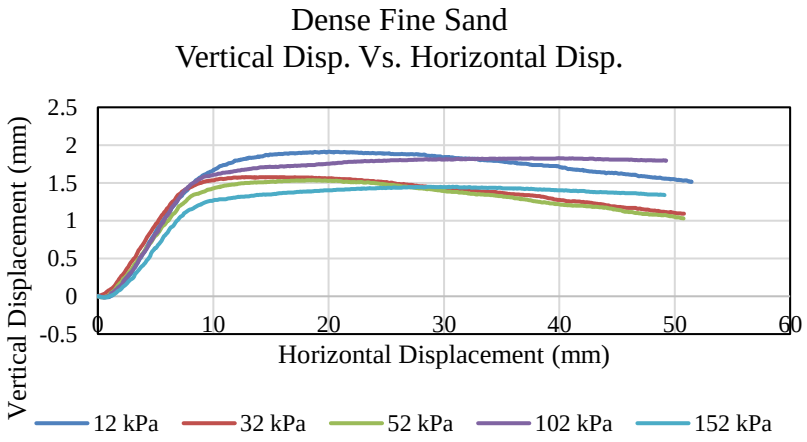

(a)

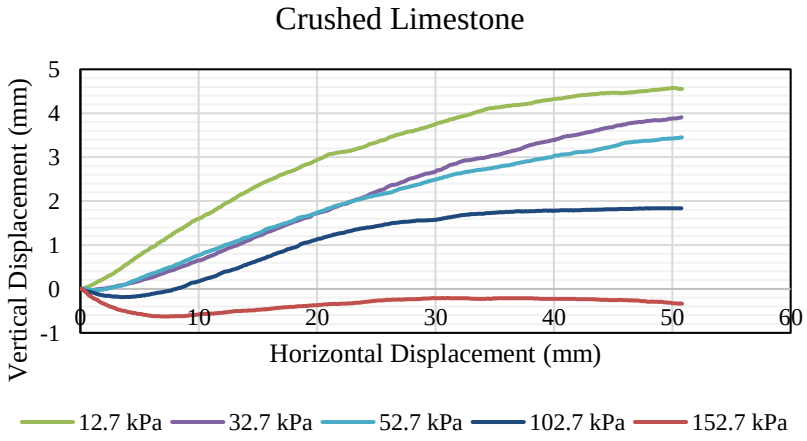

(b)

Figure 4-16. Vertical Displacement vs. Horizontal Displacement, (a) Dense Sand, (b) Crushed Limestone

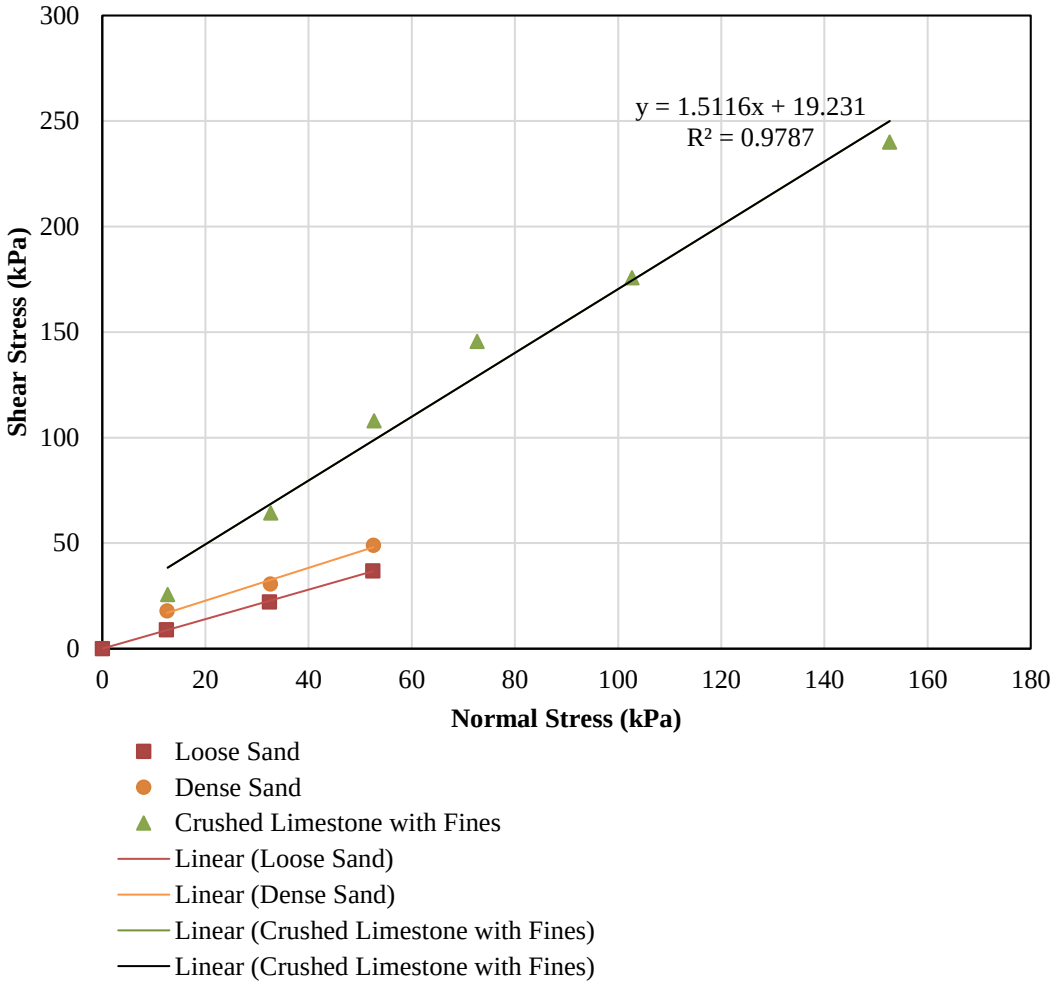

Figure 4-17. Shear Stress vs. Normal Stress for Loose Sand, Dense Sand, Crushed Limestone

4.3 Large Simple Shear test

The effective stress cohesion and the effective stress friction angle will be driven by direct shear tests. The main difference between direct shear test and the simple shear test is that in the direct shear test, the failure plane is predetermined as a shear band in the

mid-height of the sample while the shearing happens over the entire height of the sample in a simple shear test. Therefore, the simple shear test provides the shear stress-shear strain curve and consequently a shear modulus can be obtained from the slope of this curve.

Table 4-4 describes the test plan of simple shear tests on loose/dense fine sand and crushed limestone. All simple shear tests were performed under constant-load conditions. There is no specific ASTM standard is available for simple shear testing under constant load condition. However, as a reference, ASTM D 3080-11 (ASTM, 2011b), ASTM D 6528-07 (ASTM, 2007), and Zekkos et. al., 2018 were used here.

4.3.1 Test Procedure

The first step to perform the direct simple shear tests was to change the setup of the apparatus from the direct shear test to simple shear test. For this purpose, the direct shear stainless steel loading piston was removed, and the simple shear top cap was installed to the top cap piston as shown in Figure 4-18. As explained in the previous chapter, unlike the direct shear test setup, for the simple shear test, the top cap was connected to the loading piston. Then, the lateral movement supports were installed around the top cap piston and tightened the nuts. Three vertical and one horizontal displacement transducer were installed on top of the top cap and behind the water bath, respectively.

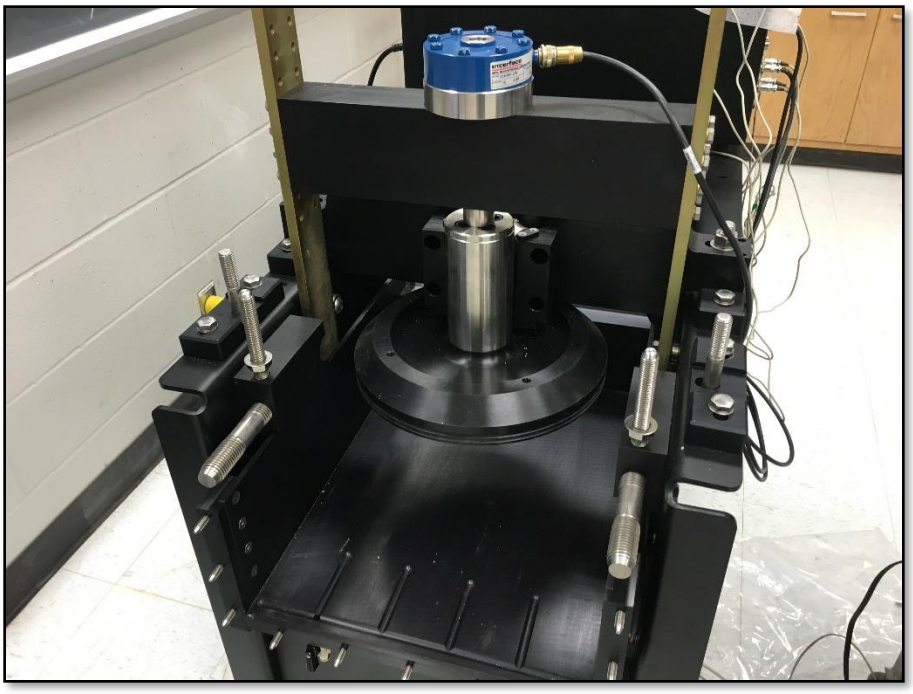

Figure 4-18. Simple Shear Test Top Cap

Then, the circular base plate for the simple shear test was placed on the shear box stand as shown in Figure 4-19. The sample membrane was pulled around the bottom plate and the O-ring were slide into the bottom O-ring groove (Figure 4-20). After placing the membrane (latex membrane or garbage bag), the shear rings were positioned on the base plate spacers. After placing the membrane and stacking the shear rings, the soil sample was prepared in the membrane. Before placing the soil specimen, the height of the rings was measured and the mass of soil which is needed to reach the target density was calculated. Preparing a specimen for the simple shear test is similar to preparing the sample for the direct shear test. The only difference was that the commotion plywood was built in a circular shape for simple shear test (Figure 4-22).

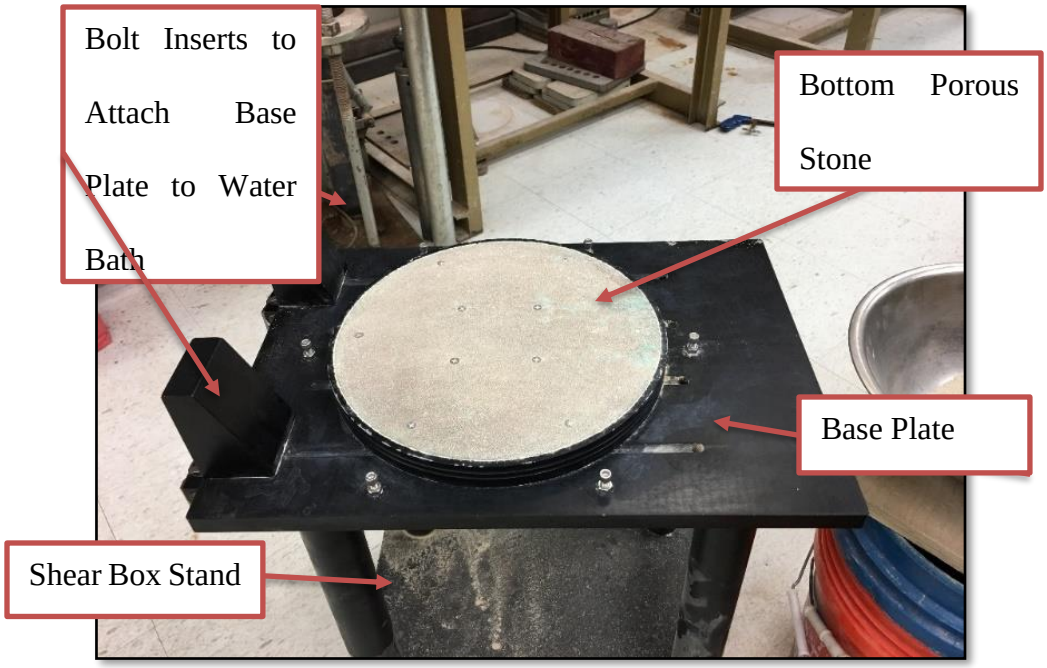

Figure 4-19. Base Plate and Sample Preparation Stand

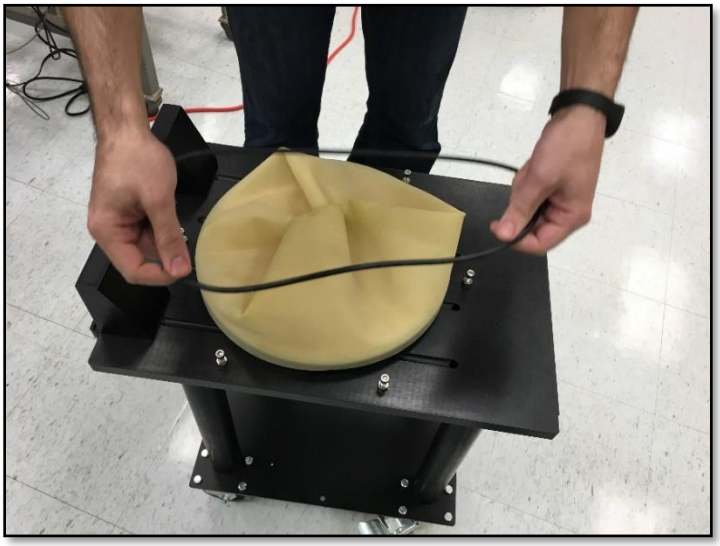

Figure 4-20. Base Plate with Membrane and O-ring Placement

Figure 4-21. Stacking of Shear Rings

Figure 4-22. Sample Preparation

The prepared specimen was shown in Figure 4-23. After completing the procedure described above, the base plate was slide into the housing unit of the apparatus. Figure 4-24 shows the sample placed in the ShearTrac III housing unit. The base plate was connected to the water bath by tightening the bolts. Once the specimen was mounted into the water bath, the top cap was initialized using the front vertical control panel and the crossbar was jogged down until it barely touches the specimen and the small gap between the top cap and the surface of the soil was created (Figure 4-24). Next, I made sure that the sample was properly aligned in the horizontal direction, back and front) such that the top cap lined up with the top shear rings.

Figure 4-23. Prepared Spacemen

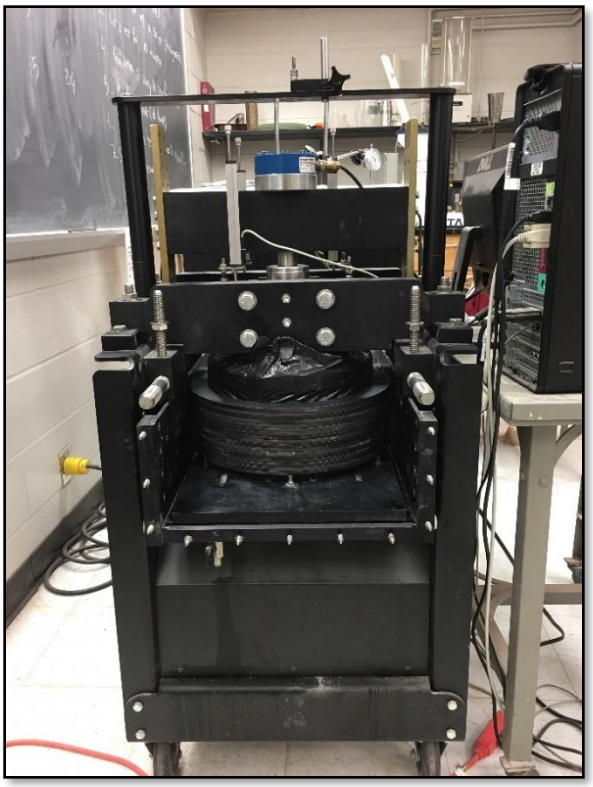

Figure 4-24. The Specimen in ShearTrac-III

Before running a test, the sitting load was applied on the sample: first, 100 N applied and then unloaded, then 200 N load was applied and unloaded. After that, 400 N load was applied and unloaded and at the end, 500 N load applied and stayed there like a sitting load. During the sitting load step, the two top rings were moved to make sure that the top cap is in good contact with the top of the soil surface (Figure 4-25).

Like a direct shear test, the simple shear tests were run in two steps. During the first step and the consolidation phase, normal pressure was applied to the soil sample; 10, 30, 50, 100, 150 kPa. During the second step, shear phase, the specimens were sheared at

a constant shearing displacement of 0.6 mm/min while the normal stress keeps constant. This means that the top cap was free to move and adjust to keep the normal load at a constant value. The maximum horizontal movement of the water bath was set 25.4 mm (1 in.). During the consolidation and the shear phase, the vertical and horizontal displacement and force were recorded.

Figure 4-25. Sitting Load Step

4.3.2 Test Results

4.3.2.1 Device Validation

In order to validate large-scale direct simple shear test results, data from an experiment done by Kim, 2009 is utilized. Kim used Nak-dong River clean sand contained sub-granular particles for conducting constant load monotonic simple shear test. A series

of monotonic constant load simple shear test was conducted on the sand specimen with nearly same gradation and properties to Nak-dong river sand. Samples were prepared in loosest possible deposit for all tests and tested at an effective normal stress of 50, 100 and 200 kPa. The shear rate was approximately 1% of shear strain per minute. As illustrated in Figure 4-26, the results are nearly identical which shows the accurate testing procedure for large-scale DSST.

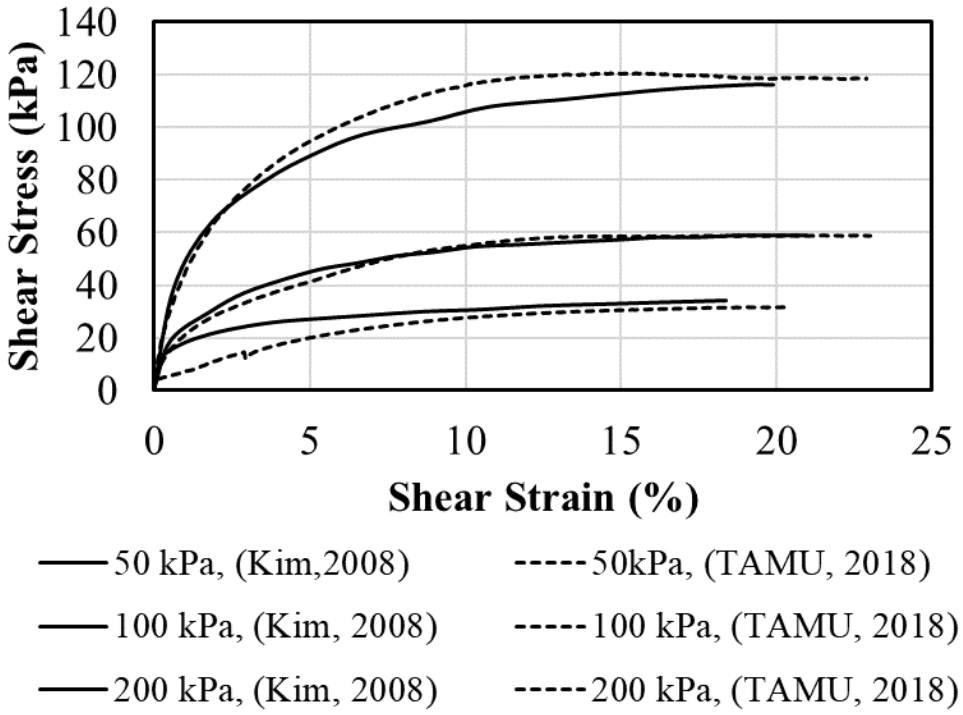

Figure 4-26. Large Simple Shear Device Validation

4.3.2.2 DSST Results on Soil Specimens

A series of monotonic simple shear tests were performed on loose sand, dense sand, and crushed limestone under 10, 30, 50, 150 kPa. As mentioned before, the bottom

base plate of the simple shear box which is located in the water bath is moving horizontally to provide the shear displacement along the height of the specimen. The tests were performed with the 20% of shear strain or 2 cm of displacement. As the base plate of the shear box moves horizontally and the shear rings are free to move on each other, the relative displacements happen between the lowest and highest shear ring. The ratio of the horizontal displacement between the top and bottom of the specimen over the initial height of the specimen is called shear strain (Ɣ) and shown in Figure 4-27. Figure 4-28, Figure 4-29, and Figure 4-30 illustrate the response of shear stress, the axial strain, the shear modulus (G), and normalized shear modulus ($\frac{G}{G_{max}}$) versus shear strain obtained from simplthe e shear test on loose sand, dense sand, and crushed limestone with fines, respectively. For all three kind of soil, it shows that increasing normal pressure increases the soil strength. As shown in Figure 4-27 (a), the shear stress increasing hyperbolically with increasing the shear strain up to the maximum shear stress (shear strength). After that the shear stress stays constant as the shear strain increasing. Unlike the direct shear test results, the results of simple shear test on dense sand does not show the significant softening behavior after the peak shear stress. Comparing the shear strength of loose sand and dense sand for each confining stress, the shear strength of dense sand is higher than the shear strength of the loose sand because with increasing the density, the dilation angle is greater and the shear strength also increasing. The shear stress response of the crushed limestone is like the sand with slightly softening behavior after maximum shear strength.

Comparing the results obtained from tests on the sand and crushed limestone with fines with shows that the shear strength of these three types of soil for all normal stresses is very similar to each other. The maximum shear stress of loose sand occurs at 20 % of shear strain while for dense sand it happens at a range of 10% to 15% of shear strain for soil specimen under 10, 30, and 50 kPa and at 20% for soil under 150 kPa normal stress. The shear strength of crushed limestone with fines occurs around 10% shear strain for all confining pressures.

In terms of axial strain, for all types of tested soil, the soil tends to contract at small strains in the simple shear test. After a certain point, the axial strain remains constant. Results of sand and CLF show that increasing normal stress will not always increase contraction because another parameter like soil structure formation is important on the axial strain of sample (see Figure 4-28 (b), Figure 4-29(b), and Figure 4-30(b)).

The results of normalized shear strength with vertical stress which is constant through the test illustrate maximum shear strength that the soil sample can reach during the test is approximately between 0.4 to 0.7 times of applied normal stress and this ratio is independent of normal stress.

The shear stress-strain relationship is used to describe the shear modulus of soil. The shear modulus is calculated as the slope of the shear stress-strain curve:

$$G = \frac{\tau'}{\gamma'}$$

Where, τ' is the shear stress and γ' is the shear strain. The shear modulus is strongly influenced by the shear strain value. It means that it decreases with increasing the shear stress. Figure 4-28 (c), Figure 4-29(c), and Figure 4-30(c) illustrates the shear modulus-shear strain for loose sand, dense sand, and crushed limestone, respectively. It is obvious that at zero strain, the shear modulus reaches its maximum value and decreases with increasing the shear strain. The shear modulus of loose sand, dense sand, and crushed limestone at 50% of shear strength (G_{50}) for different normal pressure are described in Figure 4-31. As illustrated in the figure, the shear modulus is increasing with increasing the normal stresses for all soil types. The shear modulus of crushed limestone is greater than the loose and dens sand especially in high normal stress.

The modulus ratio ($\frac{G}{G_{max}}$)(normalized shear modulus) is adopted to describe the shear stiffness degradation of soil specimen. As shown in Figure 4-28 (d), Figure 4-29(d), and Figure 4-30(d), a modulus reduction curve is observed which describes the same information as the shear modulus-shear strain curve. The modulus ratio starts at 1 at zero shear strain and decreasing to less than 0.1 at 25% shear strain. The shear stiffness of the soil is dropping dramatically at very low shear strain values. This drastically decrease of the shear stiffness is occurred at lower shear strain for smaller normal stresses than the higher normal stresses. Therefore, the shear modulus of soil is significantly influenced by the confining pressure. Comparing the normalized shear modulus curve for these three types of soil shows that the soil density and grain size distribution of soil specimen has

insigan nificant effect on stiffness degradation of soil the sample. Particle shape has more influence on the shear strength parameters.

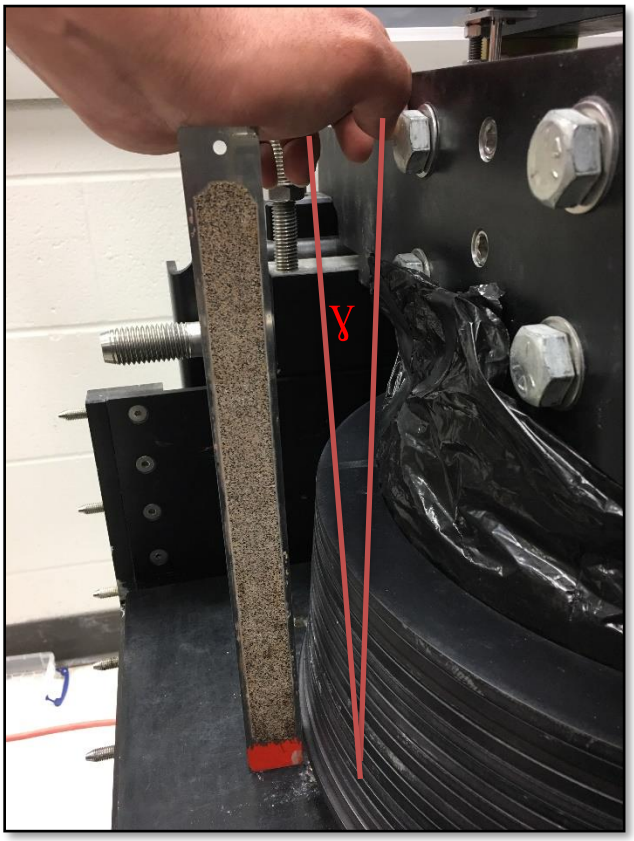

Figure 4-27. Displacement of the Shear Rings During the Test

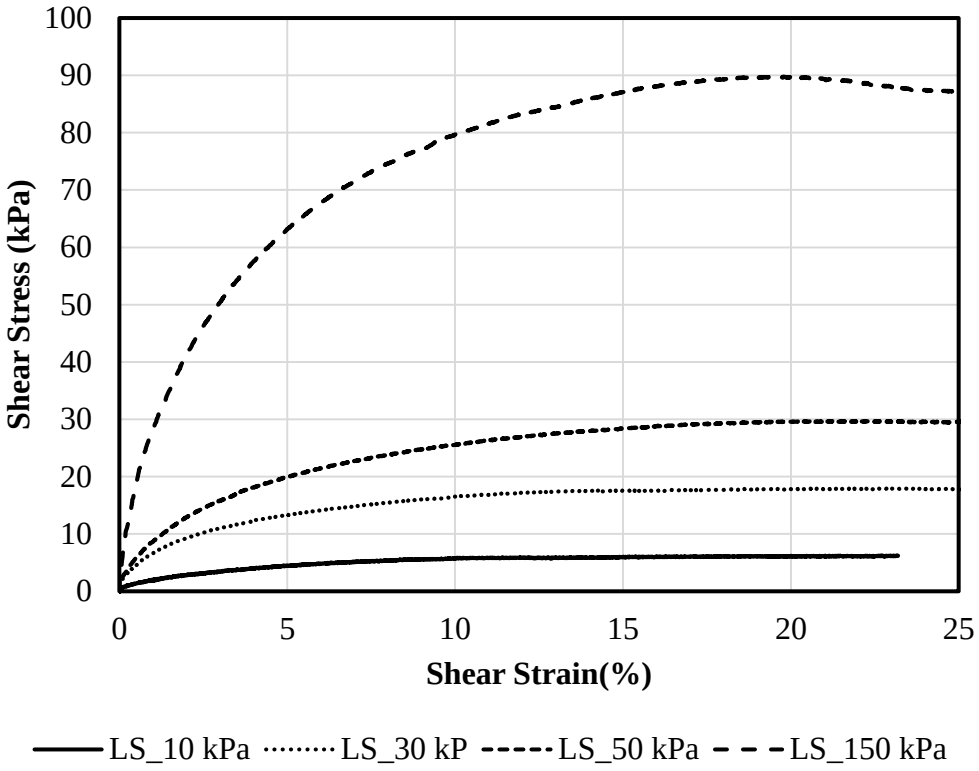

(a)

Figure 4-28. Loose Sand, (a) Shear Stress vs. Shear Strain, (b) Axial Strain vs. Shear Strain, (c) Shear Modulus vs. Shear Strain, (d) G/Gmax vs. Shear Strain

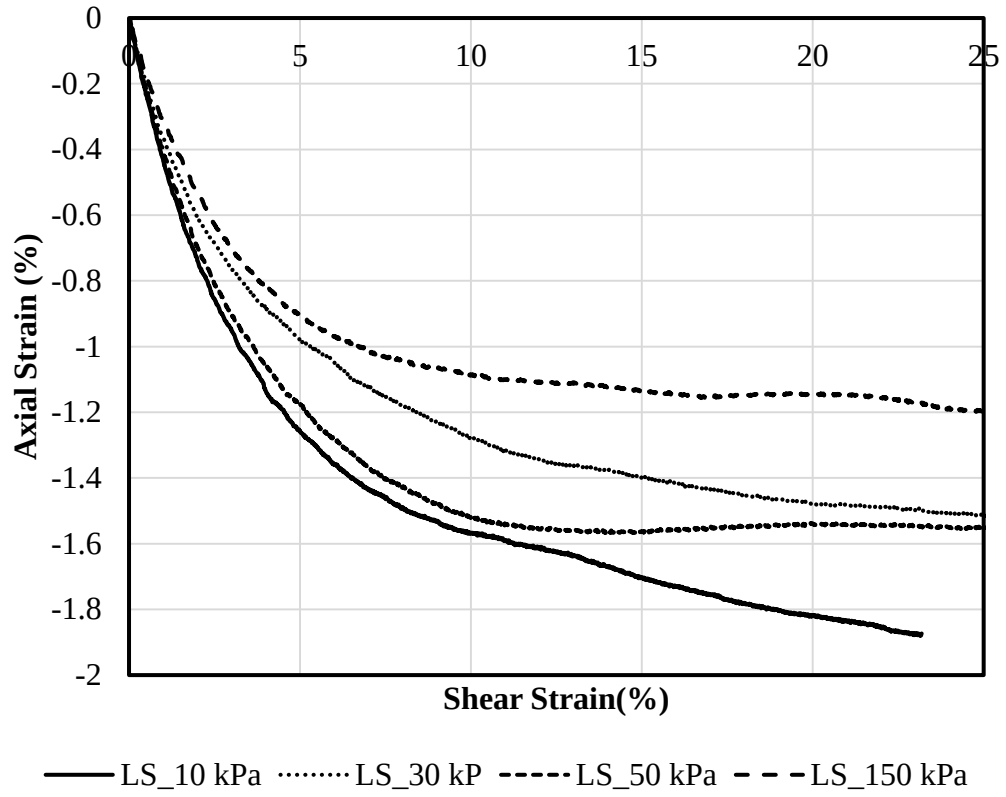

(b)

Figure 4-28. Continued.

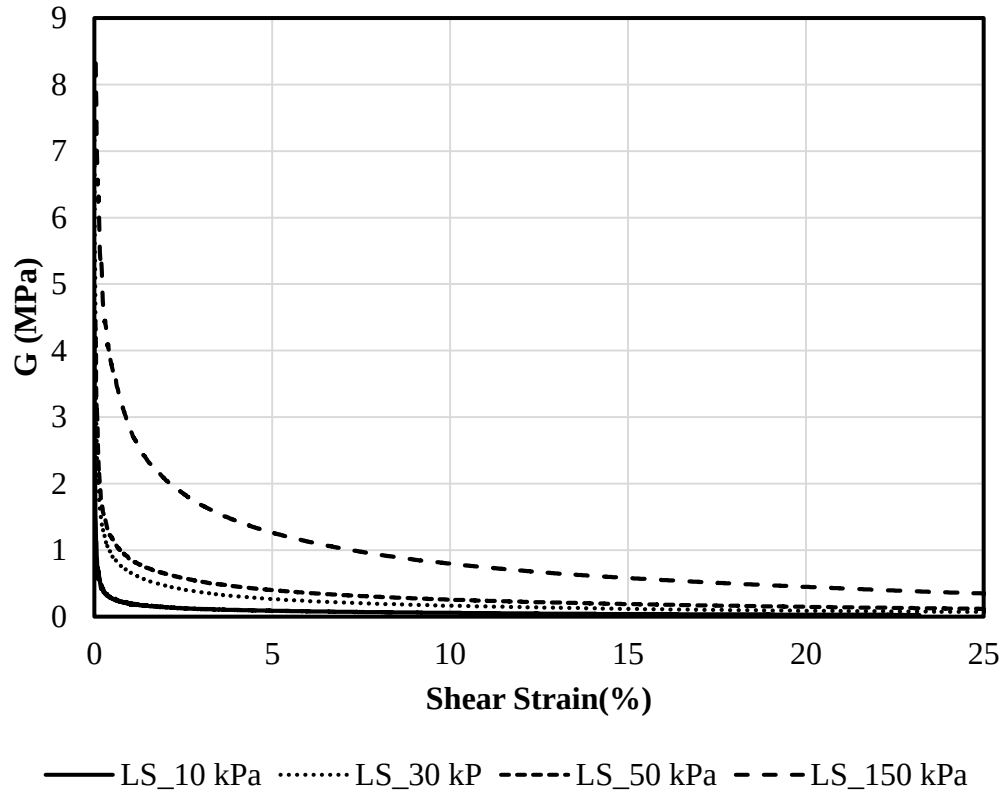

(c)

Figure 4-28. Continued.

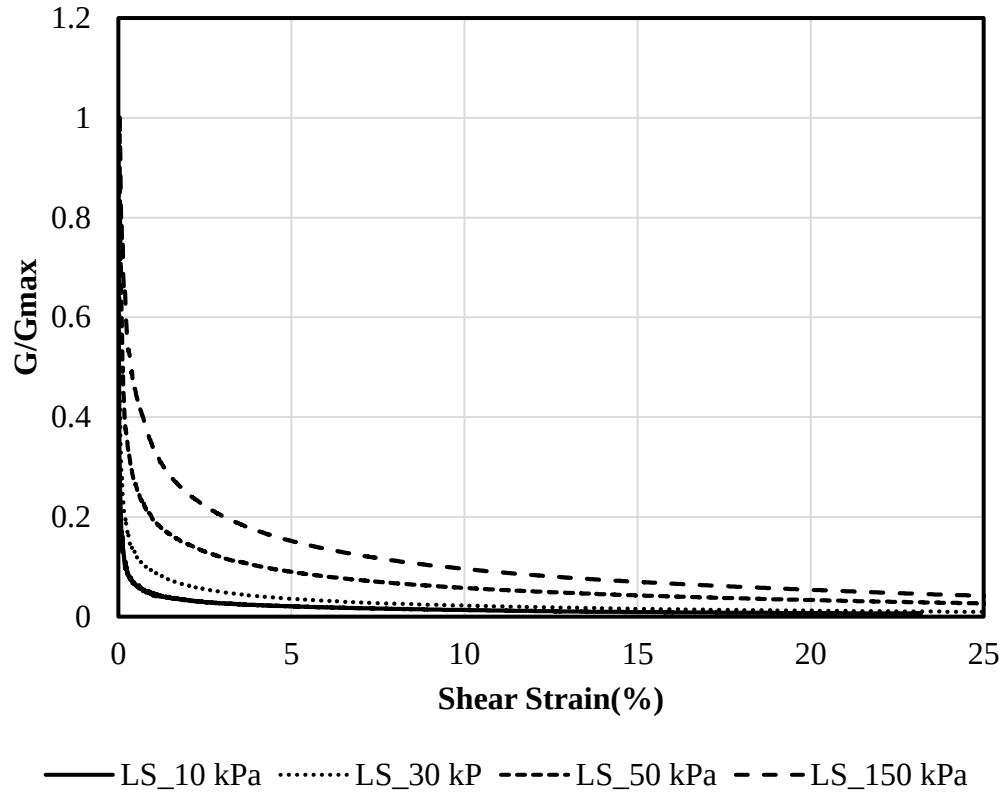

(d)

Figure 4-28. Continued.

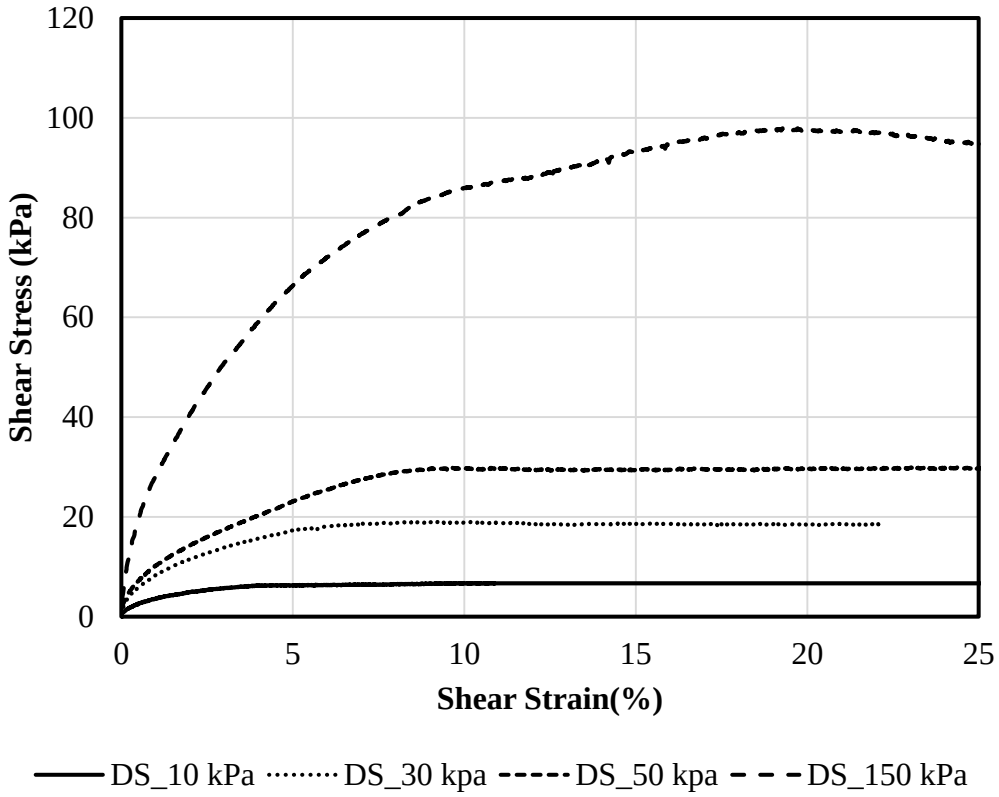

(a)

Figure 4-29. Dense Sand, (a) Shear Stress vs. Shear Strain, (b) Axial Strain vs. Shear Strain, (c) Shear Modulus vs. Shear Strain, (d) G/Gmax vs. Shear Strain

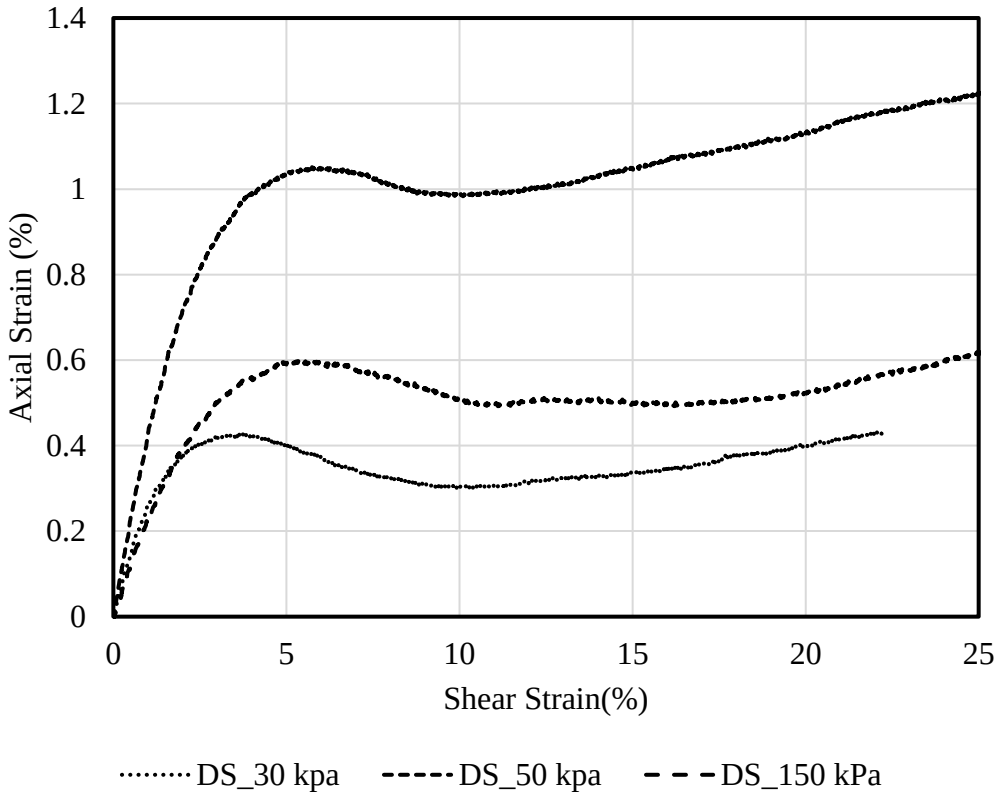

(b)

Figure 4-29. Continued.

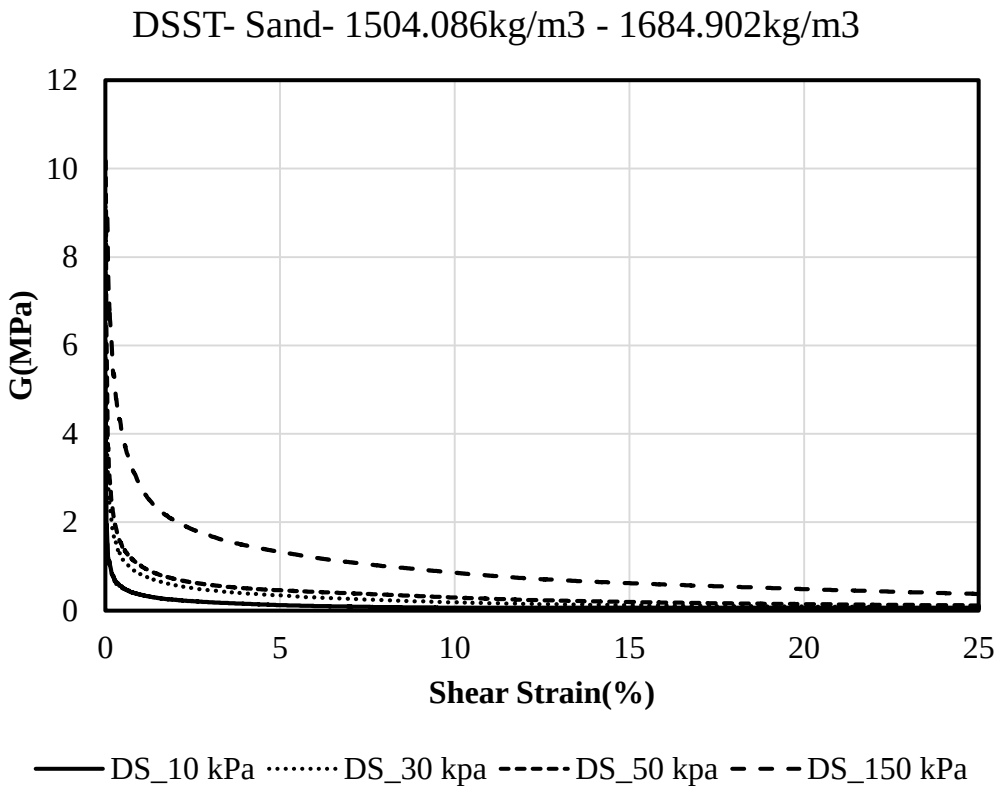

(c)

Figure 4-29. Continued.

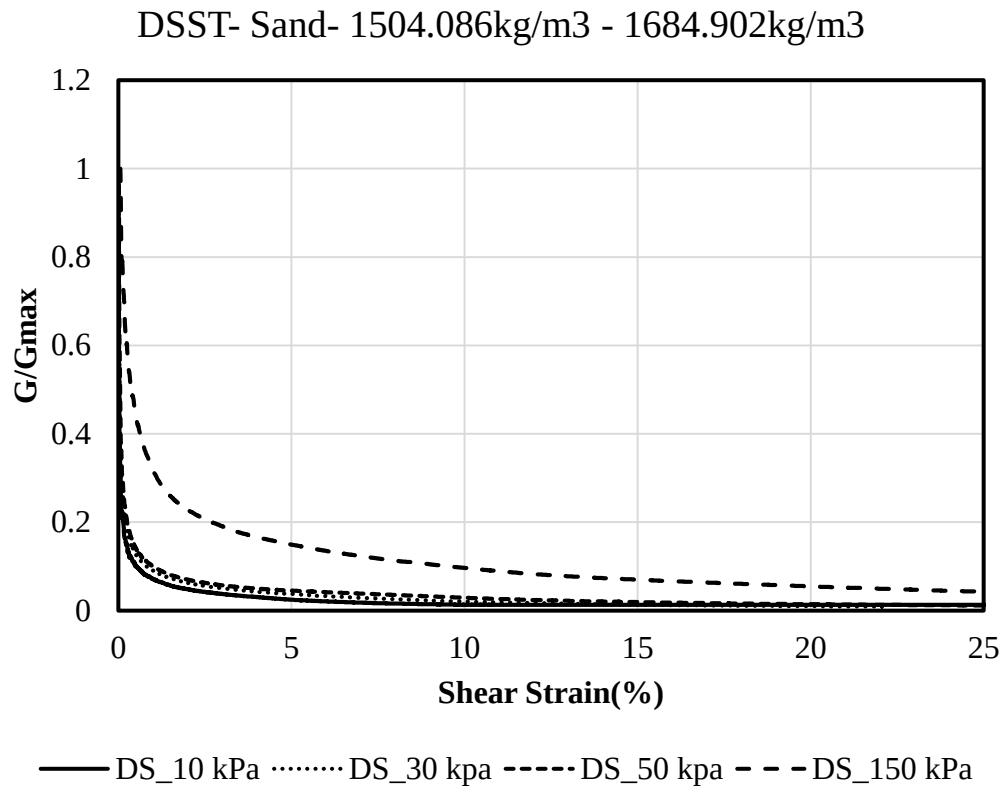

(d)

Figure 4-29. Continued.

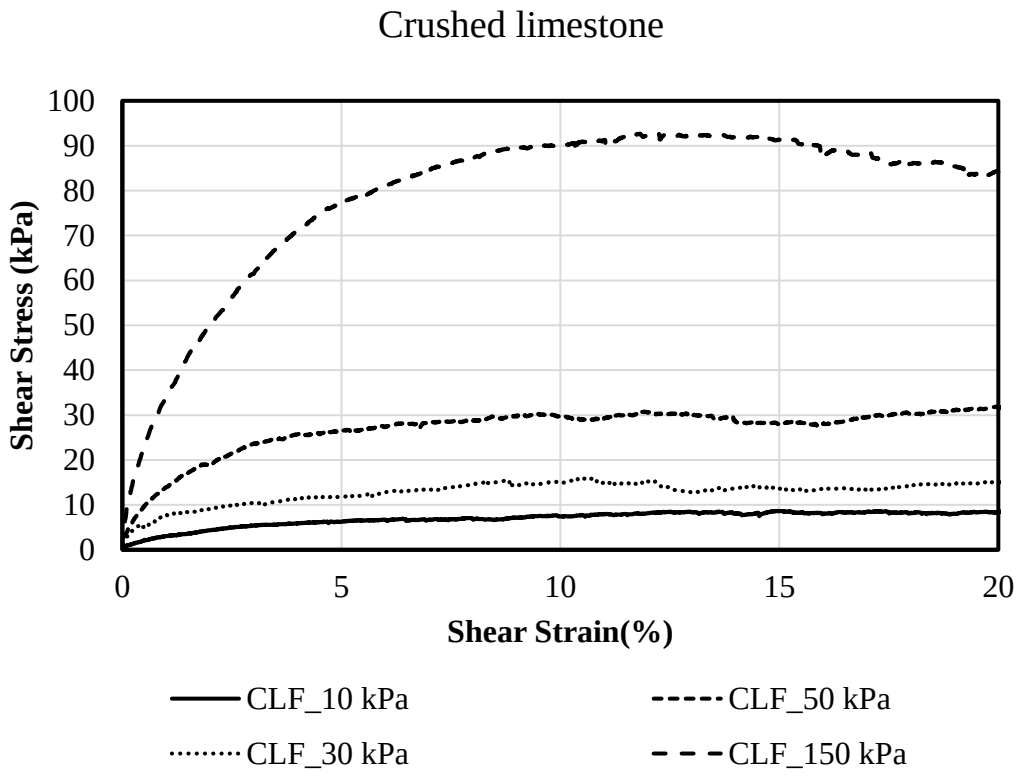

(a)

Figure 4-30. Crushed Limestone with Fines, (a) Shear Stress vs. Shear Strain, (b) Axial Strain vs. Shear Strain, (c) Shear Modulus vs. Shear Strain, (d) G/Gmax vs. Shear Strain

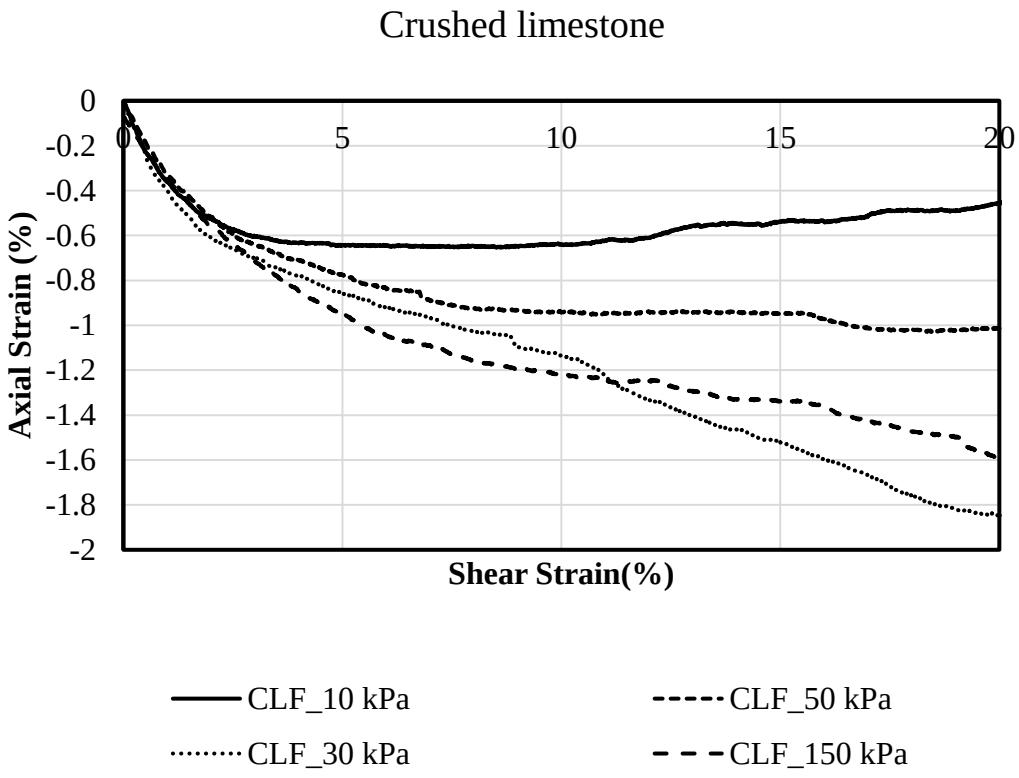

(b)

Figure 4-30. Continued.

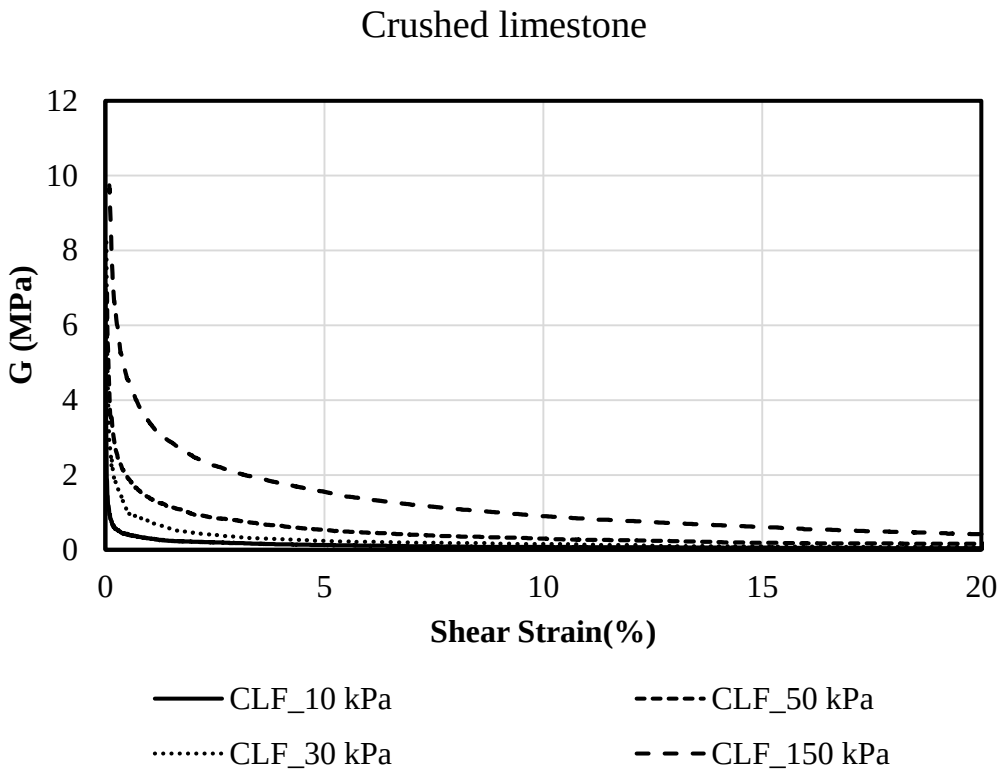

(c)

Figure 4-30. Continued.

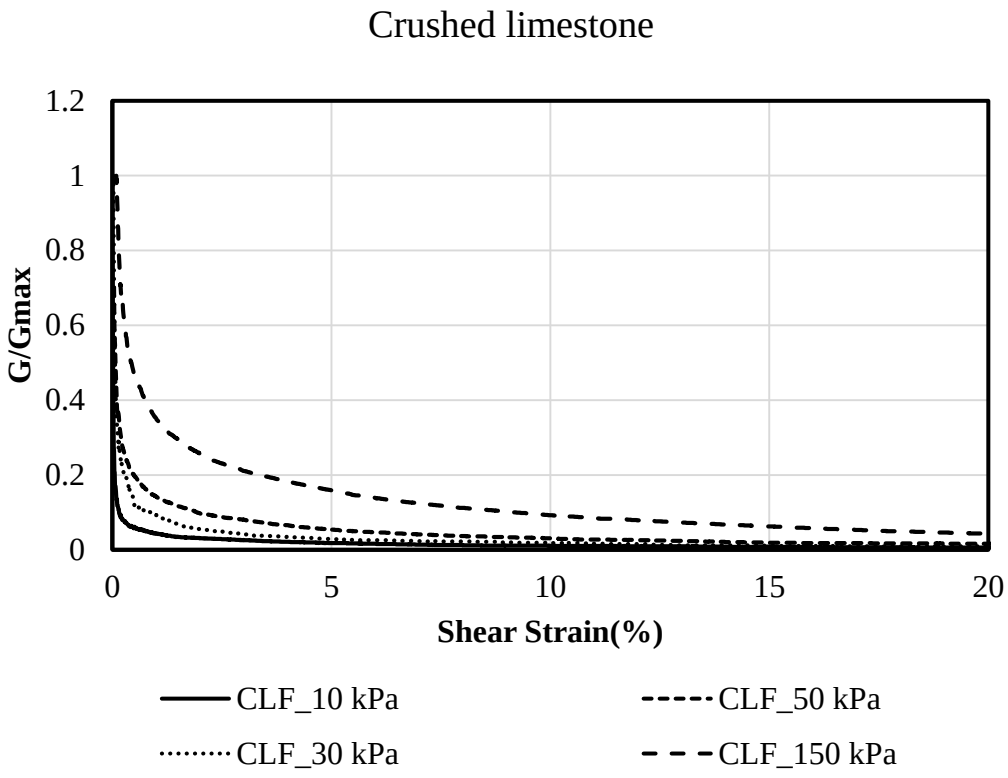

(d)

Figure 4-30. Continued.

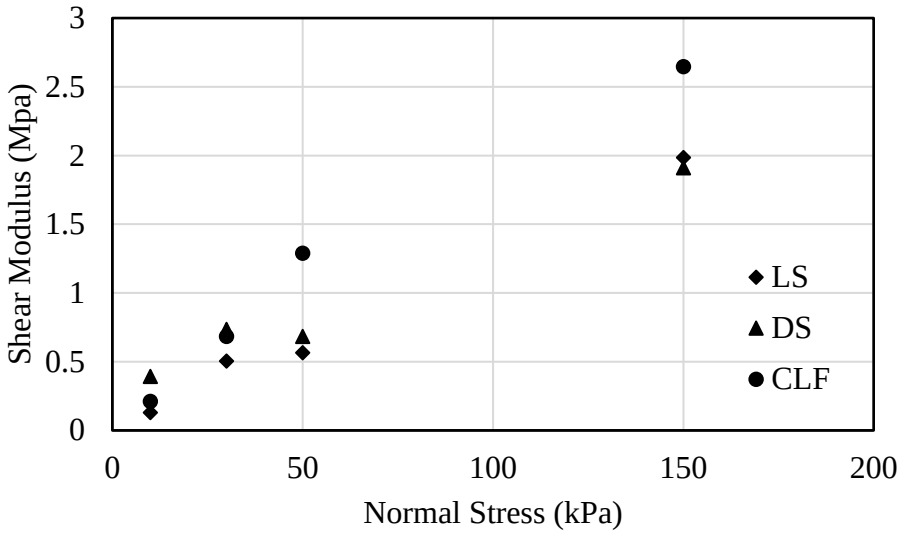

Figure 4-31. Shear Modulus (G_{50}) for Loose Sand, Dense Sand, and Crushed Limestone with Fines

The Mohr-Coulomb envelope of the soil specimens is created using the maximum shear stress obtained from simple shear test results. As illustrated in Figure 4-32 the slope of the linear trend line for LS, DS, and CLF are almost the same. Comparing the friction angle of LS, DS, and CLF which are material with approximately same particle shape (angularity) and different grain size distribution shows that particle size does not have a significant effect on the shear strength of the material (almost same friction angle). The reason for this observation is described in more detail in chapter six.

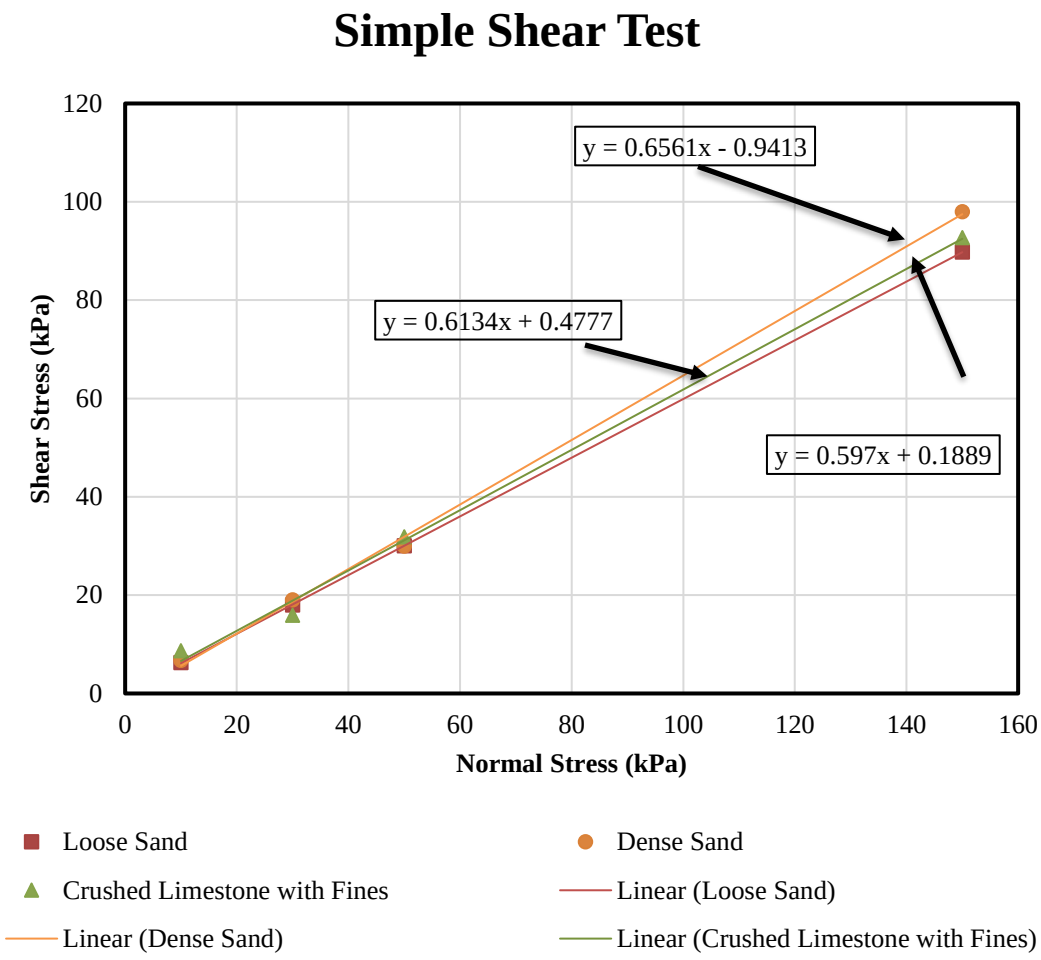

Figure 4-32. Direct Simple Shear Test, Shear Stress vs. Normal Stress, Loose/Dense Fine Sand and Crushed Limestone with Fines

4.4 Interface Direct Shear Test

The interface properties between a reinforcement (steel and geosynthetic) and soil specimen (loose/dense sand and crushed limestone) were determined by placing the soil specimen and the reinforcements in the direct shear apparatus. Table 4-5 and Table 4-6 summarized the interface tests of steel and geosynthetic reinforcements, respectively.

Although, there is no ASTM standard for interface direct shear tests between steel reinforcements and soil, I refer to ASTM D6243, *Standard Test Method for Determining the Internal and Interface Shear Resistance of Geosynthetic Clay Liner by the Direct Shear Method* and ASTM D5321, *Standard Test Method for Determining the Shear Strength of Soil–Geosynthetic and Geosynthetic–Geosynthetic Interfaces by Direct Shear* as a guidance.

4.4.1 Steel Reinforcement

4.4.1.1 Test Procedure

Table 4-5 describes the detail of the IDST between soil specimen and five aluminum plates which are explained in the previous chapter. The interface direct shear test was performed between smooth/ribbed aluminum plates and loose sand, dense sand, as well as crushed limestone with fines. The interface direct shear tests were performed using the large direct shear apparatus. As shown in Figure 4-33, the idea of the interface direct shear test was to slide the block of a soil over the reinforcement surface. For this purpose, the lower half of the box was filled with a spacer (the wood support) and the reinforcement which is here the smooth and ribbed aluminum plate as the ribs stay higher than the height of the lower box. The upper half of the shear box was filled with a soil specimen and compacted to the desired density. Tests were performed in two phases:

1- Consolidation phase which the normal stress was applied to the top cap and the soil could consolidate under the pressure.

2- The shear phase where the lower half of the box moves horizontally with a constant rate while the upper half of the shear box remains constant. Therefore, the block of the soil slides over the reinforcement during the shearing phase.

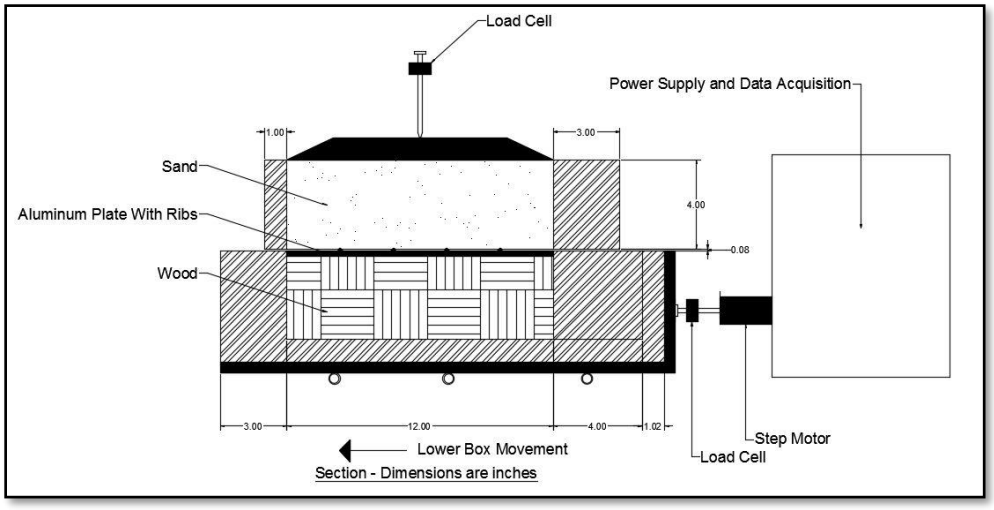

Figure 4-33. Schematic Drawing of Interface Direct Shear Test on Aluminum Plate

For testing a block of soil sample sliding on the smooth/ribbed steel plate reinforcements, the following procedure was utilized:

1. Placed the wood support inside the lower half of the shear box which is located on the shear box stand.

2. Attached the aluminum plate to the plywood support and adjusted the height of the plate as the ribs stand higher than the lower half of the box (Figure 4-34). To lift the aluminum plates and placed on the spacer, the two studs inserted into the two stud soles.

Figure 4-34. Placement of the Spacer and the Aluminum Plate inside the Lower Half of the Shear Box

3. Placed the top shear box on top of the lower half of the box and fixed the top and bottom box by inserting the alignment screws into the place.

4. Prepared the soil sample in the upper half of the box to the desired density as explained before for direct shear tests on the soil. Figure 4-35 illustrates the prepared interface direct shear specimen with dense sand and a crushed limestone soil sample.

(a) (b)

Figure 4-35. Prepared Specimen, IDST, (a) Dense Sand, (b) Crushed Limestone

5. Placed the top cap on the soil surface and removed the studs.
6. Slide the prepared sample inside the water bath (Figure 4-36)
7. Secured the sample and tighten the screws of beams
8. Applied the normal load for the consolidation phase
9. Created the gap between the two boxes and the shear phase started by moving the lower half of the box with a constant rate of 0.0001016 m/s. The maximum shear displacement set to 5 cm.

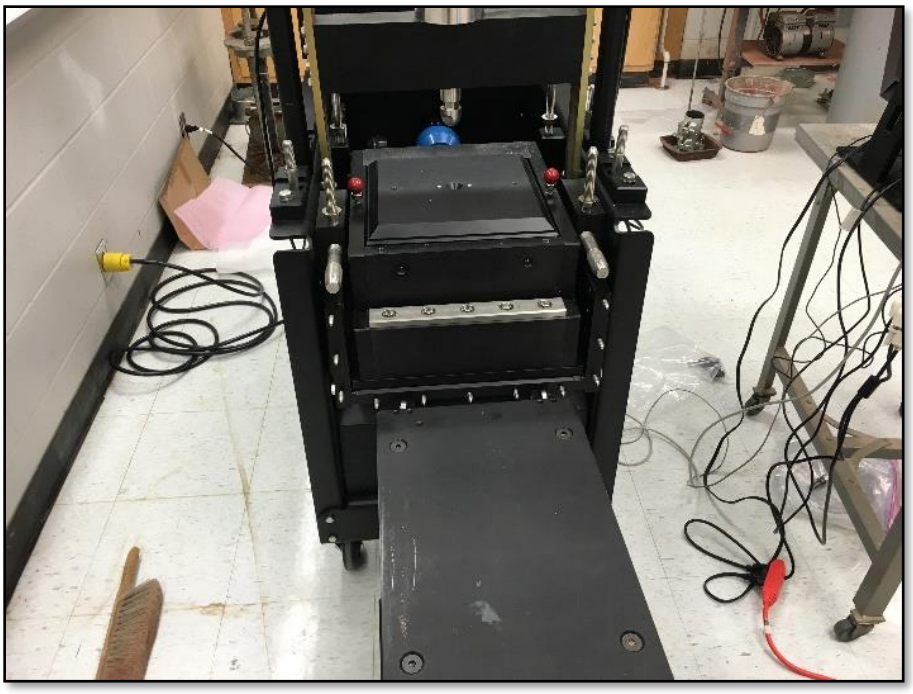

Figure 4-36. Specimen in the Housing Unit

4.4.1.2 Test Results

The results of an interface direct shear test for steel reinforcements are presented in this section in terms of shear stress, vertical displacement, and Mohr-Coulomb failure envelope. The IDST were performed between the steel reinforcement with a various number of ribs per 30.48 cm and LS, DS, and CLF. Tests were performed by applying normal stresses of 10, 30, 50, 100, and 150 kPa same as the soil/soil direct shear tests.

Interface direct shear test results between the smooth/ribbed aluminum plates and loose sand, dense sand, and crushed limestone is discussed in Figure 4-37, Figure 4-38, and Figure 4-39, respectively. Figure 4-37 (a) reports the behavior observed in interface

direct shear test on the interface between loose sand and the smooth aluminum plate placed in the lower half of the box. Comparing part (a) of Figure 4-37 with parts (b), (c), (d), and (e) of the same figure indicates that the interface shear strength obtained from ribbed reinforcements is greater than the shear strength of the interface between the smooth plate and loose sand for all confining stresses. Furthermore, the difference between peak shear strength of plates with four, six, and nine ribs are very small. Comparing Figure 4-37, the shear stress-horizontal displacement of smooth/ribbed plate-loose sand with Figure 4-10 (a), the shear behavior of soil-soil direct shear test on loose sand indicates that shear strength of soil-soil is higher than interface shear strength of smooth plate-soil and 2-rib plate-soil. The shear strength of plates with 4, 6, and 9 ribs are slightly higher than soil-soil shear strength at lower normal stresses and almost the same at higher normal stresses.

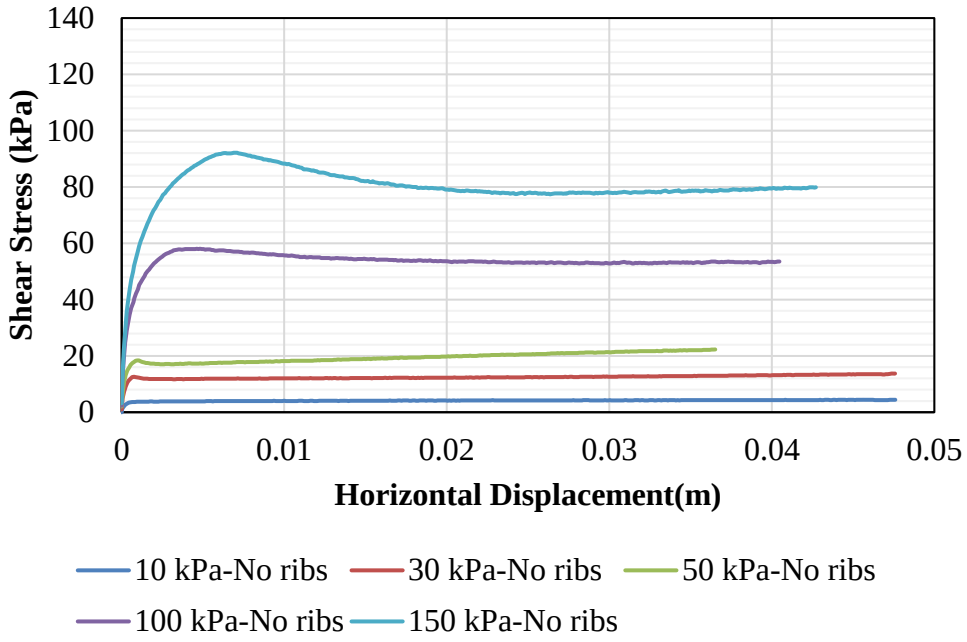

(a)

Figure 4-37. Shear Stress vs. Horizontal Displacement, Interface Direct Shear Test, Loose Sand, (a) Smooth Plate, (b) 2-Rib Plate, (c) 4-Rib Plate, (d) 6-Rib Plate, (e) 9-Rib Plate

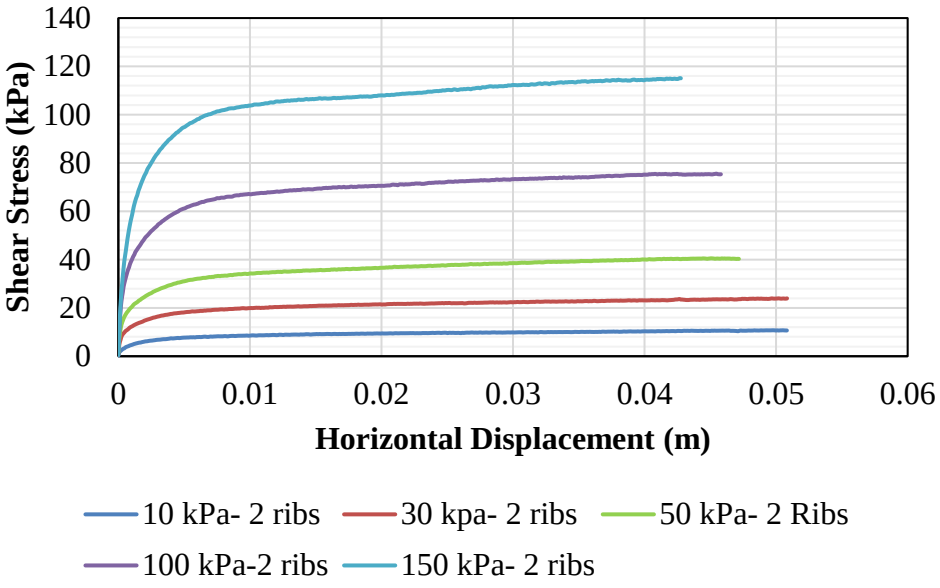

(b)

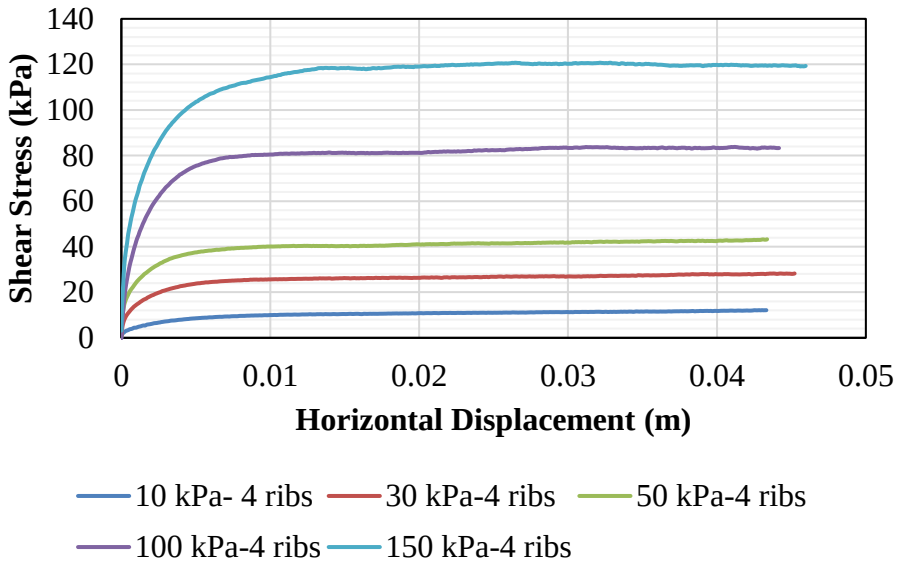

(c)

Figure 4-37. Continued.

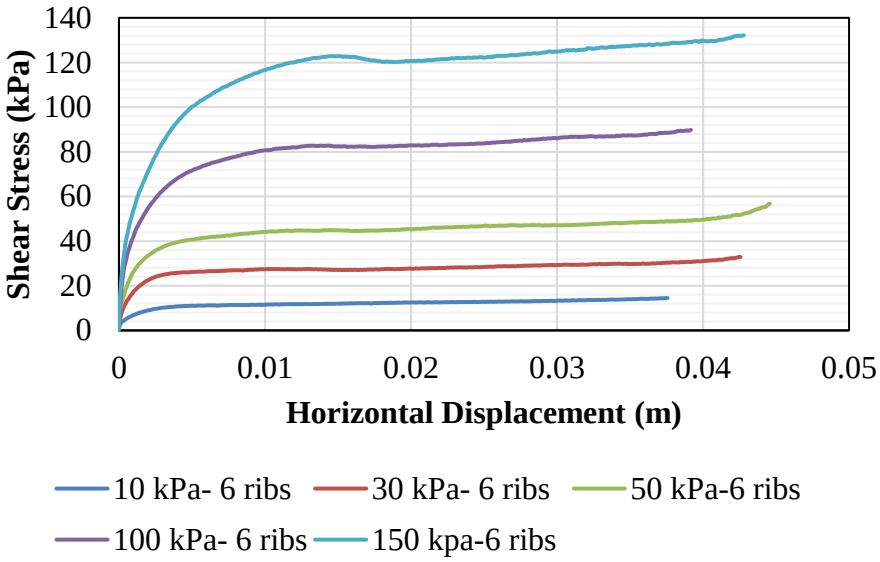

(d)

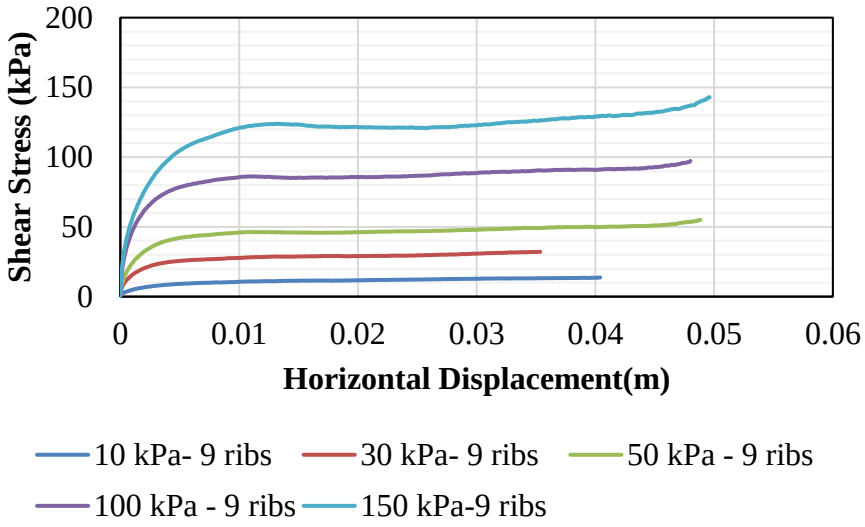

(e)

Figure 4-37. Continued.

Figure 4-38 shows the behavior of interface direct shear test between steel reinforcements and dense sand. The results report that increasing the number of the ribs per 30.48 cm increases the interface shear strength of the soil-reinforcements. Comparing shear stress-shear displacement curves of soil-soil with soil-steel reinforcement, the peak and residual shear strength of soil-soil direct shear tests are greater than interface shear strength of smooth and 2-rib plate. However, the peak and residual shear stress of 4-rib, 6-rib, and 9-rib aluminum plates are higher than the ones for soil-soil direct shear tests. This difference is greater at low normal stresses and lower at high normal stresses. Therefore, the influence of the number of the ribs on interface properties of the soil-reinforcement is much greater for reinforcements embedded at height of soil close to the ground surface and the effect of the number of the ribs is lower for embedded reinforcements at deep soil levels.

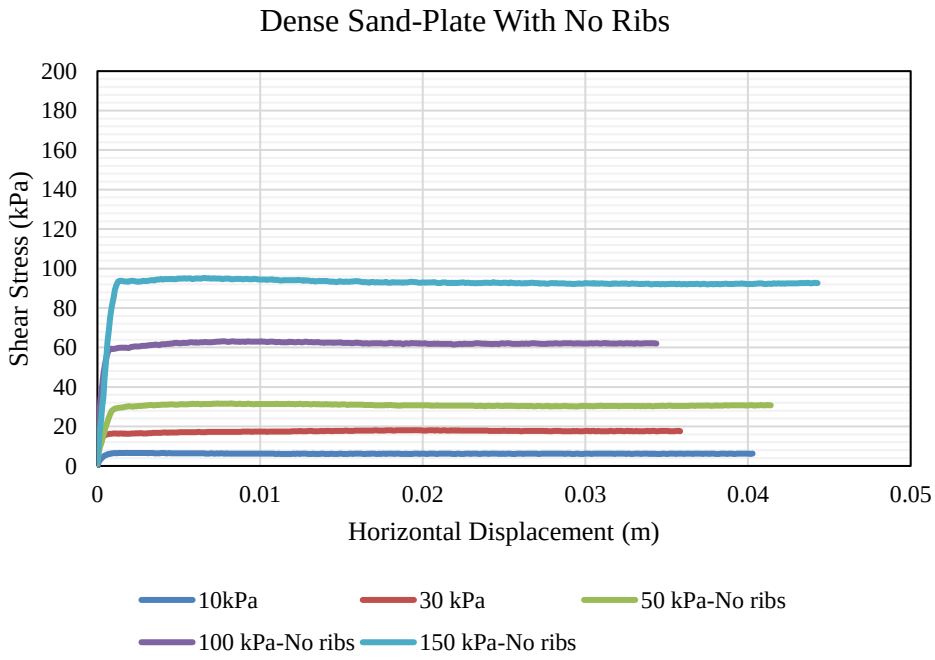

(a)

Figure 4-38. Shear Stress vs. Horizontal Displacement, Interface Direct Shear Test, Dense Sand, (a) Smooth Plate, (b) 2-Rib Plate, (c) 4-Rib Plate, (d) 6-Rib Plate, (e) 9-Rib Plate

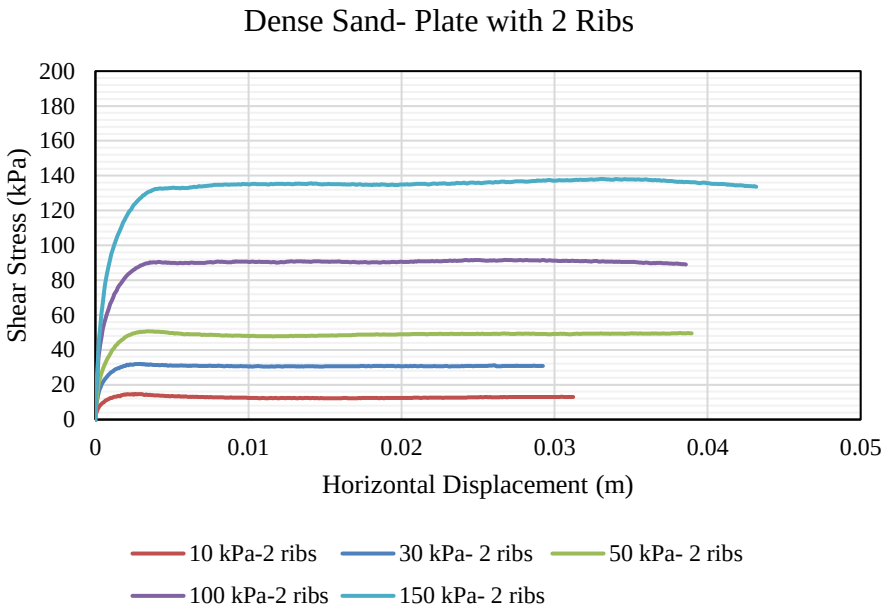

(b)

Figure 4-38. Continued.

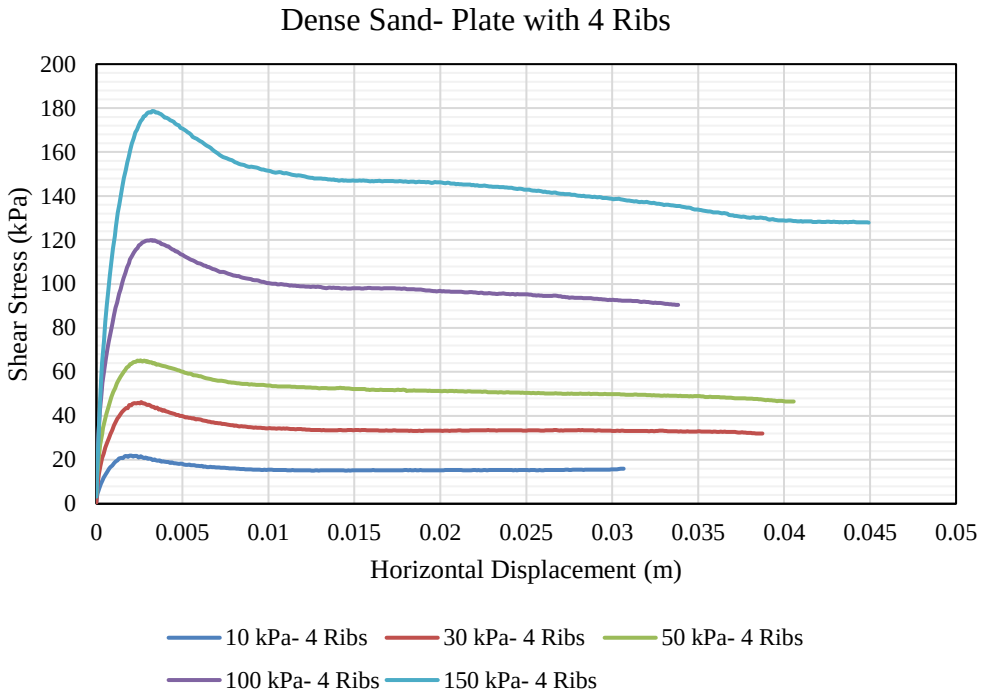

(c)

Figure 4-38. Continued.

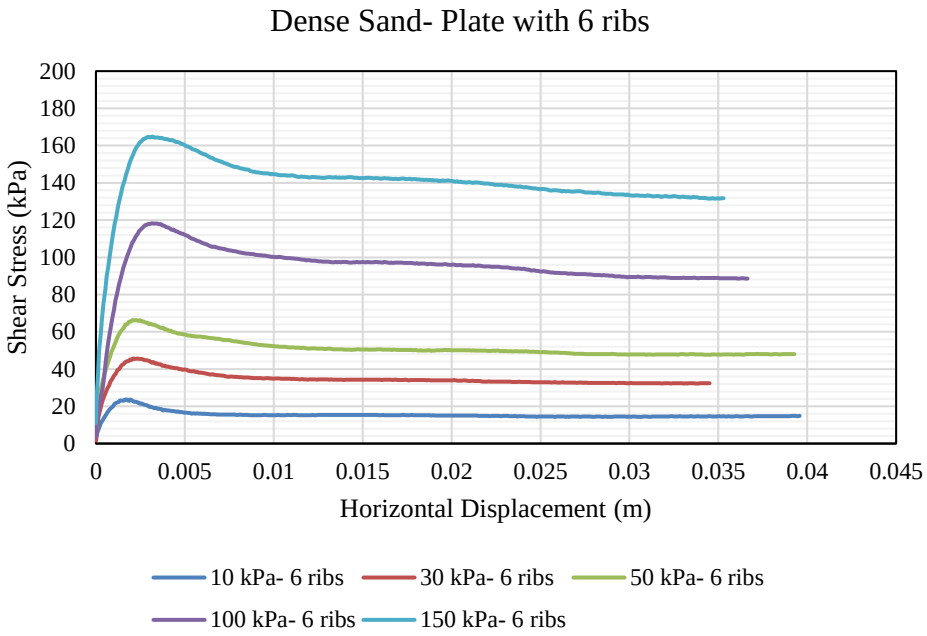

(d)

Figure 4-38. Continued.

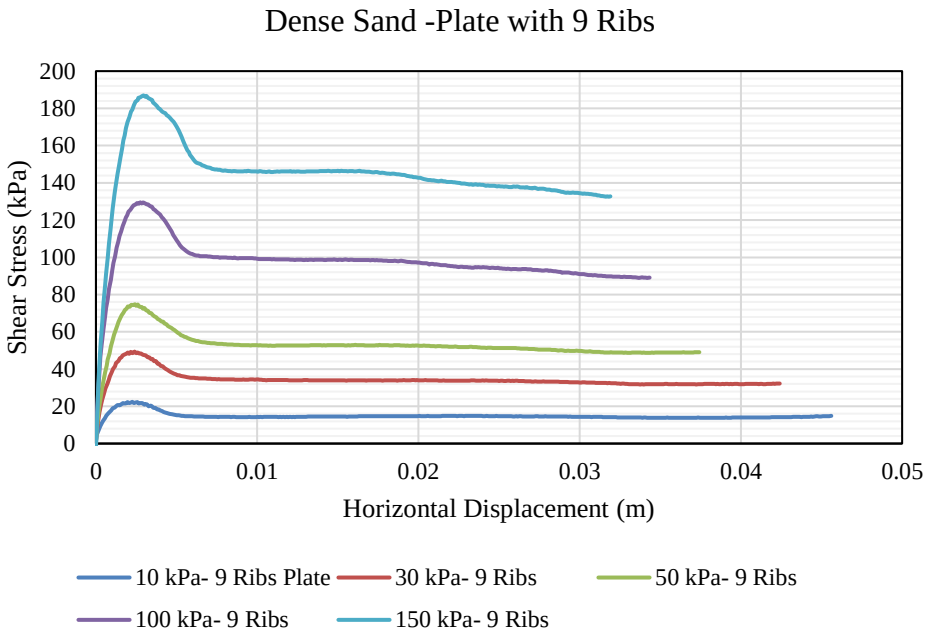

(e)

Figure 4-38. Continued.

Figure 4-39 describes the interface shear behavior of the smooth/ribbed aluminum plate-crushed limestone with fines. As seen in this figure, the results of the direct shear test on crushed limestone and aluminum plate show that thee shear strength of ribbed plates is higher than a smooth one. Although increasing the number of the ribs on plate increases the interface shear strength, comparing the internal shear strength of crushed limestone with interface shear strength of ribbed plate and soil illustrates that the interface shear strength is always lower than the internal shear strength of crushed limestone. Unlike the interface direct shear test between ribbed plates and sand, the fluctuation is observed for the graphs of interface direct shear test between plates and crushed limestone, because

of the movement of large aggregates and the breakage of the limestone aggregates under high normal pressure.

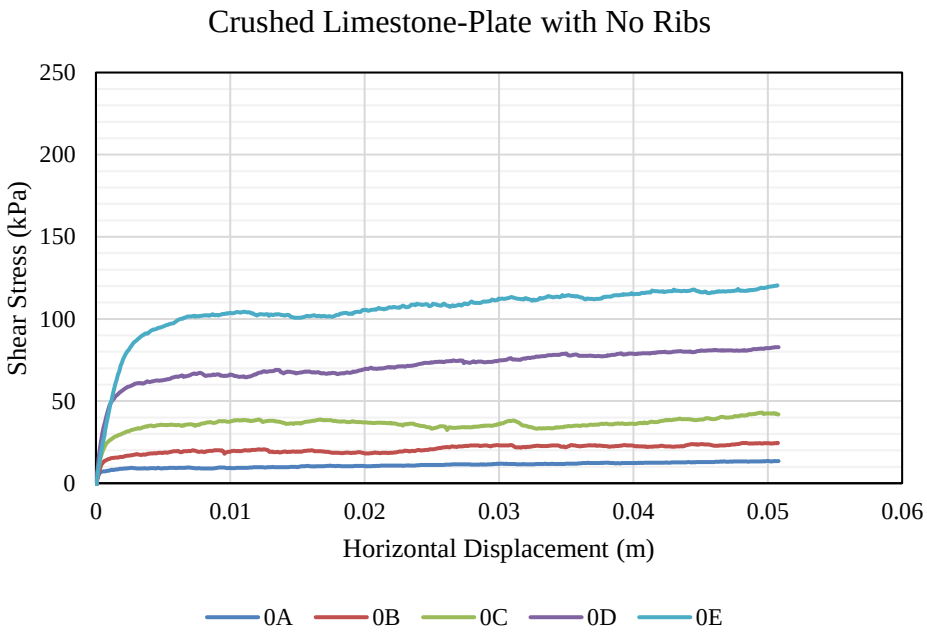

(a)

Figure 4-39. Shear Stress vs. Horizontal Displacement, Interface Direct Shear Test, Crushed Limestone with Fines, (a) Smooth Plate, (b) 2-Rib Plate, (c) 4-Rib Plate, (d) 6-Rib Plate, (e) 9-Rib Plate

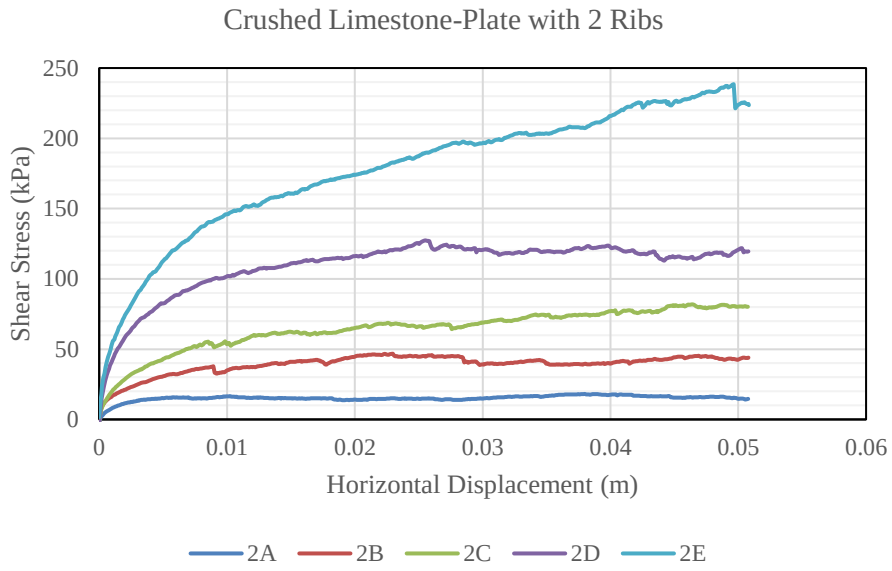

(b)

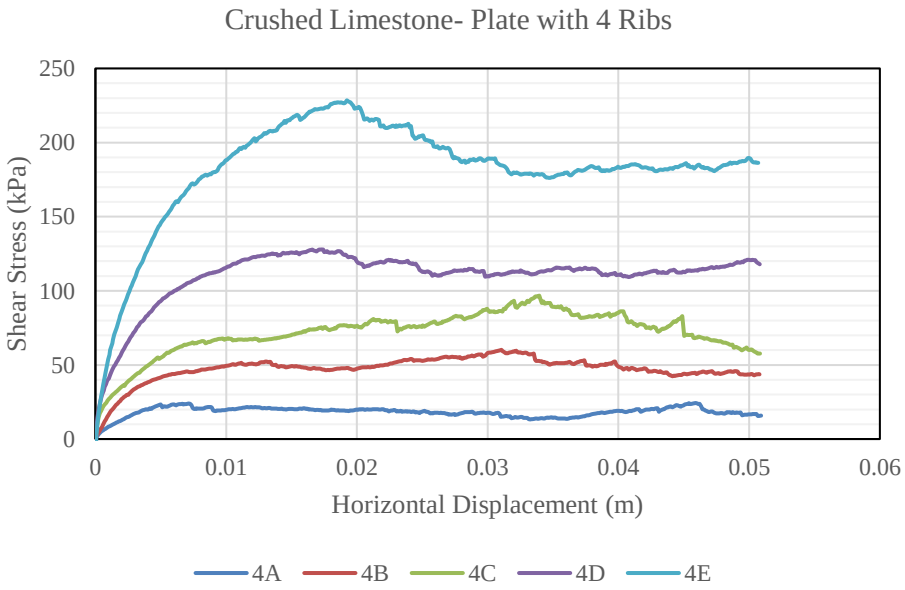

(c)

Figure 4-39. Continued.

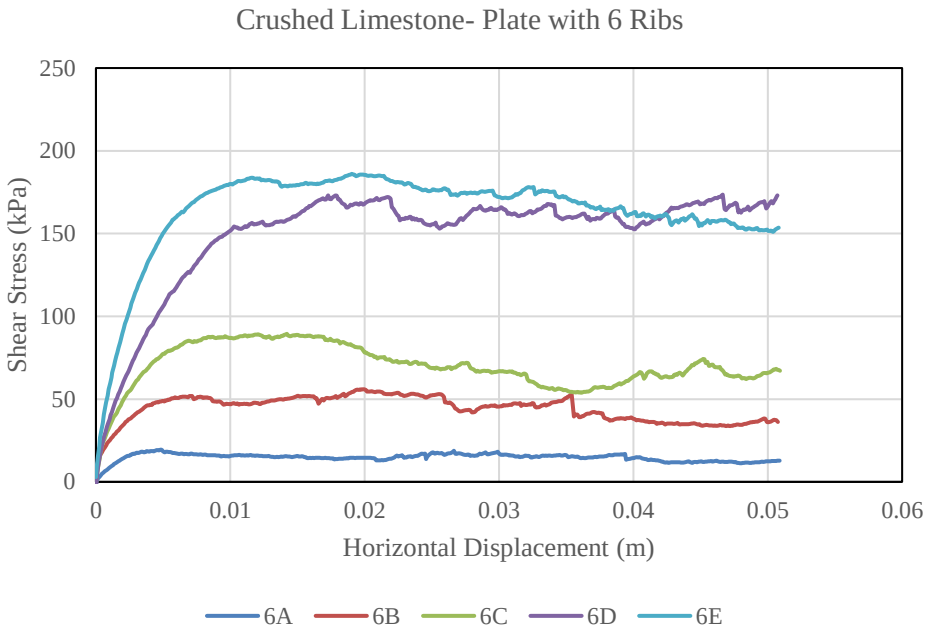

(d)

Figure 4-39. Continued.

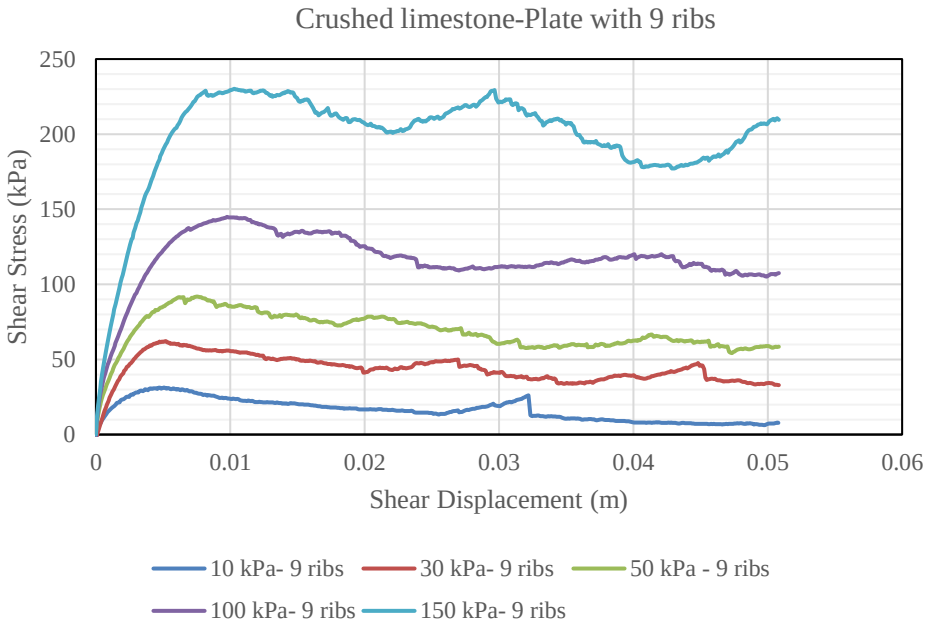

(e)

Figure 4-39. Continued.

The vertical displacement versus shear displacement curves obtained from the direct shear test on the interface of smooth/ribbed plates and loose sand, dense sand, crushed limestone are shown in Figure 4-40, Figure 4-41, and Figure 4-42, respectively. As shown in Figure 4-40, the smooth plate-loose sand interface undergoes contraction at the starting of test with the high rate and continues to contract to the end of the test with a lower rate at a certain horizontal displacement. On the other hand, the vertical displacement-horizontal displacement curves for direct shear test on a ribbed plates-loose sand interface indicates that the specimen undergoes contraction at small displacement and the specimen shows dilation for larger shear displacements (less than 5 mm). The

vertical displacement stays constant for the 2-rib plate and 4-rib plate under low normal stresses. With increasing the number of ribs on a plate or higher normal stresses, the contraction behavior is observed after the specimen dilates to the peak value.

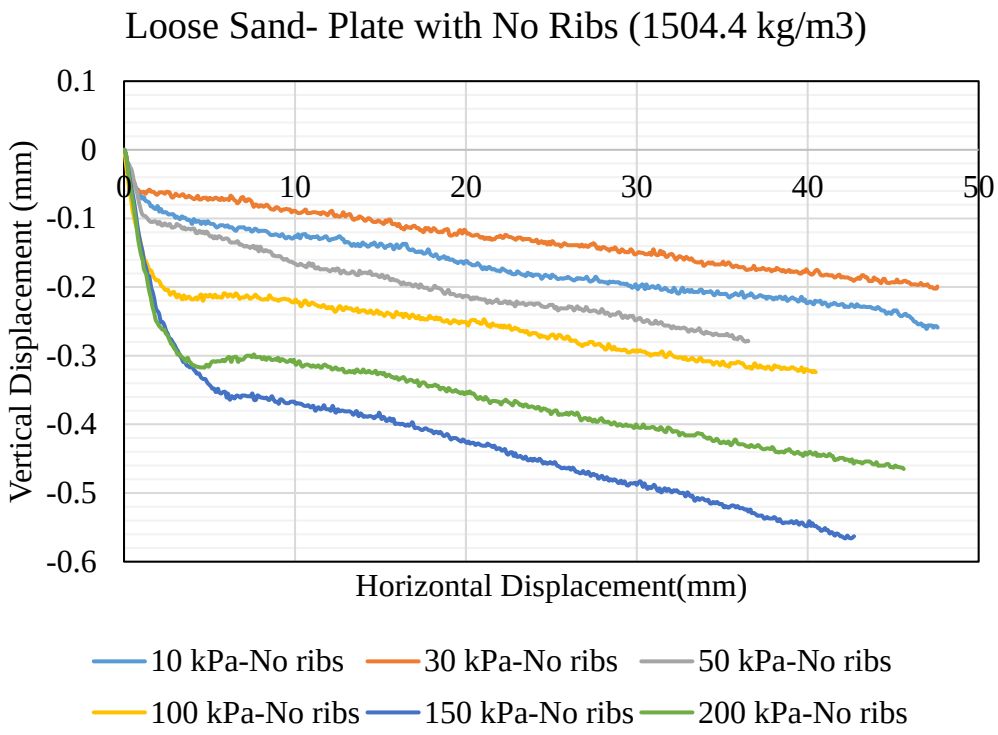

(a)

Figure 4-40. Vertical Displacement vs. Horizontal Displacement, Interface Direct Shear Test, Loose Sand, (a) Smooth Plate, (b) 2-Rib Plate, (c) 4-Rib Plate, (d) 6-Rib Plate, (e) 9-Rib Plate

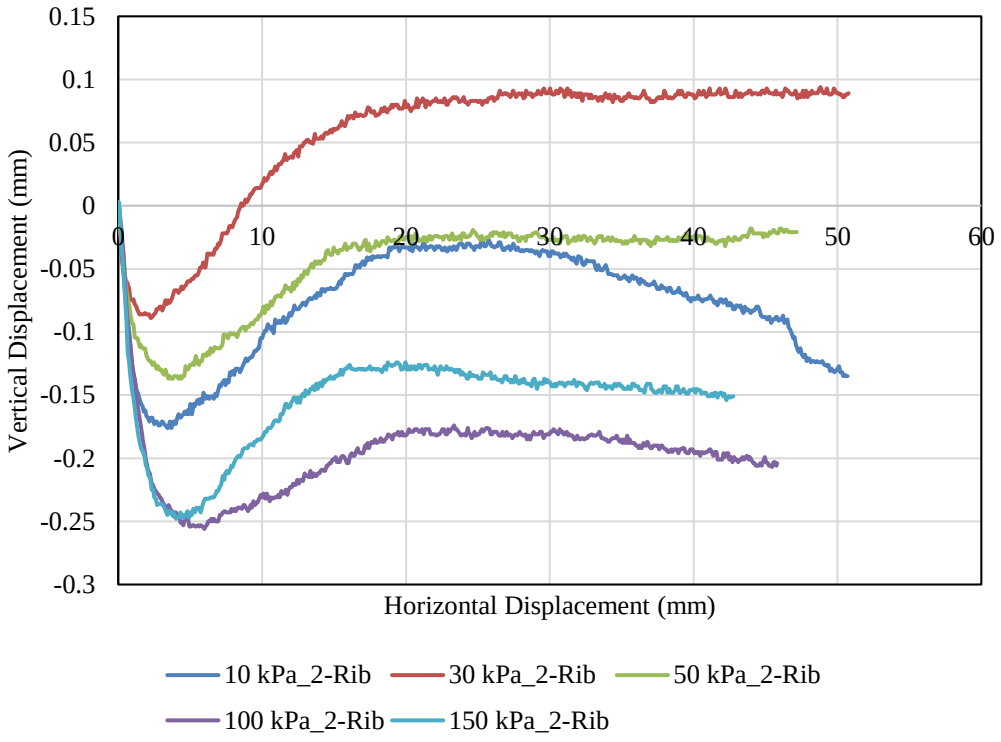

(b)

Figure 4-40. Continued.

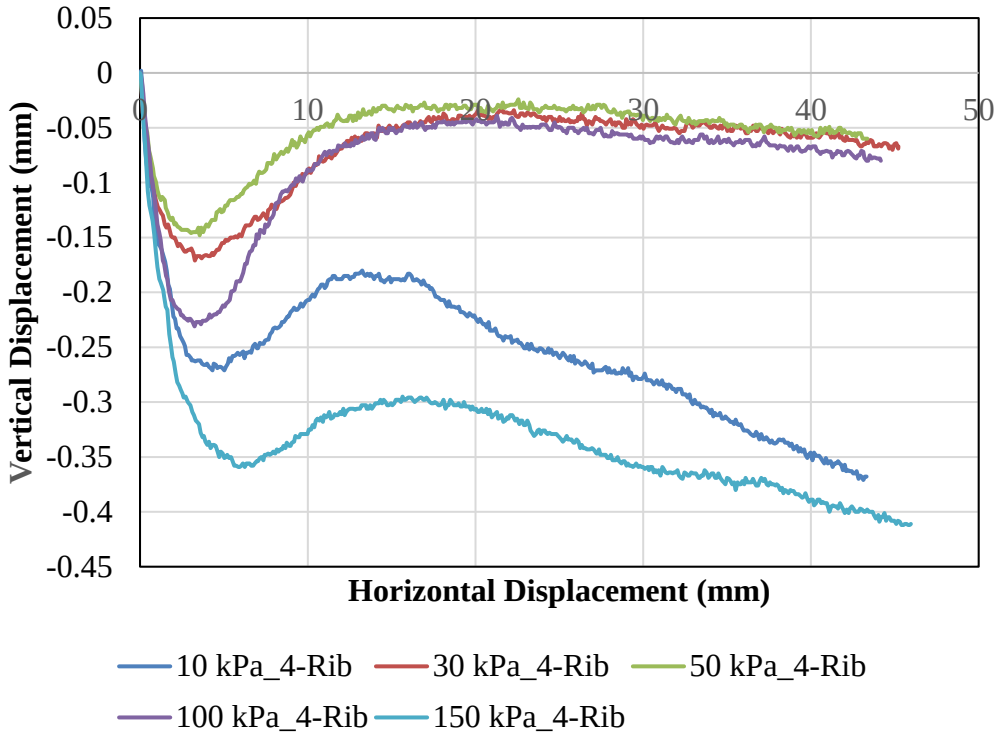

(c)

Figure 4-40. Continued.

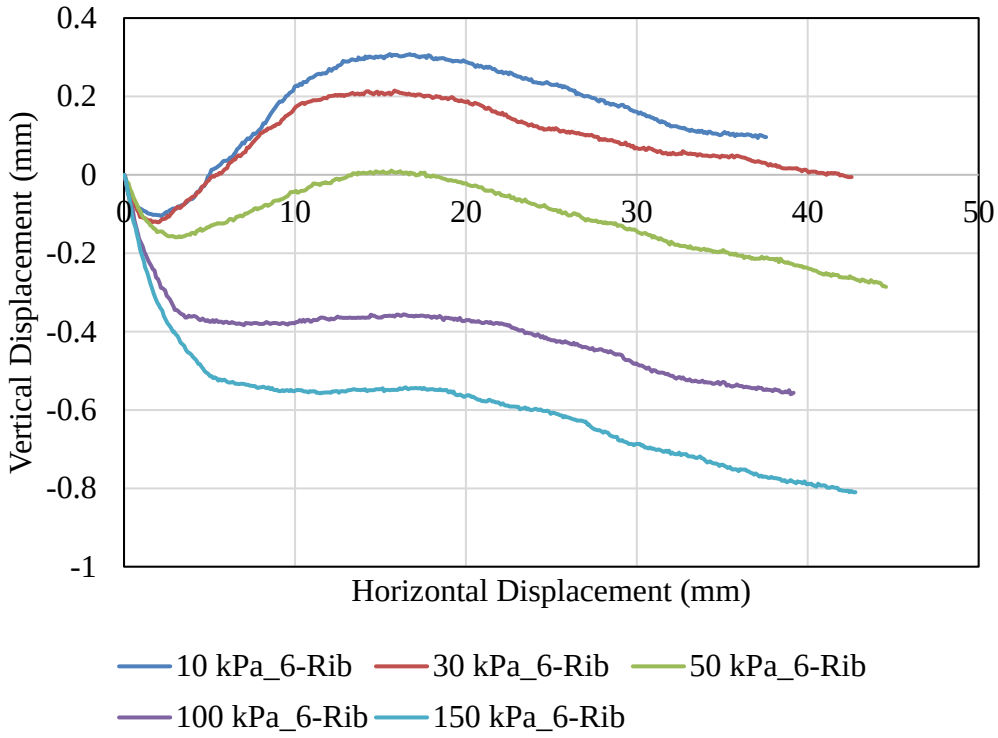

(d)

Figure 4-40. Continued.

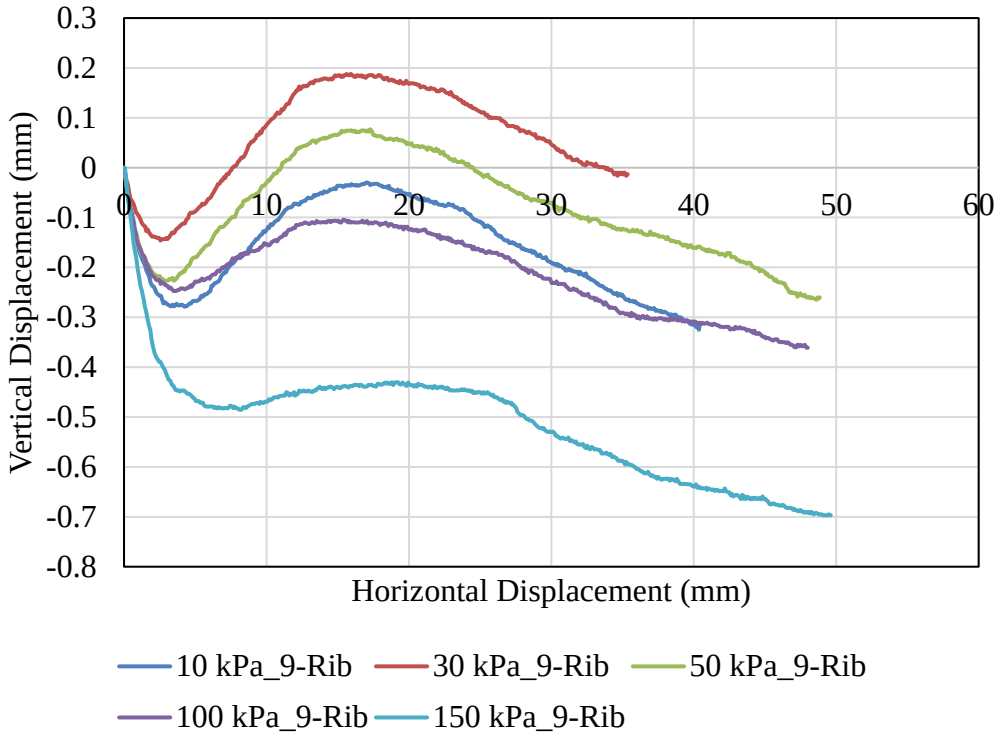

(e)

Figure 4-40. Continued.

The vertical deformation of the smooth/ribbed plate-dense sand is shown in Figure 4-41. As shown in this figure, the smooth plate-dense sand specimen exhibits dilatancy starting from small shear displacements. With increasing the shear displacement, the specimens show dilation behavior to the end of the test. Furthermore, comparing the vertical deformation of ribbed plates with a smooth one reveals that the ribbed plate-dense sand interface experiences greater vertical displacements (dilation) than smooth plate-dense sand. That is, the ribbed plate- dense sand interface shows higher dilation angle than the smooth plate-dense sand interface. Because the soil particles have to move over ribs

during shearing. Comparing the vertical displacement of Smooth/ribbed plate-dense sand interface with dense sand internal, the maximum dilation of the soil occurs at the shear displacement corresponding to the peak shear strength before 20 mm depending on the confining pressure while the maximum dilation values obtained from interface direct shear test are observed at the end of the test, not necessarily the shear displacement corresponding to the peak shear stress.

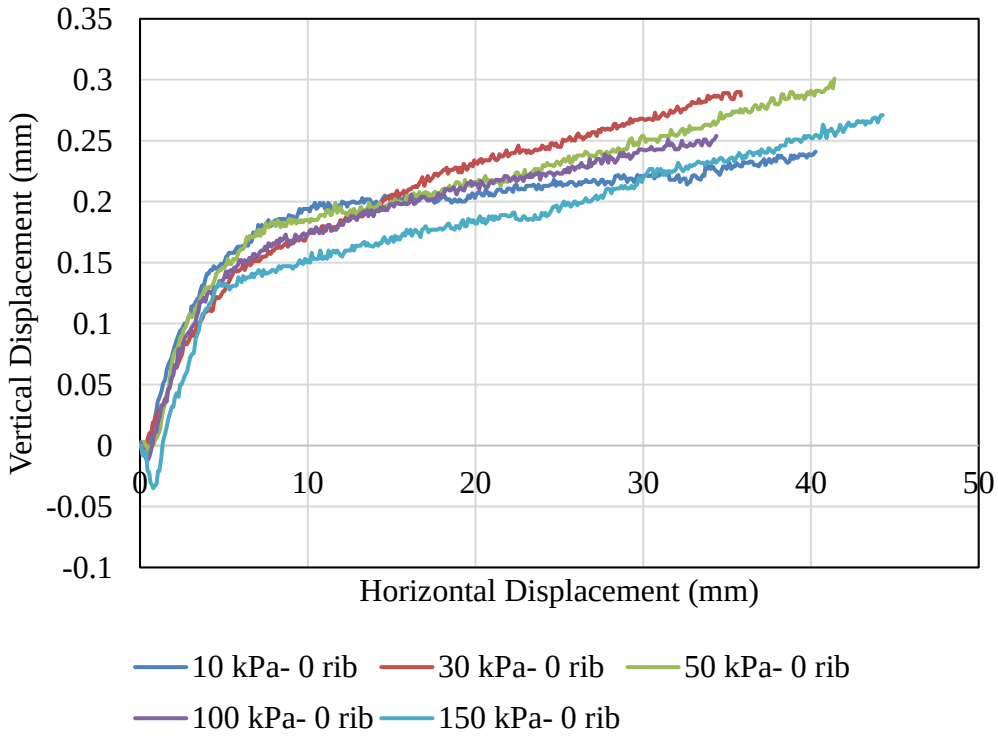

(a)

Figure 4-41. Vertical Displacement vs. Horizontal Displacement, Interface Direct Shear Test, Dense Sand, (a) Smooth Plate, (b) 2-Rib Plate, (c) 4-Rib Plate, (d) 6-Rib Plate, (e) 9-Rib Plate

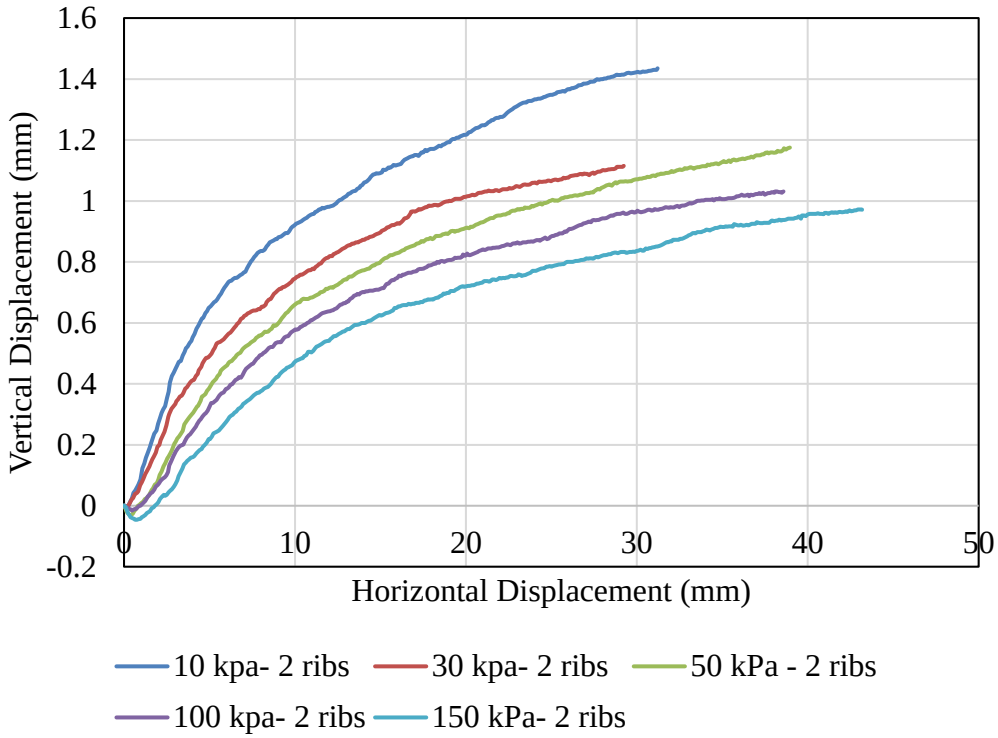

(b)

Figure 4-41. Continued.

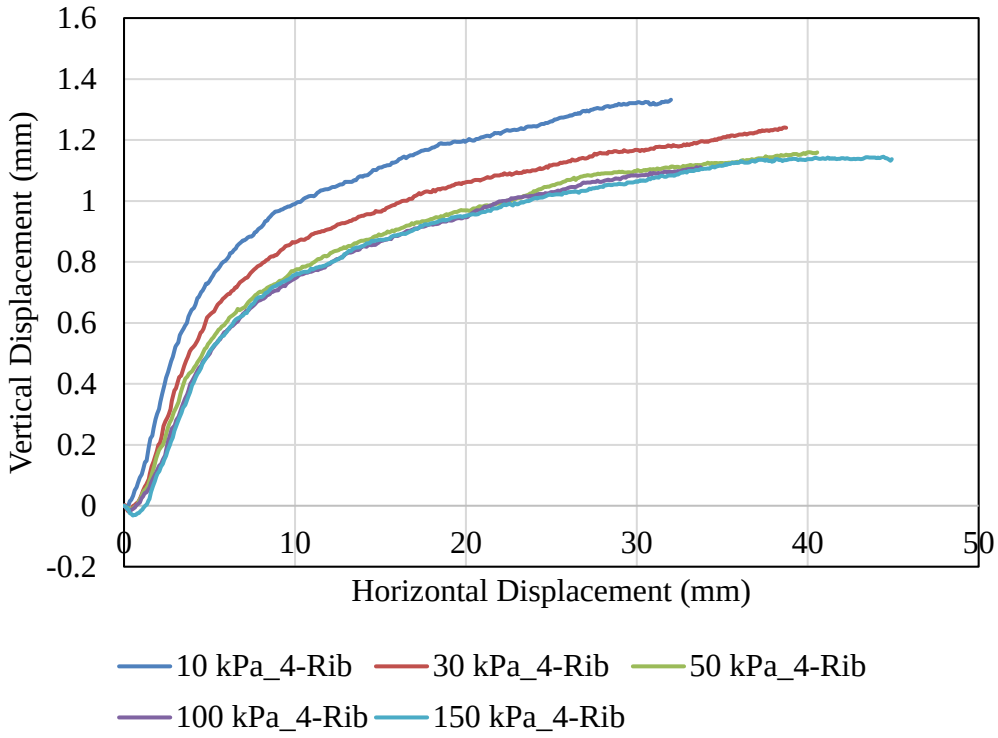

(c)

Figure 4-41. Continued.

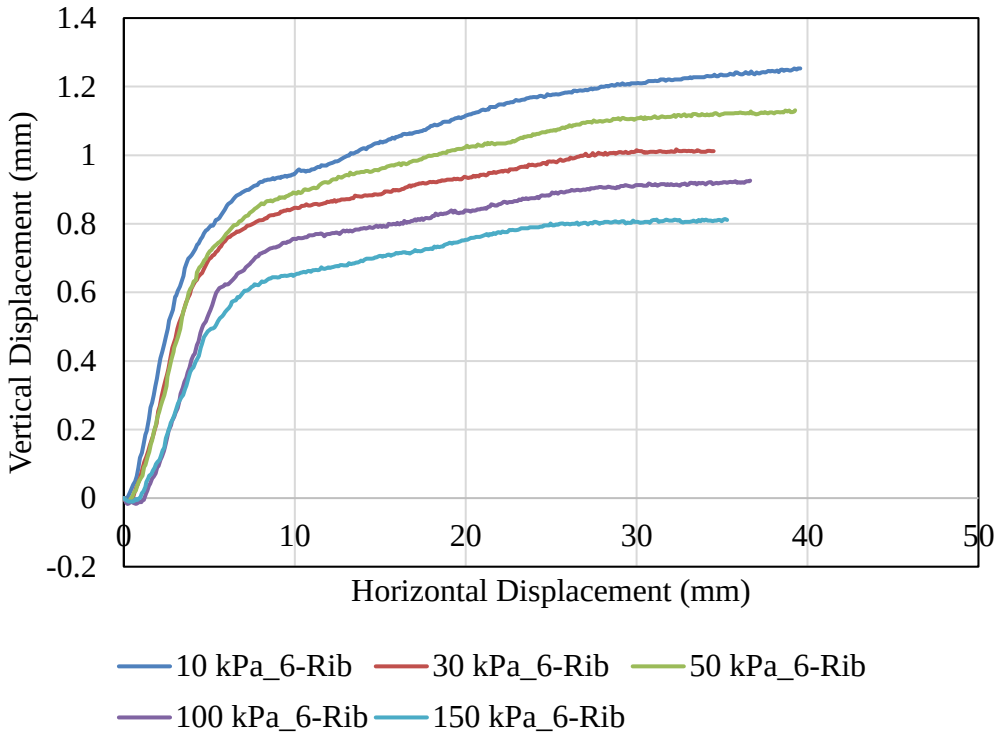

(d)

Figure 4-41. Continued.

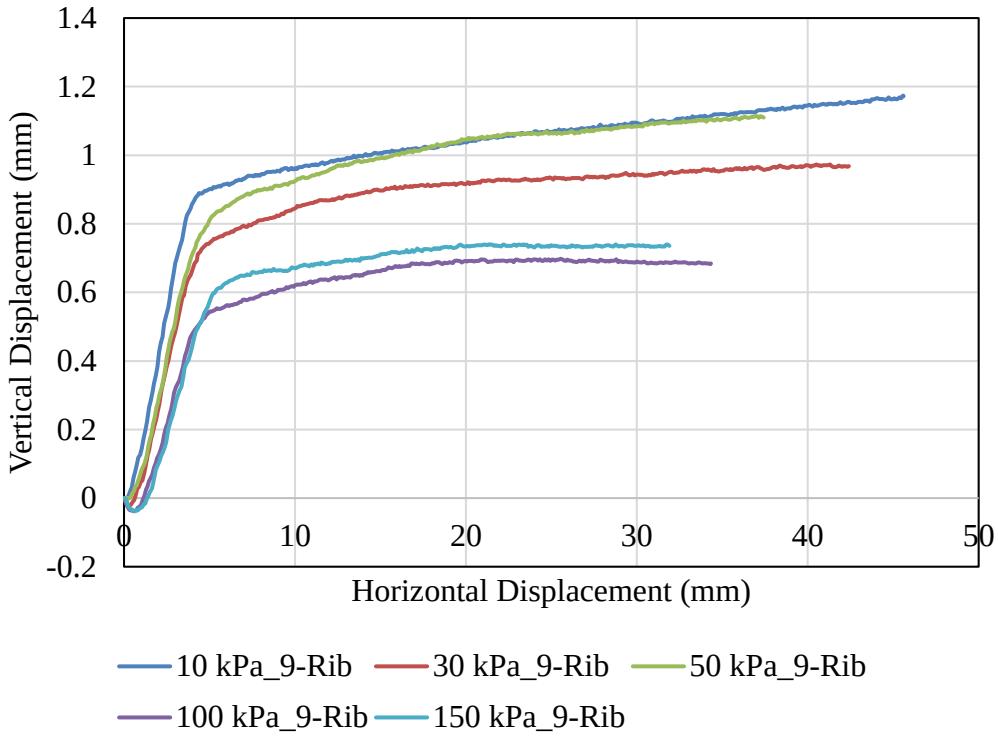

(e)

Figure 4-41. Continued.

The vertical displacement of the smooth/ribbed plate-crushed limestone with fines is shown in Figure 4-42. As shown in this figure, when the shear phase initiated, the smooth plate-CLF specimen experiences dilation at 10 kPa normal stresses and increases almost linearly as the shear displacement increases. The contraction behavior is observed for specimens under normal stresses greater than 10 kPa. The ribbed plate-CLF curves show that the specimen undergoes initial contraction at small displacements and dilates at large displacements. With increasing the number of ribs on a plate (decreasing the ribs spacing), the vertical displacement increases. For example, the maximum vertical

displacement of smooth, 2-rib, 4-rib, 6-rib, and 9-rib plates under 10 kPa normal stress is 0.4mm, 1.8mm, 2mm, 3mm, and 4 mm, respectively. The results of interface tests on crushed limestone with fine shows greater contraction compering to sand because of existence of the fine particles and pores between the coarse particles (poorly graded material) which cause contractive behavior under high normal pressure.

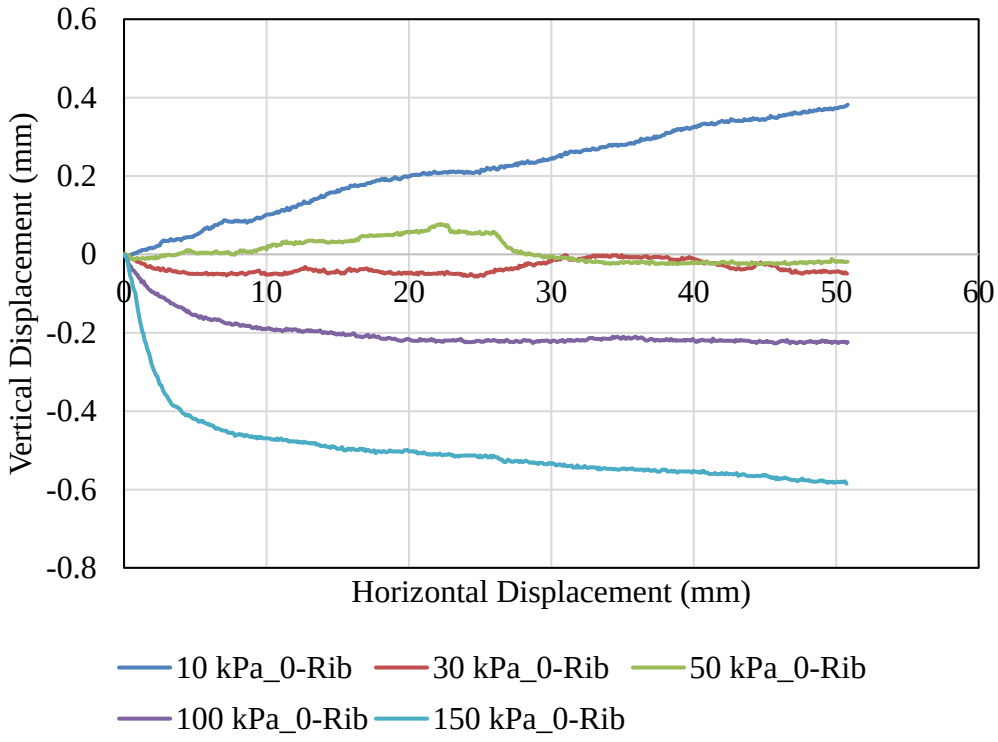

(a)

Figure 4-42. Vertical Displacement vs. Horizontal Displacement, Interface Direct Shear Test, Crushed Limestone with Fines, (a) Smooth Plate, (b) 2-Rib Plate, (c) 4-Rib Plate, (d) 6-Rib Plate, (e) 9-Rib Plate

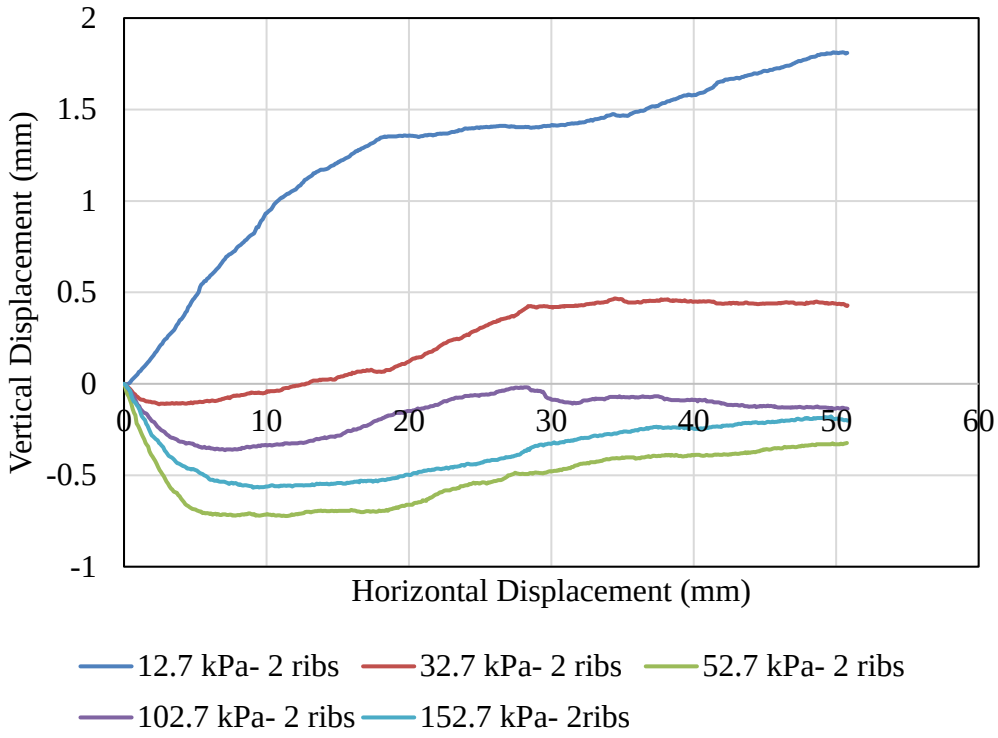

(b)

Figure 4-42. Continued.

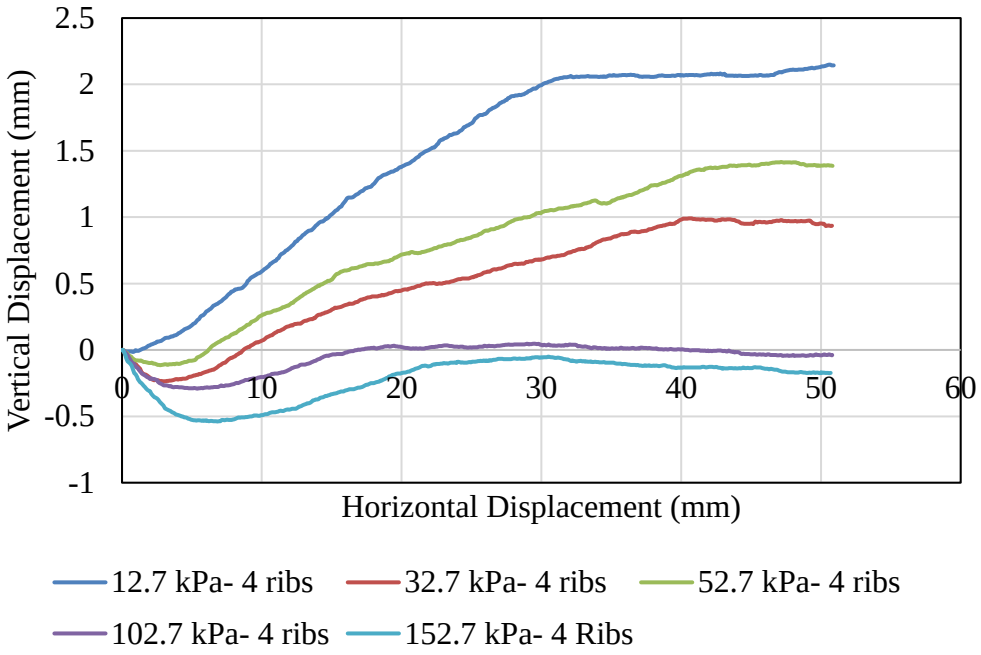

(c)

Figure 4-42. Continued.

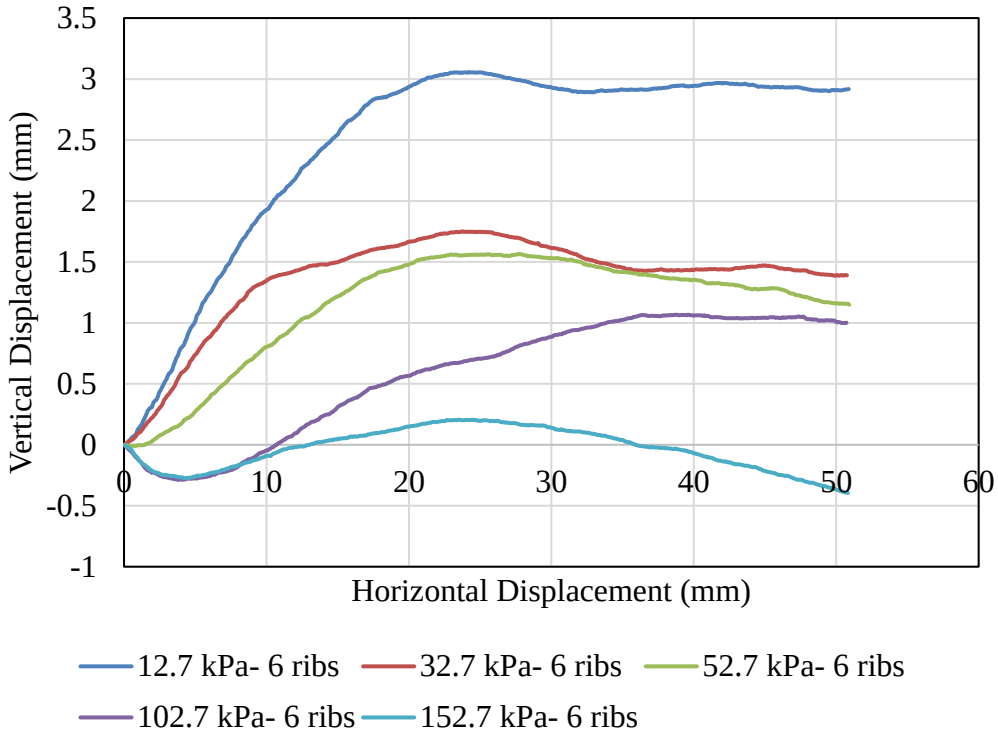

(d)

Figure 4-42. Continued.

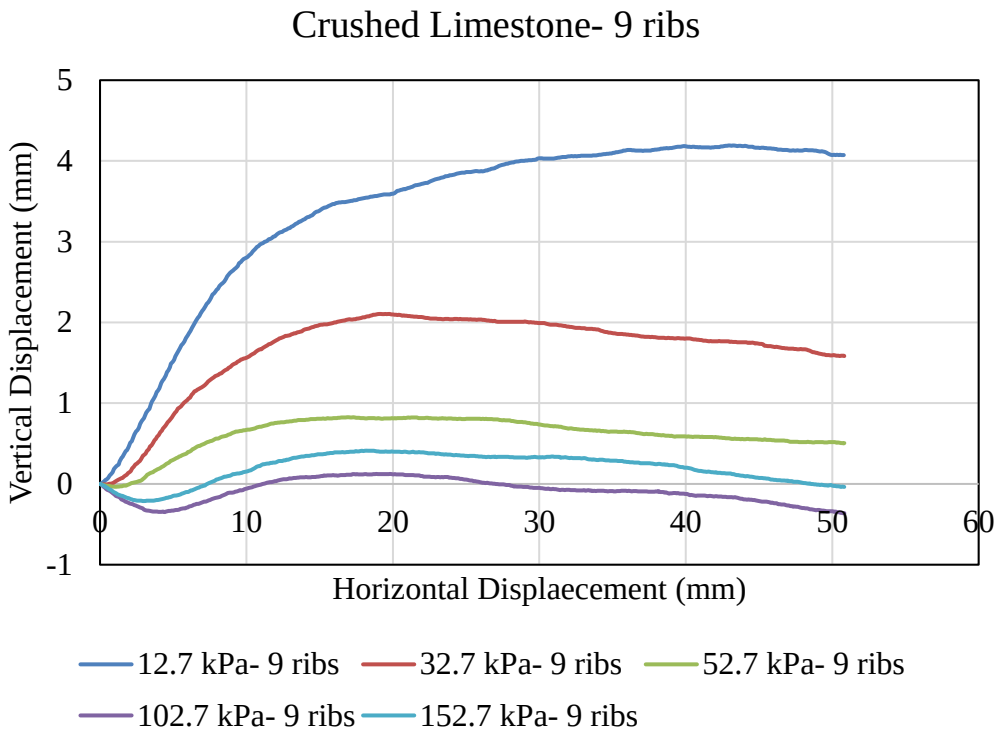

(e)

Figure 4-42. Continued.

Figure 4-43 to Figure 4-45 shows the variation of peak shear strength versus normal stress for three sets of interface tests between smooth/ribbed plates and loose sand (LS), dense sand (DS), and crushed limestone with fines (CLF). The failure criteria were considered as the maximum shear strength or the stress at ¾ inch shear displacement if the peak shear strength did not occur before ¾ inch shear displacement. As shown in Figure 4-43, the interface friction angle is in the range of 33.4º to 38º for the smooth plate to 9-Rib plate, respectively. The influence of the number of the ribs on interface friction angle between plates and loose sand is almost negligible for plates with 4, 6, and 9 ribs. On the

other hand, with increasing the density of sand, the influence of the number of ribs is more noticeable on the slope of the failure envelope (Figure 91). The interface friction angle between the smooth plate and dense sand is 32º and the interface friction angle is increasing with decreasing the ribs spacing to 49º. The figure illustrates that the rate of increasing the slope of the failure envelope is decreasing for ribbed plates with more than 4 ribs. Comparing the interface friction angle between ribbed plate-loose sand and ribbed plate-dense sand, the interface friction angle between the smooth plate and sand is independent of the density. However, the interface friction angle between 9-rib plate and loose/dense sand shows significant differences. It is worth mentioning that the friction angle of soil-soil is 38º and 47º for loose and dense sand, respectively. In conclusion, the results show that the maximum interface friction angle never exceeds the soil-soil internal friction angle, and for plates with more than 4 ribs or ribs spacing less than 6 cm (2.4 inches.), the failure plane is inside the soil and the interface friction angle is almost the same as soil-soil friction angle.

Figure 4-45 reports the shear strength versus shear displacement obtained from interface direct shear test on smooth/ribbed plate-crushed limestone. The interface friction angle is 33.7º for the smooth plate and increases to 53º for the 9-rib plate. Therefore, the interface friction angle of the smooth plate and CLF is very close to the one with sand (loose and dense). Comparison of the internal friction angle of crushed limestone (56º) with the interface friction angle of ribbed plate-CLF indicates that the internal friction

angle of the soil is slightly higher than the interface friction angle of the 9-rib plate and CLF.

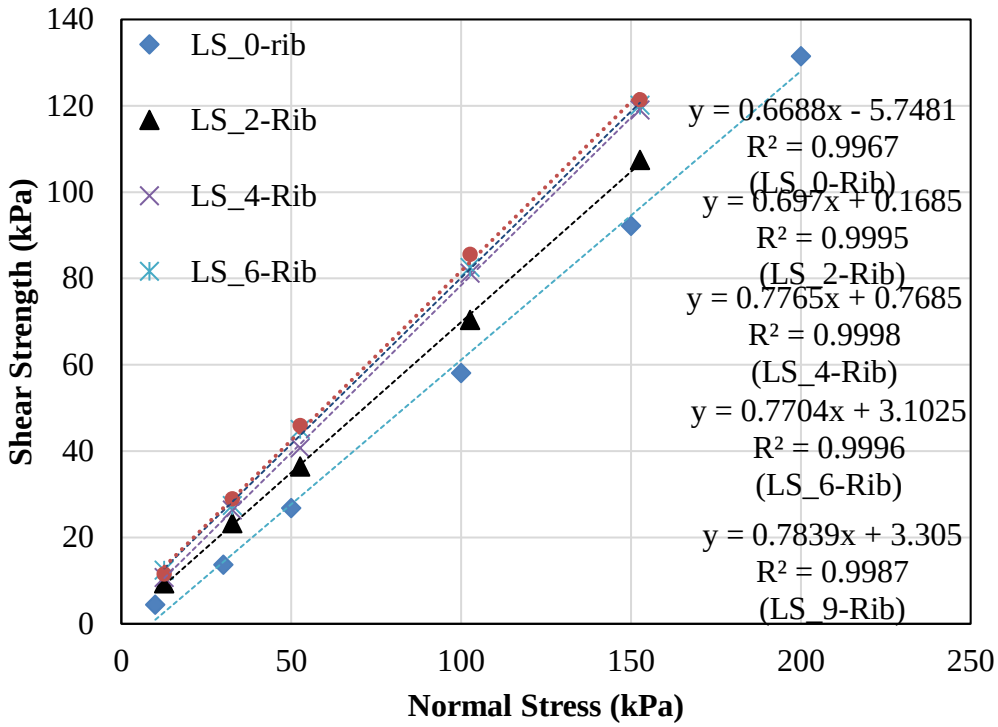

Figure 4-43. Shear Strength vs. Normal Stress, Interface Direct Shear Test, Loose Sand

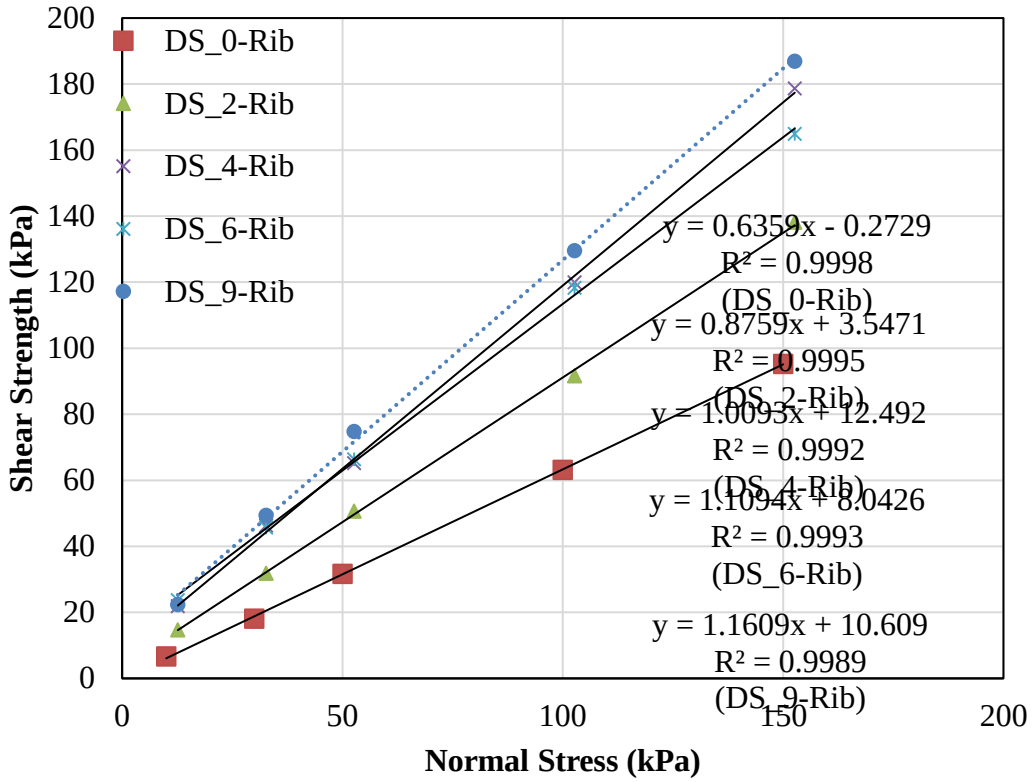

Figure 4-44. Shear Strength vs. Normal Stress, Interface Direct Shear Test, Dense Sand

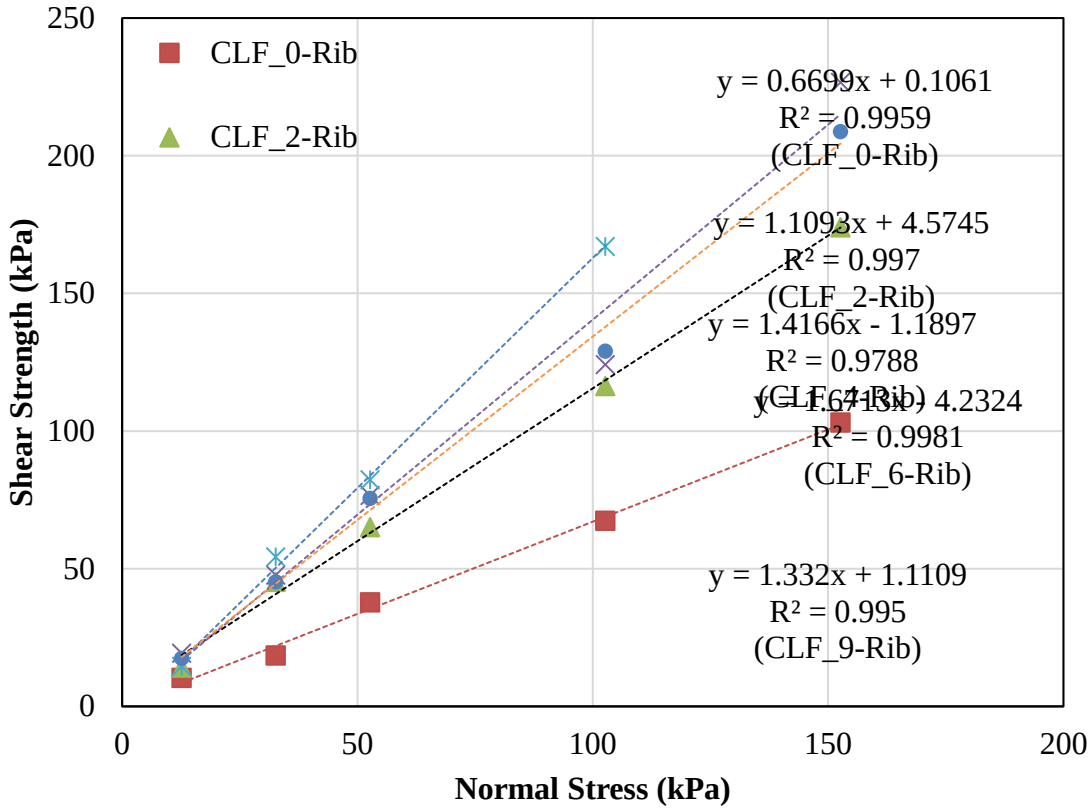

Figure 4-45. Shear Strength vs. Normal Stress, Interface Direct Shear Test, Crushed Limestone with Fines

4.4.2 Geogrid Reinforcement

4.4.2.1 Test Procedure

Table 4-6 illustrates the test plan for interface direct shear test between geogrid reinforcement and the soil specimens (LS, DS, CLF). The tests were performed using large direct shear apparatus, ShearTrac III. The tests were set up the way that the geogrid stays on the shear plane between the lower and upper shear boxes. The soil sample preparation is the same as the soil-soil direct shear test, and tests were performed for loose sand, dense sand, and crushed limestone with fines. First, the soil sample was placed in the lower half of the box and compacted as explained before. Then, the geogrid reinforcement was cut from the roll using a table saw and placed on the lower half of the box and clamped in the lower box (Figure 4-46). The geogrid was fixed to the shear box as the transverse member stays in the mid-width of the box. Then the upper half of the shear box is placed on the specimen and tightened with the alignment screws (Figure 4-47). The upper half of the shear box was filled with the soil specimen and compacted with the same method. Each series of tests were performed under 10, 30, 50, 100, and 150 kPa normal stress.

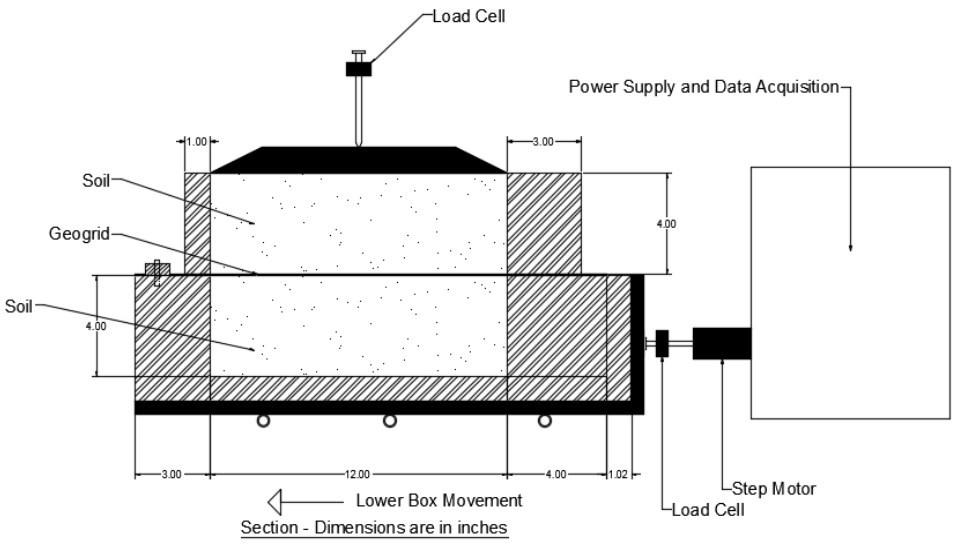

Figure 4-46. Schematic Drawing of Interface Direct Shear Test on Geogrid

Figure 4-47. Interface Direct Shear Test Setup on Geogrid

4.4.2.2 Test Results

The results of an interface direct shear test with geogrid reinforcement are presented in Figure 4-48, in terms of shear stress versus shear displacement. Also, in this figure is presented the results of unreinforced soil specimen. As shown in Figure 4-48 (a) the shear stress increases with increasing the shear displacement to a peak value and decreases to a residual value. It is observed that for geogrid-loose sand, the mobilize peak shear strength is lower than loose sand internal shear strength. Moreover, at large displacement, the difference between the shear strength of geogrid-loose sand and loose sand internal shear strength increases with increasing the normal stress.

A significant increase in shear strength is observed for geogrid embedded in dense sand compare to the shear strength of dense sand. The shear displacement required to reach the peak interface shear strength of geogrid-dense sand is observed lower than the one of the pure dens sand. The geogrid-dense sand interface shows stiffer behavior than dense sand.

Figure 4-48 (c) illustrates the shear behavior of interface geogrid-CLF and pure CLF. The comparison indicates that the peak shear stress of CLF internal is greater than geogrid-CLF. The shear stress-shear strain curves for CLF shows that as the shear displacement increases, the shear stresses increases to a peak value and after that point, the shear stress stays almost constant. In contrast, the shear behavior of geogrid-CLF shows that with increasing the shear displacement, the shear stress keeps increasing to the end of the test, and at5 cm displacement the shear stress reaches to the CLF shear strength.

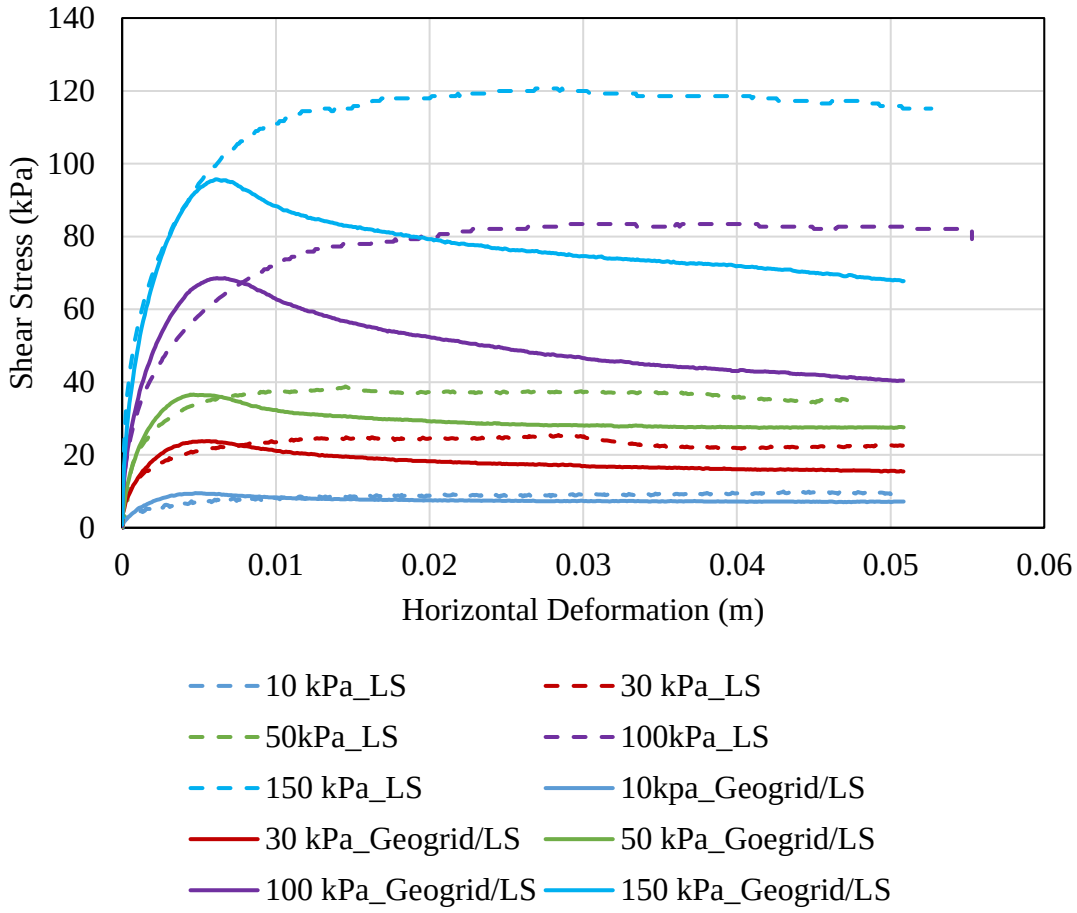

(a)

Figure 4-48. Shear Stress vs. Horizontal Displacement, Interface Direct Shear Test with Geogrid Reinforcement and, (a) Loose Sand (b) Dense Sand, (c) Crushed Limestone

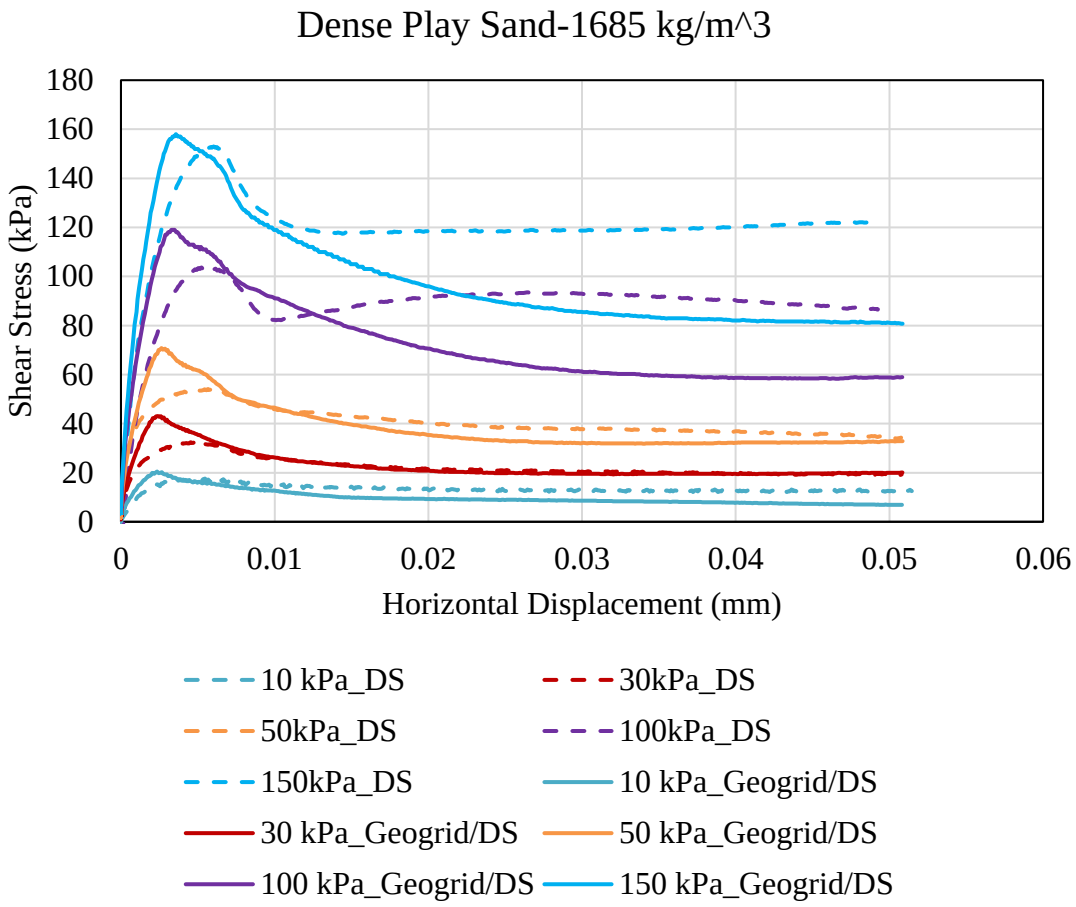

(b)

Figure 4-48. Continued.

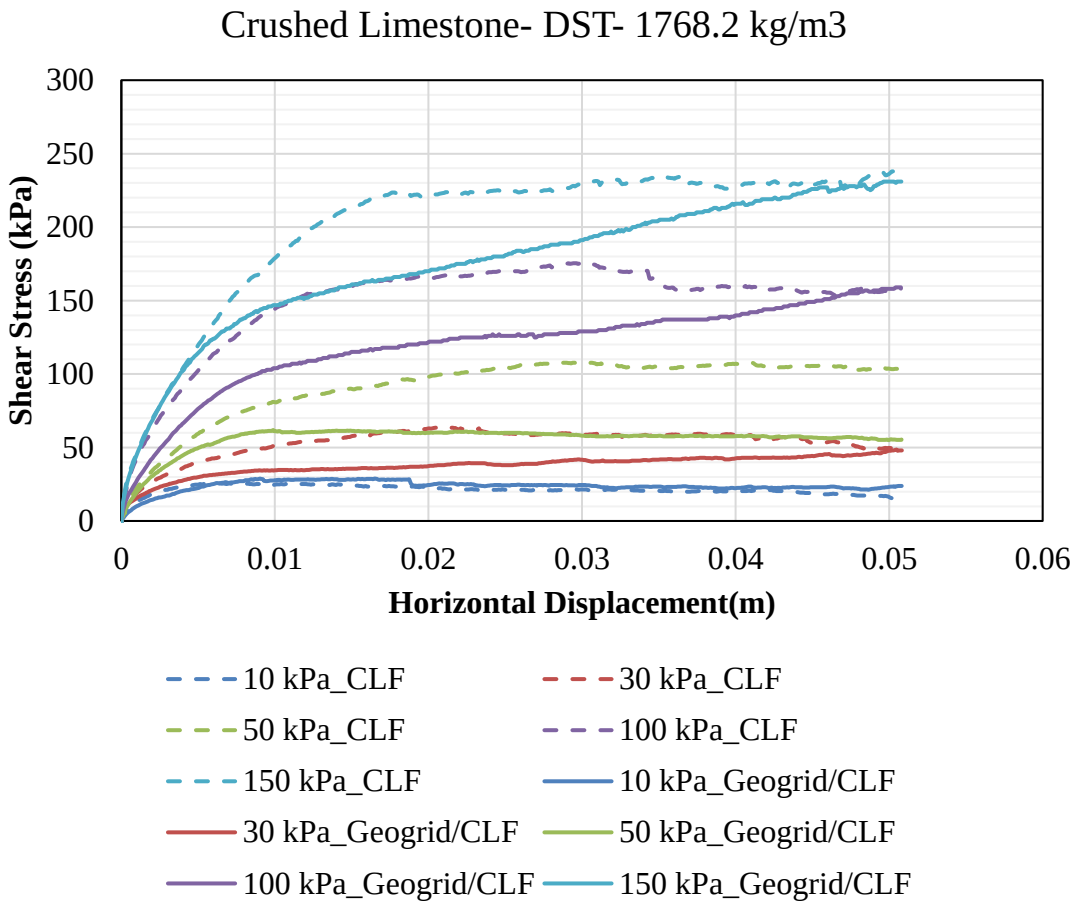

(c)

Figure 4-48. Continued.

The vertical displacement-shear displacement curves obtained from the direct shear tests on loose sand/geogrid, dense sand/geogrid and crushed limestone with fines/geogrid are shown in Figure 4-49. As shown in Figure 4-49 (a), the loose sand/geogrid interface goes under an initial contraction at small shear displacement, then the small amount of dilation is observed and after that the specimen experiences contraction at large horizontal displacement. On the other hand, vertical displacement-

horizontal displacement curves of dense sand-geogrid show the initial contraction behavior at very small shear displacement following by dilation starting at small shear displacements. Then the vertical displacements stay constant and the starts to contract again with a lower rate at large displacement. The specimen experiences a large amount of dilation for low normal stresses. The maximum vertical displacement of the dense sand-geogrid occurs at the shear displacement corresponding to the yield shear stress.

The vertical displacement versus shear displacement of CLF-geogrid shows that at low normal stresses, the specimen starts to contract from small shear displacements. The specimen under high normal stresses exhibits contraction at small and large displacements. The maximum vertical displacement occurs at the horizontal displacement corresponding to the peak shear strength of the interface test.

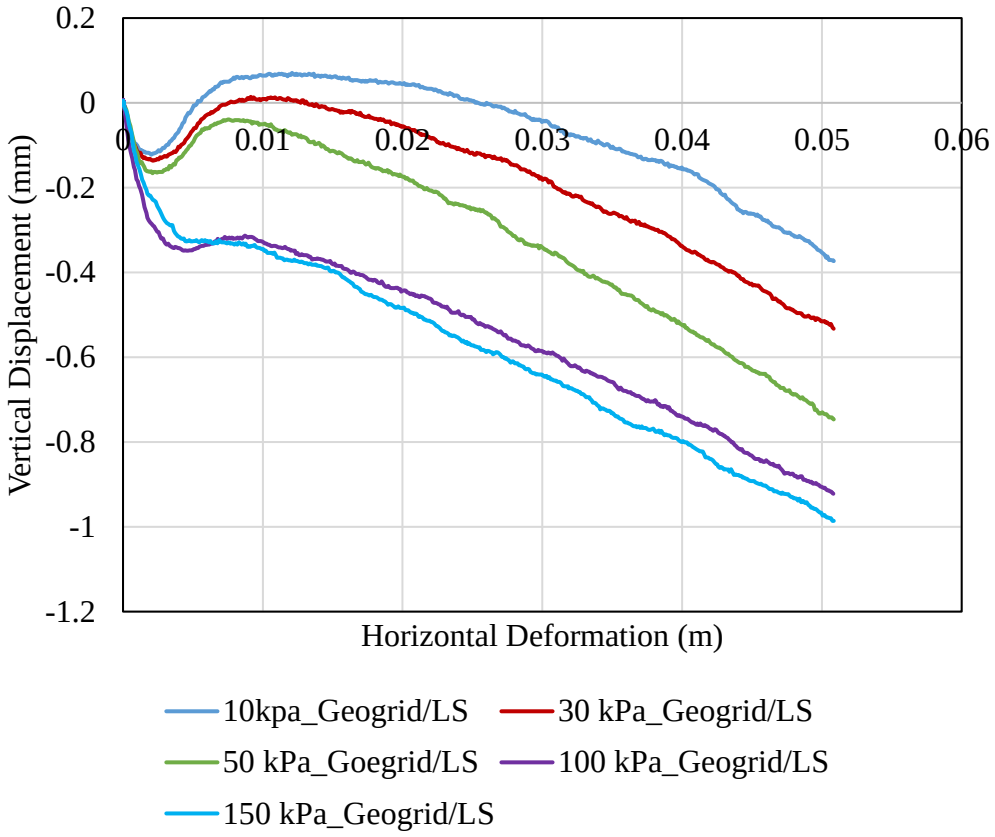

(a)

Figure 4-49. Vertical Displacement-Horizontal Displacement for Geogrid-Soil Interface Direct Shear Test, (a) Loose Sand, (b) Dense Sand, (c) Crushed Limestone with Fines

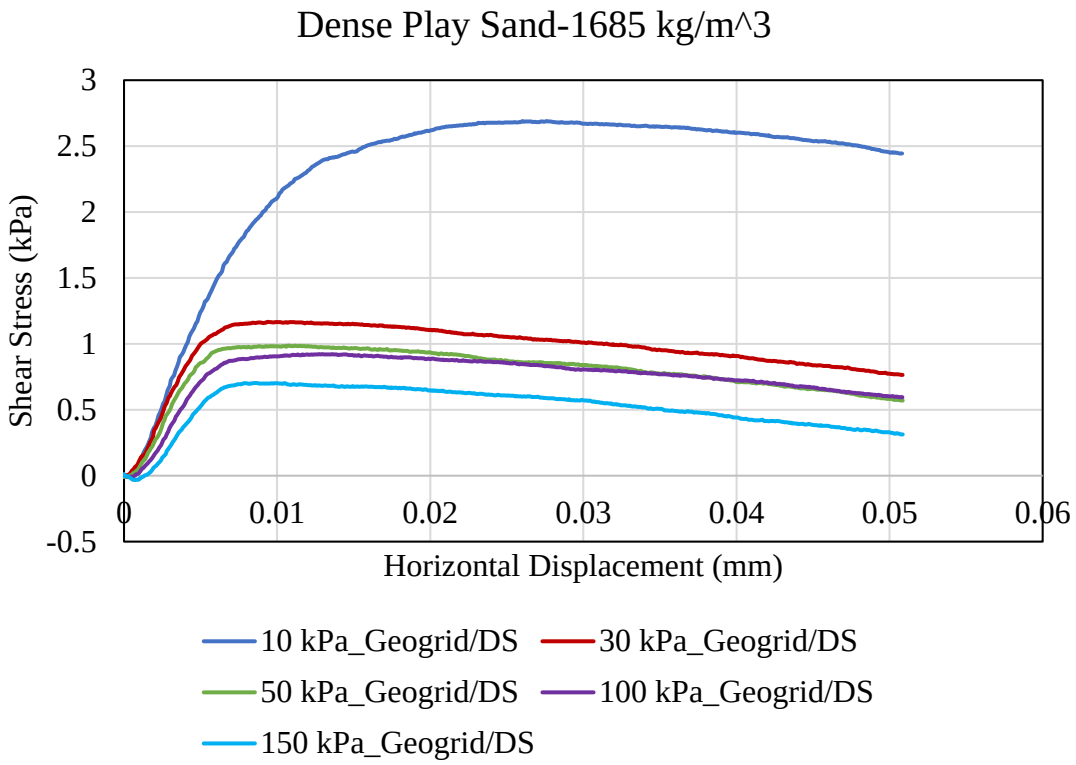

(b)

Figure 4-49. Continued.

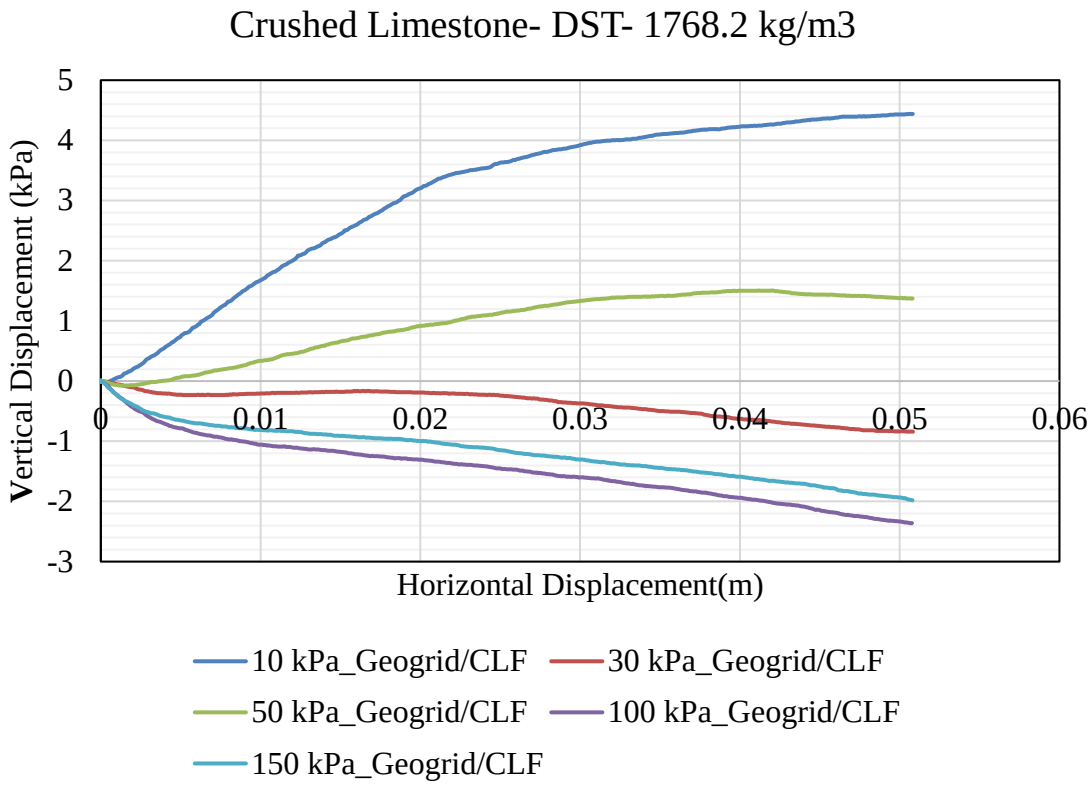

(c)

Figure 4-49. Continued.

To study the friction angle of geogrid-soil using direct shear test, shear stress-normal stress curves were plotted in Figure 4-50. The Mohr's Coulomb failure envelopes of soil-soil internal are provided in this figure to compare the friction angle of reinforced soil with the soil itself. As shown in this figure, the friction angle of geogrid-LS (31°) is lower than the friction angle of pure loose sand (38°). Because during the shear phase, the sand particles roll over the geogrid material.

The same result is observed for dense sand; the friction angle of geogrid-DS (44.5°) is lower than the friction angle of pure dense sand (47°). However, the apparent cohesion of geogrid-soil is greater than the soil itself. Comparing the slope of failure envelope of geogrid-CLF and pure CLF indicates that the interface friction angle of reinforced soil is almost the same as soil. However, the apparent cohesion of CLF-CLF is greater due to the fact that the failure envelope should not be linear.

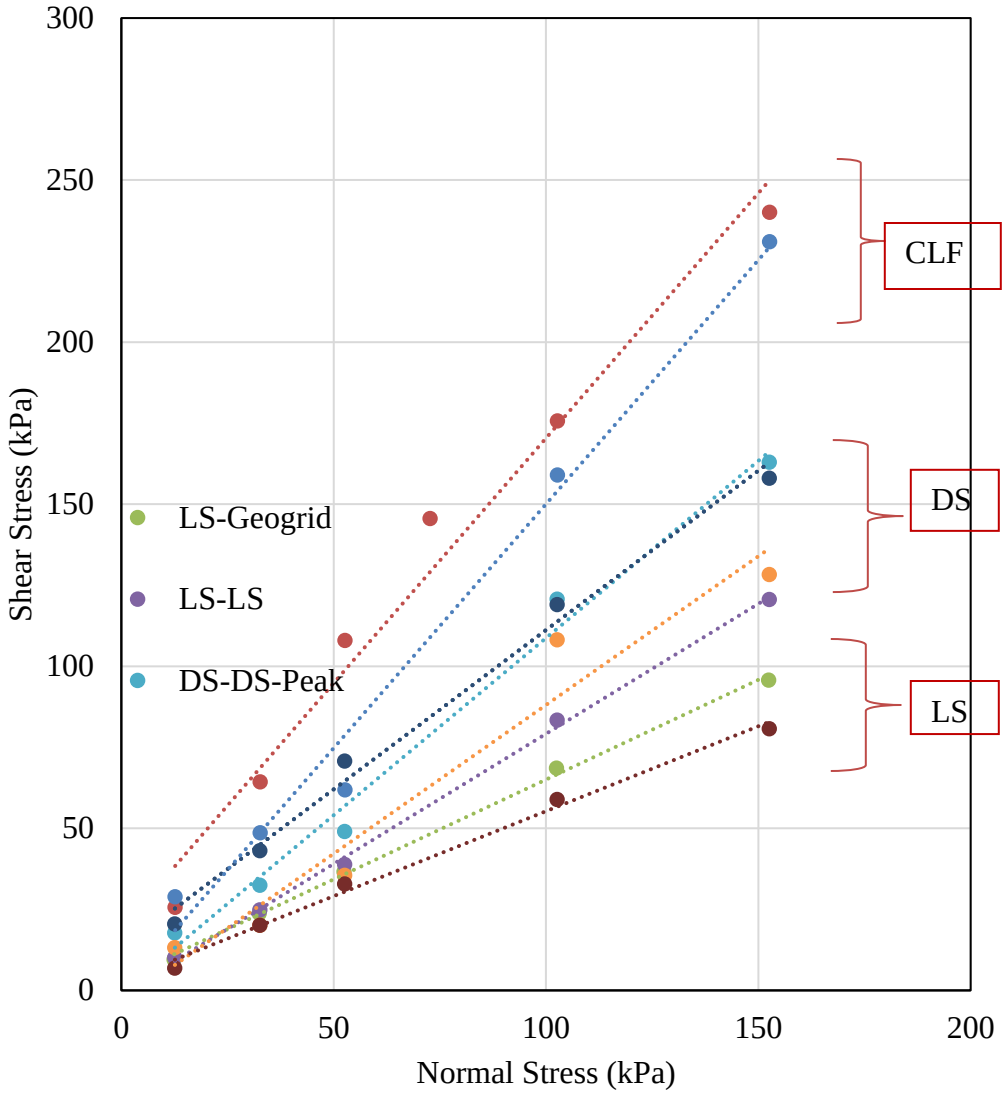

Figure 4-50. Shear Stress versus Normal Stress for Interface DST on Geogrid

4.5 Pullout Test

4.5.1 Test Procedure

A general test procedure that has been specifically developed for this study is given in the following sub-sections. The first step to perform the pullout test is to prepare the soil specimen and place inside the pullout box. When the soil is placed in the bottom of the soil-box it should be placed so that it is slightly above the exit gate sleeve (approximately 10 mm (0.4 in.)). This will prevent the soil-reinforcing from dragging on the exit gate sleeve. Then compact the soil in the bottom of the soil-box to the desired density using the method specification (Figure 4-51). After compaction, the soil surface should be leveled to ensure the load is evenly distributed on the surface of the soil.

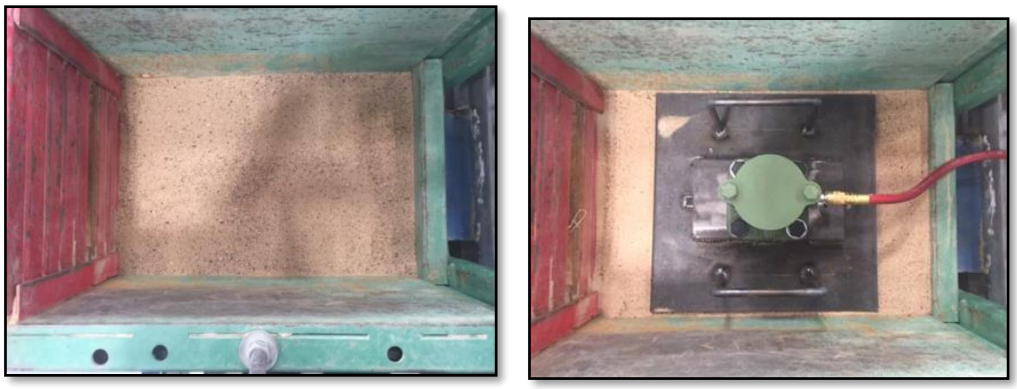

Figure 4-51.Preparation of Bottom Half of Soil-box

After preparing the soil in the bottom half of the soil box, place the steel strip reinforcement in the soil-box so it is in the center of the soil-box. Measure the location of the soil-reinforcement and record and place the soil-reinforcement in the connection-

clamp. (Figure 4-52). Place and attach the LVDT's at the front of the soil-box, at the location of each side of the connection clamp. Connect the wire-rope potentiometers to the soil-reinforcing element in the soil-box (Figure 4-53).

Figure 4-52. Placement of Soil-Reinforcing in Soil-Box

Figure 4-53. Placement of Position Sensors

Fill the top half of the soil-box with the soil in a similar manner as the bottom half of soil-box (Figure 5-4). The top chamber is filled with (7.125 inches.) of compacted soil. The total weight of soil placed in the top chamber is 210 lbs. 3-lifts of soil are placed at lift thickness equal to 2.375" and compact. A ¾" rubber bearing pad is placed on the soil and leveled. The leveling of the soil is important to achieve a uniform pressure in the air bladder and to the top of the soil.

The air-bladder is then placed. The air-bladder is wrapped in 4ml plastic to avoid binding on the sides of the pullout box. On top of the air-bladder, a ¾ "rubber bearing pad is placed. On top of the ¾" bearing pad is a ½" steel plate. The reaction beams are placed on the inflated air bladder and on top of the ½" plate and centered. After centering the air-bladder it is then deflected.

After preparing the sample, the load cell is placed on the reaction beams and centered. The reaction frame is placed on the reaction columns and secured. The data acquisition system is then activated to record the pullout test results.

The LVDT's at the front of the box is positioned. There is an LVDT on each side of the connection clamp. The load cells and LVDT's are zeroed and the initial data recorded.

The required normal pressure was applied by using the pneumatic diaphragm inflation system, by inflating the air bladder using pressure regulator flow control. (Figure 4-45).

Figure 4-54.Placing and Compacting Soil

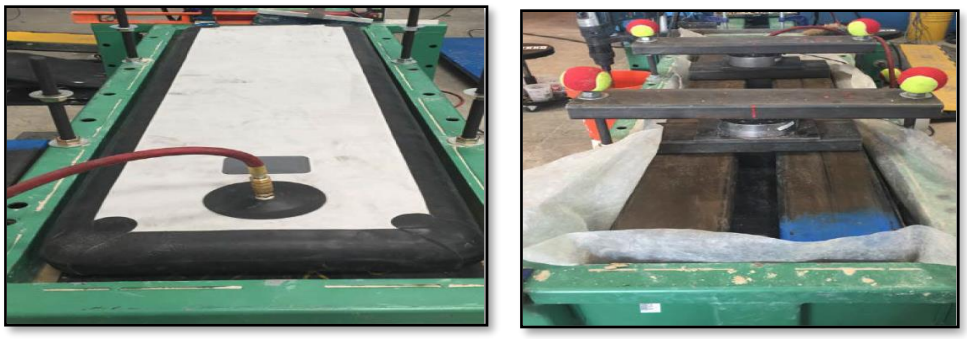

Figure 4-55. Apply overburden pressure

After setting up the apparatus, the pullout test can be performed. Ensure that complete connection of the pullout system has been achieved by applying a small seating load with the pullout force device, then take initial gauge readings. Load the soil-reinforcing by pulling at a constant rate of displacement. Continue loading until the soil-reinforcing fails, pullout occurs, or the predetermined displacement has been reached. Record the maximum pullout load and the mode of failure.

4.5.2 Pullout Test Results

4.5.2.1 Inextensible Reinforcements

Figure 4-56 and Figure 4-57 show the pullout force-displacement curves obtained from the pullout test on the smooth/ribbed steel strip reinforcements embedded in compacted fine sand with full box and half box setup, respectively. The tests were performed by applying the surcharge pressure on top of the soil specimen as the normal stress on the reinforcement calculated as equal to 10 kPa (0.3 m), 30 kPa (1.5 m), 60 kPa (3 m), 90 kPa (4.5 m), and 120 kPa (6 m). For each reinforcement type, the test was

repeated three times under 6kPa normal stresses to evaluate the repeatability of the test results. The results illustrate that the pullout forces obtained from the repeated tests are very similar to each other. Therefore, the test procedure is repetitive. For both test setup, with increasing the normal stresses, the peak force also increases. It is worth mentioning that for each reinforcement, the differences in stiffness are very small for various normal stresses.

As shown in Figure 4-56, for full box tests, as the displacement increases, the pullout force increases almost linearly to reach the peak value. Once the pullout force reaches a maximum value, the strain-softening characteristics are observed in all tests with increasing the displacement until at some point it reaches the residual point. Comparing the pullout force-displacement curves of the smooth and ribbed strip reinforcements, the peak pullout force occurs during the first 4 mm of displacement depending on the confining pressure. In contrast, the peak value of pullout forces for ribbed strip reinforcements is obtained until the 8 mm of displacement. This means that the pullout force reaches the peak value with a slightly slower rate than the smooth strip. It is worth noting that the pullout force is increasing for each confining stress with increasing the number of the ribs per 30.48 cm. Because for the smooth strip reinforcements, the frictional force along the strip is the only resisting force contributing to the pullout force. However, for the case of ribbed strips, apart from the contribution of the frictional force, the bearing capacity of reinforcing elements normal to the direction of movement (passive

resistance) has a contribution in the pullout force. Therefore, the resisting force against pulling out of the reinforcement is enhanced.

Figure 4-57 illustrates the pullout force curves obtained from half box testing. As can be seen, for each serious of tests, the pullout curves of the tests under 6 kPa confining pressure are similar, indicating the good repeatability of the used test procedure for the half box. The pullout force increasing to the peak with increasing the displacement for all reinforcements under different normal stresses. After the pullout force reaches the maximum value, the pullout force decreases drastically. In contrast to the behavior of curves obtained from tests in the full box, the softening characteristic of the curves is greater than the curves obtained from full box testing.

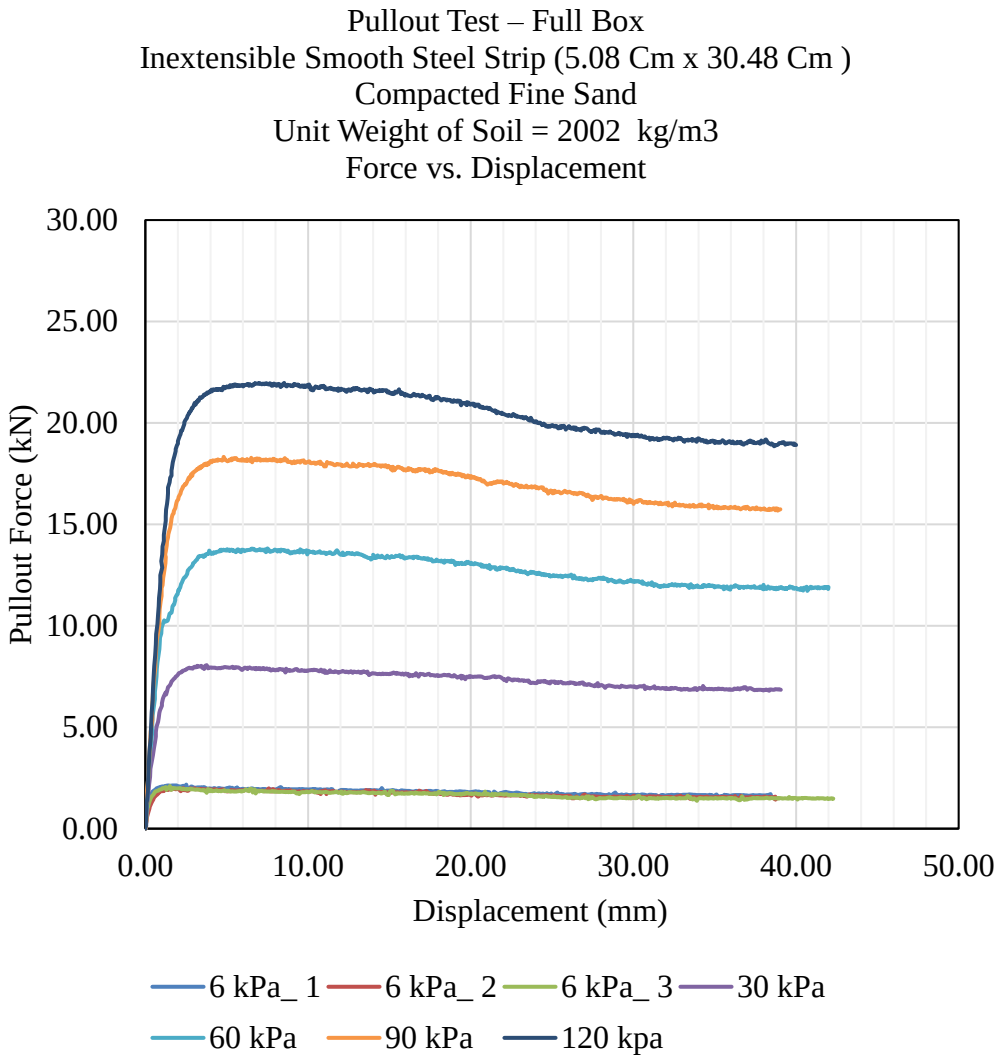

(a)

Figure 4-56. Pullout Force vs. Displacement, Full Box, Dense Sand, (a) Smooth Strip, (b) 2-Rib Strip, (c) 4-Rib Strip, (d) RECO Strip

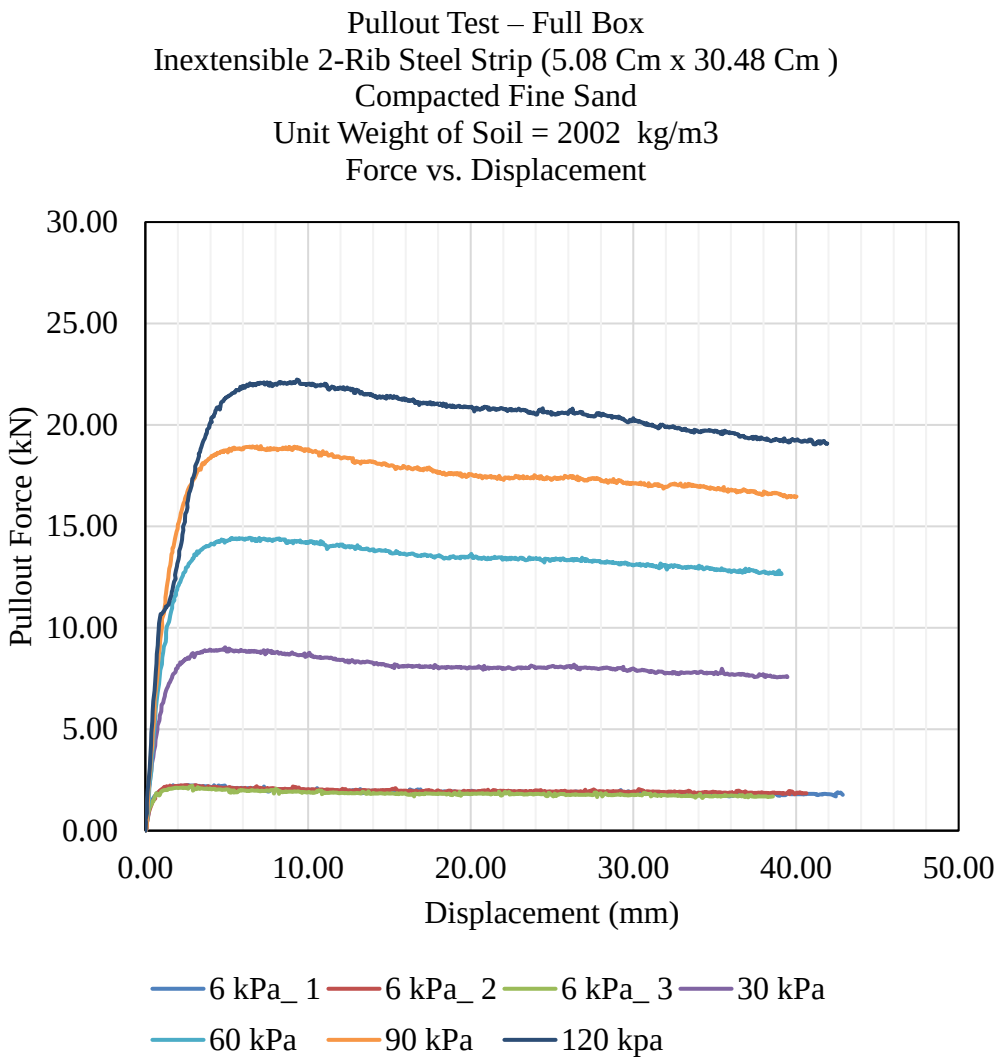

(b)

Figure 4-56. Continued.

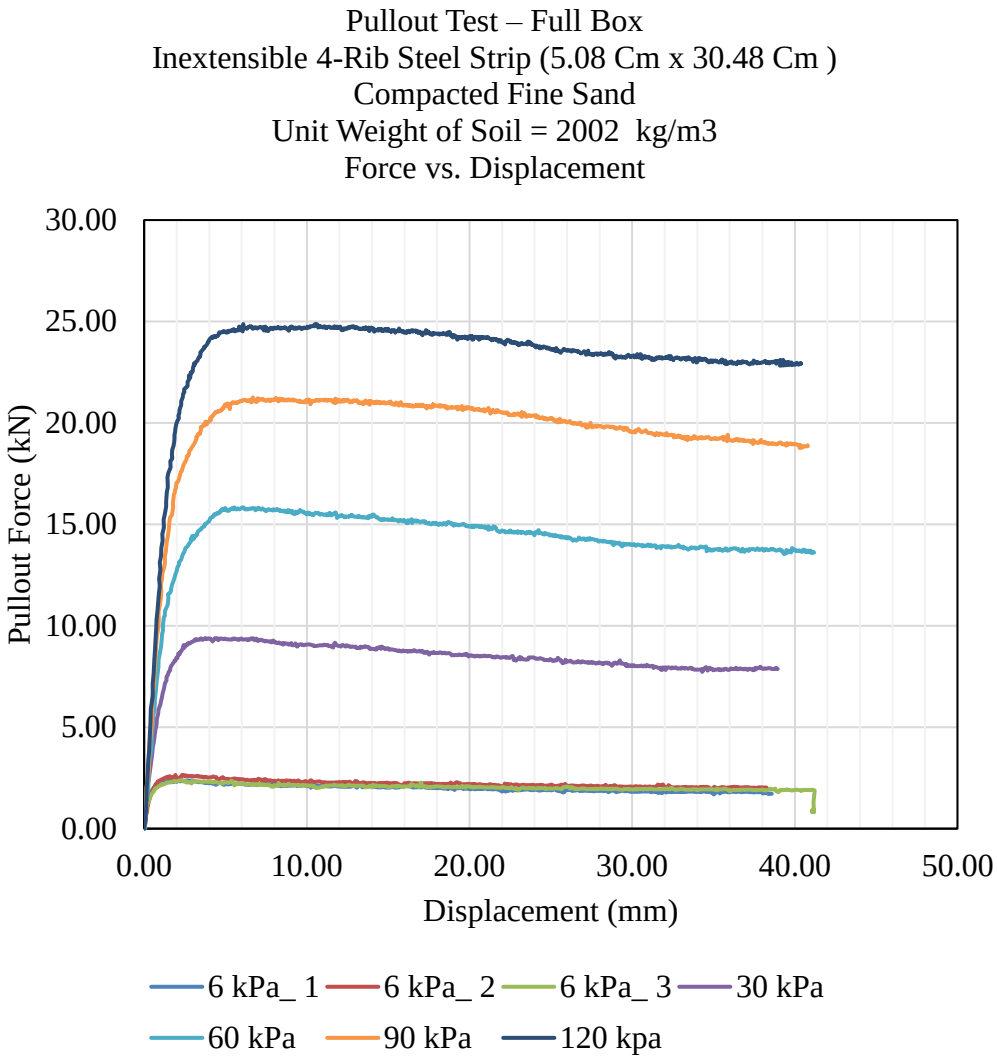

(c)

Figure 4-56. Continued.

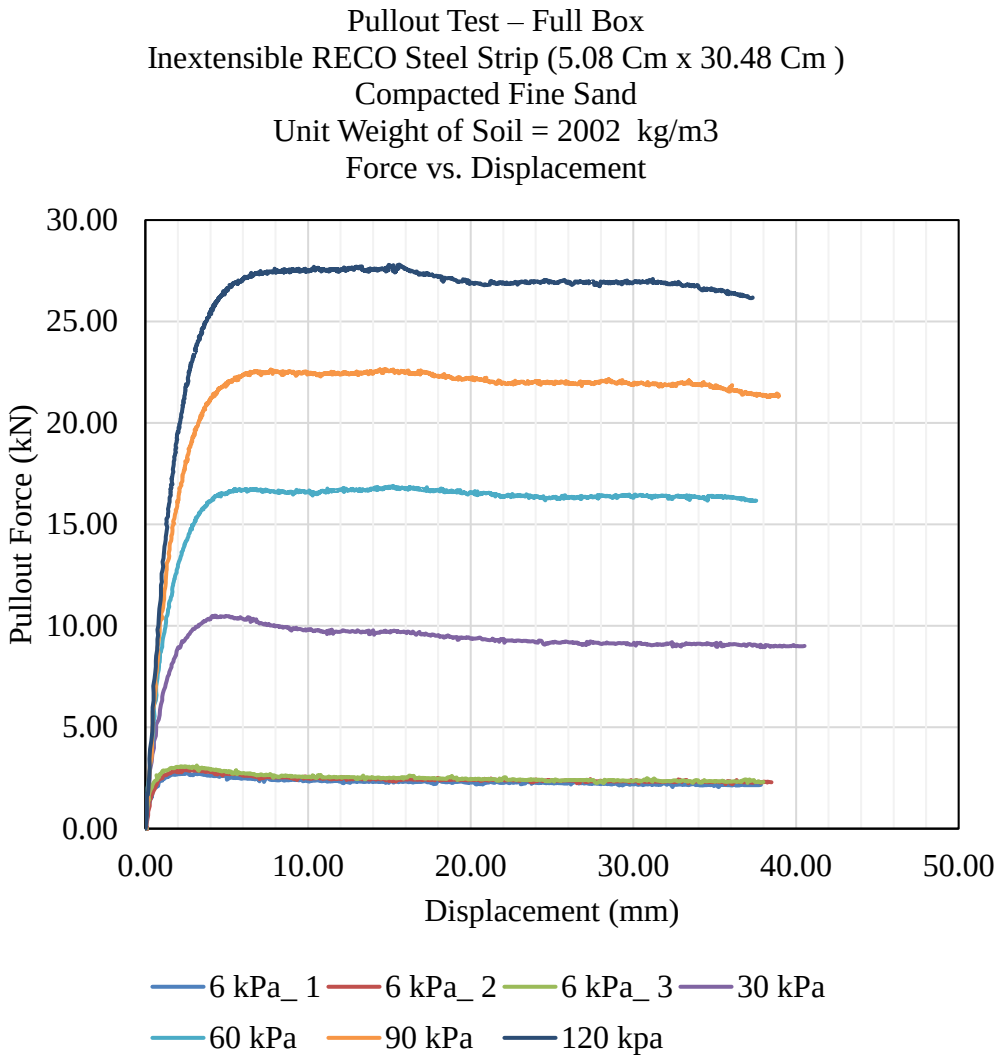

(d)

Figure 4-56. Continued.

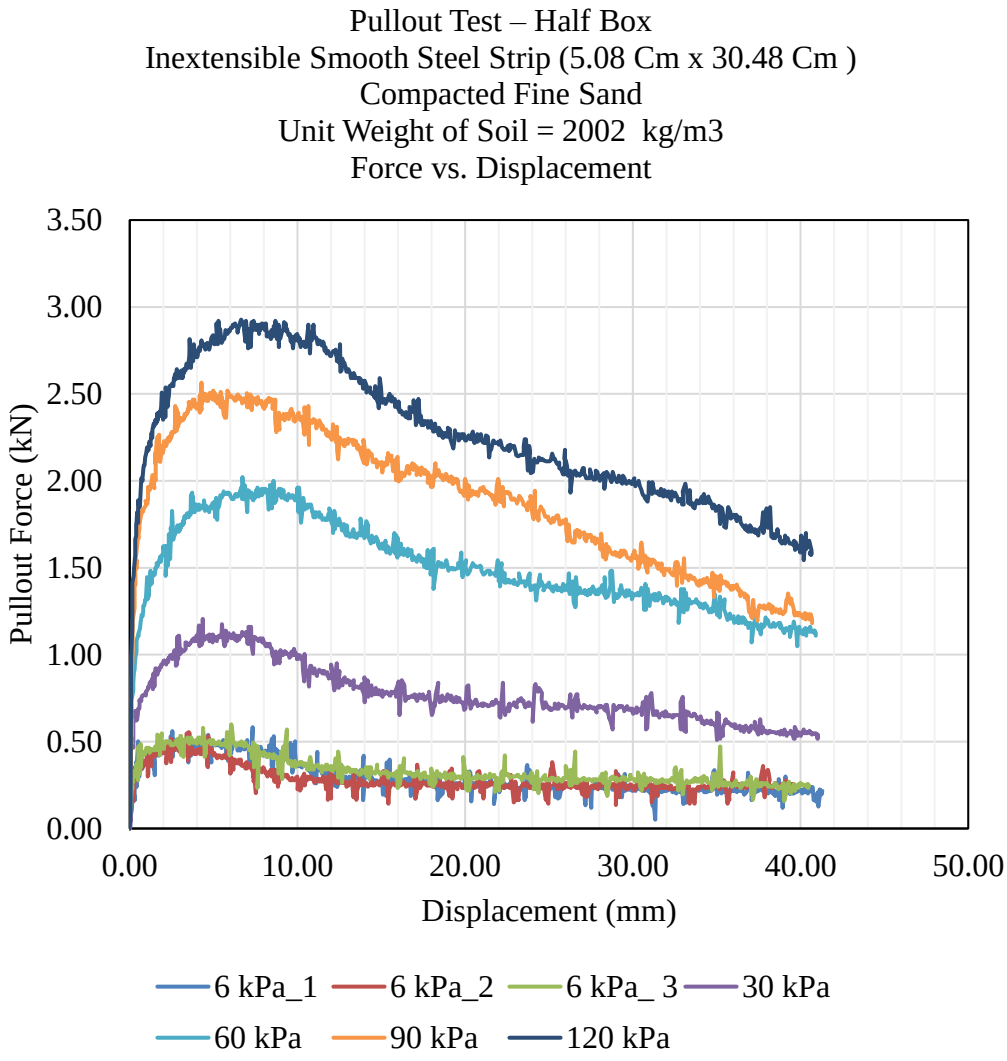

(a)

Figure 4-57. Pullout Force vs. Displacement, Half Box, Dense Sand, (a) Smooth Strip, (b) 2-Rib Strip, (c) 4-Rib Strip, (d) 9-Rib Strip

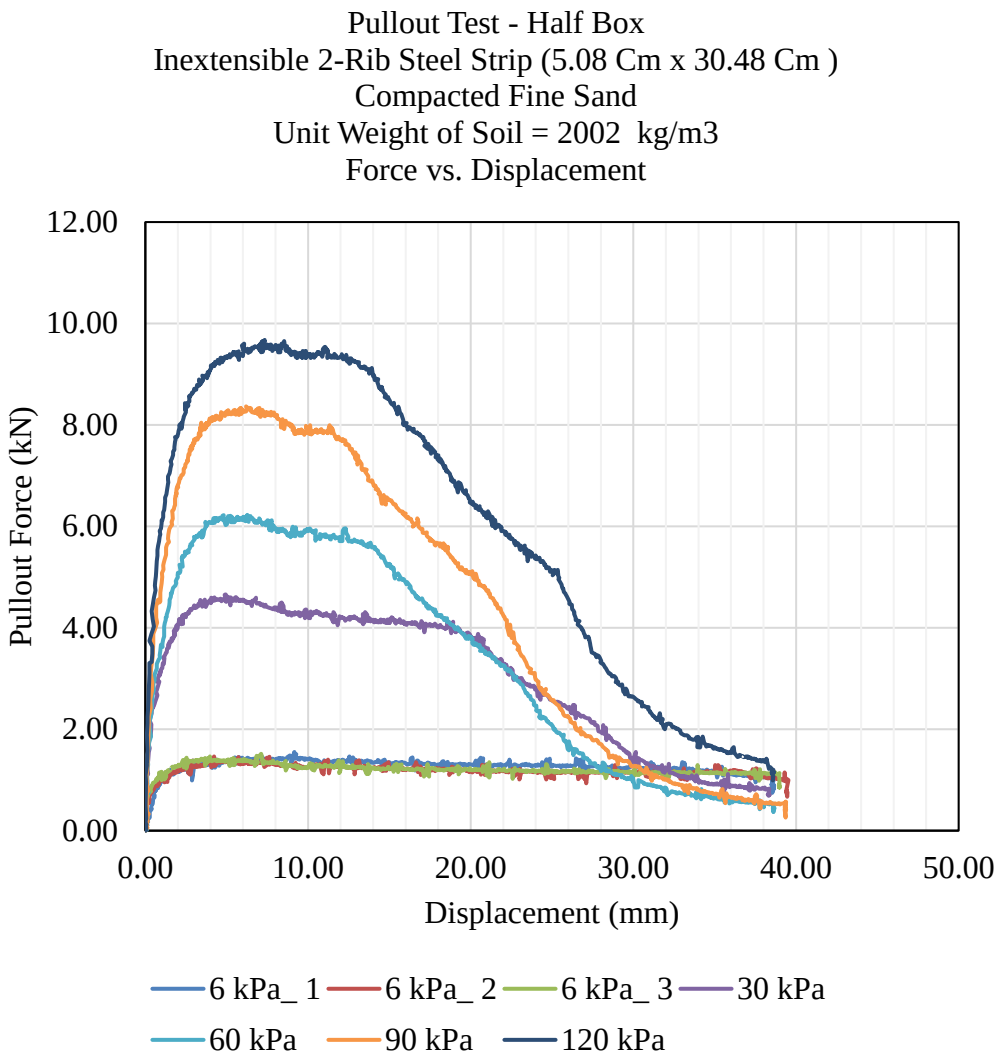

(b)

Figure 4-57. Continued.

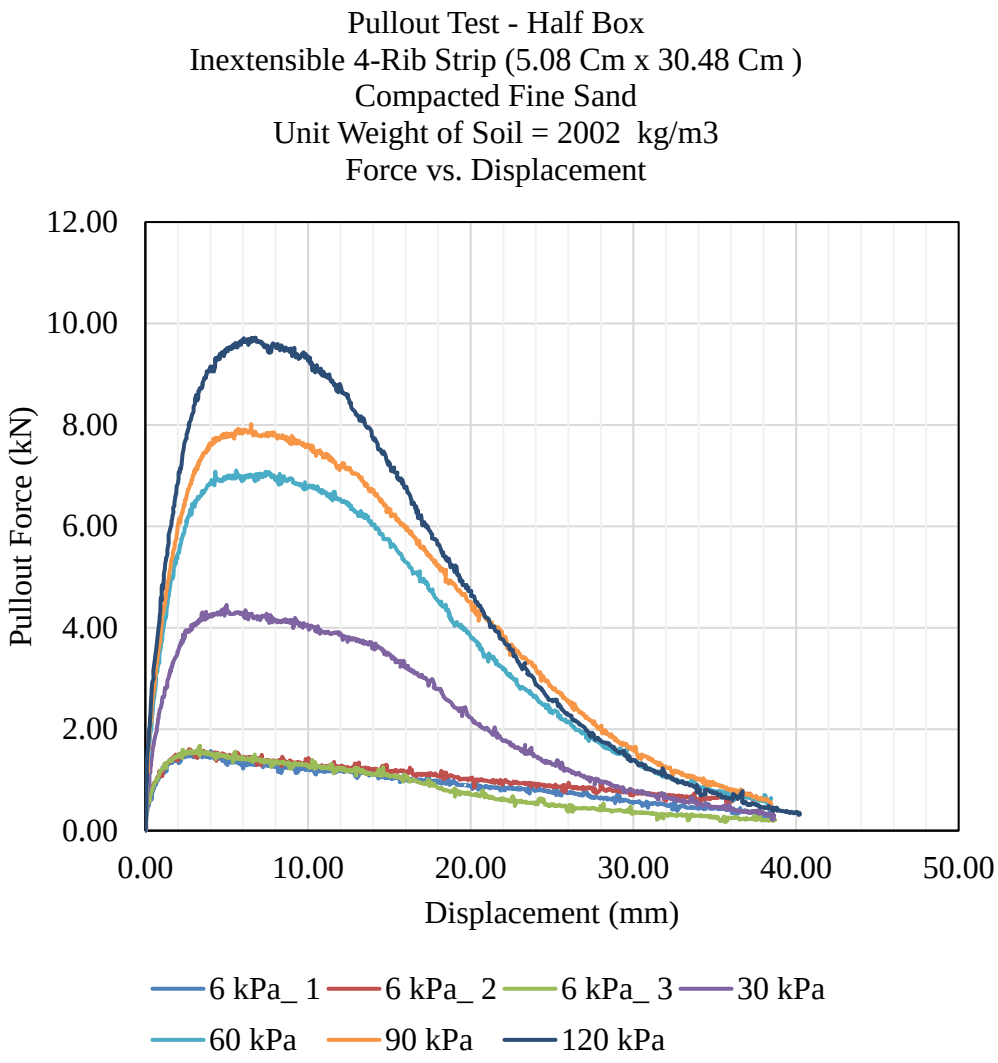

(c)

Figure 4-57. Continued.

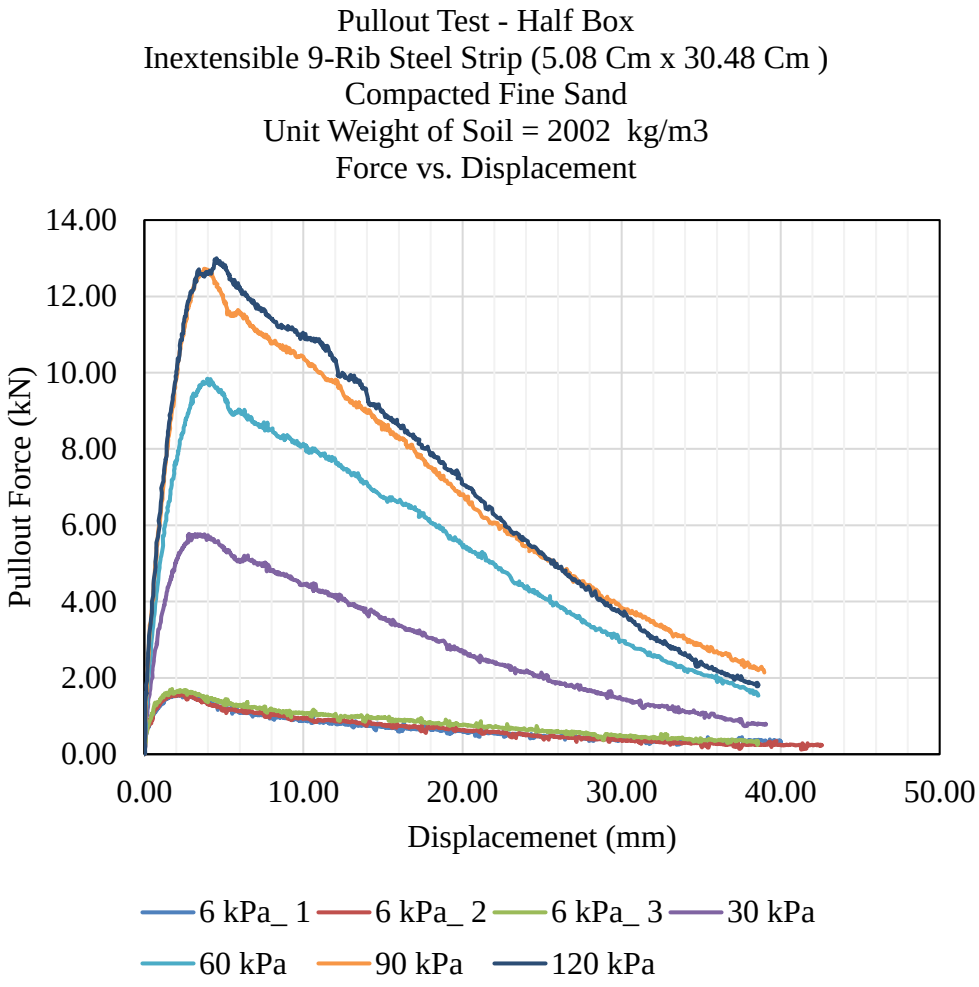

(d)

Figure 4-57. Continued.

4.5.2.2 Extensible Reinforcements

The pullout tests were performed on the geosynthetic reinforcements, geogrid and geostrap, embedded in dense sand using the full-size pullout box. The width and length of the geostrap used in pullout box is 5 Cm and 121.9 Cm, respectively. The geogrid reinforcement was used for pullout tests has a width and length of 15 Cm and 121.9 Cm.

The geostrap reinforcement was tested under the overburden pressure equal to 6 kPa, 30 kPa, 60 kPa, and 90 kPa. The corresponding depths of the overburden pressures were equal to 30 am, 152.5 cm, 305 cm, 457.5 cm and 610 cm. The overburden pressure was applied using the pneumatic diaphragm as explained in section 4.5.1. The displacement of the geostraps was recorded using the LVDT's explained in section 4.5.1, at the front face of the soil box. For geogrid reinforcement, the three wire-rope potentiometers were used to record the displacement of the three transverse members inside the soil. Each wire potentiometer was installed on 1^{st}, 2^{nd} and 3^{rd} transverse members of the geogrid reinforcement. Figure 4-58 illustrates the placement of the reinforcement element on soil material in the center of the box.

(a) (b)

Figure 4-58. Placement of Geosynthetic Reinforcements inside the Box, (a) Geogrid, (b) GeoStrap

Figure 4-59 and Figure 4-60 show the pullout force-displacement curves obtained from the pullout test on the geostrap and geogrid reinforcements embedded in compacted fine sand inside the full box. For each reinforcement type, the test was repeated three times under 6kPa normal stresses to evaluate the repeatability of the test results. The results illustrate that the pullout forces obtained from the repeated tests are very similar to each other. Therefore, the test procedure is repetitive. For both test setup, with increasing the normal stresses, the maximum pullout force also increases. It is worth mentioning that maximum pullout force for extensible reinforcements occurs at larger displacement

compare to the inextensible reinforcements. The displacement that the pullout force reach to the maximum value is lower than 10 mm for smooth and ribbed steel strip reinforcement. However, for geostrap reinforcement, the horizontal displacements corresponding to the maximum pullout force are not recognizable, and the pullout force increases with increasing the displacement (Figure 4-59).

As shown in Figure 4-60, for pullout tests on geogrid, as the test progresses, the pullout force increases to the peak value and stays constant with increasing the horizontal displacement. However, for the test at 1.5 m depth (24 kPa), the geogrid ruptured at 10 kN force. We were unable to perform tests on geogrids for depth over than 5 feet, because of the high stress concentration at the pulling point (clamping).

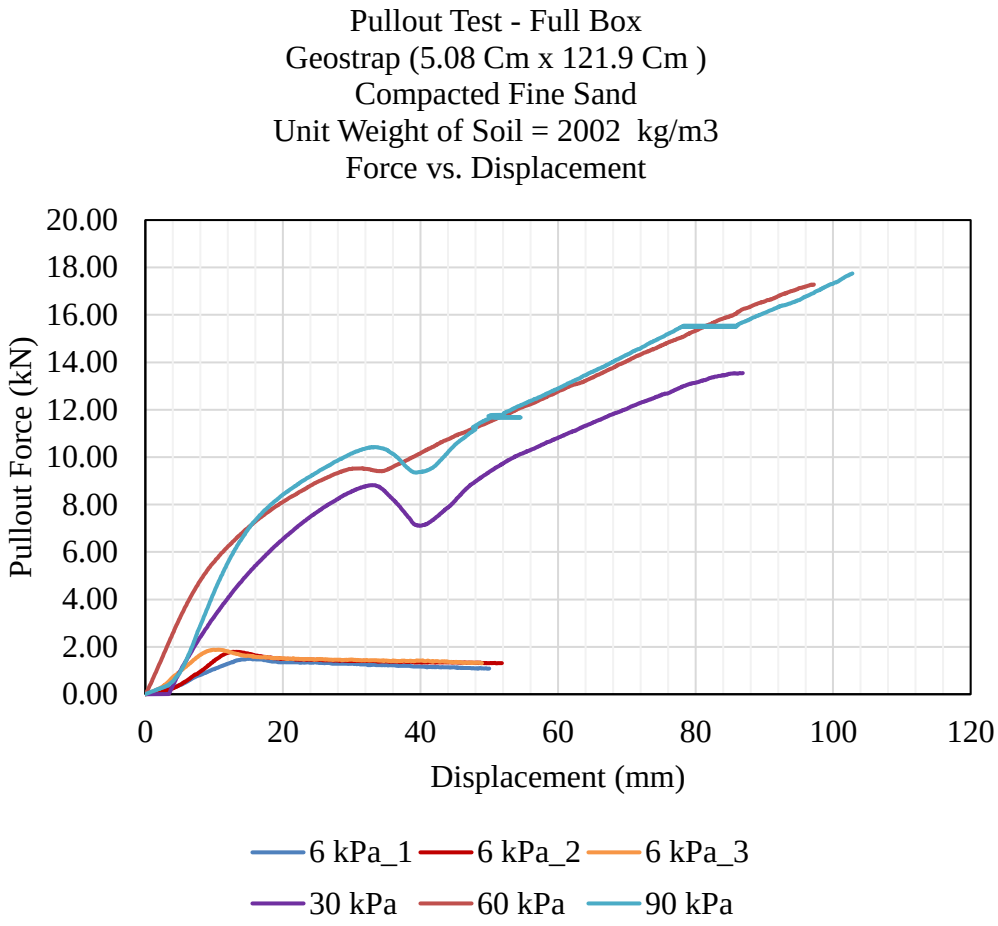

Figure 4-59. Pullout Force vs. Displacement, Full Box, Geostrap Embedded in Dense Sand

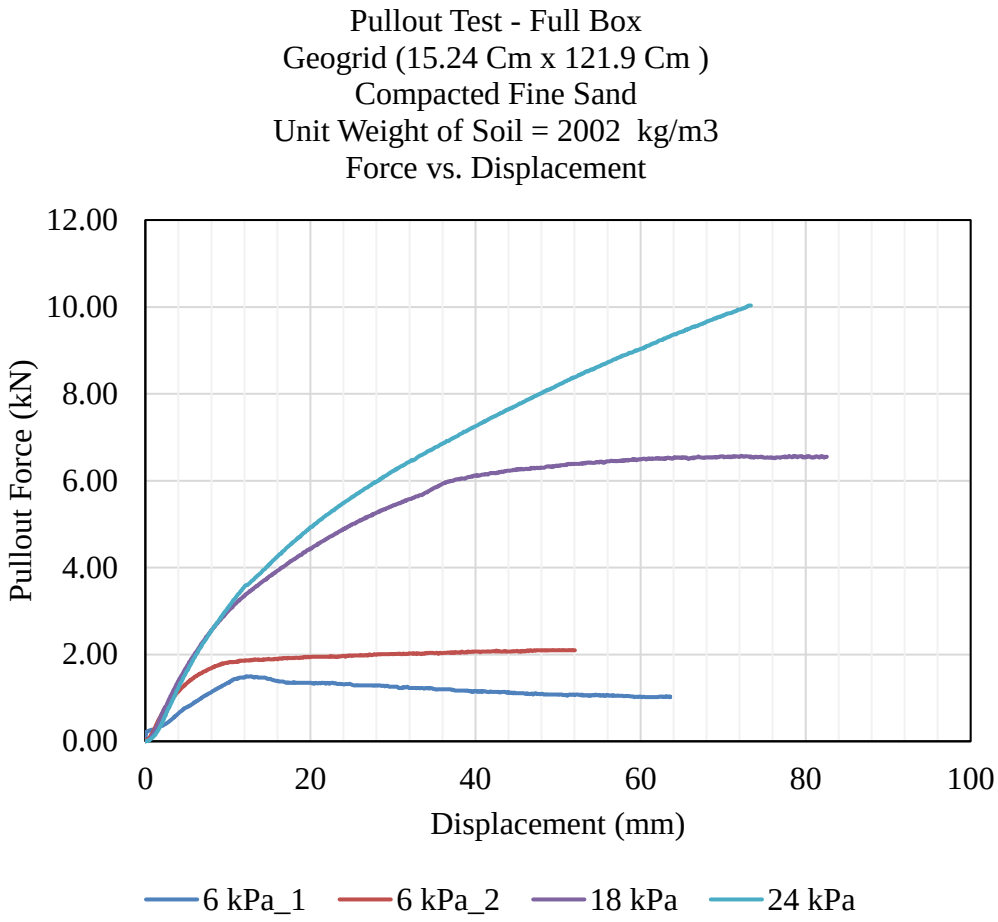

Figure 4-60. Pullout Force vs. Displacement, Full Box, Geogrid Embedded in Dense Sand

5 NUMERICAL SIMULATIONS

5.1 Introduction to FLAC3D

Various numerical methods including Discrete Element Method (DEM), Finite Element Method (FEM), and Finite Difference Method (FDM) have been widely in use for practical and research purposes to enhance and give more details of soil behavior as well as its interaction with structures. Both above methods have the capability of delivering detailed and accurate analysis of soil behavior by using proper and realistic constitutive models for elastic and plastic behavior, boundary conditions, and loading patterns. Selecting a proper numerical modeling code or software can be extremely challenging depending on the complexity of the purpose of use. For the current research study, FLAC3D 6.0 by Itasca Consulting Group Incorporation was chosen at first.

Various numerical methods including Discrete Element Method (DEM), Finite Element Method (FEM), and Finite Difference Method (FDM) have been widely in use for practical and research purposes to enhance and give more details of soil behavior as well as its interaction with structures. Both above methods have the capability of delivering detailed and accurate analysis of soil behavior by using proper and realistic constitutive models for elastic and plastic behavior, boundary conditions, and loading patterns. Selecting a proper numerical modeling code or software can be extremely challenging depending on the complexity of the purpose of use. For the current research study, FLAC3D 6.0 by Itasca Consulting Group Incorporation was chosen at first. FLAC3D is a three-dimensional explicit finite-difference program for engineering

mechanics computation and it was developed primarily for geotechnical engineering applications. FLAC3D can be used to simulate the behavior of three-dimensional structures built of soil, rock or other materials that undergo plastic flow when their yield limits are reached. Materials are represented by polyhedral elements within a three-dimensional grid that are adjusted by the user to fit the shape of the object to be modeled. Each element behaves according to a prescribed linear or nonlinear stress/strain law in response to applied forces or boundary restraints. The material can yield and flow, and the grid can deform (in large-strain mode) and move with the material that is represented. The explicit, Lagrangian calculation scheme and the mixed-discretization zoning technique used in FLAC3D ensure that plastic collapse and flow are modeled very accurately. Because no matrices are formed, large three-dimensional calculations can be made without excessive memory requirements. The drawbacks of the explicit formulation (i.e., small timestep limitation and the question of required damping) are overcome by automatic inertia scaling and automatic damping that does not influence the mode of failure. FLAC3D offers an ideal analysis tool for the solution of three-dimensional problems in geotechnical engineering.

In this section, full scale three-dimensional numerical simulation of large direct shear test and pullout test were performed to study the mechanism of soil and reinforcement interaction.

5.2 Numerical Simulation Methodology

The numerical simulation plan, details of models, modeling mechanism, and simulation results are presented in this section. The numerical simulation of the direct shear test, simple shear test, interface direct shear test, and pullout tests are discussed in detail. The constitutive model which is used to simulate the soil and steel reinforcement are explained. The results of the numerical simulation were calibrated with the obtained laboratory test results which are explained in the previous chapter.

5.3 Constitutive Model

To simulate the behavior of different soil types under various loading conditions, various soil models exist in the literature. There are 17 constitutive models in FLAC3D including 3 elastic model and 14 elastic-plastic one. In this research, the elastic model is chosen to model the steel reinforcement, and the strain softening plastic model was used to simulate the dry sand material.

5.3.1 Elastic Model

The elastic, isotropic model is for homogeneous, isotropic materials that exhibit linear stress-strain behavior with no hysteresis on unloading.

5.3.2 Strain-Hardening/Softening Model

The strain-hardening/softening model is a nonlinear model that allows material softening and hardening behavior based on prescribed variations of the Mohr-Coulomb

model properties (i.e., cohesion, friction, dilation, and tensile strength) as functions of the deviatoric plastic strain.

The model is based on the Mohr-Coulomb constitutive model with non-associated shear and associated tension flow rules. The difference is that this model has the possibility to harden or soften the cohesion, friction, dilation, and tensile strength after the onset of plastic yield while in the Mohr-Coulomb model, these parameters are assumed to stay constant. In this research, the behavior of sand shows softening behavior in some cases. Therefore, the friction angle and dilation angle of the soil material is defined to decrease as piecewise-linear functions of the plastic shear strain. The program measures the total plastic shear and tensile strains at each time step and the new parameters are defined to the model.

As shown in Figure 5-1 the stress-strain curve is linear to the yield point and the strain is elastic. After the point of yield where the total strain is the combination of elastic and plastic strain, the friction (or dilation) varies as a function of the plastic strain.

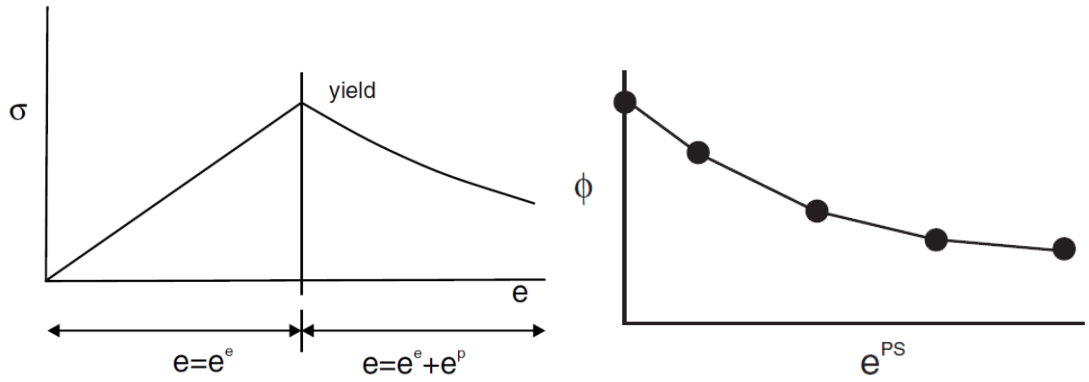

(a) (b)

Figure 5-1 (a) Shear Strain Curve, (b) Variation of Friction Angle with Plastic Strain

5.4 Numerical Simulation of Direct Shear Test

5.4.1 Model Geometry

The direct shear test is simulated in actual dimension of the large direct shear test: 0.3048m length, 0.3048 widths, and 0.2032 m depth. The soil is modeled with solid zones with strain softening model from the FLAC3D library. The mechanical boundary condition is the roller boundaries on each side of the soil. The bottom of the mesh is fixed in the z-direction, and the sides of the mesh perpendicular to the x-direction are fixed in the x-direction. The zone grid points on the sides of the mesh perpendicular to y-direction are fixed in the y-direction. Table 5-1 shows the properties of soil assigned to the soil mesh for modeling the direct shear test. The model is simulated in two phases: a consolidation phase which allows the model to converge under gravity and applied pressure on top of

the sample. At this phase of the model, the constitutive model of the soil is set as the elastic model and was changed to the strain softening model before the next phase starts. After the mesh contracts under the normal pressure, the second phase of the simulation starts by applying the x-displacement with constant rate to the nodes of the zones located on the external faces of lower half of the model perpendicular to the x-axis while the lateral walls of the upper half of the box are restrained in x, y, and z directions.

Table 5-1 Mechanical Properties of Soil, DST

Soil Type	$K(kPa)$	$G(kPa)$	ν	**Friction Angle**	**Dilation Angle**
Loose Sand	3300	1500	0.3	37	0
Dense Sand	3300	1500	0.3	47	10

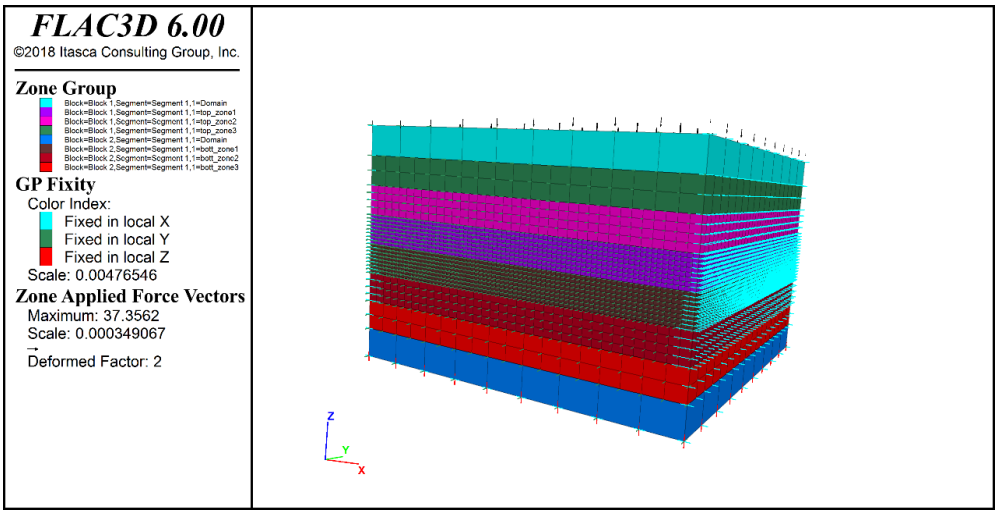

Figure 5-2. Generated Mesh of Direct Shear Test Modeling

5.4.2 Results

The results of numerical simulation of the direct shear test on loose sand is presented in Figure 5-3. The shear stress is calculated from the nodal forces located on the lateral wall of the lower half of the box because the shear stress obtained from the laboratory tests is measured using the load cell installed on the water bath as explained before. The horizontal displacement of a grid point located in the lower half of the box is measured during the shearing phase. The shear stress versus horizontal displacement of loose sand under various normal stresses obtained from numerical simulation is compared with the one obtained from laboratory tests. As shown in Figure 5-3, there is a good agreement between the experimental and the numerical results.

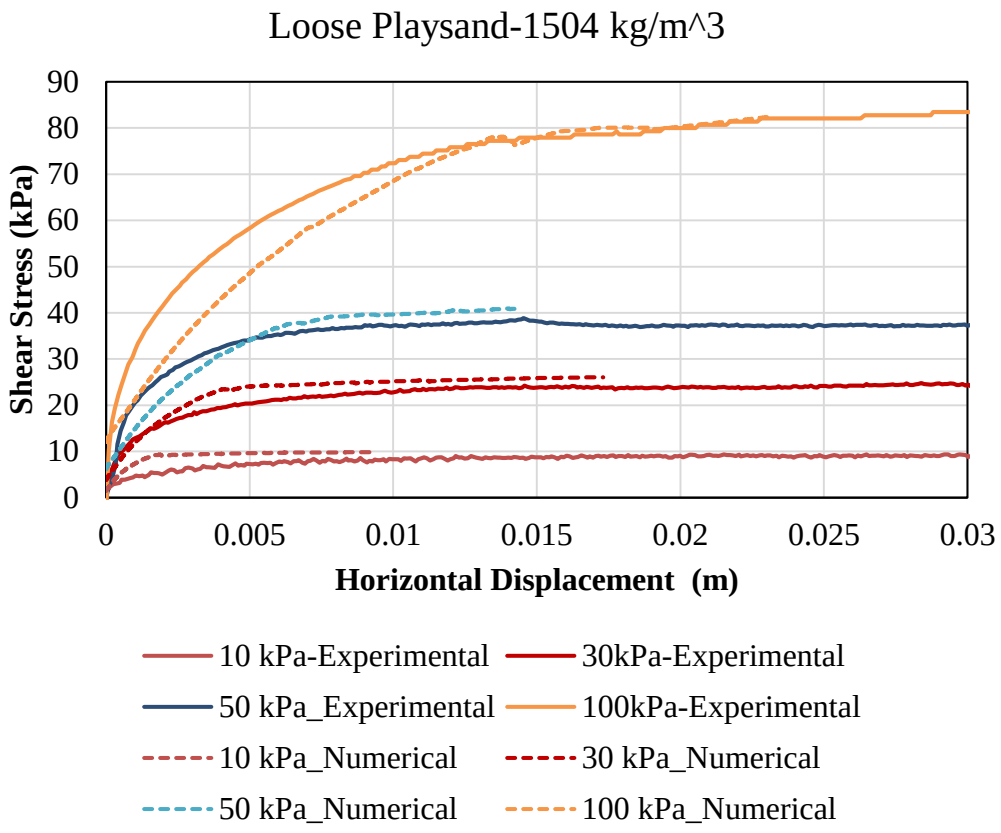

Figure 5-3. Shear Stress-Horizontal Displacement of Loose Sand under Direct Shear Test

The numerical simulation of the direct shear test provides more details to understand in depth of the direct shear mechanism and explanation of the behavior of the specimen under direct shear loading. The first observation is the deformation of the specimen and displacement of the mesh along z-direction during the shear phase. Figure 5-4 shows the deformation of the elements during the shear phase and contour of the z-displacements for the specimen under 50 kPa normal stresses. As shown in this figure, the

contraction occurs at the back side of the upper wall and, the dilation behavior is observed at the front wall of the box. The movement of the particle is shown in this figure. The same observation was reported by Liu (2006), Cui and O'Sullivan (2006) and Zhang and Thornton (2007). Also, the distribution of the xx-shear stress is shown in Figure 5-5. The concentration of forces is illustrated at the front wall of the upper half of the box and back wall of the lower half of the box close to the shear band. This force concentration between the wall of the box and the particles due to the dilation effect causes the measured shear resistance to enhance at the end of the test. This phenomenon is observed by rotation of the top cap for the laboratory tests (Figure 4-13).

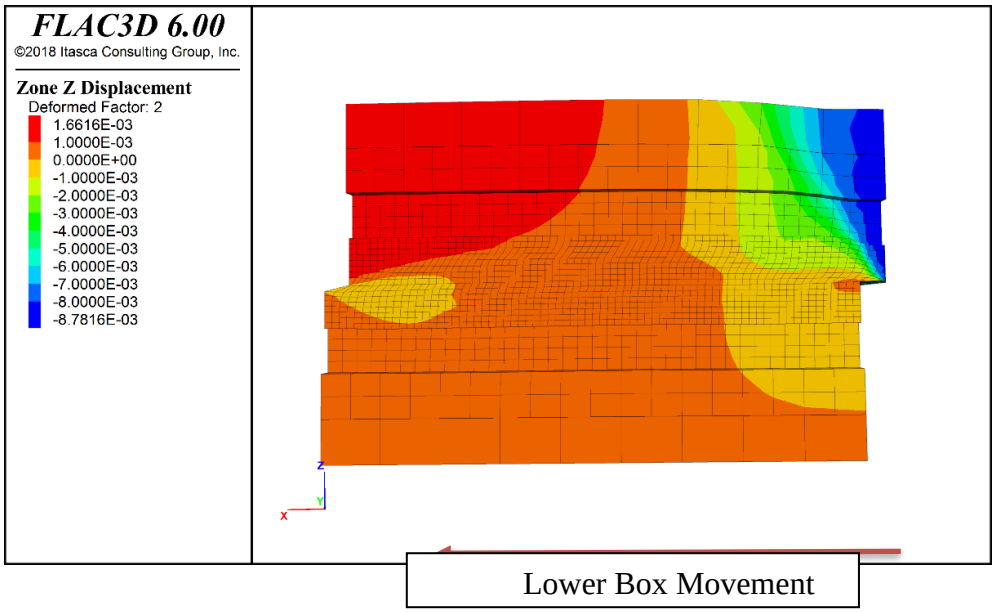

Figure 5-4. Specimen Deformation during Shear Phase

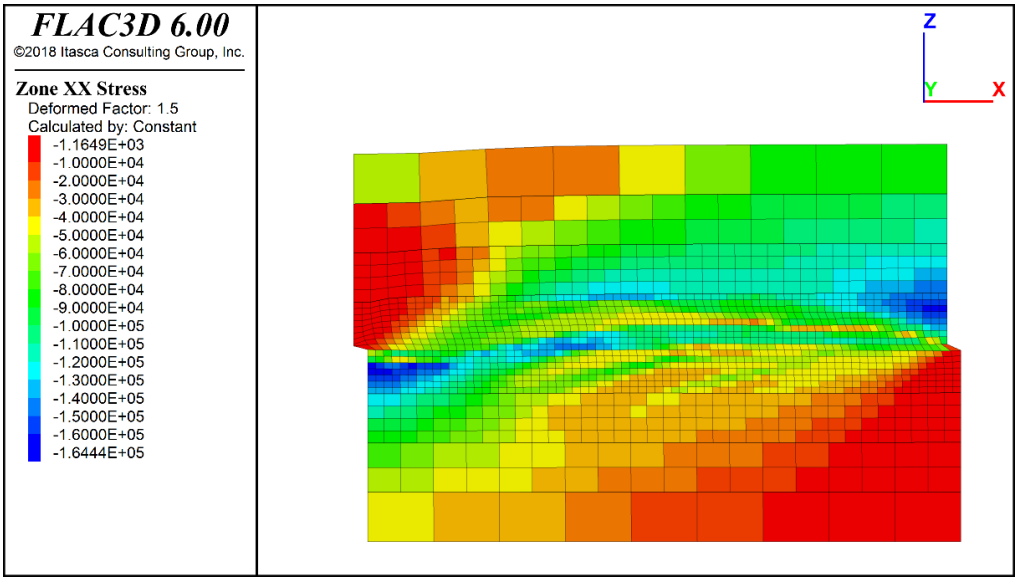

Figure 5-5. Contour of XX Stress for Direct Shear Test

5.5 Numerical Simulation of Simple Shear Test

5.5.1 Model Geometry

To understand the mechanism of the simple shear test, to explain the obtained shear behavior of the specimen under shear loading, and to compare the shear strength parameters obtained from the direct shear test as well as simple shear test, numerical simulation of the simple shear test is performed. The model built with the actual shape (cylindrical) and dimension of large simple shear test with an internal dimension of 0.3048 cm and height of 0.11 m.

The mesh generated, and the boundary condition of the simple shear test is shown in Figure 5-6. The model simulated in two steps: the consolidation phase where the normal stress was applied on top of the specimen and shear phase where the nodes on top of the

specimen stay constant in x and y-direction and the displacement with constant rate is applied to the nodes at the bottom of the specimen. As shown in this figure, the bottom of the specimen is fixed in the z-direction for both phases. During the consolidation phase, the grid points located surrounding the cylinder are fixed in x and y directions.

The mechanical constitutive model of the sandy soil is selected the FLAC3D Mohr-Coulomb with the properties that summarized in Table 5-2.

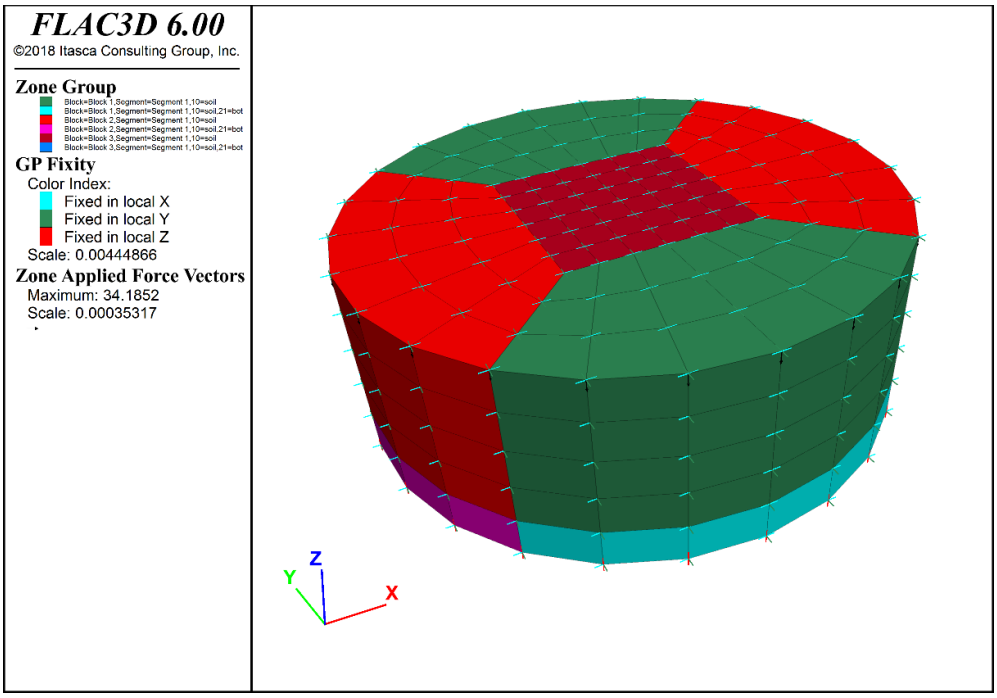

Figure 5-6. Generated Mesh of Simple Shear Test Modeling

Table 5-2. Mechanical Properties of Soil, DSST

Soil Type	$K(kPa)$	$G(kPa)$	**υ**	**Friction Angle**	**Dilation Angle**
Loose Sand	3300	1500	0.3	37	0
Dense Sand	3300	1500	0.3	47	10

5.5.2 Results

The shear stress versus shear strain measured from numerical work and experimental work presented in Figure 5-7. As shown in this figure, the numerical results are in a good match with experimental results.

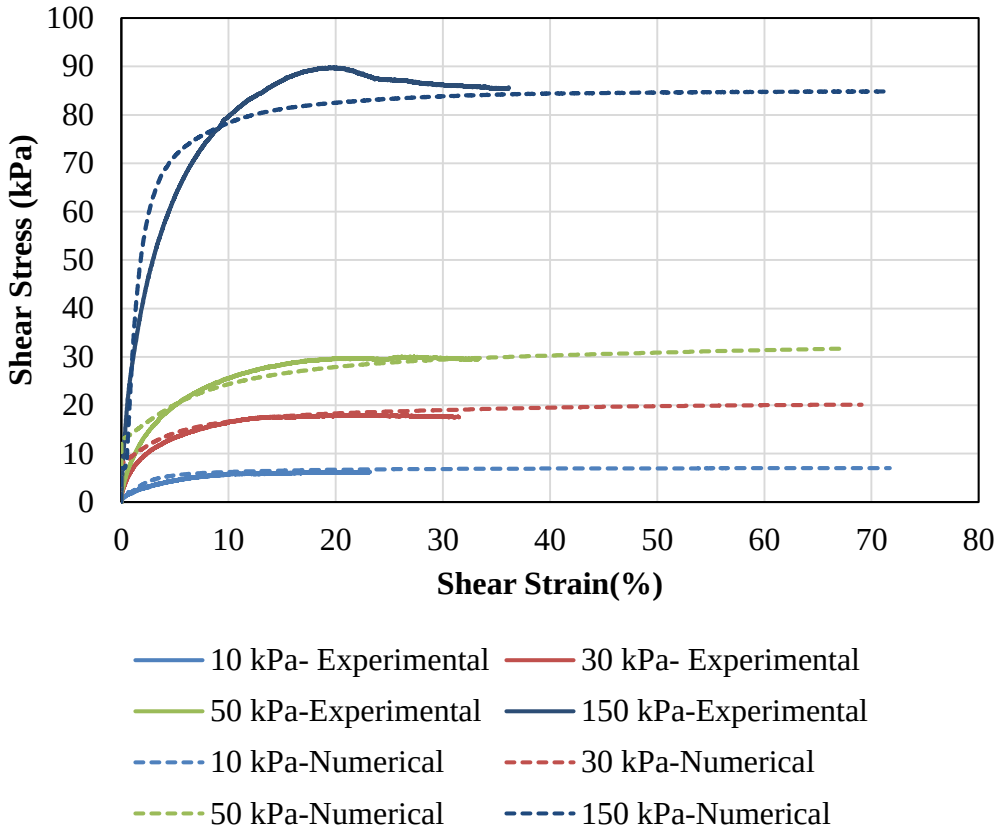

Figure 5-7 Comparison between the Numerical and Experimental Results of the Simple Shear Test under Different Normal Stresses

5.6 Numerical Simulation of Interface Direct Shear Test

5.6.1 Model Geometry

The numerical model was developed using FLAC3D to simulate the performed interface direct shear test. In order to calibrate the numerical results with the experimental ones, the geometry of a model and the properties of the components were chosen the same as actual tests. The geometry and boundary condition of the interface direct shear test

simulation is similar to the direct shear test model. The bottom box is an elastic material with the streel properties and the upper box was simulated with elements which have Mohr Coulomb's constitutive model. Table 5-2 describes the constitutive model of soil. The bulk and shear modulus of the reinforcement plate is 2.3×10^5 and 7.6×10^4 MPa. The bottom of the box is fixed against in movements in the z direction, and the lateral walls of the upper and lower boxes are restrained in the x and y directions in the first step. In this step, the normal stresses were applied on the top surface of the specimen. The model was run under the same normal stresses as experimental work (10, 30, 50, 100, 150 kPa). In the second step, the upper box is restrained in x, y, and z-direction while a horizontal displacement of constant rate is applied to the bottom box in x-direction.

The ribs modeled on the surface of the bottom box with the same geometry of the actual ribs in the laboratory tests. The interface direct shear tests were simulated on smooth, 2-rib, 4-rib, 6-rib, and 9-rib plates. As an example, the created mesh for interface direct shear test with 2-rib and 9-rib plate are presented in Figure 5-8.

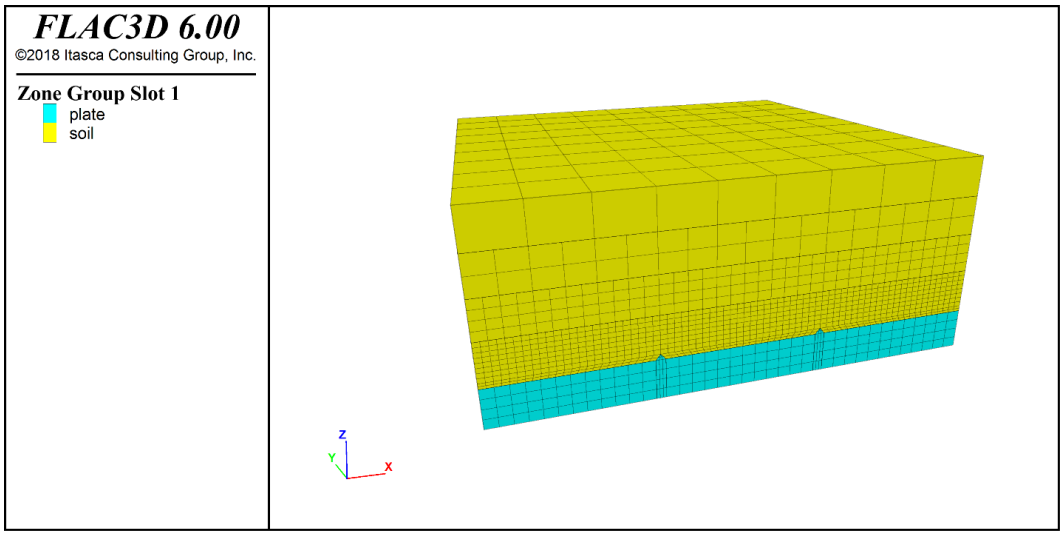

(a)

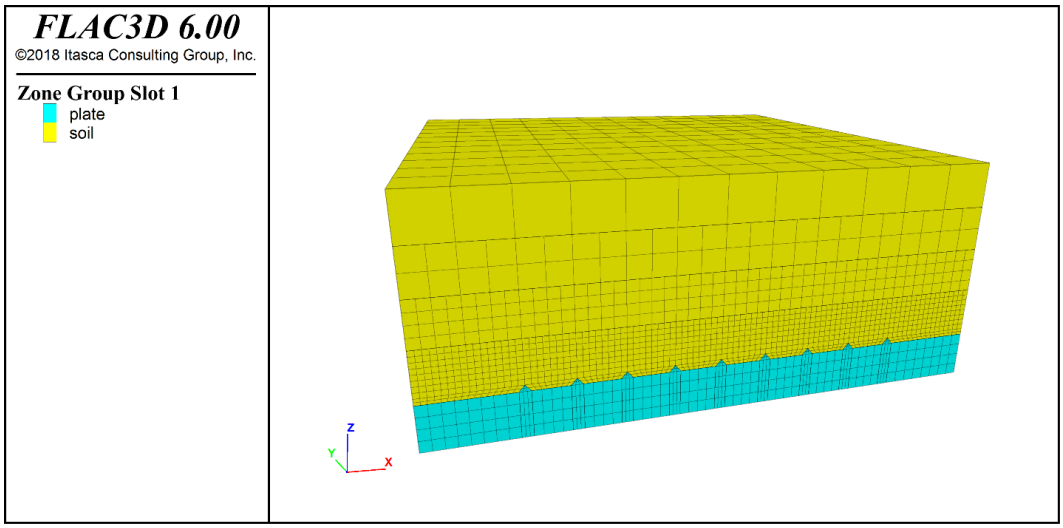

(b)

Figure 5-8. Generated mesh of IDST with FLAC3D, (a) 2-rib plate, (b) 9-rib plate

5.6.2 Results

The results from the numerical analyses of interface direct shear test between loose sand and smooth, 2-rib, 4-rib, 6-rib, and 9-rib plate with different normal pressures (10, 30, 50, 100, 150 kPa) are shown in Figure 5-9. As can be seen in this figure, for all plates and loose sand, there is an agreement results in the interface shear stress versus horizontal displacement curves between the experimental and numerical analyses.

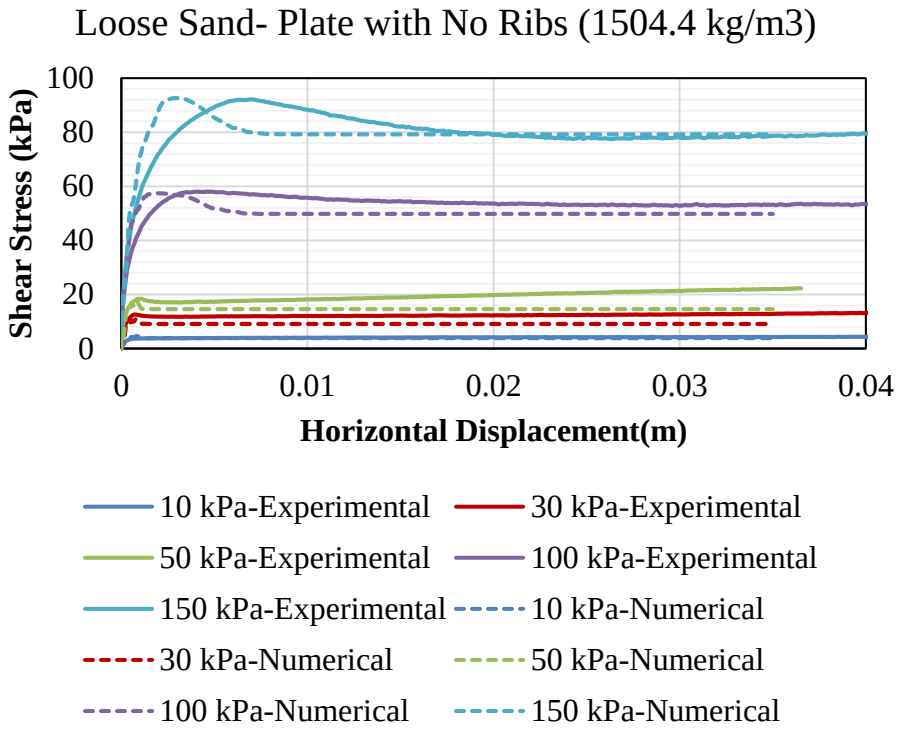

(a)

Figure 5-9. Comparison between the Numerical and Experimental Results of the IDT under different normal stresses, (a) Smooth Plate, (b) 2-Rib Plate, (c) 4-Rib Plate, (d) 6-Rib Plate, (e) 9-Rib Plate

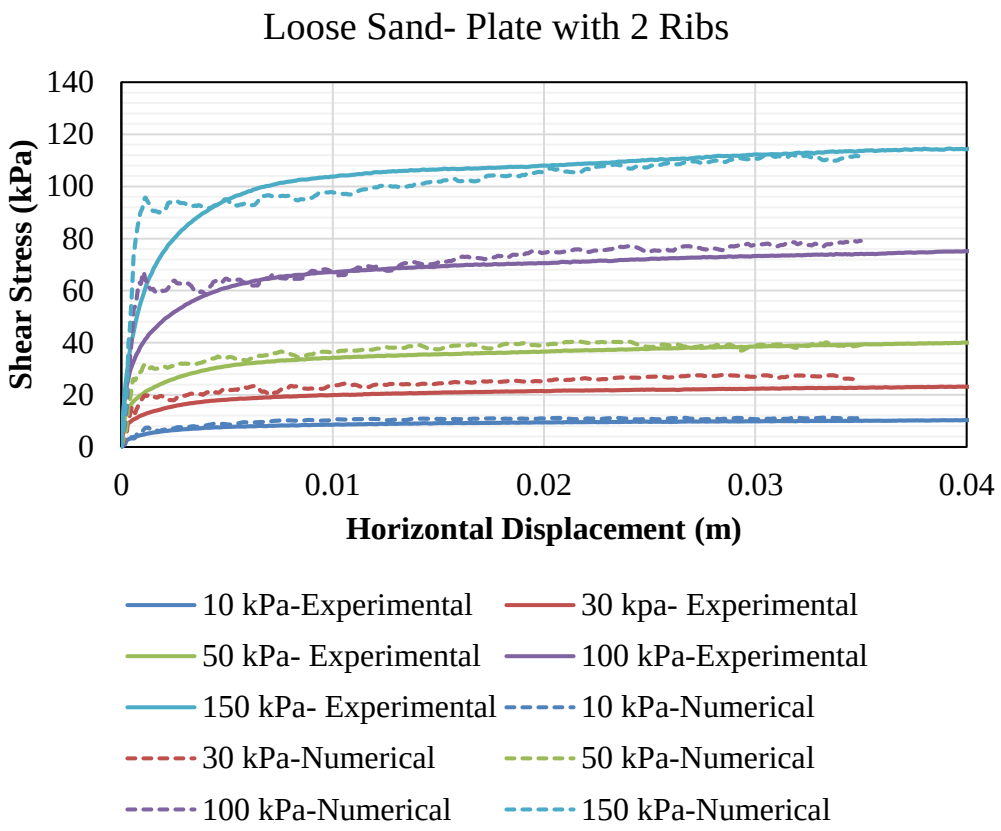

(b)

Figure 5-9. Continued.

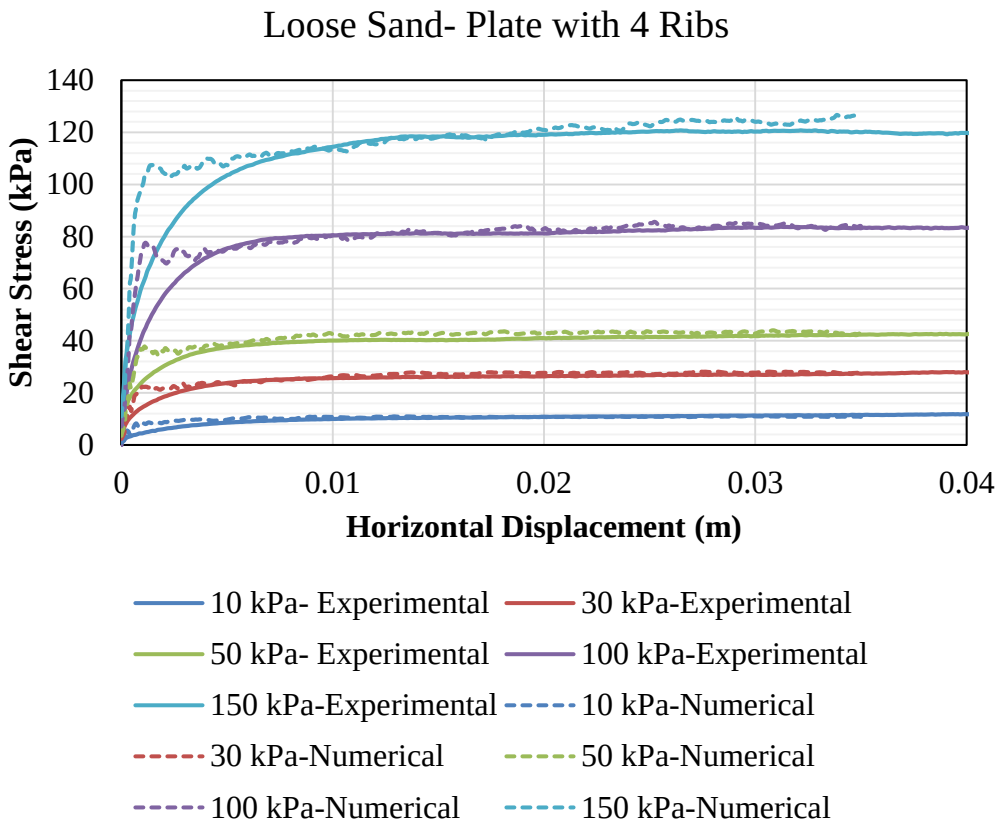

(c)

Figure 5-9. Continued.

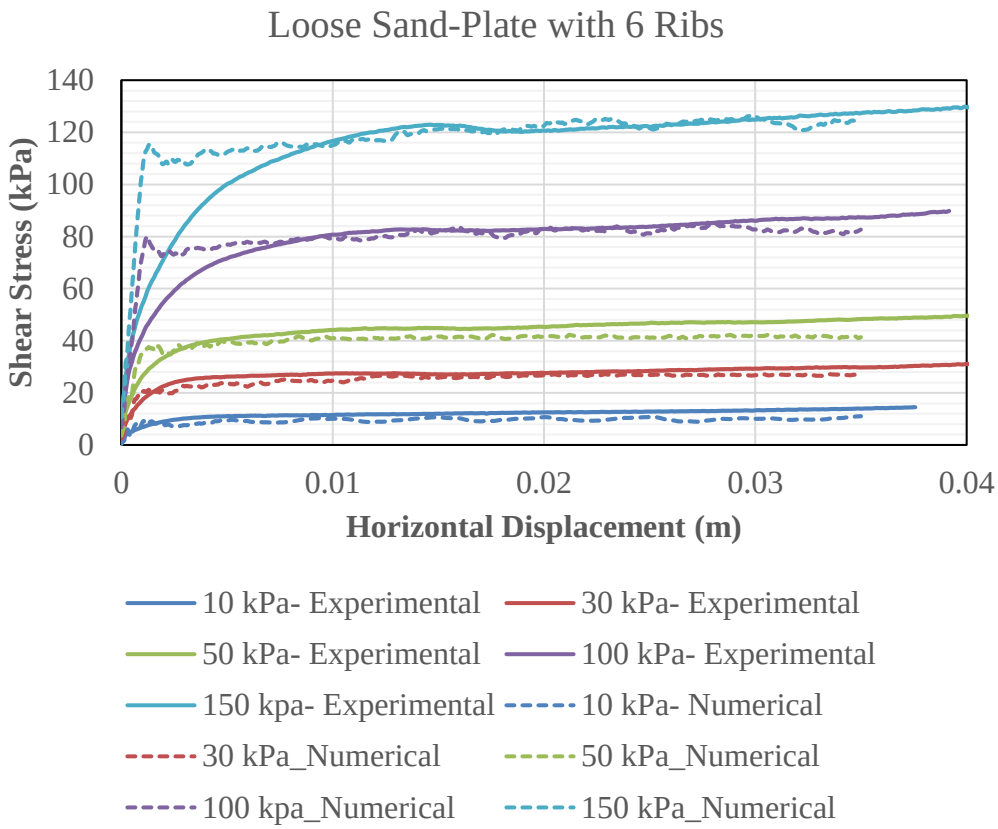

(d)

Figure 5-9. Continued.

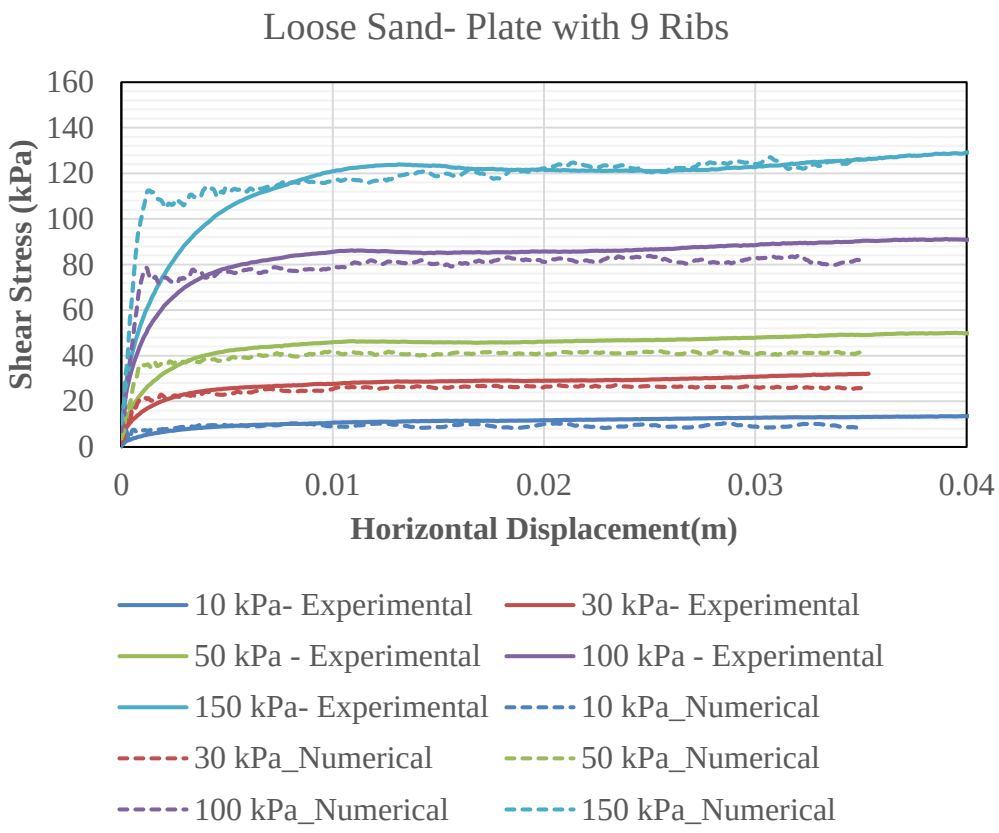

(e)

Figure 5-9. Continued.

5.7 Numerical Simulation of Pullout Test

5.7.1 Model Geometry

The FLAC3d model of the full box and half box pullout test were simulated to understand in depth of the pullout test mechanism, to better explain the effect of the ribs spacing on pullout force, and to find the optimum ribs spacing. The model includes the soil domain inside the box and the smooth/ribbed reinforcements embedded inside the soil. The steel reinforcements were modeled with zones and grid points with the elastic constitutive model. The soil medium simulated with the FLAC 3D strain softening/hardening constitutive model, and the mechanical properties of soil for various normal stresses are summarized in Table 5-3.

The geometry and boundary condition of the model is the same as the actual laboratory pullout tests. The full box and half box dimensions are 1.5m (L) × 0.4318 m (w) × 0.381 m (H) and 0.66m (L) × 0.4318 m (w) × 0.381 m (H). The bottom of the model is restrained in the Z direction, and the lateral walls are restrained in x and y directions. The generated mesh of the model is shown in Figure 5-10.

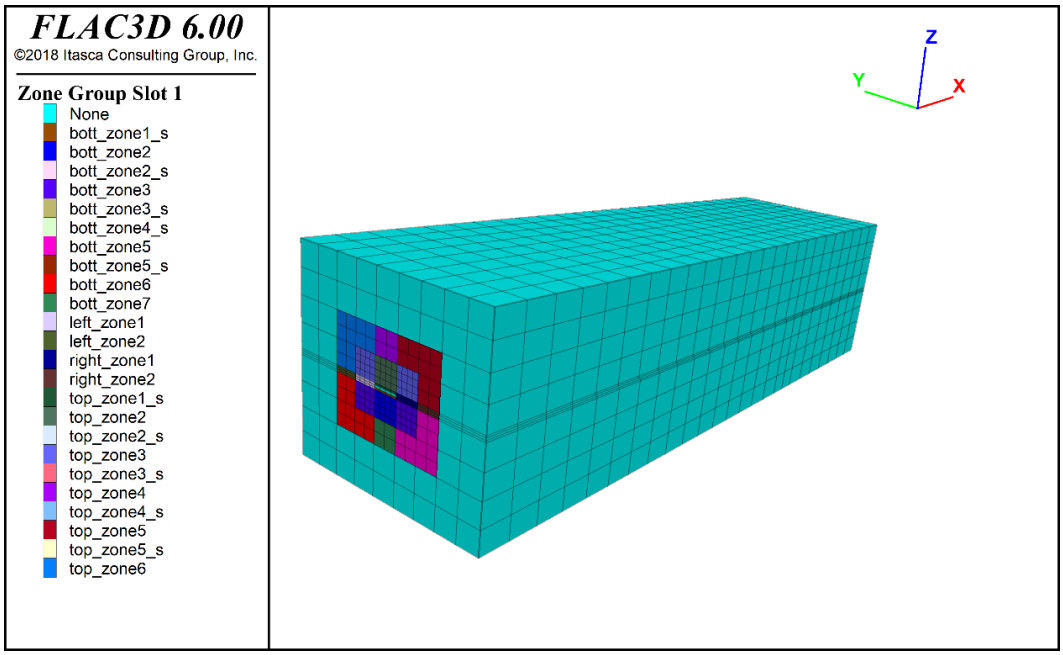

Figure 5-10. Generated mesh of Pullout Test with FLAC3D

The smooth, 2-rib, 4-rib, and RECO steel strip reinforcements were simulated with the actual geometry of the steel strip and ribs and using elements. The steel strip reinforcements in the full box and the half box has a dimension of 1.06 m (L) × 0.0508 (W) × 0.004m (H), and 0.3048 m (L) × 0.0508 (W) × 0.004m (H). As an example, the generated mesh of RECO steel strip and the soil around is shown in Figure 5-11.

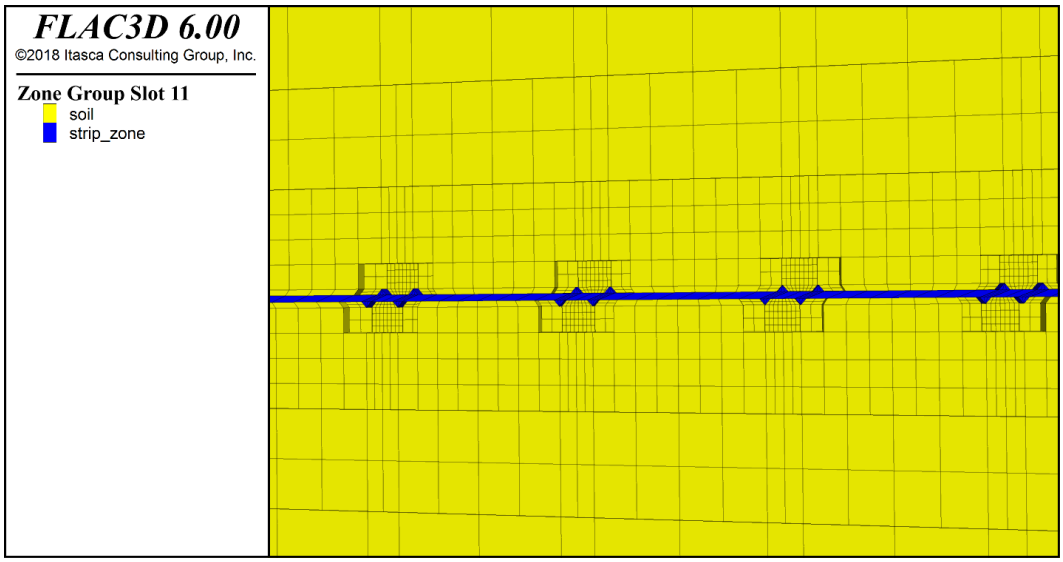

Figure 5-11. The Generated Mesh of Ribs Geometry of RECO Steel Strip Reinforcement

Similar to the geometry of the laboratory pullout test in a full box and half box, the pullout test was modeled in multi-steps. After generating the geometry, boundary condition, and loading conditions, the model was solved in three steps:

1- Converge the model under gravity force

2- Solve the model under applied normal stresses

3- Cycle the model while applying a displacement at a constant rate to the face of the steel strip reinforcement

The mechanical properties of the dense sand were used in the software are summarized in Table 5-3. As shown in this table to simulate the softening behavior of the soil material using the strain-hardening/softening model in FLAC, the friction and dilation angle of the soil decreases gradually with increasing the plastic strain. As explained in section 5.3.2,

the changes in dilation and friction angle were introduced as a table to the software. Table 5-4 shows the friction angle and the dilation angle changes with respect to the plastic strain of the elements.

Table 5-3. Mechanical Properties of Dense sand, Pullout Test

Normal Stress (kPa)	**Density Kg/m^3**	**E (kPa)**	ν	**Friction Angle (°)**	**Dilation Angle (°)**
6	1685	81000	0.3	31	10
30	1685	81000	0.3	30	9
60	1685	81000	0.3	29	8.5
90	1685	81000	0.3	28	8
120	1685	81000	0.3	28	7.5

Table 5-4. Strain-Softening Model Parameters

Normal Stress = 6 kPa						
Plastic Strain	0	0.2	0.3	0.4	0.5	1
Friction Angle (°)	31	26	24	23	22	22
Dilation Angle (°)	10	7	4	1	0	0
Normal Stress = 30 kPa						
Plastic Strain	0	0.3	0.3	0.4	0.5	1
Friction Angle (°)	30	25	23	22	21	21
Dilation Angle (°)	9	6	3	2	0	0
Normal Stress = 60 kPa						
Plastic Strain	0	0.2	0.3	0.4	0.5	1
Friction Angle (°)	29	25	23	22	21	21
Dilation Angle (°)	8.5	5	3	2	0	0
Normal Stress = 90 kPa						
Plastic Strain	0	0.2	0.3	0.4	0.5	1
Friction Angle (°)	28	24	22	21	20	20
Dilation Angle (°)	8	5.5	3.5	2.5	0	0

Table 5-4. Continued.

Normal Stress = 120 kPa						
Plastic Strain	0	0.2	0.3	0.4	0.5	1
Friction Angle (°)	28	24	22	21	20	20
Dilation Angle (°)	7.5	5	3	2	0	0

5.7.2 Results

The analyses was carried out for each normal stress at 6, 30, 90,120 kPa. The pullout force and pullout displacement of the strip reinforcement is measured for smooth, 2-rib, 4-rib, and RECO strip reinforcements under various normal stresses. The comparison of experimental and numerical results of these tests illustrate in Figure 5-12. The results are in a good agreement with experimental data obtained from the pullout test on smooth/ribbed steel strip reinforcements embedded in dense sand.

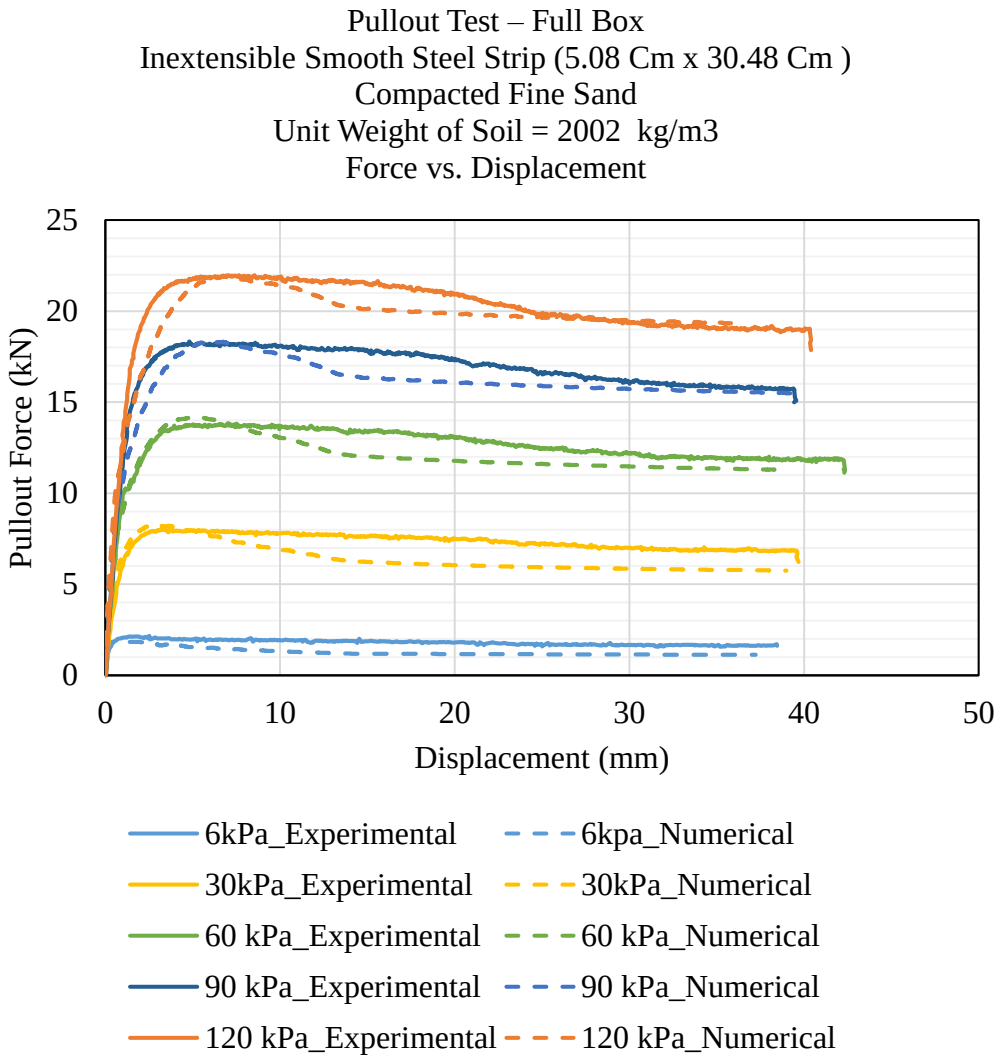

(a)

Figure 5-12. Comparison of Experimental and Numerical modeling of Pullout Test in Full Box on Dense Sand

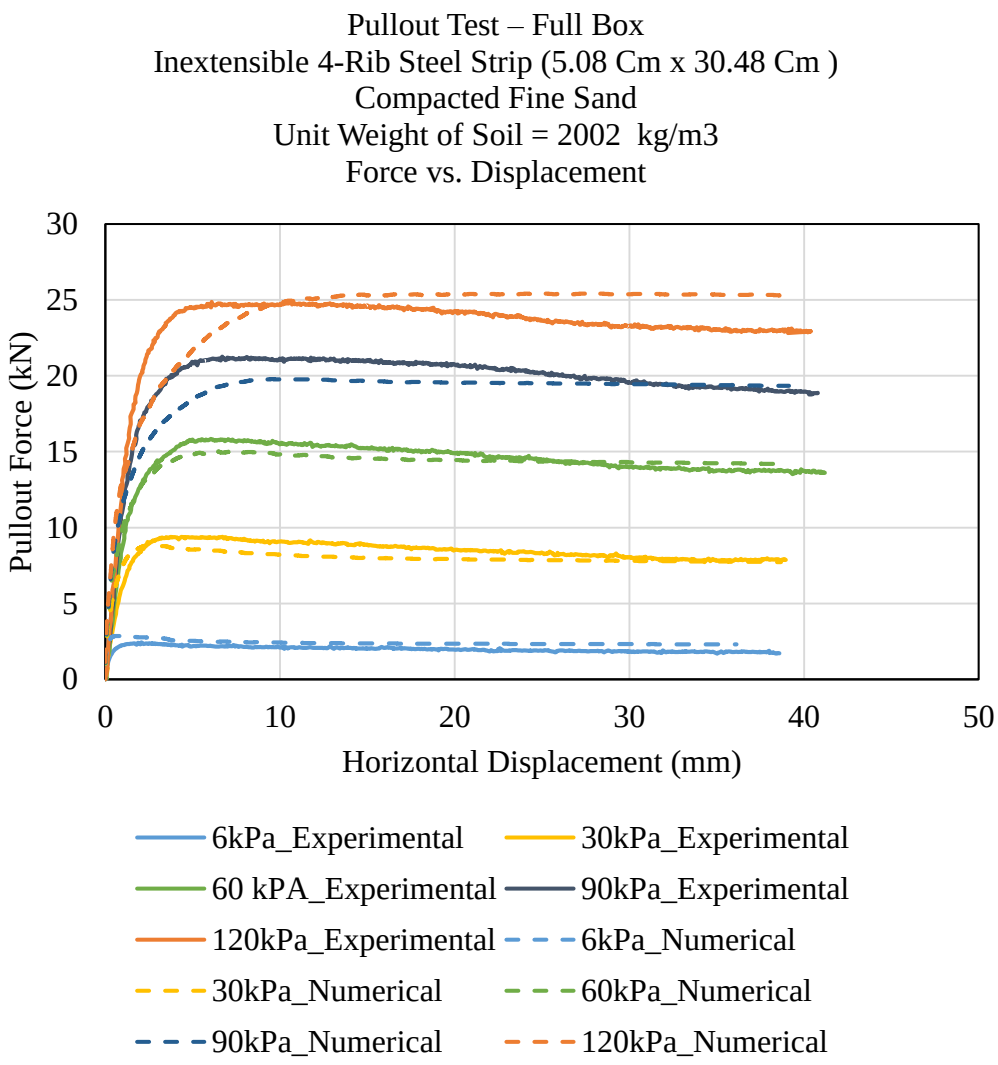
Pullout Test – Full Box
Inextensible 4-Rib Steel Strip (5.08 Cm x 30.48 Cm)
Compacted Fine Sand
Unit Weight of Soil = 2002 kg/m3
Force vs. Displacement
Pullout Force (kN)
0
5
10
15
20
25
30
0
10
20
30
40
50
Horizontal Displacement (mm)
6kPa_Experimental
30kPa_Experimental
60 kPA_Experimental
90kPa_Experimental
120kPa_Experimental
6kPa_Numerical
30kPa_Numerical
60kPa_Numerical
90kPa_Numerical
120kPa_Numerical

(b)

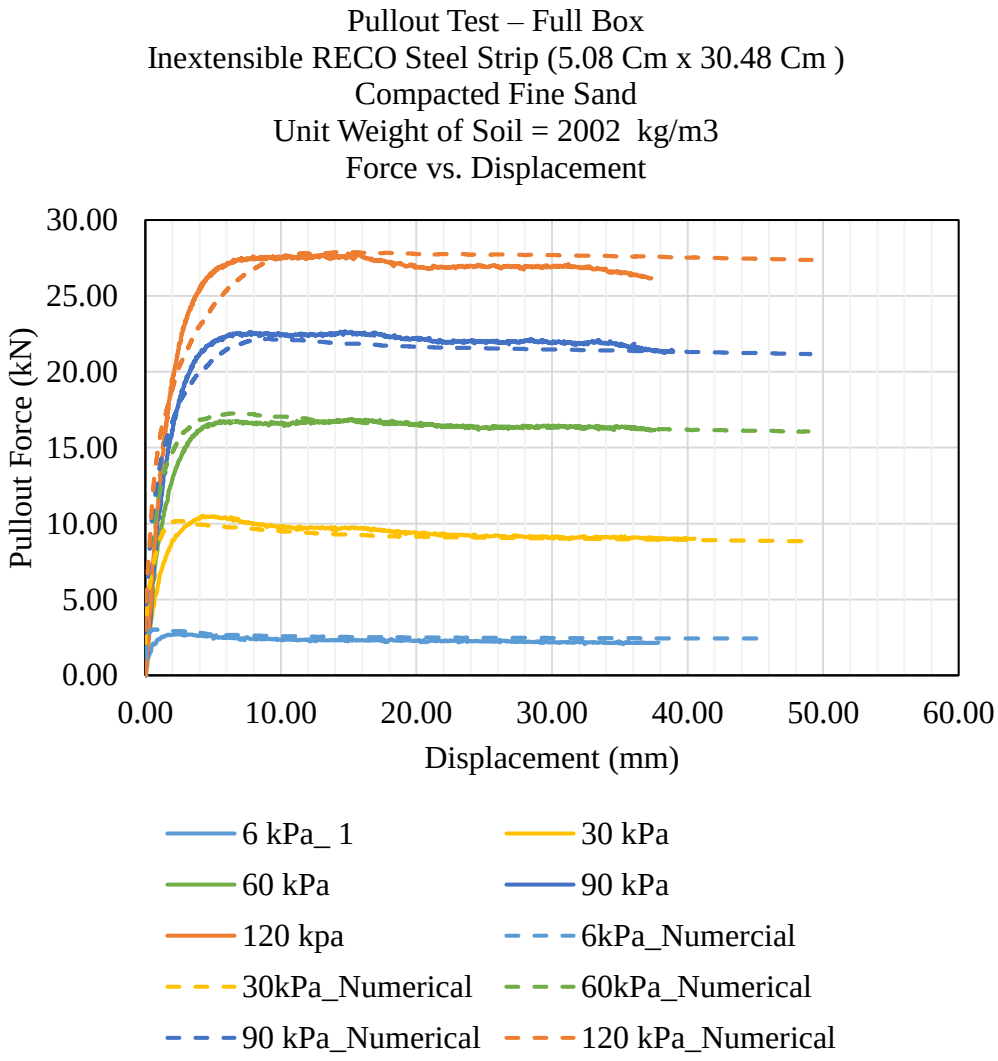

(c)

Figure 5-12. Continued.

To find the optimum ribs spacing, a numerical model was built with FLAC3D for a steel strip with 6-rib per 30.48 cm (1 ft.) per side. The ribs spacing, and configuration are shown in Figure 5-13. It is worth nothing that the ribs dimension is exactly the same

as previous simulations and same as RECO steel strip reinforcement. Figure 5-14 illustrates the comparison of the pullout force for the 6-rib strip and the RECO steel strip reinforcements. The results of the 6-rib strip are mentioned by the name of "Numerical_B". As can be seen in this figure, the results indicate that increasing the number of ribs does not have any influence on the pullout force. As the failure plain located inside the soil zone

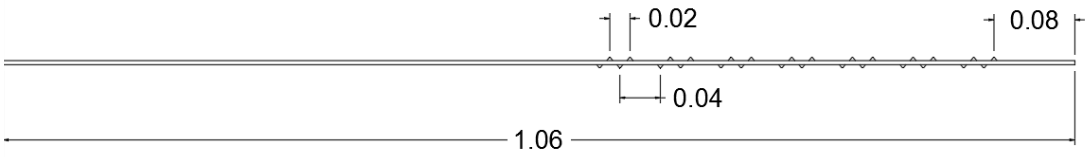

Figure 5-13. Cross Section of Ribbed Steel Strip Reinforcement with 6 ribs per 30.48 cm per side-B

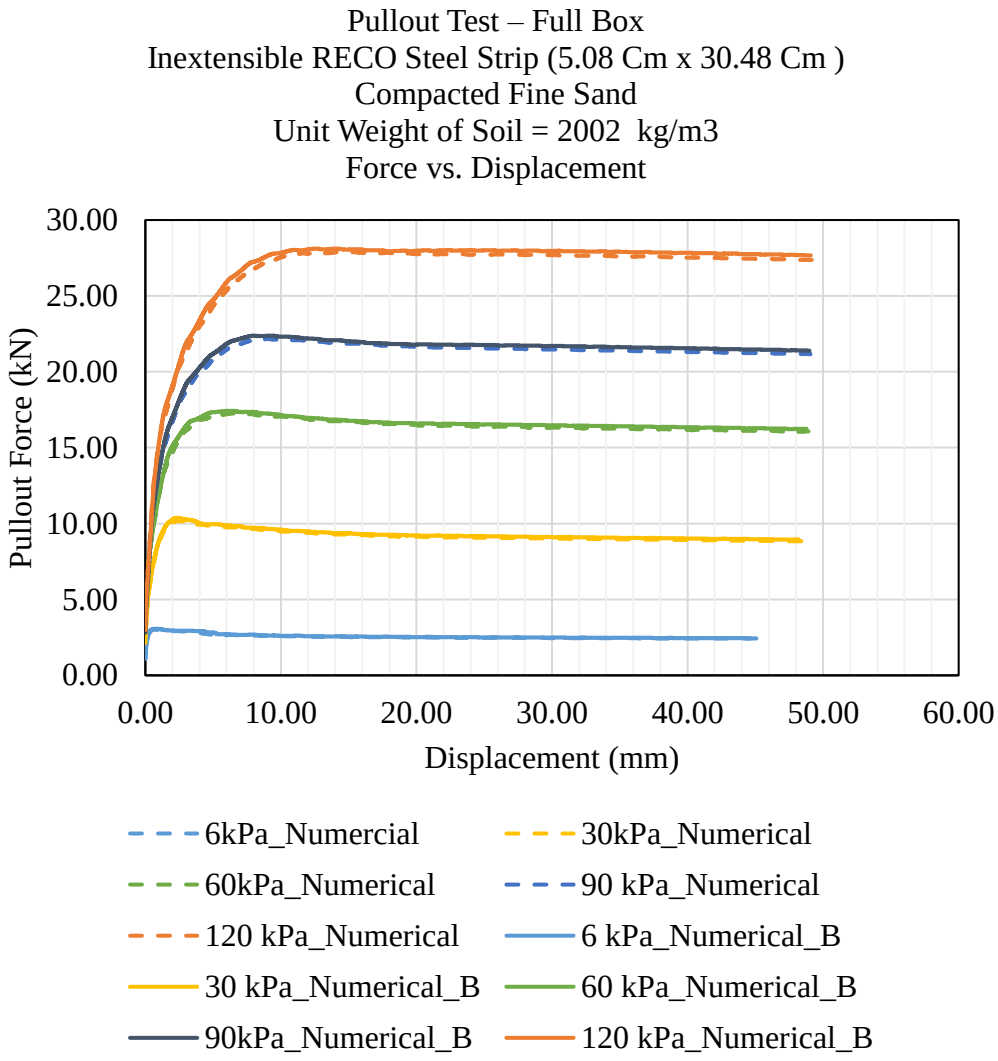

Figure 5-14. Comparison of the Pullout Force of 6-Rib per 30.48 Cm per Side Steel Strip and RECO Reinforcement

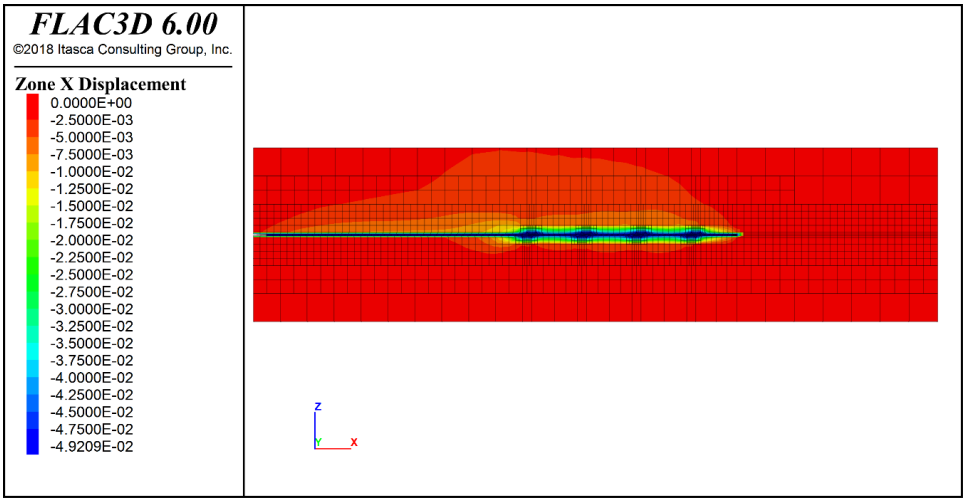

(a)

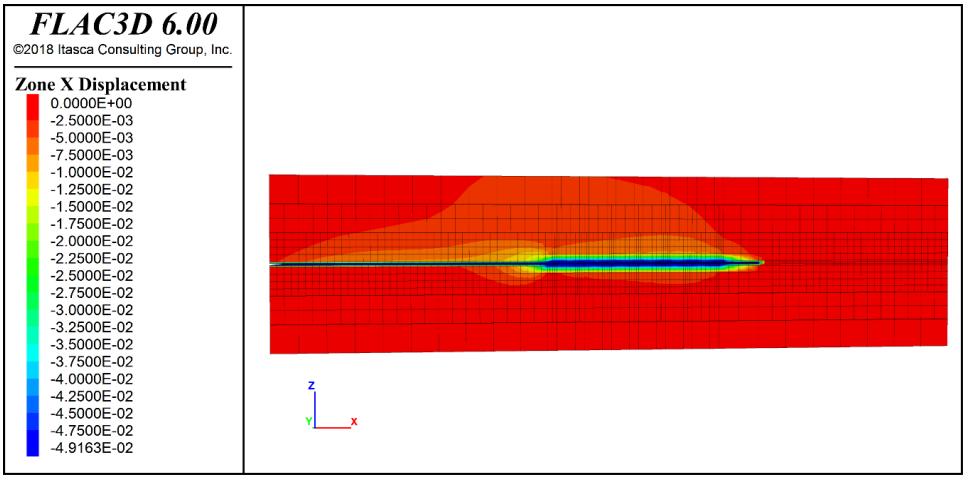

(b)

Figure 5-15. Contour of Displacement in X Direction, (a) RECO Steel Strip Reinforcement, (b) 6-Rib per 30.48 cm per side steel strip (B)

6 DATA ANALYSIS

6.1 Comparison of DST and SST

The direct shear test is the most widely used laboratory test to obtain the shear strength parameters of soil. During the first part of the direct shear test, the soil sample is allowed to consolidate under the vertical stress applied. During the second part of the test, the sample is sheared and shearing takes place along a thin horizontal band at mid-height of the sample near the junction between the two steel rings. The shear stress versus horizontal movement curve is obtained point by point. The shear strength is the maximum shear stress on the shear stress versus horizontal movement curve. The most important parameter which can be obtained from the direct shear test is the soil friction angle, the slope of the Mohr-Coulomb envelope. At least three points are needed in shear strength-normal stress curve to calculate friction angle. Although the direct shear test has several advantages, it also has disadvantages which are summarized in Table 6-1 and is explained in the following paragraph.

The shortcomings of the direct shear test resulting attempts to develop the simple shear test. In the case of the direct shear test, the soil is forced to shear in a predetermined plane, the horizontal plane, which is not necessarily the weakest plane. Second, there is an unequal distribution of the stress over the shear surface. During the shearing phase, the progress failure is observed and the stress is greater at the edges than at the center. In the case of direct shear test, the lower half box is moved while the upper half box is remained fixed. The major difference between the direct shear test and the simple shear test is that

in the direct shear test, the shearing takes place along a predetermined thin band of soil near the middle of the sample. In the simple shear test, the shearing takes places over the entire height of the sample. Figure 6-1 illustrates the schematic drawing of these two types of tests.

Table 6-1. Advantages and Disadvantages of Direct Shear and Simple Shear Test

Direct shear test	
Advantages	**Disadvantages**
• Inexpensive and fast • Can be used to determine interface strength parameters	• Failure occurs along a predetermined plane • Non-uniform distribution of shear stress along the failure surface • Area of the sliding surface changes as the test progresses
Simple shear test	
• Shearing over the entire height of the sample • Gives Shear Strain • Gives Shear Modulus	• Expensive

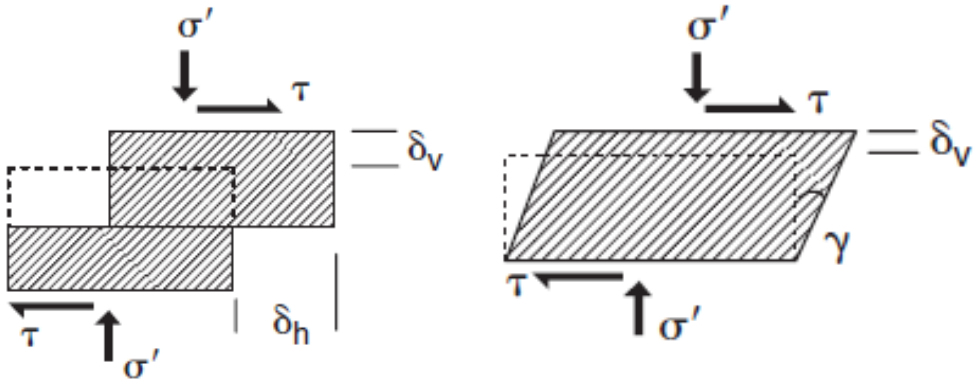

Figure 6-1. Schematic Drawing of Direct Shear Test and Simple Shear Test

Although the simple shear test has improvements over the direct shear test, the shear stresses are not uniformly distributed on the specimen. As shown in Figure 6-1, the shear stress on the lateral walls of the simple shear specimen is missing and pure shear only exists at the center of the specimen. Comparing the contour of the maximum shear strain rate obtained from FLAC3D simulation for direct simple shear test and direct shear test, as shown in Figure 6-2 (a), the shear band along the mid-height of the DS box is clearly showing the predetermined failure plane. However, the failure in the simple shear test can occur on different planes, horizontal or vertical planes and the failure planes rotating during the shearing phase (Figure 6-2 (b)). The sample will choose the weakest planes to fail. This approach is also proposed by Worth (1984) and de Josselin de Jon (1971).

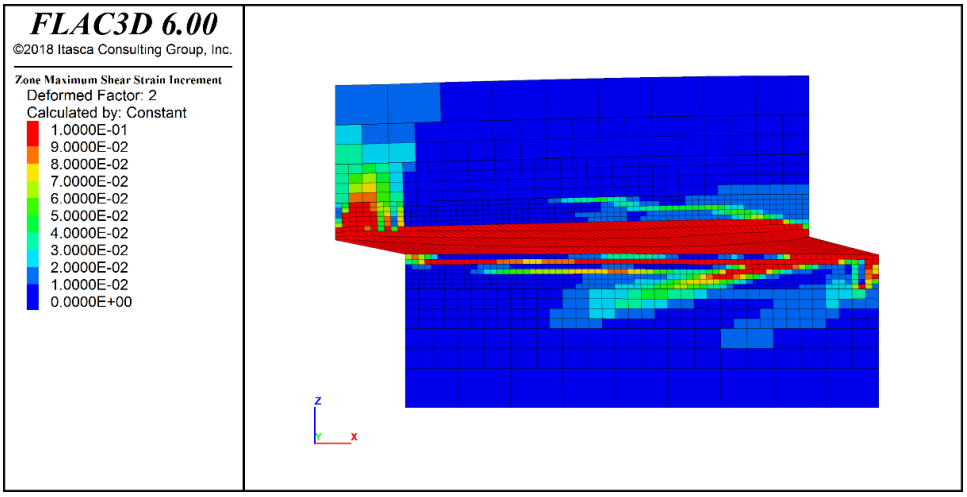

(a)

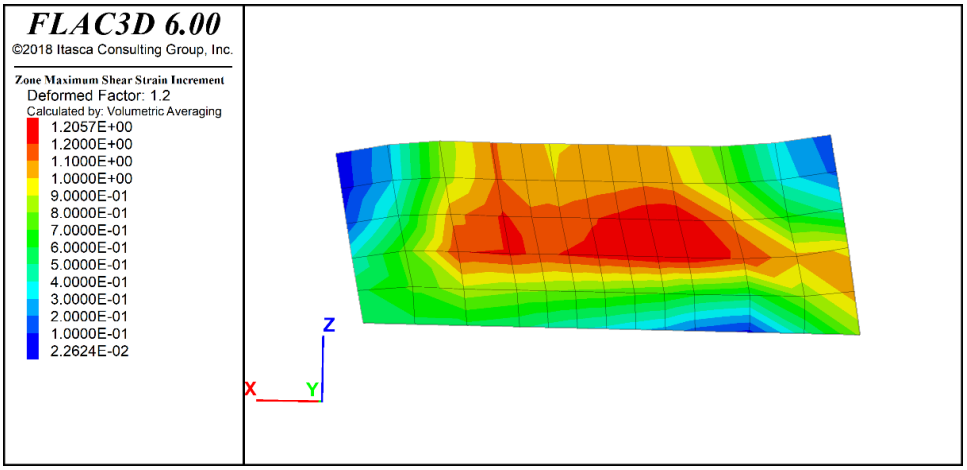

(b)

Figure 6-2. Shear Strain Increment and Deformed Section of the Specimen, (a) Direct Shear Test, (b) Simple Shear Test

The shear strength parameter from the direct shear test can be obtained from the slope of the Mohr-Coulomb failure envelope as the failure plane is the horizontal plane

and the Mohr circle is developed by the normal stress and shear strength parameters. However, the failure plane in the simple shear test is unknown and the Mohr Circle cannot be created without assuming the failure plain. Three approaches were proposed by Budhu, 1988 using Coulomb failure to calculate the strength parameters of soil from simple shear test results.

1-The horizontal plane is the failure plane (β-method) as shown in Figure 6-3 (a). Therefore, the friction angle can be obtained as follow:

$$\beta = \tan^{-1}\frac{\tau_{yx}}{\sigma_y}$$

2- The horizontal plane is the plane of maximum shear stress (α-method). Figure 6-3 (b) illustrates the Mohr's Circle with this assumption. The friction angle is calculated as the slope of the line tangent to the circle:

$$\alpha = \sin^{-1}\frac{\tau_{yx}}{\sigma_y}$$

3- Failure happens on the vertical planes (Figure 6-3 (c)), and the friction angle is calculated as follow:

$$\delta = \tan^{-1}\frac{\tau_{xy}}{\sigma_x}$$

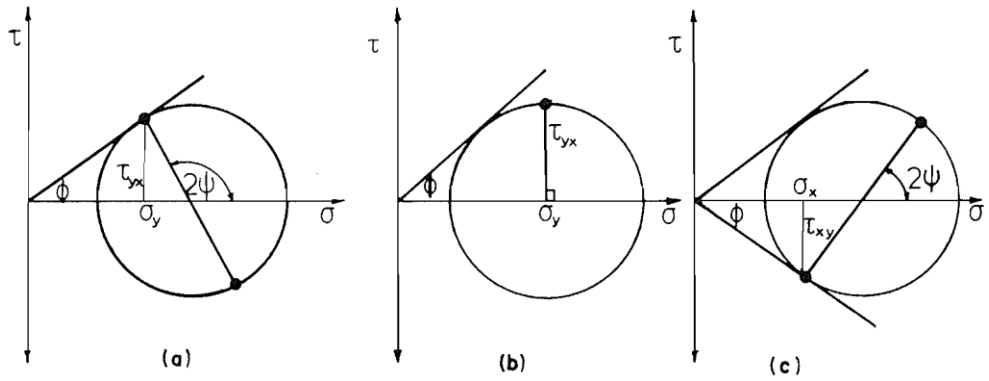

Figure 6-3. Mohr's Circles for various assumptions of Failure Modes (Budhu, 1988)

Utilizing the numerical simulation of simple shear test on the loose and dense sand, the beforementioned assumptions were investigated for the core sample where the pure shear occurs. Four parameters including τ_{xy}, τ_{yx}, σ_y, and σ_x were measured for core element inside the simple shear specimen. Figure 6-4 shows the ratio of the shear stress over normal stress versus shear strain ($\frac{\tau_{yx}}{\sigma_y}$ and $\frac{\tau_{xy}}{\sigma_x}$) for a core sample in loose and dense specthe imen. For the case of loose sand, the shear stress increases drastically on the vertical plane to reach the value of 0.75 (= $\tan 37$), and then decreases to 0.6 (= $\tan 31$). The shear stress ratio on horizontal plain increases to 0.6 (= $\sin 37$ *or* $\tan 31$), and stays constant for large shear strain. On the the other hand, the shear stress ration of dense sand on vertical plane reaches a to 1.07 (= $\tan 47$) and drops to 0.67 (= $\tan 34$), and the one on the horizontal plain reaches to 0.79 (= $\sin 52$ *or* $\tan 38$) at 19% shear strain. Therefore, for loose sand the failure initiated o,n vertical plane (the weaka est plane) and at large displacements, the horizontal or vertical plain can both be the failure planes. For

dense sand, however, the failure plains initiate on the vertical plain at small shear strain values, then the horizontal plain is the failure plain at large shear strain.

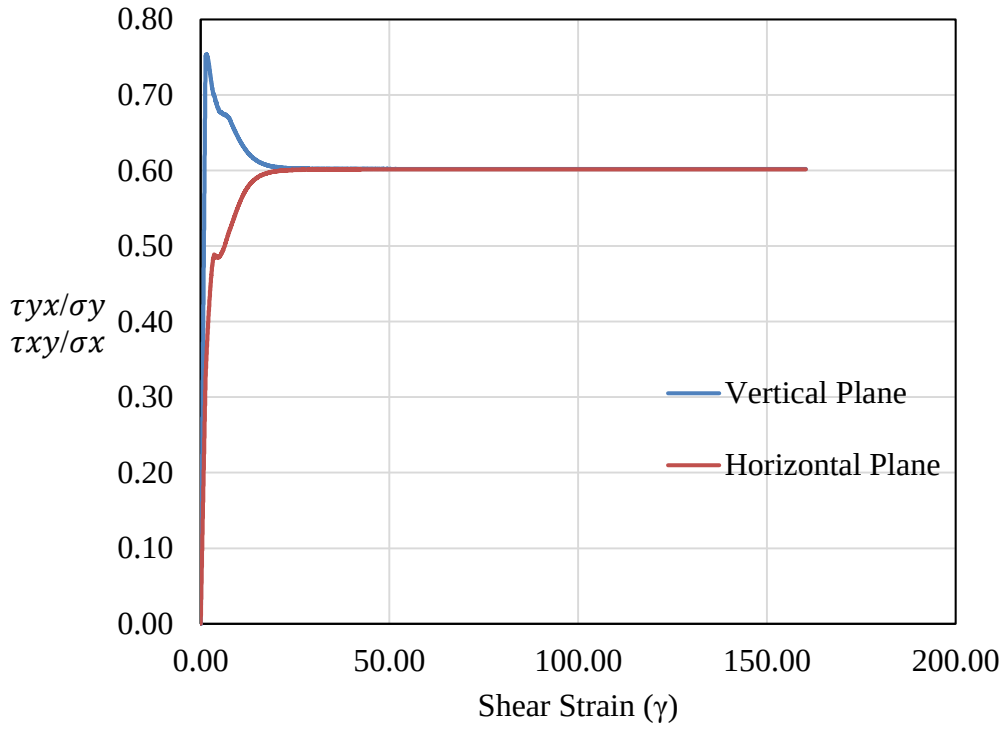

(a)

Figure 6-4. Shear Stress Ratio versus Shear Strain, (a) Loose Sand, (b) Dense Sand

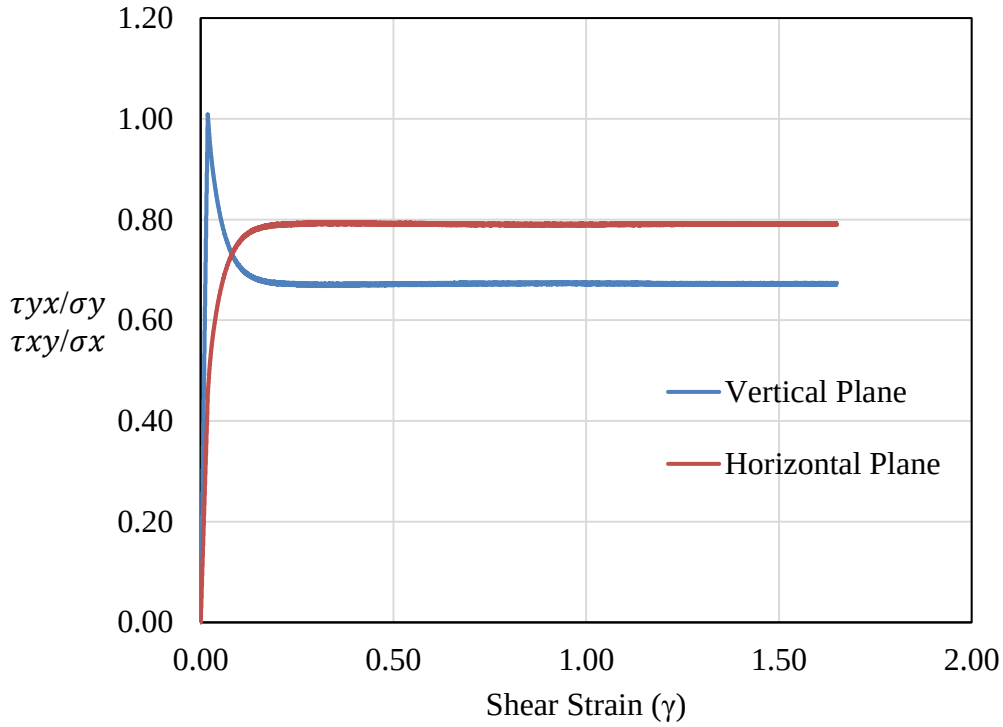

(b)

Figure 6-4. Continued.

Therefore, the friction angle obtained from the direct shear test is an overestimated friction angle because the failure plane is not the weakest one. To calculate the friction angle from the simple shear test results, the laboratory measurements of the simple shear test is not adequate, and the numerical simulation or correlations are needed. Because the stress state rotates during the shear phase and the maximum shear stress ratio may happen on different planes. Moreover, the maximum shear stress ratio does not occur for all planes at the same time and the failure plane will follow the weakest plains.

Table 6-2 summarizes the friction angle of loose sand, dense sand, and crushed limestone from laboratory direct shear and simple shear test measurements. As shown in this table, the friction angle of loose sand, dense sand, and crushed limestone obtained from the direct shear test are 38º, 47º, and 56º, respectively. On the other hand, the friction angle of those three types of soils was calculated using the simple shear test measurements by β-method and α-method.

Table 6-2. Summary of Friction angle of Loose/Dense Fine Sand and Crushed Limestone

	Simple Shear Test		Large Direct Shear Test		Small Direct Shear Test	
Soil Type	**β-method**	**α-method**	**φ(tan), Peak**	**φ(tan), Residual**	**φ(tan), Peak**	**φ(tan), Residual**
Loose sand	30.5	36	38	37.5	35	34
Dense sand	33	40.5	47	42	44.5	32
Crushed limestone with fines	31.5	37.6	56	54.5	-	-

6.2 Interface Parameters

Three interface parameters were calculated as they defined in the literature by precious researchers to study the influence of various parameters including the number of

ribs per side per 30.48 cm (1ft), soil density, soil grain size, and test type. These parameters are apparent friction coefficient (F*), apparent friction coefficient ratio (F* ratio), and coefficient of direct sliding (C_i) and they defined as follow:

$$\text{Apparent Friction Coefficient } (F^*) = \frac{\text{Interface Shear Strength}}{\text{Normal stress on plate}}$$

$$\text{Apparent Friction Coefficient Ratio } (F^* \text{ratio}) = \frac{\text{Apparent Friction Coefficient of ribbed strip}}{\text{Apparent Friction Coefficient of Smooth Strip}}$$

$$\text{Coefficient of Direct Sliding } (C_i) = \frac{\text{Interface shear strength}}{\text{Soil shear strength}}$$

Apparent friction coefficient (F*) factor was calculated for the results obtained from IDST of aluminum plates with 0, 2-rib, 4-rib, 6-rib, and 9-rib reinforcements and loos sand, dense sand, and crushed limestone with fines. The F* values vs. depth of soil equivalent to the applied normal stress are reported in Figure 6-5. Furthermore, the AASHTO recommendation default value for smooth and ribbed reinforcements as well as soil-soil friction coefficient ($\tan \emptyset$) are presented in theses graphs to compare the obtained results with AASHTO recommended criteria and the soil-soil friction angle, respectively. The F* value obtained from interface tests between smooth strip and soil is higher than the AASHTO smooth strip default value. The F* value of smooth plate sheared over dense sand specimen is higher than the one sheared over loose sand. Also, the F* value obtained from interface direct shear test between crushed limestone and the smooth plate is higher than AASHTO recommendation for the smooth strip and higher than F* value for sandy soil. However, for both loose and dense sand, the F* value of smooth and 2-rib reinforcement is lower than the friction coefficient of soil-soil. Because the soil particles

roll over and slide on the surface of the smooth plate, and as expected the friction angle between soil aggregate and the smooth plate is lower than friction angle between the soil aggregates itself. The F* value of smooth plate in IDST with loose and dense sand starts from 0.35 and 0.53 at 10 kPa normal stress and increases slightly to 0.67 and 0.63 at 150 kPa normal stresses, respectively. With increasing the number of ribs on a plate, the F* value of reinforcements also increasing. For loose sand, the F* value of 9-rib plate is 1 at depth of 0.85 m and 0.8 at depth of 10.5 m. This means that for loose sand the effect of the normal stress (depth of embedment) is negligible on the F* value because the loose sand does not show the dilation behavior. However, the results of IDST between the reinforcements and dense sand indicates that with increasing the density, sand will show dilation behavior and the F* value is greater at low normal stresses and smaller at higher stresses. With increasing the number of the ribs, the local dilation will lead to an increase in difference of F* value between the low and high normal stresses. For example, the F* value calculated from IDST between the smooth plate and dense sand is 0.53 at 0.75 m deep and the one is 0.67 at 9.1 m deep soil. The F* value of 9-rib plate and dense sand calculated equal to 1.8 at depth of 0.78m and 1.2 at depth of 9.1m.

For CLF, Figure 6-5 (c) indicates that the obtained F* value for all reinforcements are greater than AASHTO criteria for both smooth and ribbed strip. Furthermore, comparing the F* value for a different number of ribs on the plate indicates that increasing the number of the ribs on the aluminum plate increase the F* value. However, the F* value of all ribbed plates is lower than soil-soil friction angle. Because the friction angle of the

soil-soil for crushed limestone is 56° while the interface friction angle between the smooth plate and CLF is 33.7°. Therefore, because the grain size of the crushed limestone is larger than rib's height, the ribs will increase the friction between the soil and the reinforcement although the failure still occurs at the interface of CLF and plate.

In conclusion, the density and soil grain size have an influence on F* value. With increasing of the density and grain size of the soil, the F* value is also increasing. Moreover, if the grain size of the soil is smaller than the height of the ribs, the interface shear stress is the combination of the friction force between the smooth plate and soil as well as the bearing capacity due to the ribs. However, for the case of soil with grain size greater than the height of the ribs, the passive resistance (bearing capacity) contribution of the ribs does not mobilize, and the failure occurs on the interface between the soil and reinforcement. The soil grains turn over the reinforcement surface and slide over it. The influence of the ribs will be increasing the roughness of the surface, therefore, increasing the friction angle between the plate and soil grains.

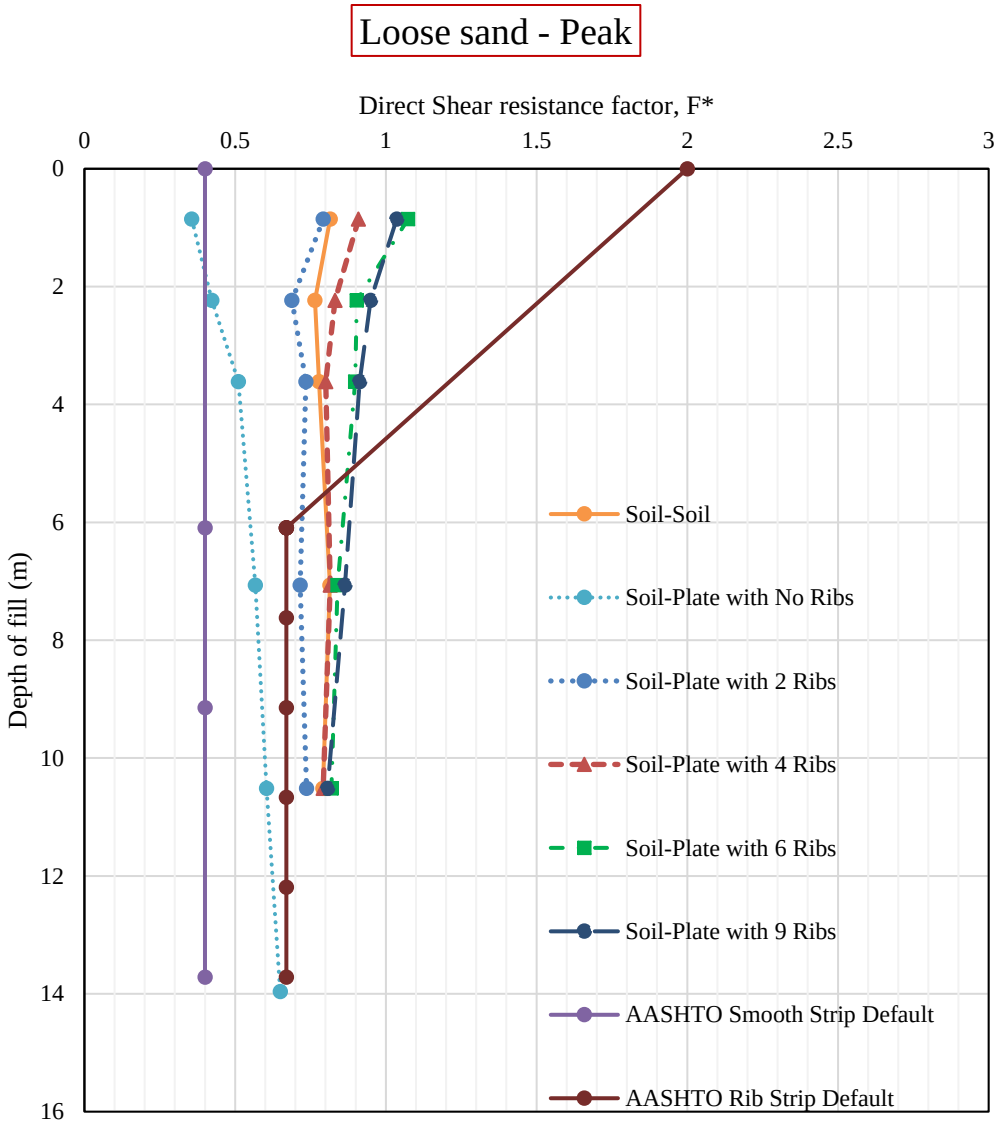

(a)

Figure 6-5. Apparent Friction Coefficient (F*), IDST, (a) Loose Sand, (b) Dense Sand, (c) Crushed Limestone with Fines

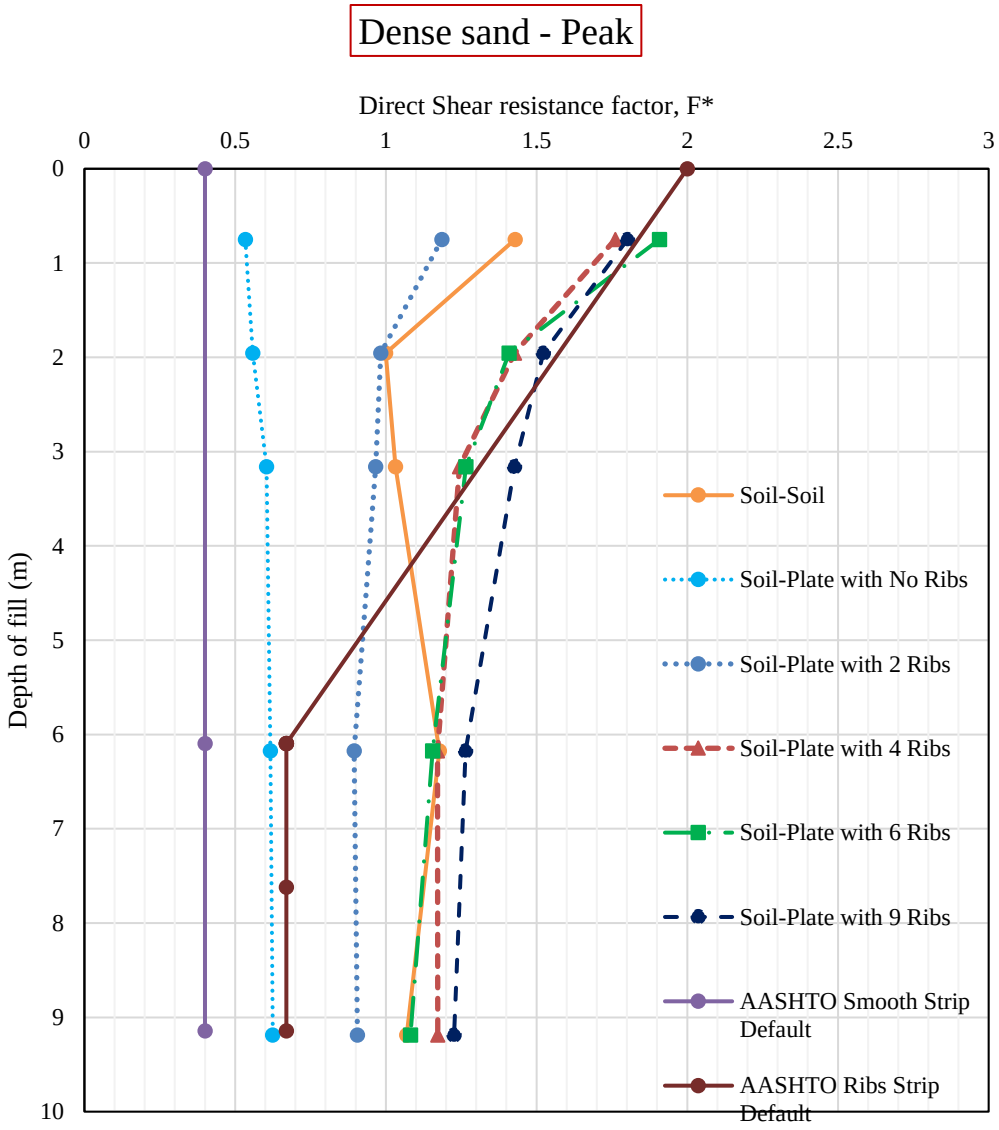

(b)

Figure 6-5. Continued.

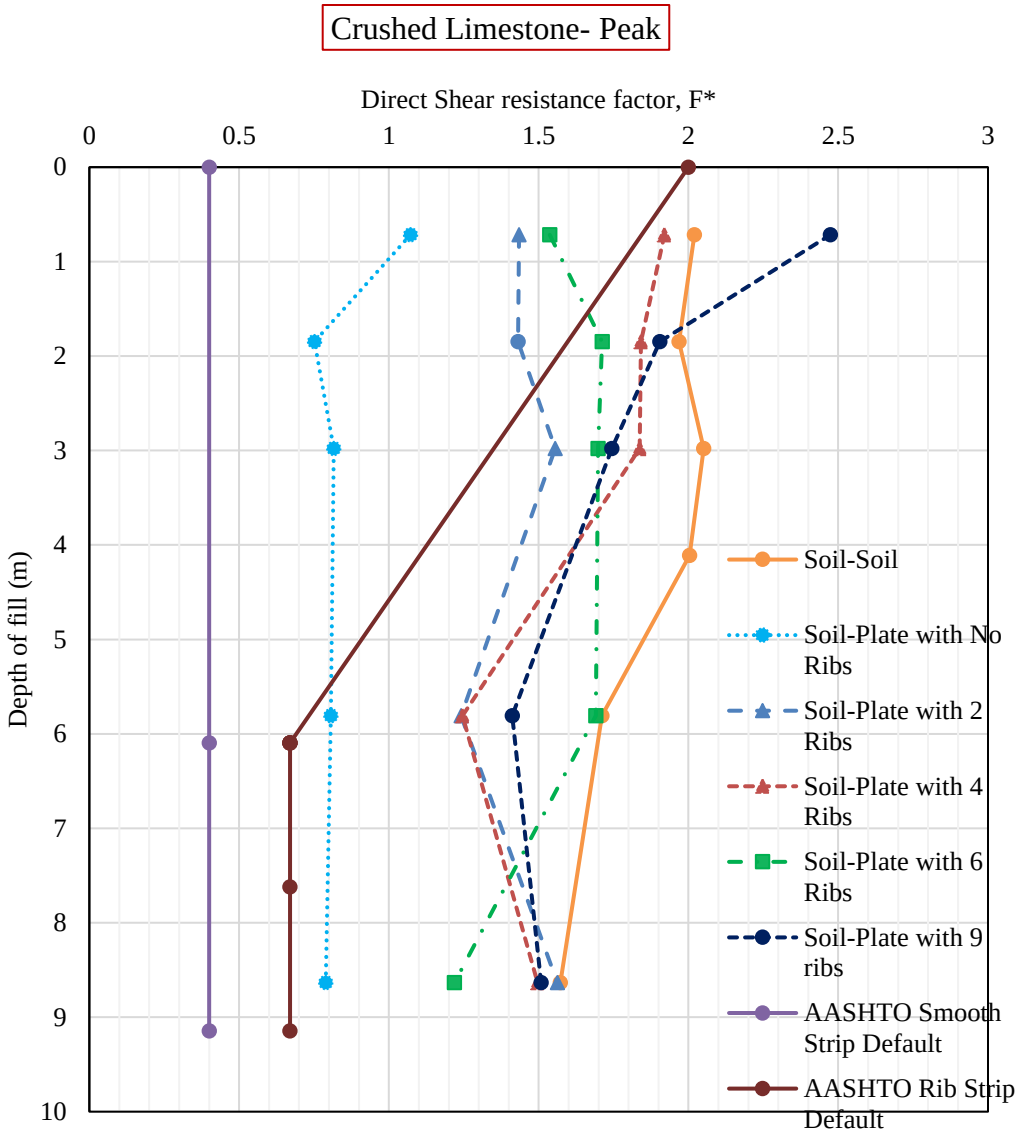

(c)

Figure 6-5. Continued.

The F* value of smooth/ribbed steel strip reinforcements embedded in dense sand using the pullout test in the half box and full box is illustrated in Figure 6-6. As shown in Figure 6-6 (a) and (b), The F* values obtained from the half box and full box pullout tests

are greater than AASHTO default value for all reinforcement types, and with increasing the number of the ribs, the F* value also increases. The F* value of smooth strip in half box is equal to 3 at 0.3 m depth of soil and 0.79 at 6 m deep soil. The F* value of smooth strip in full box is equal to 3 at 0.3 m depth of soil and 1.69 at 6 m deep soil. With increasing the number of ribs of steel strip reinforcement to 4 ribs per 30.48 cm (RECO) in full box, the F* value increasing to 3.7 at depth of 0.3 m and to 2 at depth of 6 m.

The F* values obtained from ribbed steel strip reinforcements embedded in half box pullout test are in the range of 8-9 at depth of 0.3 m and 2.5-3.5 at depth of 6 m. However, pullout tests on ribbed steel strips embedded in the full box show that F* values are in the range of 2.5- 4.8 at depth of 0.3 m and the one are in the range of 1.7-2 at depth of 6m. The results describe that pullout testing in half box provides the overestimated F* value because of the influence of the boundary condition. Since there is not an ASTM standard for pullout test on steel strip reinforcements, ASTM D6706 – 01, Standard Test Method for Measuring Geosynthetic Pullout Resistance in Soil is used as a guidance. Based on ASTM D6706 – 01, the pullout box should be square or rectangular with minimum dimensions 610 mm (24 in.) long by 460 mm (18 in.) wide by 305 mm (12 in.) deep, if sidewall friction is minimized, otherwise the minimum width should be 760 mm (30 in.). The minimum width of the box should be greater than 20 times of D85 of the soil or 6 times of the maximum soil particle size. The minimum length of the box is 5 times the maximum geosynthetic aperture size, and the minimum depth of the box is recommended to be 150 mm above and below the geosynthetic. Therefore, the half box

does not follow this standard criterion and the results are greater than full box results. This can be shown using the numerical simulation tools which are explained in section 6.6.

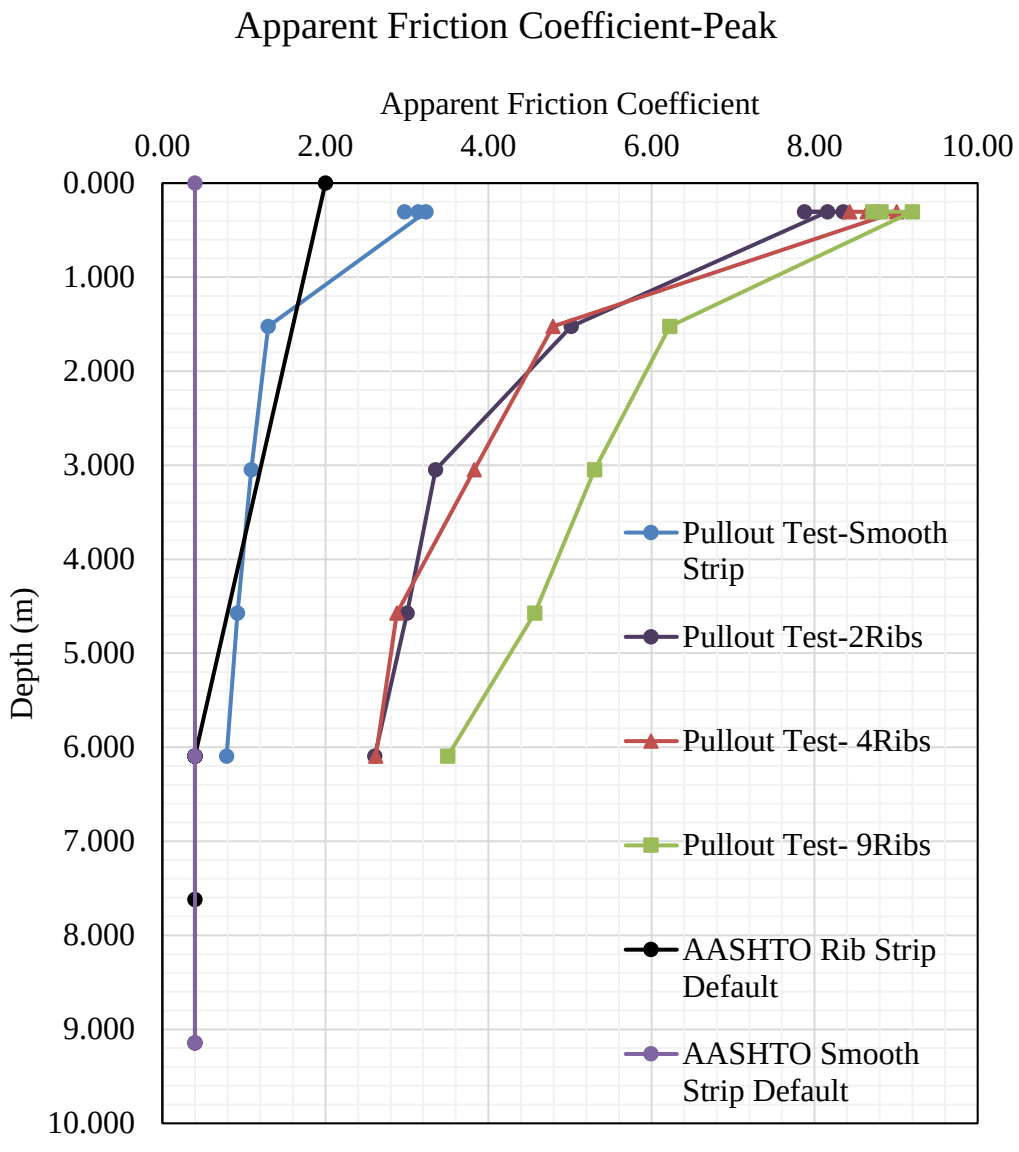

(a)

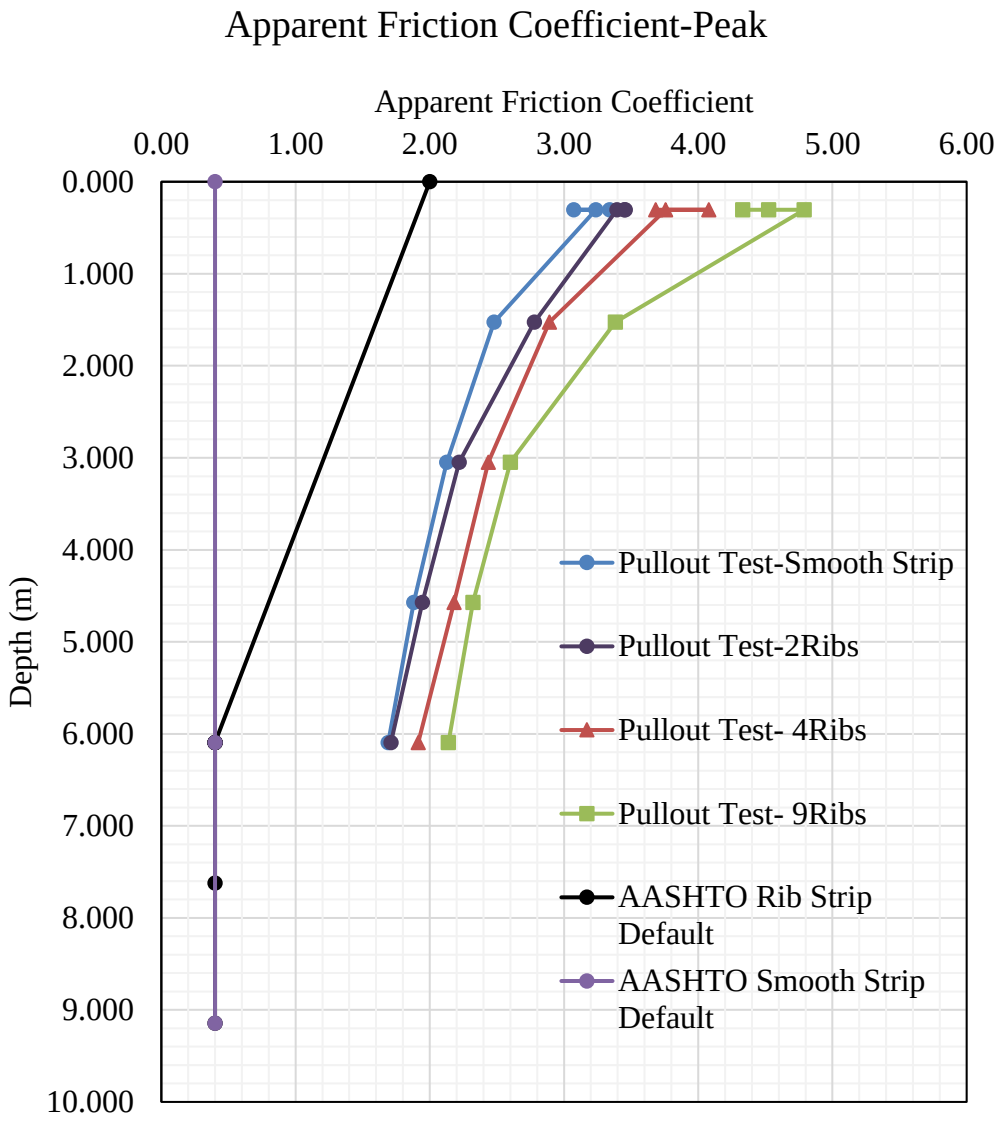

(b)

Figure 6-6. Apparent Friction Coefficient (F*), Pullout Test Smooth/Ribbed Steel Strip Reinforcements, (a) Half Box, (b) Full Box

Figure 6-7 shows the apparent friction coefficient (F*) for geogrid and geotextile reinforcements. As illustrated, the F* value is greater than AASHTO recommendation for

geotextile and geogrid (F* = 0.67 *tan (37°)). The F* value for geogrid is equal to 2.5 at low normal stress and decreases to 1 at high normal stresses.

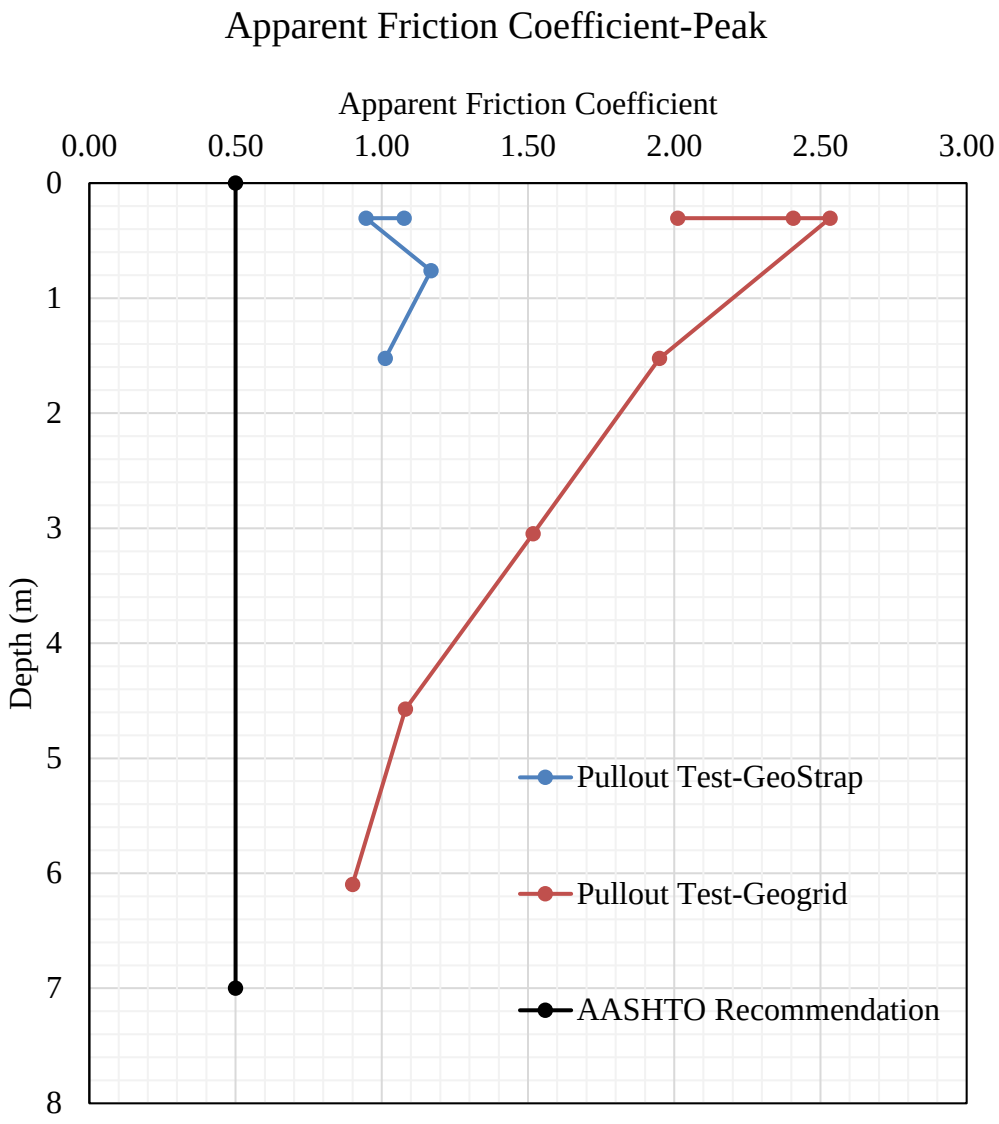

Figure 6-7 Apparent Friction Coefficient (F*), Pullout Test Geosynthetic Reinforcements

To study the influence of the ribs spacing or the number of ribs per side per 30.48 cm (1ft) of the steel reinforcements, apparent friction coefficient ratio is defined as the ratio of the F* value of ribbed strip over the F* value of smooth strip. Figure 6-8 indicates the apparent friction coefficient ratio of reinforcements obtained from interface direct shear test between reinforcement plates and loose sand, dense sand, and crushed limestone. The peak/residual shear interface shear stress, F* value, F* ratio, and Ci are summarized in Table 6-3, Table 6-4, and Table 6-5.

The curves indicate that the influence of the number of the ribs is a function of the normal stresses, soil density, and soil particle size. Considering the results of loose sand, the F* value of 2-rib plate is 2.2 at 0.7 m depth, and 1.22 at depth of 8.6 m. The graph shows that the F* ratio is increasing for 4-rib plate compare to the 2-rib plate, and 6-rib plate shows greater F* value than the 4-rib plate. However, the F* value ratio for the 9-rib plate is observed the same as a 6-rib plate. The same behavior is observed for dense sand and the F* value ratio is at the range of 2.2-3.5 at 0.7 m depth and 1.8-1.9 at depth of 8.6 m. The F* ratio of 4-rib and 6-rib plates are almost similar.

Comparing the F* ratio of crushed limestone and sand, the effect of the number of ribs on F* value of ribbed plate-CLF is almost negligible.

The influence of the number of the ribs is greater at low normal stresses than high normal stresses. The effect of the number of ribs on reinforcement is greater for dense soil than loose soil for all normal stresses.

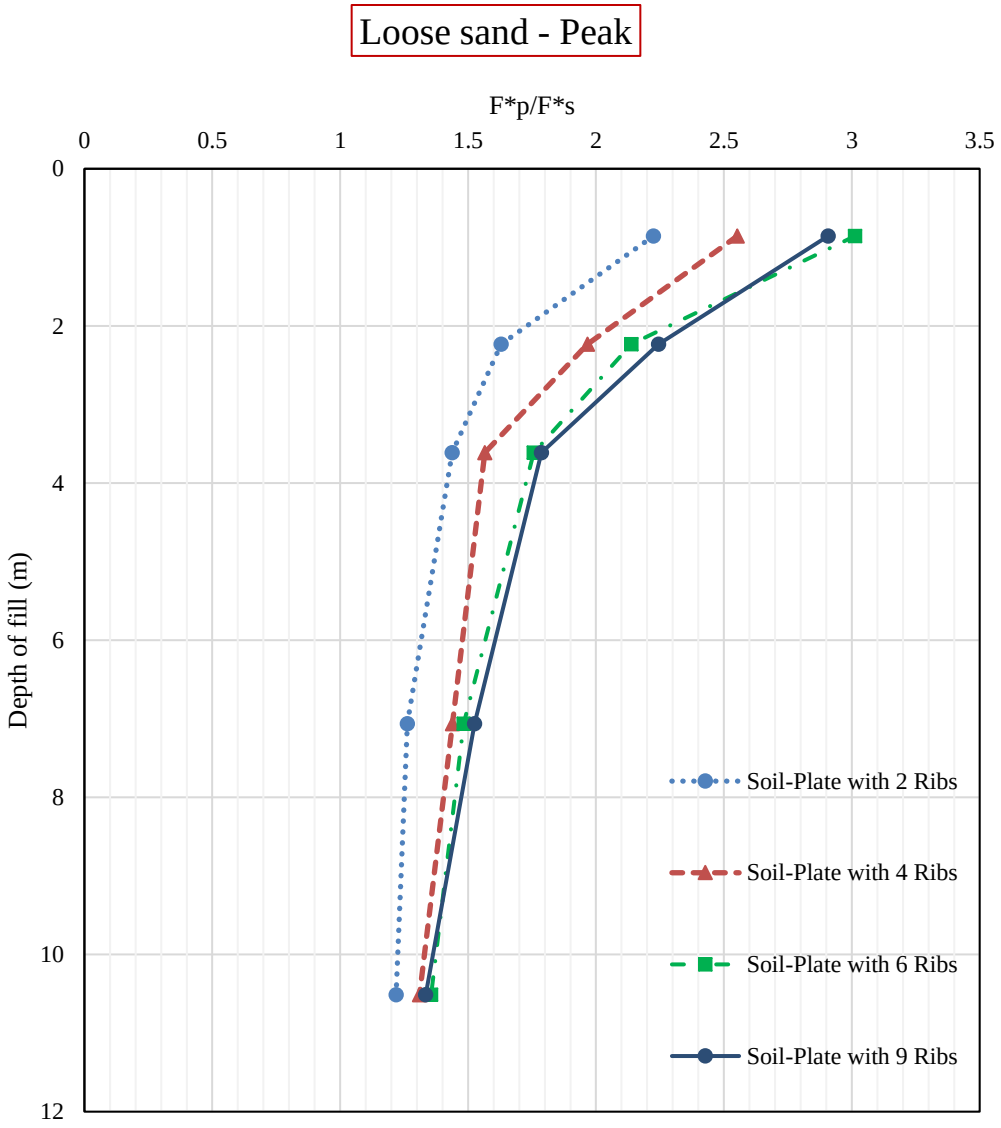

(a)

Figure 6-8. Apparent Friction Coefficient Ratio, IDST, (a) Loose Sand, (b) Dense Sand, (c) Crushed limestone

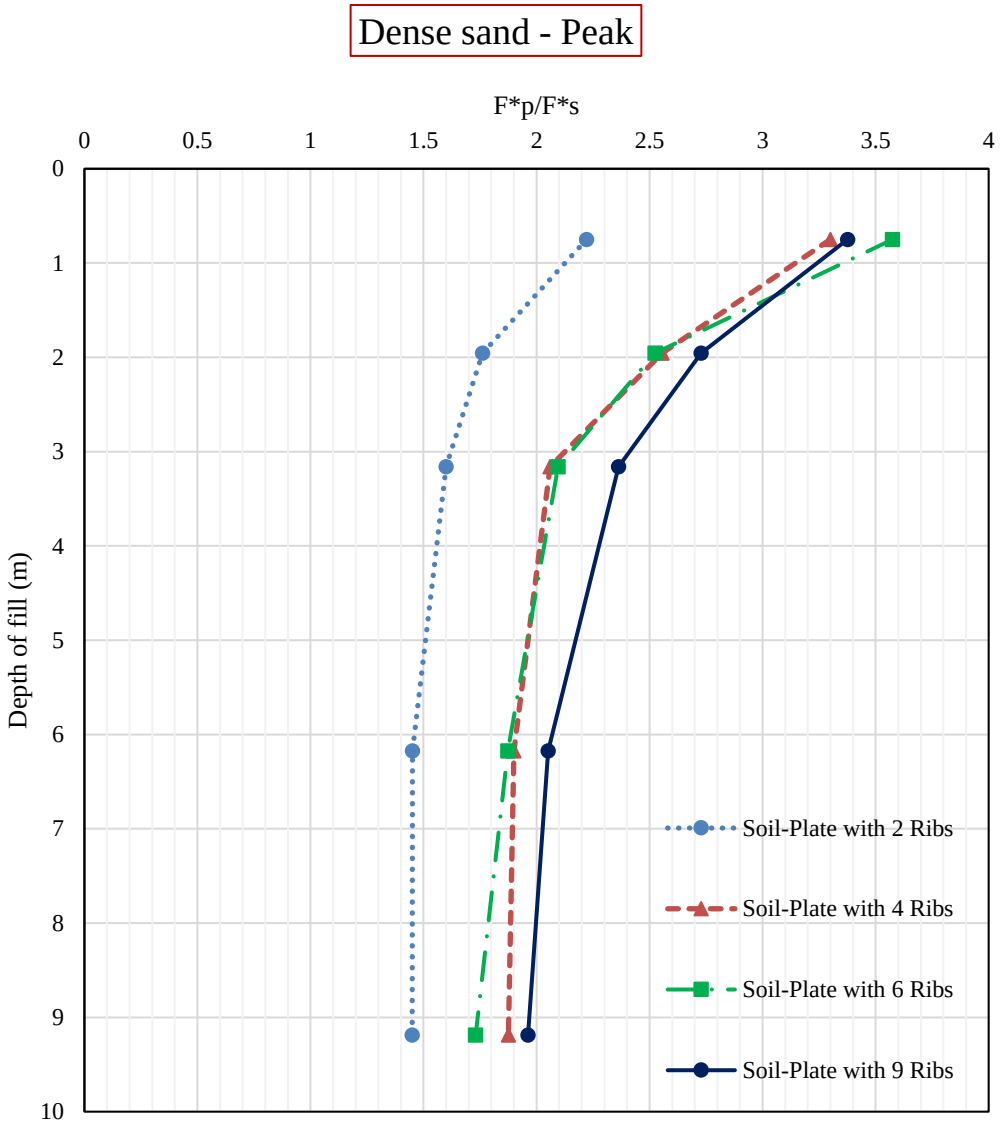

(b)

Figure 6-8. Continued.

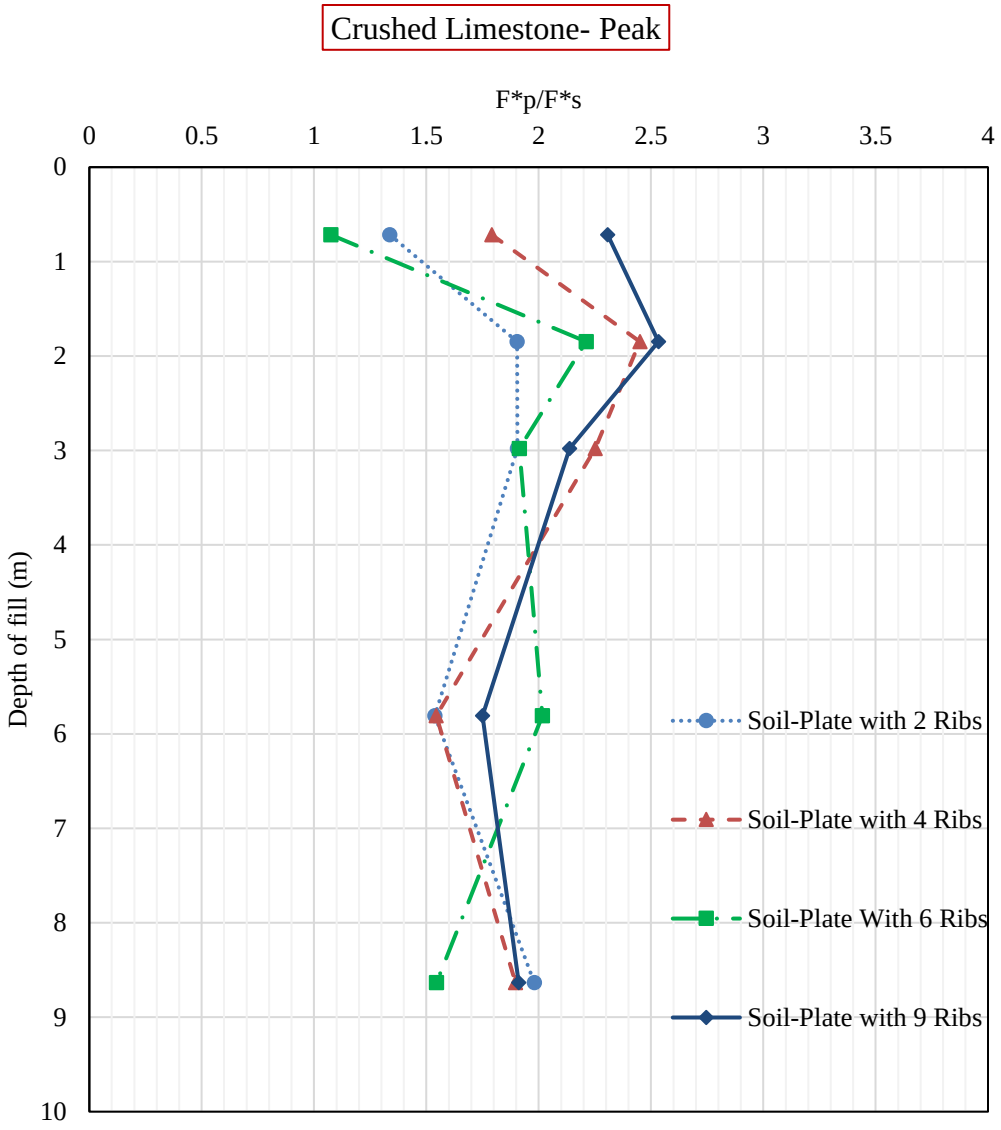

(c)

Figure 6-8. Continued.

The coefficient of the direct sliding parameter (Ci) describes the interface shear strength over the soil/soil shear strength. Figure 6-9 illustrates the Ci coefficient obtained from IDST between smooth/ribbed aluminum plates and loose sand, dense sand, and

crushed limestone with fines. Ci equal to 1 means that the interface shear strength is equal to the shear strength of soil-soil. For both loose and dense sand, with increasing the number of ribs, the Ci factor also increasing. The Ci factor for loose sand shows that the interface shear strength of soil and smooth as well as the 2-rib plate is lower than the shear strength of soil-soil. The interface shear strength of soil and 4-rib plate is very close to soil-soil shear strength, and the interface shear strength of 6-rib and 9-rib plates are similar to each other and greater than soil-soil shear strength. The same behavior is observed for dense sand results. However, the Ci factor is greater for IDST between 9-rib plate and dense sand than the 9-rib plate and loose sand.

Figure 6-9 (c) shows the Ci curve for IDST between CLF and steel reinforcements. The Ci value of smooth plate and CLF is lower than 1. It is worth noting that, independent of the type of the soil, particle size, and density, the Ci value is obtained around 0.5 for the smooth plate and three types of soil. As the soil slides over the smooth plate, the friction angle between the soil and smooth plate is estimated as half of the friction angle of soil-soil obtained from the direct shear test. The increase of the number of the ribs does not have a significant influence on the Ci value of the CLF and ribbed/strip, and the interface shear strength of ribbed plates and CLF is still lower than the shear strength of soil-soil for CLF. This means that the passive resistance of the ribs is not mobilized for large aggregates (particle size greater than rib's size).

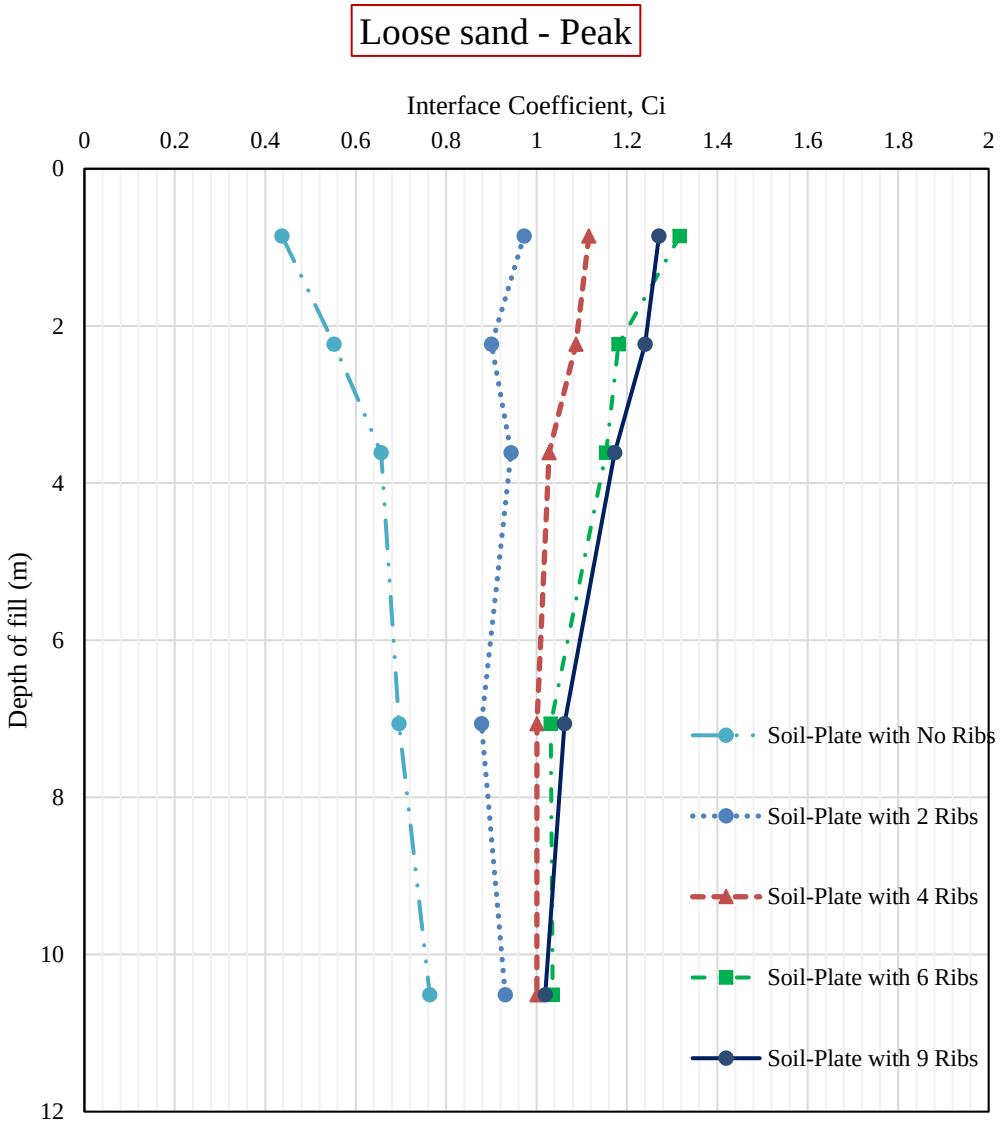

(a)

Figure 6-9. The Coefficient of Direct Sliding, IDST, (a) Loose Sand, (b) Dense Sand, (c) Crushed limestone

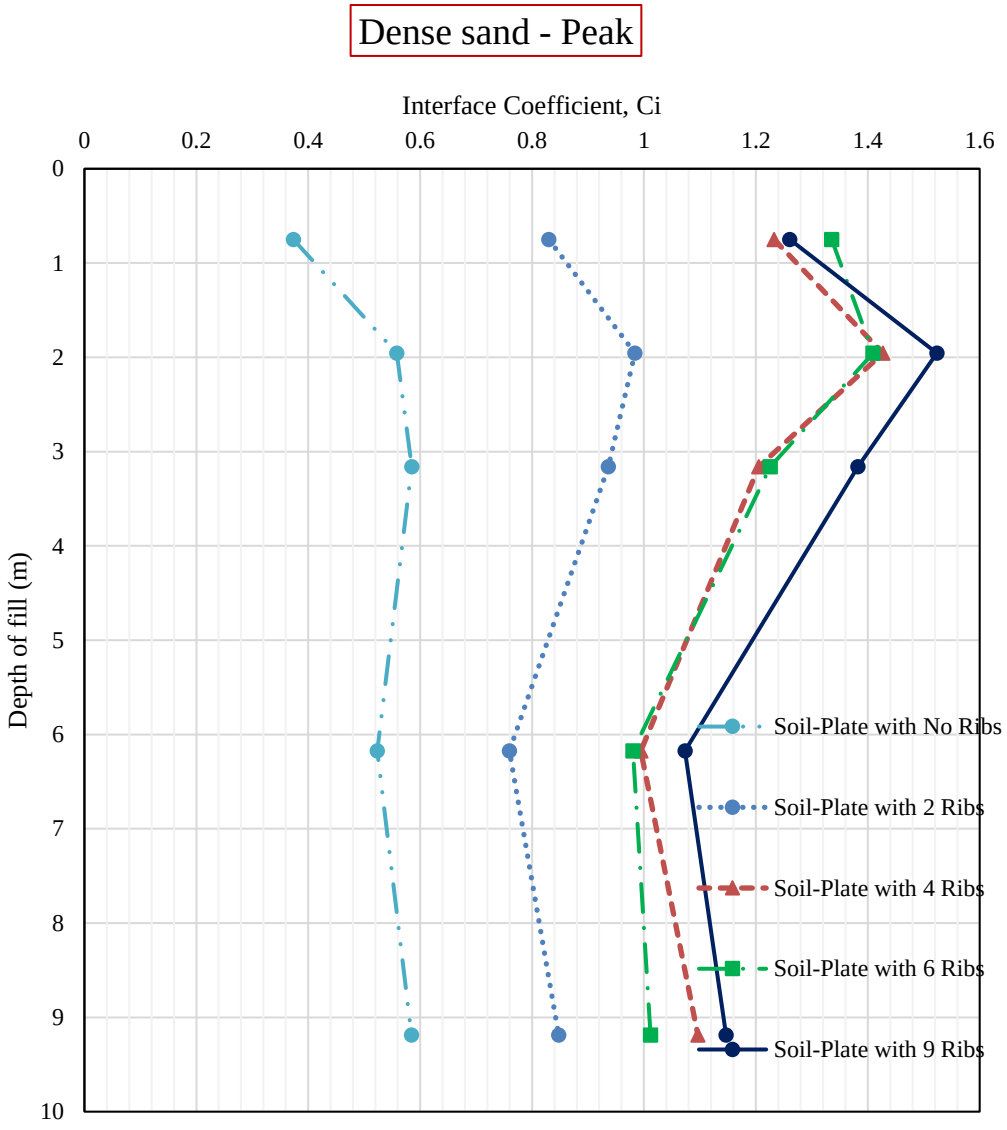

(b)

Figure 6-9. Continued.

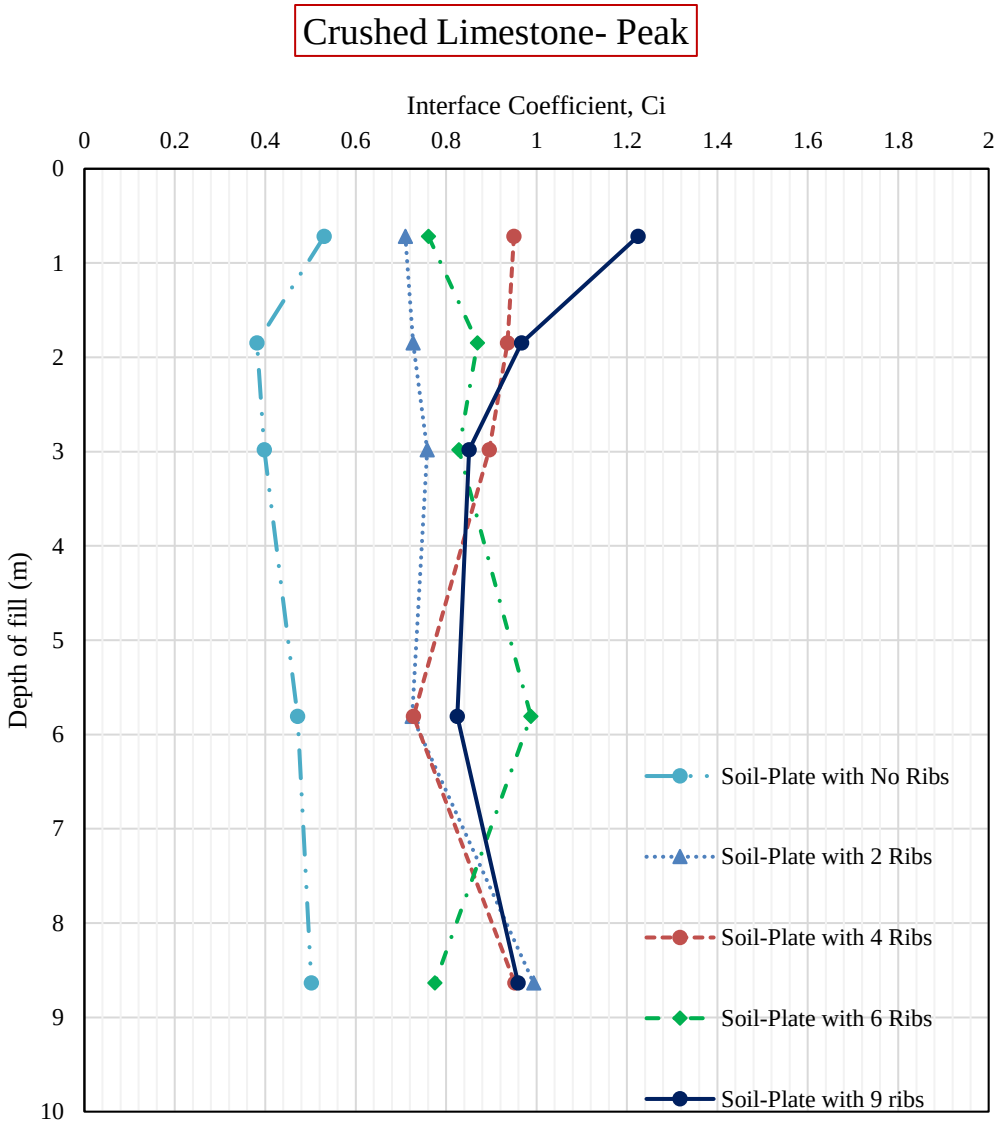

(c)

Figure 6-9. Continued.

Table 6-3. Summary of Results for IDST, Loose Sand

Loose Sand										
Number of ribs per 30.48 cm (1 ft) = 0										
Normal Pressure psf (kPa)	Depth (m)	Normal Pressure (kPa)	Shear Strength, Peak (kPa)	Shear Strength, at 3/4 " (kPa)	Interfaec Shear Stress, Peak (kPa)	Interfaec Shear Stress, at 3/4 "(kPa)	F* (Peak Apparent Friction Coefficient)	F* (Residual Apparent Friction Coefficient)	Ci (Coefficient of Direct Sliding)	Apparent Friction Coefficient Ratio
208.8 psf (10 kPa)	0.70	12.43	10.13	8.97	4.43	4.15	0.36	0.33	0.44	
625 psf (30 kPa)	1.83	32.43	24.81	23.91	13.71	12.29	0.42	0.38	0.55	
1044 psf (50 kPa)	2.97	52.43	40.83	39.11	26.81	19.65	0.51	0.37	0.66	
2088.5 psf (100 kPa)	5.79	102.43	83.43	79.29	58.06	53.74	0.57	0.52	0.70	
3132.8 psf (150 kPa)	8.62	152.43	120.66	117.90	92.16	79.69	0.60	0.52	0.76	
Number of ribs per 30.48 cm (1 ft) = 2 (Ribs Spacing = 101.6 mm)										
Normal Pressure	Depth (m)	Normal Pressure (kPa)	Shear Strength, Peak (kPa)	Shear Strength, at 3/4 " (kPa)	Interfaec Shear Stress, Peak (kPa)	Interfaec Shear Stress, at 3/4 "(kPa)	F* (Peak Apparent Friction Coefficient)	F* (Residual Apparent Friction Coefficient)	Ci (Coefficient of Direct Sliding)	Apparent Friction Coefficient Ratio
208.8 psf (10 kPa)	0.70	12.43	10.13	8.97	9.85	9.37	0.79	0.75	0.97	2.22
625 psf (30 kPa)	1.83	32.43	24.81	23.91	22.33	21.31	0.69	0.66	0.90	1.63
1044 psf (50 kPa)	2.97	52.43	40.83	39.11	38.54	36.41	0.74	0.69	0.94	1.44
2088.5 psf (100 kPa)	5.79	102.43	83.43	79.29	73.27	70.40	0.72	0.69	0.88	1.26
3132.8 psf (150 kPa)	8.62	152.43	120.66	117.90	112.29	107.48	0.74	0.71	0.93	1.22
Number of ribs per 30.48 cm (1 ft) = 4 (Ribs Spacing = 60.96 mm)										
Normal Pressure	Depth (m)	Normal Pressure (kPa)	Shear Strength, Peak (kPa)	Shear Strength, at 3/4 " (kPa)	Interfaec Shear Stress, Peak (kPa)	Interfaec Shear Stress, at 3/4 "(kPa)	F* (Peak Apparent Friction Coefficient)	F* (Residual Apparent Friction Coefficient)	Ci (Coefficient of Direct Sliding)	Apparent Friction Coefficient Ratio
208.8 psf (10 kPa)	0.70	12.43	10.13	8.97	11.31	10.71	0.91	0.86	1.12	2.55
625 psf (30 kPa)	1.83	32.43	24.81	23.91	26.97	26.37	0.83	0.81	1.09	1.97
1044 psf (50 kPa)	2.97	52.43	40.83	39.11	41.96	40.75	0.80	0.78	1.03	1.57
2088.5 psf (100 kPa)	5.79	102.43	83.43	79.29	83.52	81.13	0.82	0.79	1.00	1.44
3132.8 psf (150 kPa)	8.62	152.43	120.66	117.90	120.75	118.84	0.79	0.78	1.00	1.31
Number of ribs per 30.48 cm (1 ft) = 6 (Ribs Spacing = 40.64 mm)										
Normal Pressure	Depth (m)	Normal Pressure (kPa)	Shear Strength, Peak (kPa)	Shear Strength, at 3/4 " (kPa)	Interfaec Shear Stress, Peak (kPa)	Interfaec Shear Stress, at 3/4 "(kPa)	F* (Peak Apparent Friction Coefficient)	F* (Residual Apparent Friction Coefficient)	Ci (Coefficient of Direct Sliding)	Apparent Friction Coefficient Ratio
208.8 psf (10 kPa)	0.70	12.43	10.13	8.97	13.34	12.45	1.07	1.00	1.32	3.01
625 psf (30 kPa)	1.83	32.43	24.81	23.91	29.31	27.52	0.90	0.85	1.18	2.14
1044 psf (50 kPa)	2.97	52.43	40.83	39.11	47.10	45.09	0.90	0.86	1.15	1.76
2088.5 psf (100 kPa)	5.79	102.43	83.43	79.29	86.05	82.58	0.84	0.81	1.03	1.48
3132.8 psf (150 kPa)	8.62	152.43	120.66	117.90	124.93	120.35	0.82	0.79	1.04	1.36
Number of ribs per 30.48 cm (1 ft) = 9 (Ribs Spacing = 25.4 mm)										
Normal Pressure	Depth (m)	Normal Pressure (kPa)	Shear Strength, Peak (kPa)	Shear Strength, at 3/4 " (kPa)	Interfaec Shear Stress, Peak (kPa)	Interfaec Shear Stress, at 3/4 "(kPa)	F* (Peak Apparent Friction Coefficient)	F* (Residual Apparent Friction Coefficient)	Ci (Coefficient of Direct Sliding)	Apparent Friction Coefficient Ratio
208.8 psf (10 kPa)	0.70	12.43	10.13	8.97	12.88	11.57	1.04	0.93	1.27	2.91
625 psf (30 kPa)	1.83	32.43	24.81	23.91	30.77	28.88	0.95	0.89	1.24	2.25
1044 psf (50 kPa)	2.97	52.43	40.83	39.11	47.90	46.05	0.91	0.88	1.17	1.79
2088.5 psf (100 kPa)	5.79	102.43	83.43	79.29	88.59	85.53	0.86	0.84	1.06	1.53
3132.8 psf (150 kPa)	8.62	152.43	120.66	117.90	122.98	121.38	0.81	0.80	1.02	1.33

Table 6-4. Summary of Results for IDST, Dense Sand

Dense Sand										
Number of ribs per 30.48 cm (1 ft) = 0										
Normal Pressure psf (kPa)	Depth (m)	Normal Pressure (kPa)	Shear Strength, Peak (kPa)	Shear Strength, at 3/4 " (kPa)	Interfaec Shear Stress, Peak (kPa)	Interfaec Shear Stress, at 3/4 " (kPa)	F* (Peak Apparent Friction Coefficient)	F* (Residual Apparent Friction Coefficient)	Ci (Coefficient of Direct Sliding)	Apparent Friction Coefficient Ratio
208.8 psf (10 kPa)	0.70	12.43	17.76	13.08	6.63	6.11	0.53	0.49	0.37	
625 psf (30 kPa)	1.83	32.43	32.42	21.74	18.11	18.01	0.56	0.56	0.56	
1044 psf (50 kPa)	2.97	52.43	54.13	40.65	31.67	30.69	0.60	0.59	0.59	
2088.5 psf (100 kPa)	5.79	102.43	120.67	102.60	63.16	62.04	0.62	0.61	0.52	
3132.8 psf (150 kPa)	8.62	152.43	162.99	128.34	95.27	92.98	0.62	0.61	0.58	
Number of ribs per 30.48 cm (1 ft) = 2 (Ribs Spacing = 101.6 mm)										
Normal Pressure	Depth (m)	Normal Pressure (kPa)	Shear Strength, Peak (kPa)	Shear Strength, at 3/4 " (kPa)	Interfaec Shear Stress, Peak (kPa)	Interfaec Shear Stress, at 3/4 " (kPa)	F* (Peak Apparent Friction Coefficient)	F* (Residual Apparent Friction Coefficient)	Ci (Coefficient of Direct Sliding)	Apparent Friction Coefficient Ratio
208.8 psf (10 kPa)	0.70	12.43	17.76	13.08	14.74	12.38	1.19	1.00	0.83	2.22
625 psf (30 kPa)	1.83	32.43	32.42	21.74	31.90	30.70	0.98	0.95	0.98	1.76
1044 psf (50 kPa)	2.97	52.43	54.13	40.65	50.68	48.75	0.97	0.93	0.94	1.60
2088.5 psf (100 kPa)	5.79	102.43	120.67	102.60	91.66	90.25	0.89	0.88	0.76	1.45
3132.8 psf (150 kPa)	8.62	152.43	162.99	128.34	138.14	134.79	0.91	0.88	0.85	1.45
Number of ribs per 30.48 cm (1 ft) = 4 (Ribs Spacing = 60.96 mm)										
Normal Pressure	Depth (m)	Normal Pressure (kPa)	Shear Strength, Peak (kPa)	Shear Strength, at 3/4 " (kPa)	Interfaec Shear Stress, Peak (kPa)	Interfaec Shear Stress, at 3/4 " (kPa)	F* (Peak Apparent Friction Coefficient)	F* (Residual Apparent Friction Coefficient)	Ci (Coefficient of Direct Sliding)	Apparent Friction Coefficient Ratio
208.8 psf (10 kPa)	0.70	12.43	17.76	13.08	21.89	15.26	1.76	1.23	1.23	3.30
625 psf (30 kPa)	1.83	32.43	32.42	21.74	46.27	33.20	1.43	1.02	1.43	2.55
1044 psf (50 kPa)	2.97	52.43	54.13	40.65	65.24	51.43	1.24	0.98	1.21	2.06
2088.5 psf (100 kPa)	5.79	102.43	120.67	102.60	120.00	97.17	1.17	0.95	0.99	1.90
3132.8 psf (150 kPa)	8.62	152.43	162.99	128.34	178.68	146.37	1.17	0.96	1.10	1.88
Number of ribs per 30.48 cm (1 ft) = 6 (Ribs Spacing = 40.64 mm)										
Normal Pressure	Depth (m)	Normal Pressure (kPa)	Shear Strength, Peak (kPa)	Shear Strength, at 3/4 " (kPa)	Interfaec Shear Stress, Peak (kPa)	Interfaec Shear Stress, at 3/4 " (kPa)	F* (Peak Apparent Friction Coefficient)	F* (Residual Apparent Friction Coefficient)	Ci (Coefficient of Direct Sliding)	Apparent Friction Coefficient Ratio
208.8 psf (10 kPa)	0.70	12.43	17.76	13.08	23.72	15.11	1.91	1.22	1.34	3.58
625 psf (30 kPa)	1.83	32.43	32.42	21.74	45.70	33.95	1.41	1.05	1.41	2.52
1044 psf (50 kPa)	2.97	52.43	54.13	40.65	66.35	49.97	1.27	0.95	1.23	2.10
2088.5 psf (100 kPa)	5.79	102.43	120.67	102.60	118.31	96.24	1.15	0.94	0.98	1.87
3132.8 psf (150 kPa)	8.62	152.43	162.99	128.34	164.88	141.28	1.08	0.93	1.01	1.73
Number of ribs per 30.48 cm (1 ft) = 9 (Ribs Spacing = 25.4 mm)										
Normal Pressure	Depth (m)	Normal Pressure (kPa)	Shear Strength, Peak (kPa)	Shear Strength, at 3/4 " (kPa)	Interfaec Shear Stress, Peak (kPa)	Interfaec Shear Stress, at 3/4 " (kPa)	F* (Peak Apparent Friction Coefficient)	F* (Residual Apparent Friction Coefficient)	Ci (Coefficient of Direct Sliding)	Apparent Friction Coefficient Ratio
208.8 psf (10 kPa)	0.70	12.43	17.76	13.08	22.40	14.71	1.80	1.18	1.26	3.38
625 psf (30 kPa)	1.83	32.43	32.42	21.74	49.39	34.06	1.52	1.05	1.52	2.73
1044 psf (50 kPa)	2.97	52.43	54.13	40.65	74.81	52.69	1.43	1.00	1.38	2.36
2088.5 psf (100 kPa)	5.79	102.43	120.67	102.60	129.52	98.00	1.26	0.96	1.07	2.05
3132.8 psf (150 kPa)	8.62	152.43	162.99	128.34	186.95	144.21	1.23	0.95	1.15	1.96

Table 6-5. Summary of Results for IDST, Crushed Limestone with Fines

Crushed Limestone										
Number of ribs per 30.48 cm (1 ft) = 0										
Normal Pressure psf (kPa)	Depth (m)	Normal Pressure (kPa)	Shear Strength, Peak (kPa)	Shear Strength, at 3/4 " (kPa)	Interfaec Shear Stress, Peak (kPa)	Interfaec Shear Stress, at 3/4 "(kPa)	F* (Peak Apparent Friction Coefficient)	F* (Residual Apparent Friction Coefficient)	Ci (Coefficient of Direct Sliding)	Apparent Friction Coefficient Ratio
208.8 psf (10 kPa)	0.72	12.67	25.59	23.34	13.58	10.41	1.07	0.82	0.53	
625 psf (30 kPa)	1.85	32.67	64.32	61.18	24.56	18.45	0.75	0.56	0.38	
1044 psf (50 kPa)	2.98	52.67	108.01	95.62	42.99	37.74	0.82	0.72	0.40	
2088.5 psf (100 kPa)	5.81	102.67	175.73	165.50	82.82	67.43	0.81	0.66	0.47	
3132.8 psf (150 kPa)	8.64	152.67	240.06	222.05	120.43	103.11	0.79	0.68	0.50	
Number of ribs per 30.48 cm (1 ft) = 2 (Ribs Spacing = 101.6 mm)										
Normal Pressure	Depth (m)	Normal Pressure (kPa)	Shear Strength, Peak (kPa)	Shear Strength, at 3/4 " (kPa)	Interfaec Shear Stress, Peak (kPa)	Interfaec Shear Stress, at 3/4 "(kPa)	F* (Peak Apparent Friction Coefficient)	F* (Residual Apparent Friction Coefficient)	Ci (Coefficient of Direct Sliding)	Apparent Friction Coefficient Ratio
208.8 psf (10 kPa)	0.72	12.67	25.59	23.34	18.17	14.10	1.43	1.11	0.71	1.34
625 psf (30 kPa)	1.85	32.67	64.32	61.18	46.77	45.18	1.43	1.38	0.73	1.90
1044 psf (50 kPa)	2.98	52.67	108.01	95.62	81.90	65.04	1.56	1.23	0.76	1.91
2088.5 psf (100 kPa)	5.81	102.67	175.73	165.50	127.40	116.34	1.24	1.13	0.73	1.54
3132.8 psf (150 kPa)	8.64	152.67	240.06	222.05	238.51	174.04	1.56	1.14	0.99	1.98
Number of ribs per 30.48 cm (1 ft) = 4 (Ribs Spacing = 60.96 mm)										
Normal Pressure	Depth (m)	Normal Pressure (kPa)	Shear Strength, Peak (kPa)	Shear Strength, at 3/4 " (kPa)	Interfaec Shear Stress, Peak (kPa)	Interfaec Shear Stress, at 3/4 "(kPa)	F* (Peak Apparent Friction Coefficient)	F* (Residual Apparent Friction Coefficient)	Ci (Coefficient of Direct Sliding)	Apparent Friction Coefficient Ratio
208.8 psf (10 kPa)	0.72	12.67	25.59	23.34	24.32	19.27	1.92	1.52	0.95	1.79
625 psf (30 kPa)	1.85	32.67	64.32	61.18	60.17	47.72	1.84	1.46	0.94	2.45
1044 psf (50 kPa)	2.98	52.67	108.01	95.62	96.76	76.63	1.84	1.45	0.90	2.25
2088.5 psf (100 kPa)	5.81	102.67	175.73	165.50	127.91	124.17	1.25	1.21	0.73	1.54
3132.8 psf (150 kPa)	8.64	152.67	240.06	222.05	228.49	226.61	1.50	1.48	0.95	1.90
Number of ribs per 30.48 cm (1 ft) = 6 (Ribs Spacing = 40.64 mm)										
Normal Pressure	Depth (m)	Normal Pressure (kPa)	Shear Strength, Peak (kPa)	Shear Strength, at 3/4 " (kPa)	Interfaec Shear Stress, Peak (kPa)	Interfaec Shear Stress, at 3/4 "(kPa)	F* (Peak Apparent Friction Coefficient)	F* (Residual Apparent Friction Coefficient)	Ci (Coefficient of Direct Sliding)	Apparent Friction Coefficient Ratio
208.8 psf (10 kPa)	0.72	12.67	25.59	23.34	19.48	14.60	1.54	1.15	0.76	1.43
625 psf (30 kPa)	1.85	32.67	64.32	61.18	55.92	54.30	1.71	1.66	0.87	2.28
1044 psf (50 kPa)	2.98	52.67	108.01	95.62	89.44	82.30	1.70	1.56	0.83	2.08
2088.5 psf (100 kPa)	5.81	102.67	175.73	165.50	173.55	167.07	1.69	1.63	0.99	2.10
3132.8 psf (150 kPa)	8.64	152.67	240.06	222.05	186.08	186.08	1.22	1.22	0.78	1.55
Number of ribs per 30.48 cm (1 ft) = 9 (Ribs Spacing = 25.4 mm)										
Normal Pressure	Depth (m)	Normal Pressure (kPa)	Shear Strength, Peak (kPa)	Shear Strength, at 3/4 " (kPa)	Interfaec Shear Stress, Peak (kPa)	Interfaec Shear Stress, at 3/4 "(kPa)	F* (Peak Apparent Friction Coefficient)	F* (Residual Apparent Friction Coefficient)	Ci (Coefficient of Direct Sliding)	Apparent Friction Coefficient Ratio
208.8 psf (10 kPa)	0.72	12.67	25.59	23.34	31.34	17.46	2.47	1.38	1.22	2.31
625 psf (30 kPa)	1.85	32.67	64.32	61.18	62.21	45.17	1.90	1.38	0.97	2.53
1044 psf (50 kPa)	2.98	52.67	108.01	95.62	91.89	75.61	1.74	1.44	0.85	2.14
2088.5 psf (100 kPa)	5.81	102.67	175.73	165.50	144.94	129.04	1.41	1.26	0.82	1.75
3132.8 psf (150 kPa)	8.64	152.67	240.06	222.05	230.21	208.75	1.51	1.37	0.96	1.91

Table 6-6. Summary of Results for Pullout Test in Half Box, Dense Sand

Number of ribs per side per 30.48 cm (1 ft) = 0										
Normal Pressure psf (kPa)	Depth (m)	Normal Pressure (kPa)	Pullout Force, Peak (kN)	Pullout Force, at 3/4 "(kN)	Displacement at Peak Force, mm	Max- Pullout Force (kN) / Displacement at Peak Force (mm)	F* (Peak Apparent Friction Coefficient)	F* (Residual Apparent Friction Coefficient)	Ci (Coefficient of Direct Sliding)	Apparent Friction Coefficient Ratio
125 psf (6 kPa)	0.30	6.00	0.58	0.24	7.328	0.08	3.14	1.28	3.64	
125 psf (6 kPa)	0.30	6.00	0.55	0.33	3.52	0.16	2.98	1.78	3.35	
125 psf (6 kPa)	0.30	6.00	0.60	0.30	6.06	0.10	3.23	1.61	3.53	
625 psf (30 kPa)	1.50	30.00	1.21	0.75	4.36	0.28	1.30	0.81	2.70	
1250 psf (60 kPa)	3.00	60.00	2.02	1.50	6.72	0.30	1.09	0.81	2.32	
1875 psf (89.8 kPa)	4.50	89.80	2.56	2.00	4.28	0.60	0.92	0.72	2.05	
2500 psf (119.7 kPa)	6.00	119.70	2.93	2.26	6.64	0.44	0.79	0.61	1.84	
Number of ribs per side per 30.48 cm (1 ft) = 2 (Ribs Spacing = 101.6 mm)										
Normal Pressure	Depth (m)	Normal Pressure (kPa)	Pullout Force, Peak (kN)	Pullout Force, at 3/4 "(kN)	Displacement at Peak Force (Front), mm	Max- Pullout Force (kN) / Displacement at Peak Force (mm)	F* (Peak Apparent Friction Coefficient)	F* (Residual Apparent Friction Coefficient)	Ci (Coefficient of Direct Sliding)	Apparent Friction Coefficient Ratio
125 psf (6 kPa)	0.30	6.00	1.55	1.30	8.86	0.17	8.35	7.02	3.77	2.66
125 psf (6 kPa)	0.30	6.00	1.46	1.20	4.22	0.35	7.87	6.46	3.76	2.64
125 psf (6 kPa)	0.30	6.00	1.52	1.17	7.11	0.21	8.15	6.30	3.70	2.53
625 psf (30 kPa)	1.50	30.00	4.66	3.95	4.94	0.94	5.01	4.25	3.03	3.86
1250 psf (60 kPa)	3.00	60.00	6.23	3.97	6.26	0.99	3.35	2.13	2.42	3.08
1875 psf (89.8 kPa)	4.50	89.80	8.37	5.28	6.18	1.35	3.01	1.90	2.12	3.26
2500 psf (119.7 kPa)	6.00	119.70	9.68	6.85	7.34	1.32	2.61	1.85	1.86	3.31
Number of ribs per side per 30.48 cm (1 ft) = 4 (Ribs Spacing = 60.96 mm)										
Normal Pressure	Depth (m)	Normal Pressure (kPa)	Pullout Force, Peak (kN)	Pullout Force, at 3/4 "(kN)	Displacement at Peak Force (Front), mm	Max- Pullout Force (kN) / Displacement at Peak Force (mm)	F* (Peak Apparent Friction Coefficient)	F* (Residual Apparent Friction Coefficient)	Ci (Coefficient of Direct Sliding)	Apparent Friction Coefficient Ratio
125 psf (6 kPa)	0.30	6.00	1.57	0.95	4.00	0.39	8.44	5.10	4.01	2.69
125 psf (6 kPa)	0.30	6.00	1.61	1.05	2.69	0.60	8.64	5.66	4.45	2.90
125 psf (6 kPa)	0.30	6.00	1.68	0.67	3.37	0.50	9.02	3.58	4.10	2.80
625 psf (30 kPa)	1.50	30.00	4.45	2.42	4.99	0.89	4.79	2.61	3.15	3.69
1250 psf (60 kPa)	3.00	60.00	7.10	4.10	5.59	1.27	3.82	2.21	2.66	3.51
1875 psf (89.8 kPa)	4.50	89.80	8.02	4.84	6.50	1.23	2.88	1.74	2.38	3.13
2500 psf (119.7 kPa)	6.00	119.70	9.72	5.23	6.78	1.43	2.62	1.41	2.09	3.32
Number of ribs per side per 30.48 cm (1 ft) = 9 (Ribs Spacing = 25.4 mm)										
Normal Pressure	Depth (m)	Normal Pressure (kPa)	Pullout Force, Peak (kN)	Pullout Force, at 3/4 "(kN)	Displacement at Peak Force (Front), mm	Max- Pullout Force (kN) / Displacement at Peak Force (mm)	F* (Peak Apparent Friction Coefficient)	F* (Residual Apparent Friction Coefficient)	Ci (Coefficient of Direct Sliding)	Apparent Friction Coefficient Ratio
125 psf (6 kPa)	0.30	6.00	1.64	0.55	2.35	0.70	8.80	2.96	4.72	2.81
125 psf (6 kPa)	0.30	6.00	1.62	0.66	2.54	0.64	8.72	3.56	4.93	2.92
125 psf (6 kPa)	0.30	6.00	1.71	0.84	1.75	0.98	9.21	4.53	5.22	2.85
625 psf (30 kPa)	1.50	30.00	5.78	2.75	2.81	2.06	6.22	2.96	3.69	4.79
1250 psf (60 kPa)	3.00	60.00	9.84	5.73	3.98	2.48	5.30	3.08	2.83	4.87
1875 psf (89.8 kPa)	4.50	89.80	12.72	7.18	3.75	3.40	4.58	2.58	2.53	4.96
2500 psf (119.7 kPa)	6.00	119.70	13.00	7.47	4.55	2.86	3.51	2.01	2.33	4.44

Table 6-7. Summary of Results for Pullout Test in Full Box, Dense Sand

Number of ribs per side per 30.48 cm (1 ft) = 0										
Normal Pressure psf (kPa)	Depth (m)	Normal Pressure (kPa)	Pullout Force, Peak (kN)	Pullout Force, at 3/4 " (kN)	Displacement at Peak Force, mm	Max- Pullout Force (kN) / Displacement at Peak Force (mm)	F* (Peak Apparent Friction Coefficient)	F* (Residual Apparent Friction Coefficient)	Ci (Coefficient of Direct Sliding)	Apparent Friction Coefficient Ratio
125 psf (6 kPa)	0.30	6.00	2.17	1.83	2.51	0.86	3.34	2.81	3.64	
125 psf (6 kPa)	0.30	6.00	2.00	1.69	2.34	0.86	3.07	2.60	3.35	
125 psf (6 kPa)	0.30	6.00	2.10	1.71	1.51	1.39	3.23	2.62	3.53	
625 psf (30 kPa)	1.50	30.00	8.06	7.50	3.77	2.14	2.48	2.31	2.70	
1250 psf (60 kPa)	3.00	60.00	13.81	13.00	7.52	1.84	2.12	2.00	2.32	
1875 psf (89.8 kPa)	4.50	89.80	18.33	17.49	4.81	3.81	1.88	1.80	2.05	
2500 psf (119.7 kPa)	6.00	119.70	21.97	21.08	7.00	3.14	1.69	1.62	1.84	
Number of ribs per side per 30.48 cm (1 ft) = 2 (Ribs Spacing = 259.6 mm)										
Normal Pressure	Depth (m)	Normal Pressure (kPa)	Pullout Force, Peak (kN)	Pullout Force, at 3/4 " (kN)	Displacement at Peak Force (Front), mm	Max- Pullout Force (kN) / Displacement at Peak Force (mm)	F* (Peak Apparent Friction Coefficient)	F* (Residual Apparent Friction Coefficient)	Ci (Coefficient of Direct Sliding)	Apparent Friction Coefficient Ratio
125 psf (6 kPa)	0.30	6.00	2.25	1.90	2.60	0.86	3.46	2.92	3.77	1.04
125 psf (6 kPa)	0.30	6.00	2.24	1.94	3.06	0.73	3.45	2.99	3.76	1.12
125 psf (6 kPa)	0.30	6.00	2.21	1.78	2.88	0.77	3.40	2.74	3.70	1.05
625 psf (30 kPa)	1.50	30.00	9.04	8.06	4.91	1.84	2.78	2.48	3.03	1.12
1250 psf (60 kPa)	3.00	60.00	14.43	13.45	6.45	2.24	2.22	2.07	2.42	1.04
1875 psf (89.8 kPa)	4.50	89.80	18.96	17.61	7.10	2.67	1.95	1.81	2.12	1.03
2500 psf (119.7 kPa)	6.00	119.70	22.24	20.90	9.32	2.39	1.71	1.61	1.86	1.01
Number of ribs per side per 30.48 cm (1 ft) = 4 (Ribs Spacing = 129.8 mm)										
Normal Pressure	Depth (m)	Normal Pressure (kPa)	Pullout Force, Peak (kN)	Pullout Force, at 3/4 " (kN)	Displacement at Peak Force (Front), mm	Max- Pullout Force (kN) / Displacement at Peak Force (mm)	F* (Peak Apparent Friction Coefficient)	F* (Residual Apparent Friction Coefficient)	Ci (Coefficient of Direct Sliding)	Apparent Friction Coefficient Ratio
125 psf (6 kPa)	0.30	6.00	2.44	2.00	2.06	1.19	3.75	3.07	4.01	1.12
125 psf (6 kPa)	0.30	6.00	2.65	2.21	2.35	1.13	4.07	3.40	4.45	1.33
125 psf (6 kPa)	0.30	6.00	2.39	2.06	2.35	1.02	3.67	3.17	4.10	1.14
625 psf (30 kPa)	1.50	30.00	9.40	8.55	4.36	2.16	2.89	2.63	3.15	1.17
1250 psf (60 kPa)	3.00	60.00	15.84	15.02	6.06	2.61	2.44	2.31	2.66	1.15
1875 psf (89.8 kPa)	4.50	89.80	21.26	20.75	6.69	3.18	2.18	2.13	2.38	1.16
2500 psf (119.7 kPa)	6.00	119.70	24.88	24.29	10.57	2.35	1.92	1.87	2.09	1.13
Number of ribs per side per 30.48 cm (1 ft) = 8 (Ribs Spacing = 9.9 mm, 104.9 mm)										
Normal Pressure	Depth (m)	Normal Pressure (kPa)	Pullout Force, Peak (kN)	Pullout Force, at 3/4 " (kN)	Displacement at Peak Force (Front), mm	Max- Pullout Force (kN) / Displacement at Peak Force (mm)	F* (Peak Apparent Friction Coefficient)	F* (Residual Apparent Friction Coefficient)	Ci (Coefficient of Direct Sliding)	Apparent Friction Coefficient Ratio
125 psf (6 kPa)	0.30	6.00	2.82	2.30	2.51	1.12	4.33	3.53	4.72	1.30
125 psf (6 kPa)	0.30	6.00	2.94	2.40	2.03	1.45	4.52	3.68	4.93	1.47
125 psf (6 kPa)	0.30	6.00	3.11	2.50	3.16	0.98	4.79	3.84	5.22	1.48
625 psf (30 kPa)	1.50	30.00	10.50	9.43	4.25	2.47	3.23	2.90	3.69	1.30
1250 psf (60 kPa)	3.00	60.00	16.90	16.60	15.24	1.11	2.60	2.55	2.83	1.22
1875 psf (89.8 kPa)	4.50	89.80	22.64	22.16	14.74	1.54	2.33	2.28	2.53	1.24
2500 psf (119.7 kPa)	6.00	119.70	27.80	27.05	15.62	1.78	2.14	2.08	2.33	1.27

6.3 Comparison of Interface DST and Pullout Test Results

During the pullout test, as the steel strip reinforcement is pulled out, the zone of soil around the strip starts to dilate (Figure 6-10). As shown in Figure 6-10, the numerical simulation of the pullout test on ribbed steel strip illustrates that as the normal stresses increasing from 6 kPa to 120 kPa, the displacement in the z-direction decreases. Also, the numerical simulation results on a various number of ribs illustrate that with increasing the

number of ribs, the amount of dilation increases slightly. The soil around the strip reinforcement resist to dilate and creates the normal stress due to the resist of the volume change enhances. As the applied confining pressure increases, the normal force around the reinforcement which resist the soil movement due to the pulling out the strip increases. The distribution of normal stresses on the width of the smooth steel strip was measured from the numerical simulation of the pullout test of smooth steel strip in full box. As shown in Figure 6-11, the normal stresses are greater at the edges of reinforcement which shows the restrained soil dilatancy effect due to the 3-dimensional interaction of pullout test. The increase in normal stress and shear stress because of restrained soil dilatancy is also observed for pulling out the rod (plumelle, 1988) and geogrid (Hayashi et. al., 1999). On the other hand, in interface direct shear test the width of the reinforcement is equal to the width of the soil on top of it. Therefore, the 3-dimensional effect of embedded strip inside the soil and the restrained soil dilatancy is missing. Thus, the normal stress distribution and the shear stress on the edges of the reinforcement is not the same as the pullout test.

As mentioned before, the dilation of the dense sand decreases with increasing the normal stresses which explain the behavior of F* value versus depth of soil graph, where the pullout resistance is higher at low normal stresses than at higher normal stresses. The dilation of soil particles is higher in low normal stresses and is minimized under high normal stresses. This fact was considered in simulating the pullout test. To fit the pullout force curves under various normal stresses obtained from numerical simulation with

experimental results, the dilation angle of soil is given higher for low normal stresses (Table 5-3).

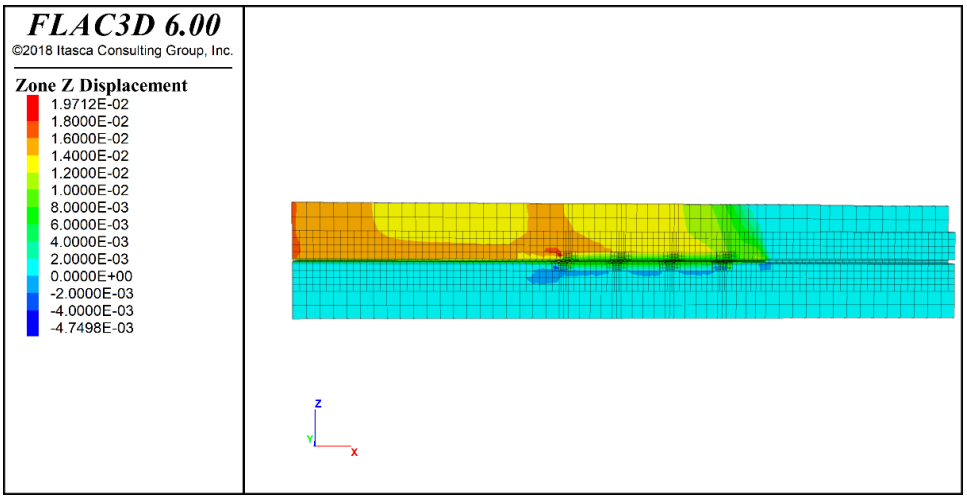

(a)

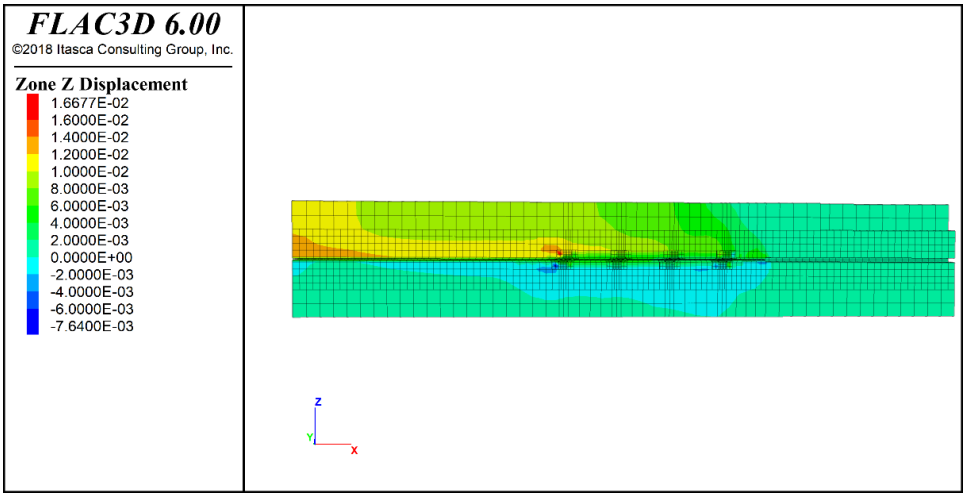

(b)

Figure 6-10. Displacement in Z-direction along the section of pullout test on RECO steel Strip Reinforcement embedded in Dense Sand, (a) 6 kPa Normal Stresses, (b) 120 kPa Normal Stresses

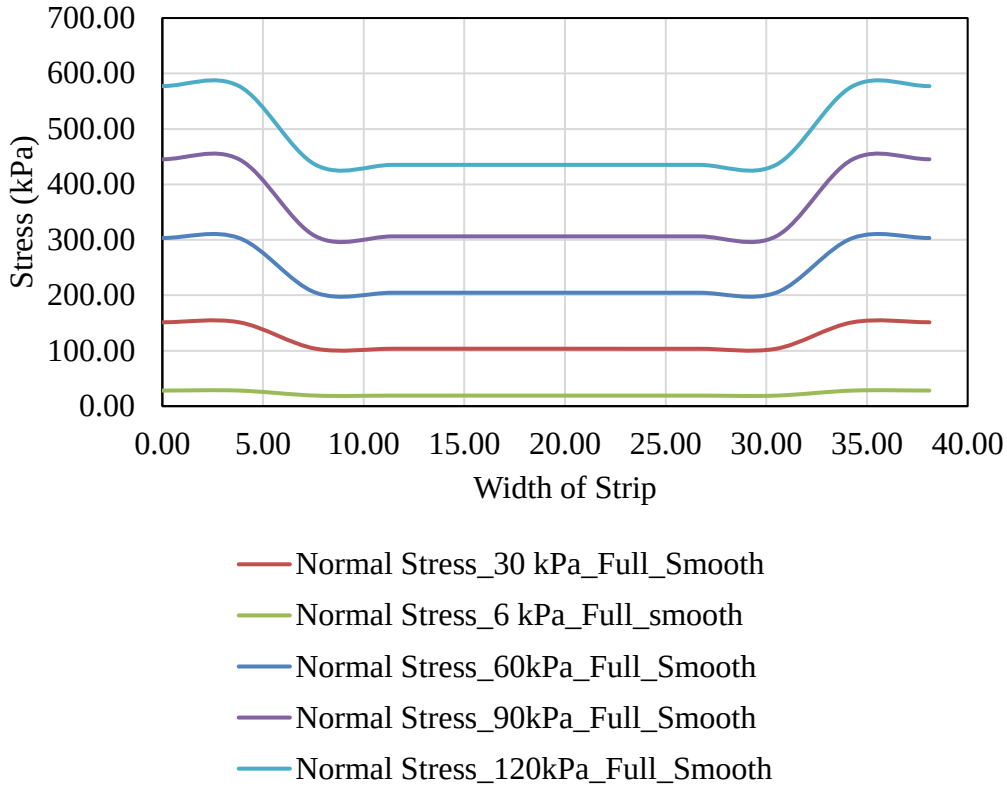

Figure 6-11. Distribution of Normal Forces on Width of the Smooth Steel Strip Reinforcement in Full Box on the Pullout side

Figure 6-12 shows the coefficient of direct sliding (Ci) versus depth of the embedment for IDST on smooth and ribbed plates and pullout test in the half box on the steel strip reinforcements with the same length and same ribs spacing. The test results indicate that at low normal stresses the effect of soil dilation of pullout test enhances the interface shear strength. As the normal stresses increases, the influence of the soil dilatancy eliminated and the pullout test results tend to interface direct shear test results.

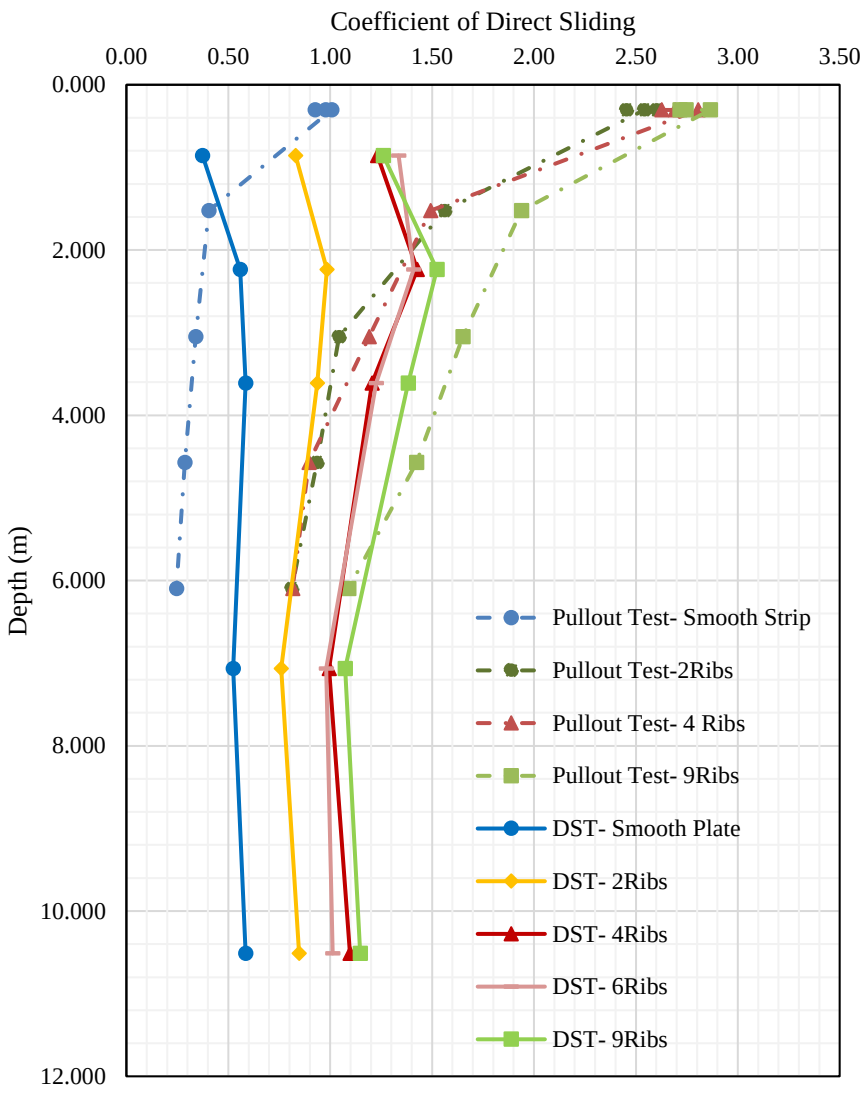

Figure 6-12. Comparison of Ci Value for IDST and Pullout Test on Same ribs spacing

6.4 Effect of Testing Parameters on Interface Response

6.4.1 Reinforcement Type

The shear stress versus shear displacement curves obtained from the direst shear tests on dense sand-dense sand, dense sand-smooth steel plate, dense sand-Geogrid are presented in Figure 6-13. The peak shear strength of sand, sand-geogrid interface, and sand-smooth plate interface are defined clearly which shows that sand-smooth plate peak shear strength occurs at smallest shear displacement, and sand shear strength reaches largest shear displacement. The greatest peak shear stress is observed for the sand-geogrid interface, and the lowest shear strength belongs to sand-smooth plate interface. The shear characteristic of sand-smooth plate interface shows linearly elastic-perfectly plastic behavior while soil internal and sand-geogrid interface indicates the strain softening behavior after reaching the peak value. Comparing the post-peak characteristic of dense sand internal and sand-geogrid interface, the shear stress at a critical state of soil is higher than the sand-geogrid interface. With increasing the normal stresses, the difference between the critical state shear stress of dense sand and sand-geogrid interface increases. Figure 6-14 illustrates the Mohr-Coulomb envelope of peak shear strength of dense sand-dense sand, dense sand-smooth steel plate, dense sand-Geogrid. The failure envelope of the soil ($\varphi° = 43$) stands between the dense sand-smooth steel interface ($\varphi° = 32$) and dense sand-Geogrid interface ($\varphi° = 44.5$). However, at large displacement, the friction angle of the soil is higher than sand-smooth steel interface and dense sand-Geogrid

interface. For large shear displacements, at low normal stresses, the shear stress of dense sand-Geogrid interface approaches to the shear strength of sand.

The observations suggest that the shear resistance of the sand particle across the openings of the geogrid, the shear resistance between the longitudinal and transversal ribs and sand, and the passive resistance of transverse rib contributed to the total direct shear strength at small displacements. On the other hand, the shear resistance of ribs and soil particles contribute mainly at the overall shear resistance of geogrid/DS at large displacement.

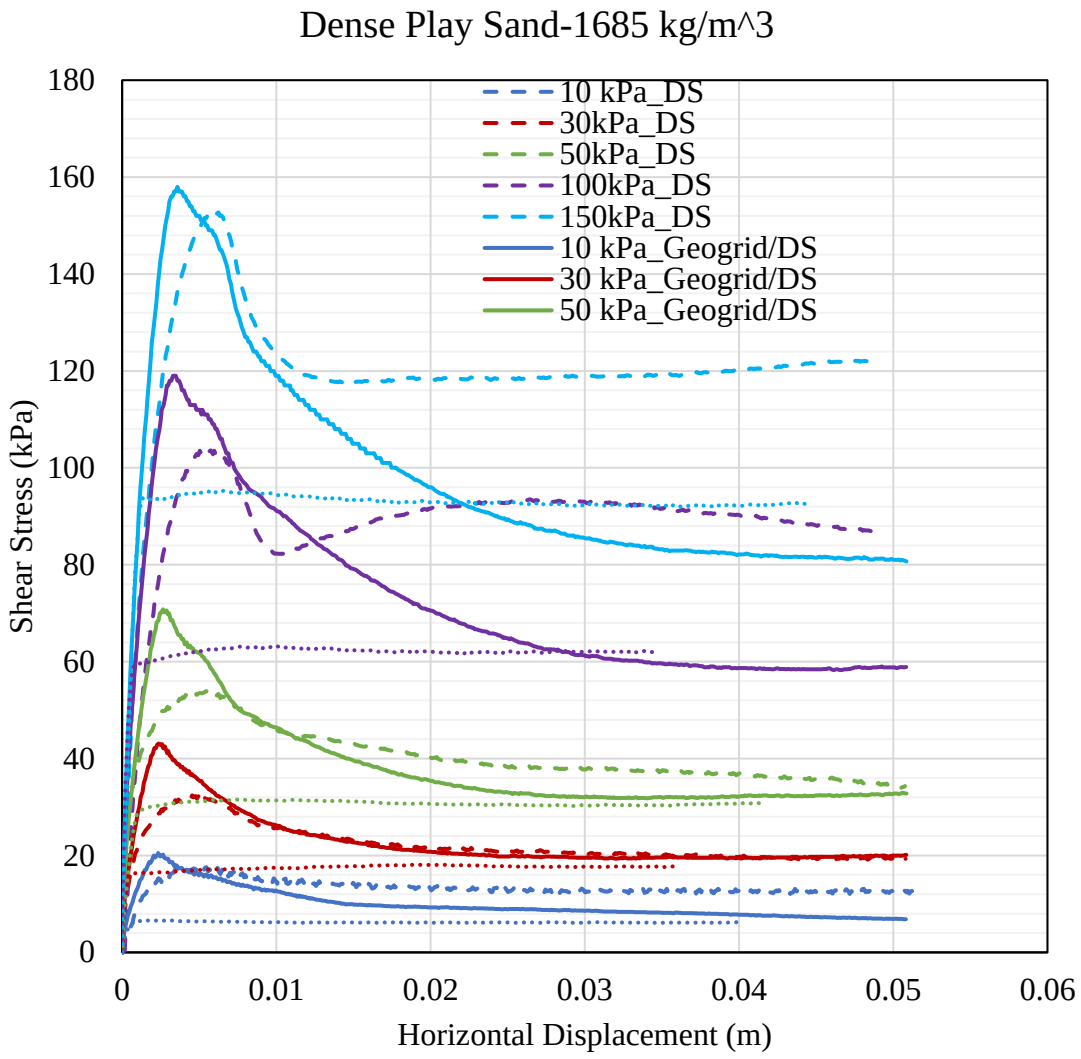

Figure 6-13. Shear Stress-Shear Displacement Behavior of dense sand-dense sand internal, dense sand-smooth steel plate interface, dense sand-Geogrid interface

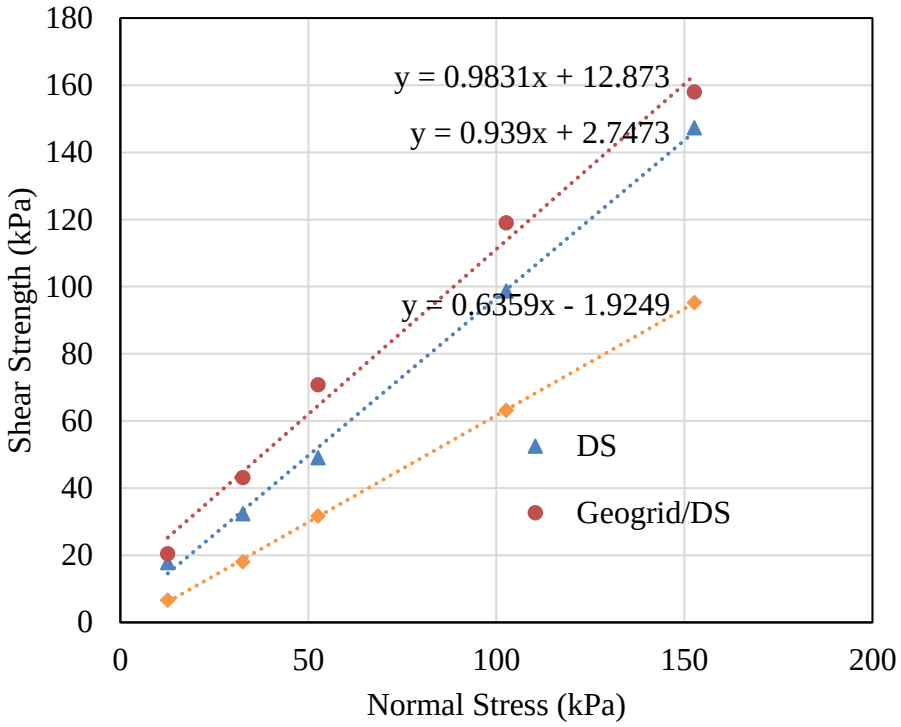

(a)

Figure 6-14. Shear Strength-Normal Stress of dense sand-dense sand internal, dense sand-smooth steel plate interface, dense sand-Geogrid interface, (a) Peak, (b) Large Displacement

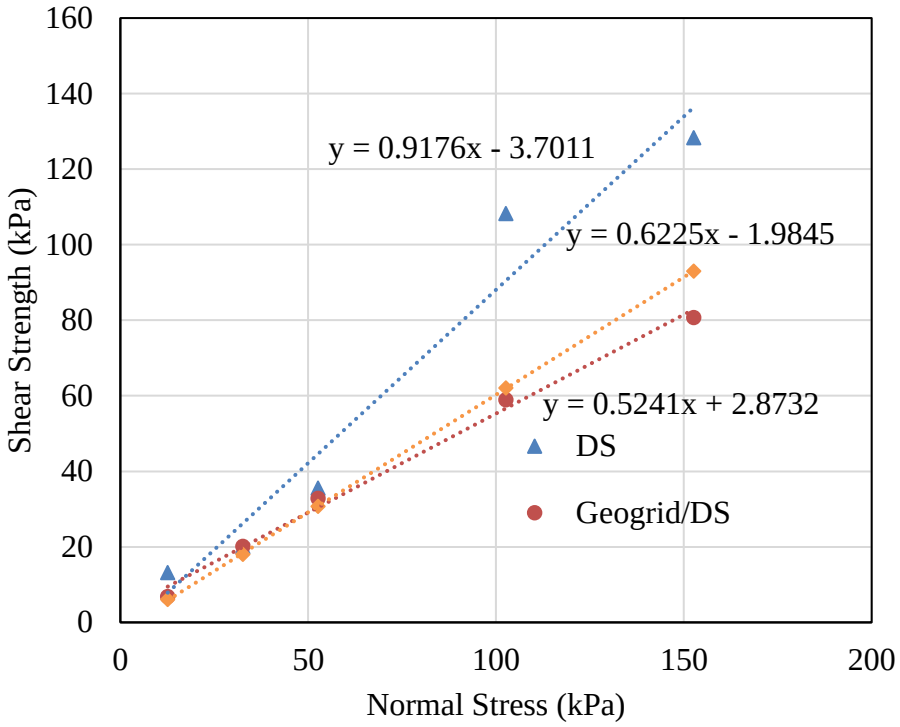

(b)

Figure 6-14. Continued.

6.4.2 Ribs Spacing

IDST: One of the main purposes of this research is to study the influence of the ribs spacing on the interface properties of reinforcements. The interface direct shear test and pullout tests results are analyzed in this section considering different parameters including soil type, soil density, and test type. Figure 6-15, Figure 6-16, and Figure 6-17 describe the shear stress-horizontal displacement obtained from the direct shear test on smooth/ribbed reinforcements and loose sand, dense sand, and crushed limestone, respectively, for various normal stresses starting from 10 kpa (a) to 150 kPa (e). Also, the

results soil-soil internal direct shear test is added to graphs to compare the reinforced and unreinforced specimens. Figure 6-15 illustrates that for all applied normal stresses, the shear strength of smooth plate-loose sand is almost half of the shear strength of soil-soil. The 2-rib plate-loose sand shear strength is lower than soil-soil shear strength regardless of normal stresses. On the other hand, the shear strength of 4-rib, 6-rib, and 9-rib plates and soil are greater than soil-soil internal shear strength. As shown in Figure 6-15, for loose sand, the influence of the ribs spacing is greater at low normal stresses, and with increasing the confining pressure, the influence of the number of the ribs on the plate is almost negligible and very close to the internal shear strength of soil-soil. Because of the fact that the shear strength of ribbed plates/soil under high normal stresses is very close to the soil-soil shear strength, it can be concluded that under high confining pressure, the failure plane occurs on top of the ribs and inside the soil specimen. The passive resistance of ribs shows more contribution at low confining pressures. Table 6-8 summarizes the percentage of increase in interface shear strength of ribbed reinforcements-soil compare to the shear strength of smooth reinforcement-soil. As shown in this table, the shear strength of 2-rib, 4-rib, 6-rib, and 9-rib plate and loose sand at large displacement are 55.7%, 61.25%, 66.67%, and 64.12% greater than smooth plate-loose sand, respectively. For specimen under 150 kPa, the shear strength of 2-rib, 4-rib, 6-rib, and 9-rib plate and loose sand are 25.85%, 32.95%, 33.78%, and 37.17% greater than smooth plate-loose sand, respectively. Increasing the number of ribs from 2 (ribs spacing = 101.6 mm) to 9 (ribs spacing = 25.4 mm) provides 55% to 65% improvement at 10 kPa normal stress and

18% to 25% improvement at 150 kPa normal stress in interface shear strength with loose sand.

The results of shear stress-shear displacement of smooth/ribbed reinforcements and dense sand are shown in Figure 6-16. Same as loose sand, the smooth plate and 2-rib plate show lower shear strength than soil-soil internal. However, the behavior of the shear curves is different from loose sand. That is, the specimen experiences the peak shear strength at small shear displacement. However, at large displacements, the interface shear strength of all ribbed plates are very close to each other. In another word, the ribs spacing less than 101.6 mm (ribs number more than 2) has a very small influence on the interface shear strength at large horizontal displacements. Table 6-8 (b) reports the peak shear stress of 2-rib, 4-rib, 6-rib, and 9-rib plate and dense sand under 10 kPa normal stress are 54.99%, 69.7%, 72%, and 70.4% greater than smooth plate-dense sand, respectively. As shown in Table 6-8 (b), the shear strength at large displacement of 2-rib, 4-rib, 6-rib, and 9-rib plate and dense sand is 50.64%, 59.94%, 59.54%, and 58.45% greater than smooth plate-dense sand, respectively. For specimen under 150 kPa, the shear strength of 2-rib, 4-rib, 6-rib, and 9-rib plate and loose sand are 31.02%, 36.48%, 34.19%, and 35.53% greater than smooth plate-loose sand, respectively.

The same data sets for crushed limestone with fines illustrates that the influence of the ribs is much lower than tests with sand. Unlike sand that with increasing the applied pressure, the percentage of influence decreases, there is not a pattern for crushed limestone with normal stresses.

It is also worth noting that the peak shear stress occurs at large displacements for loose sand while the peak shear stress is observed at small shear displacements. With increasing the density of the soil the effect of the number of the ribs slightly decreases. For this study, the influence of the number of the ribs at large displacements in tests with loose sand is slightly higher than the one with dense sand by means of interface shear properties (Table 6-8 (c)). Furthermore, the shear stress-shear displacement curves of ribbed plates are almost lower than soil-soil internal curves.

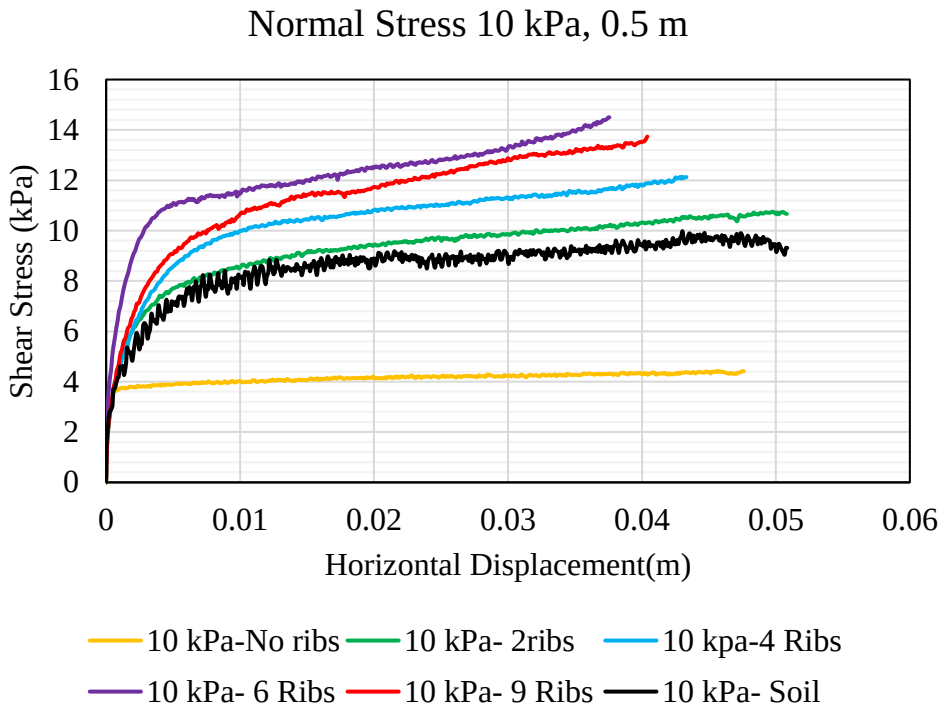

(a)

Figure 6-15. Effect of the Ribs Spacing on the Interface Shear Stress at Various Depth of Soil, Loose Sand, (a) 0.5 m, (b) 1.5 m, (c) 2.5 m, (d) 5 m, (e) 7.5 m

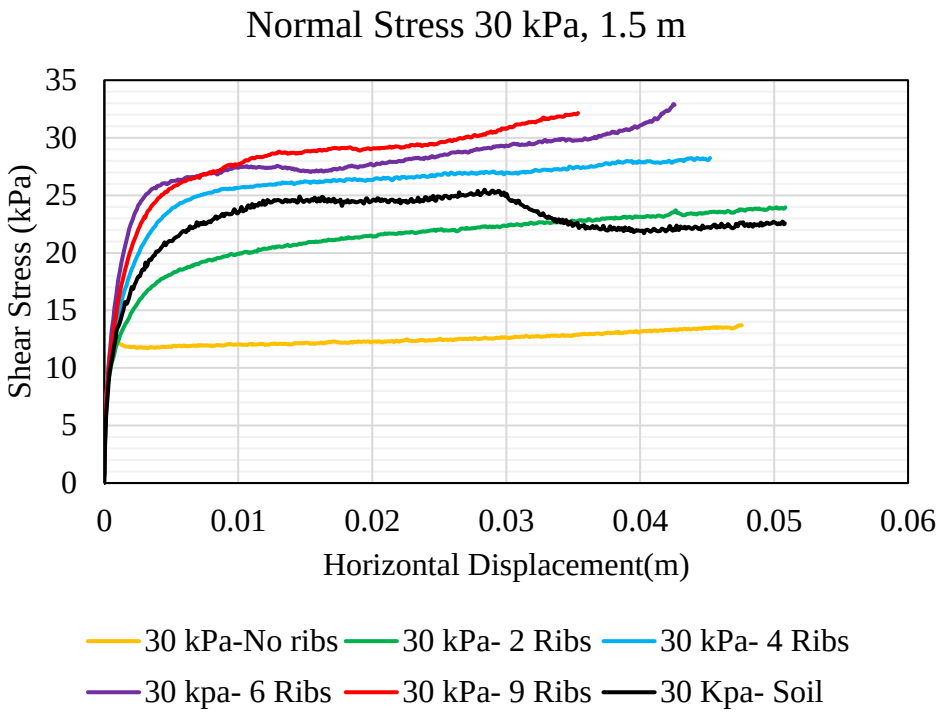

(b)

Figure 6-15. Continued.

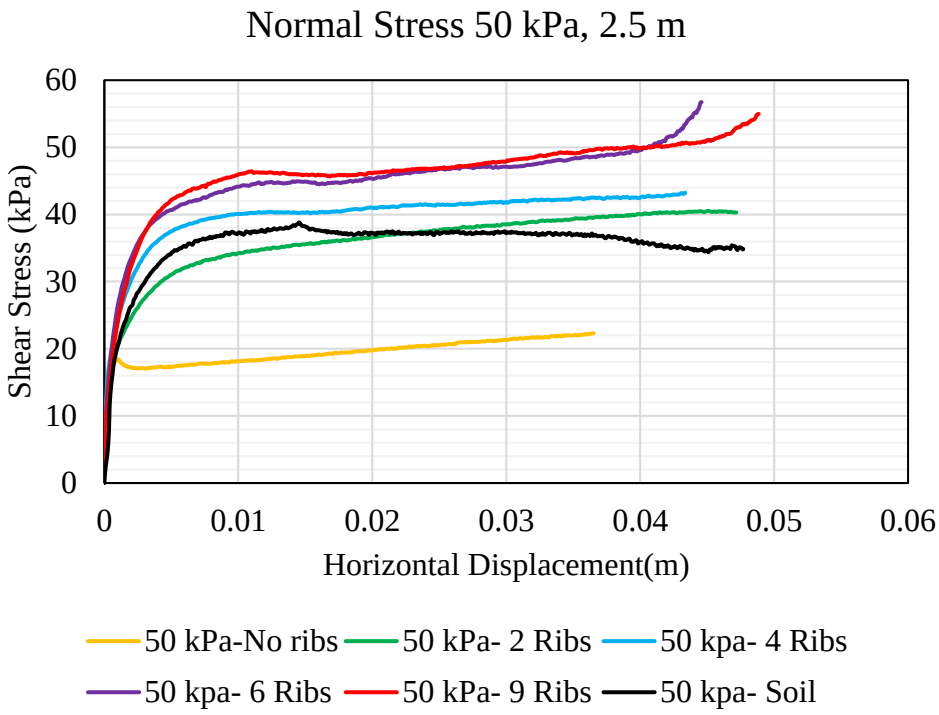

(c)

Figure 6-15. Continued.

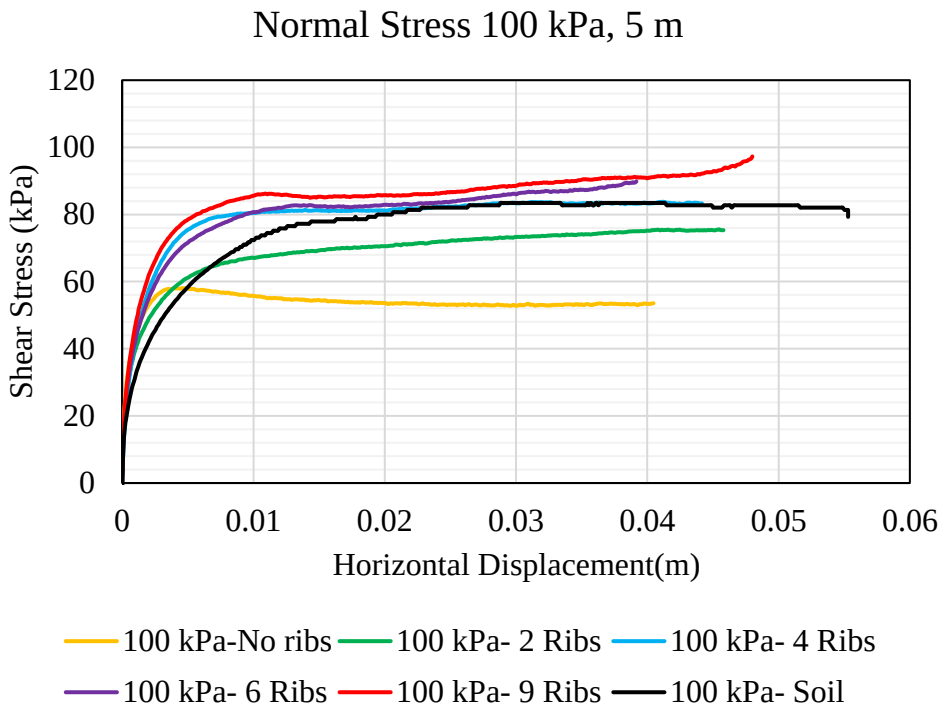

(d)

Figure 6-15. Continued.

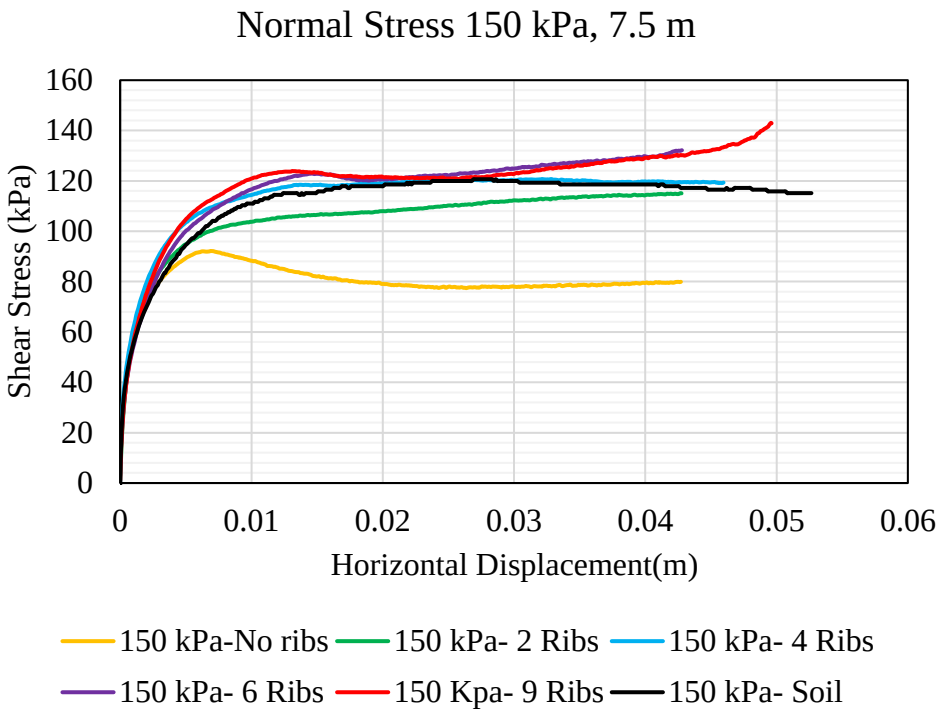

(e)

Figure 6-15. Continued.

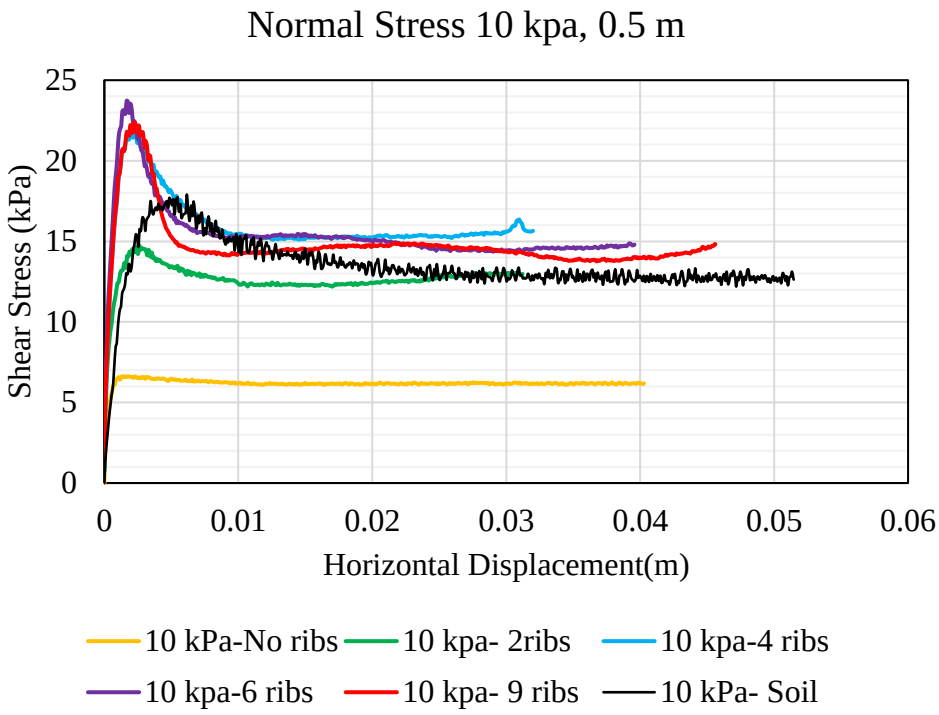

(a)

Figure 6-16. Effect of the Ribs Spacing on the Interface Shear Stress at Various Depth of Soil, Dense Sand, (a) 0.5 m, (b) 1.5 m, (c) 2.5 m, (d) 5 m, (e) 7.5 m

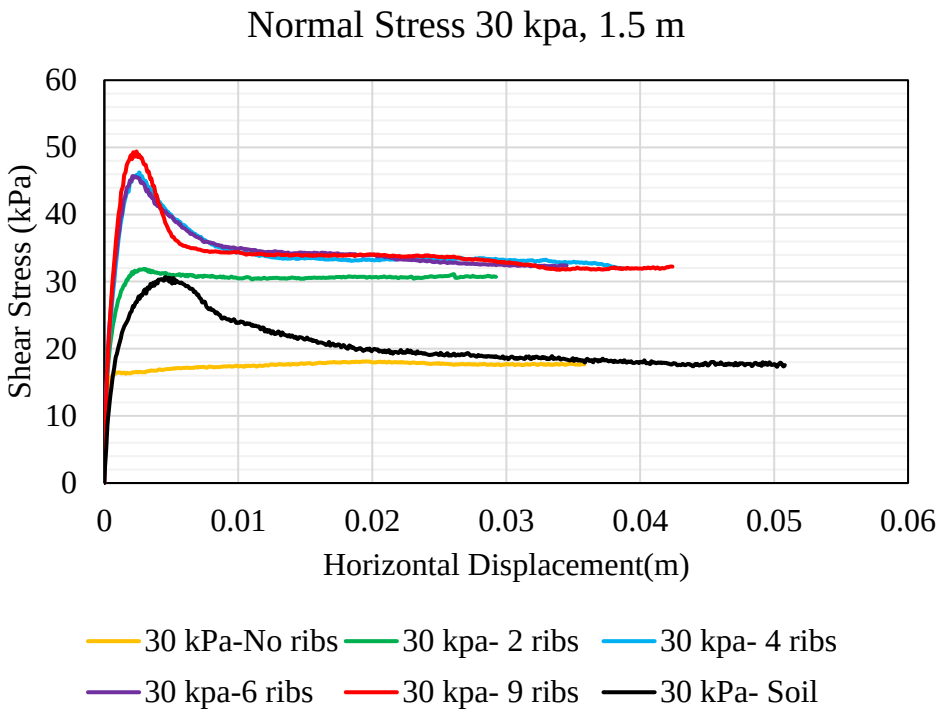

(b)

Figure 6-16. Continued.

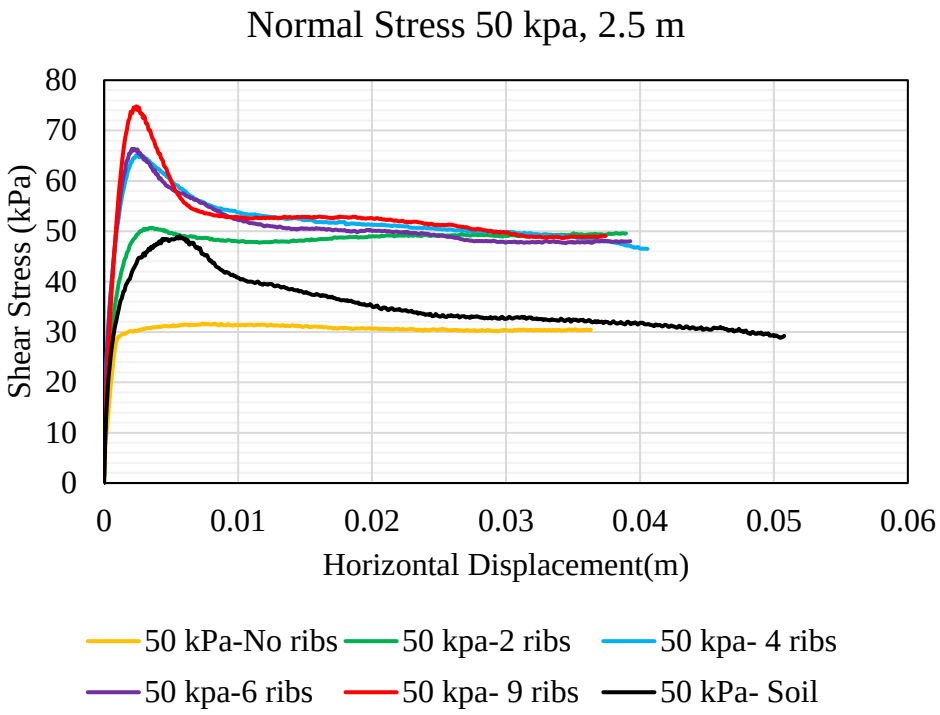

(c)

Figure 6-16. Continued.

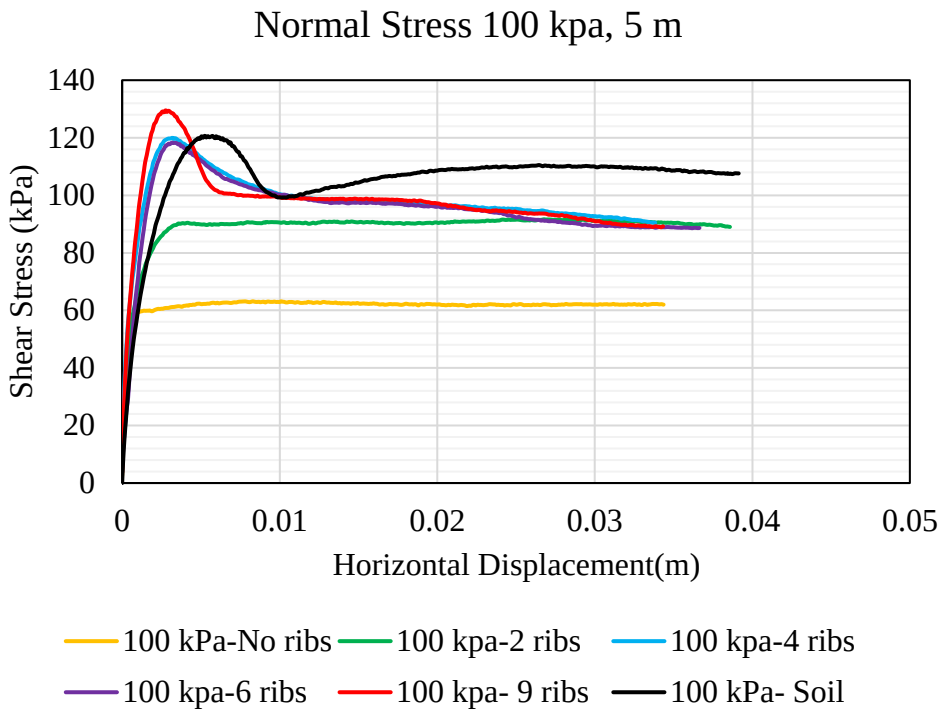

(d)

Figure 6-16. Continued.

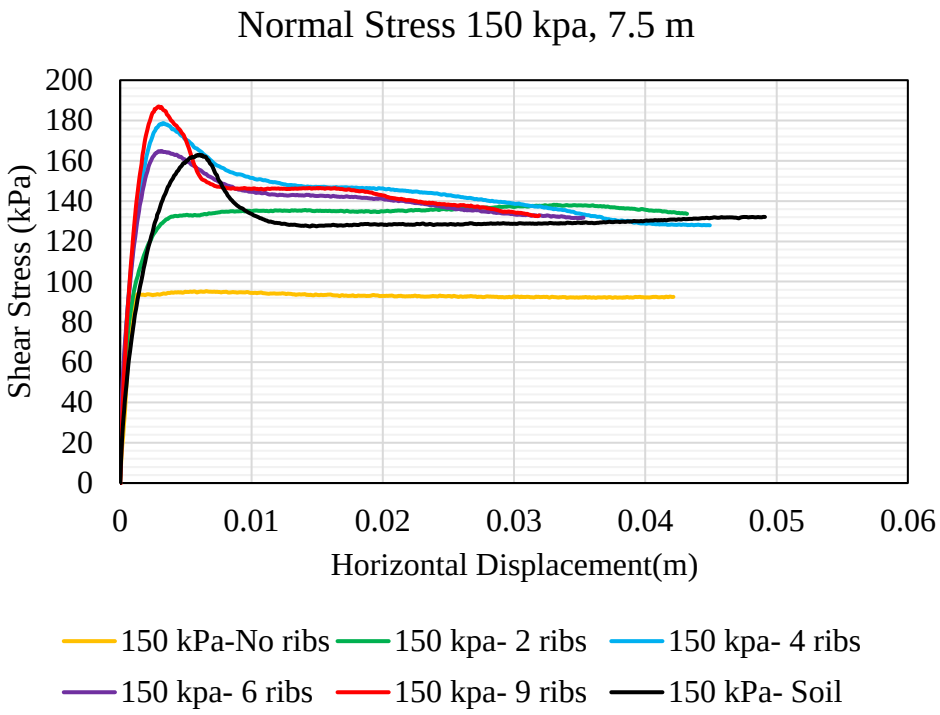

(e)

Figure 6-16. Continued.

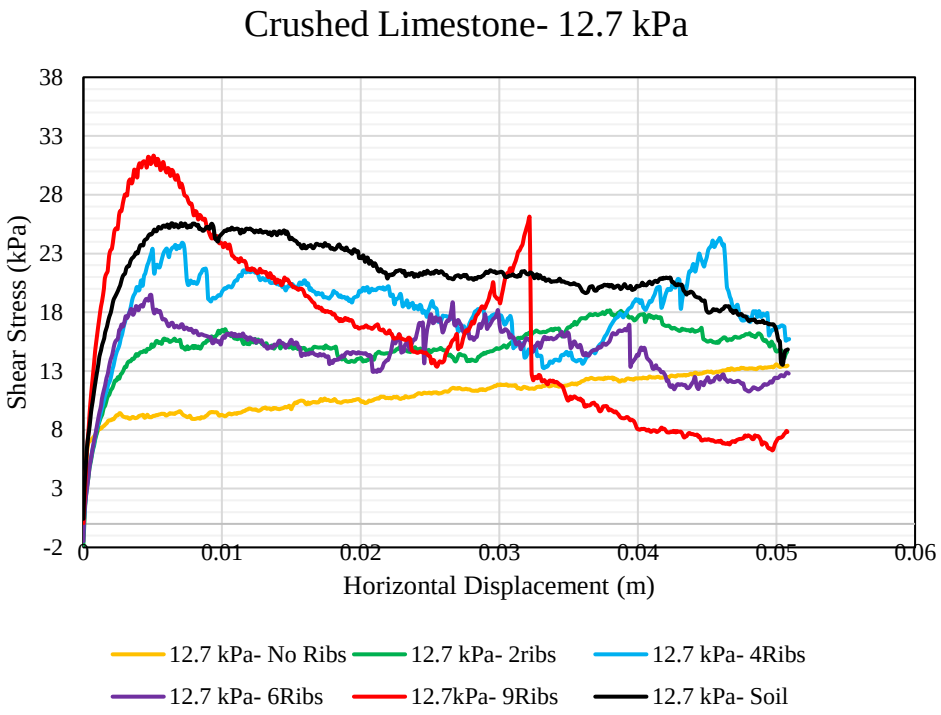

(a)

Figure 6-17. Effect of the Ribs Spacing on the Interface Shear Stress at Various Depth of Soil, Crushed Limestone with Fines, (a) 0.5 m, (b) 1.5 m, (c) 2.5 m, (d) 5 m, (e) 7.5 m

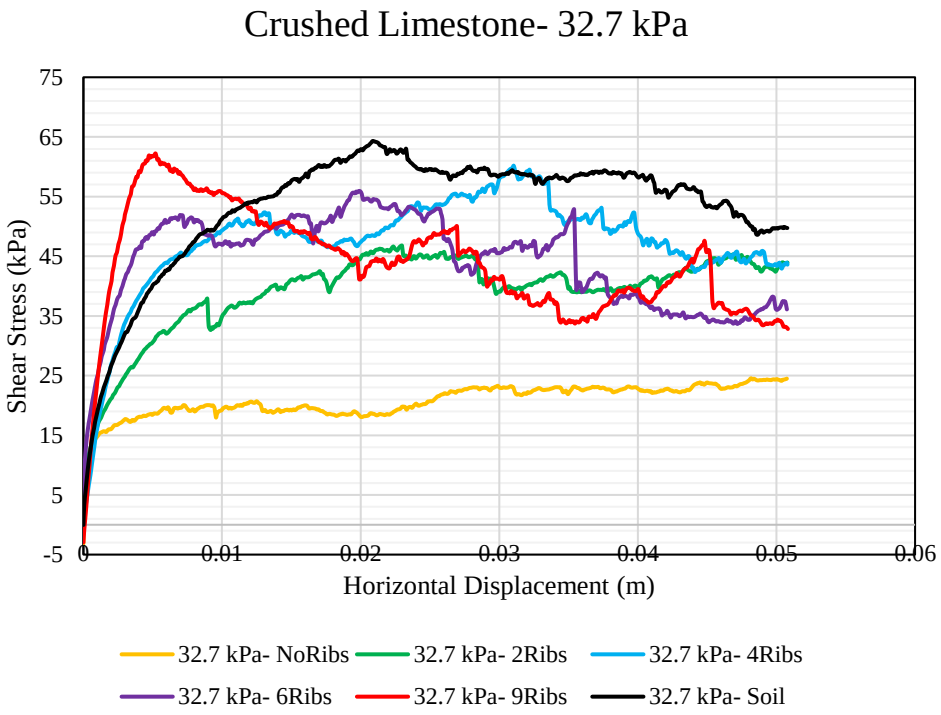

(b)

Figure 6-17. Continued.

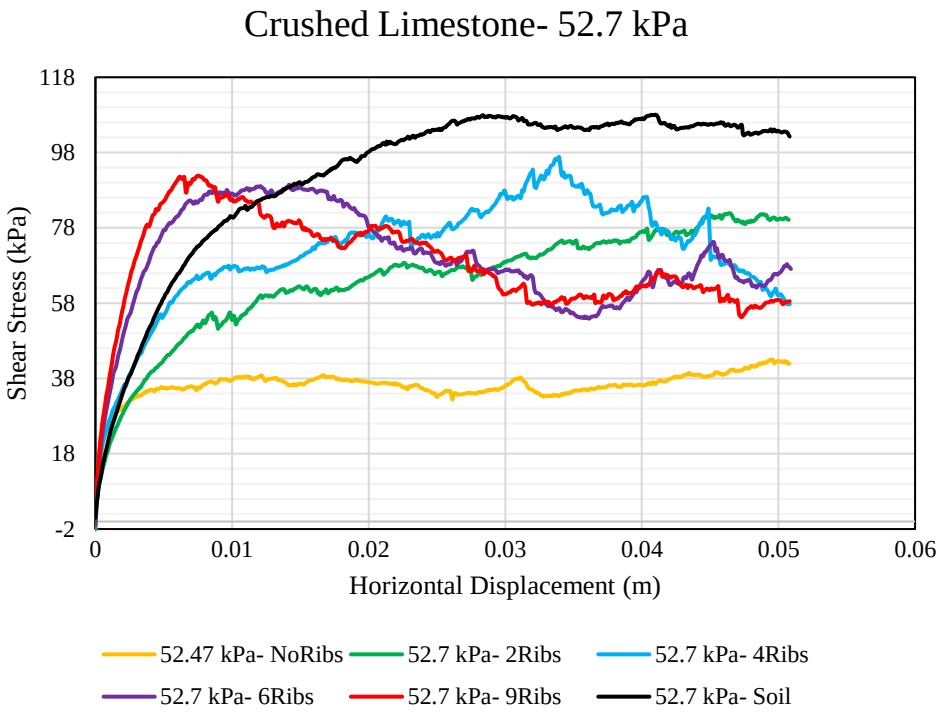

(c)

Figure 6-17. Continued.

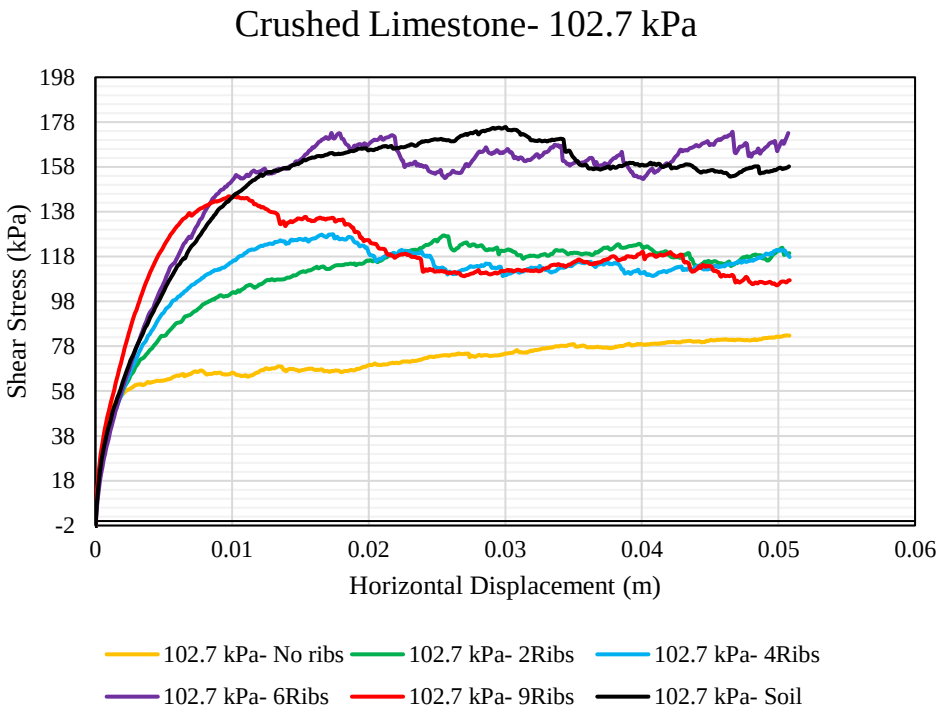

(d)

Figure 6-17. Continued.

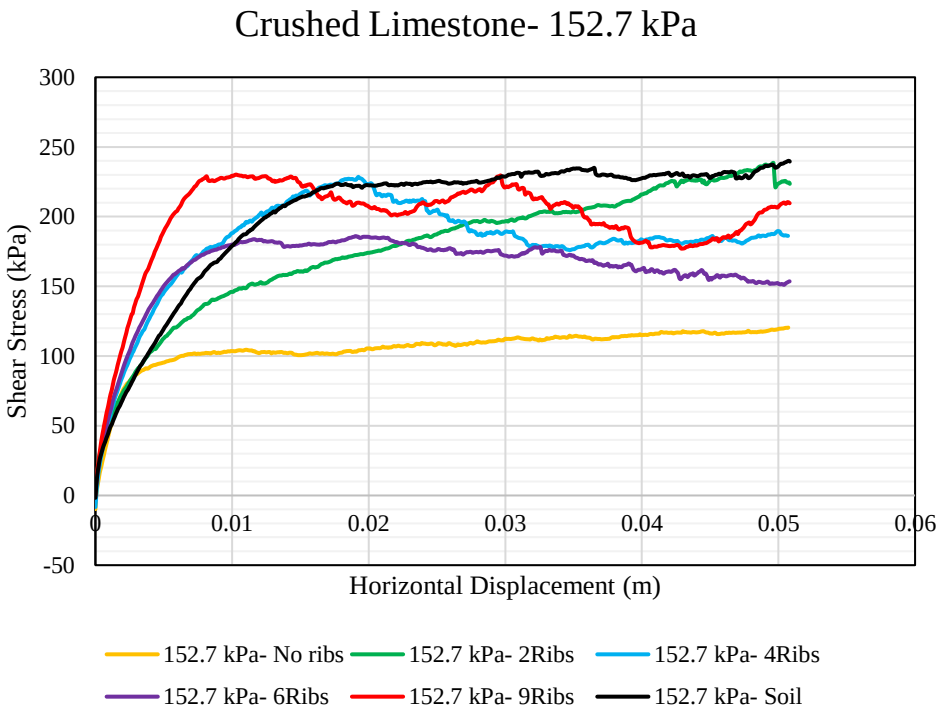

(e)

Figure 6-17. Continued.

Table 6-8. Effect of the Number of Ribs per 30.48 cm on Interface Shear Strength, (a) Loose Sand, (b) Dense Sand, (c) Crushed Limestone with Fines

Number of ribs per 30.48 cm (1 ft) =2		
Normal Pressure (kPa)	**Percentage of Influence on Shear Strength (%)-Peak**	**Percentage of Influence on Shear Strength (%)- Large Displacement**
12.43	55.05	55.71
32.43	38.63	42.31
52.43	30.44	46.03
102.43	20.77	23.67
152.43	17.93	25.85
Number of ribs per 30.48 cm (1 ft) =4		
12.43	60.82	61.25
32.43	49.17	53.39
52.43	36.11	51.77
102.43	30.49	33.77
152.43	23.68	32.95
Number of ribs per 30.48 cm (1 ft) =6		
12.43	66.81	66.67
32.43	53.24	55.33
52.43	43.09	56.42
102.43	32.53	34.93
152.43	26.23	33.78
Number of ribs per 30.48 cm (1 ft) =9		
12.43	65.61	64.12
32.43	55.46	57.44
52.43	44.04	57.32
102.43	34.46	37.17
152.43	25.06	34.35

Table 6-8. Continued.

Number of ribs per 30.48 cm (1 ft) =2		
Normal Pressure (kPa)	**Percentage of Influence on Shear Strength (%)-Peak**	**Percentage of Influence on Shear Strength (%)- Large Displacement**
12.43	54.99	50.64
32.43	43.23	41.34
52.43	37.51	37.05
102.43	31.10	31.26
152.43	31.04	31.02
Number of ribs per 30.48 cm (1 ft) =4		
12.43	69.70	59.94
32.43	60.86	45.77
52.43	51.46	40.33
102.43	47.37	36.15
152.43	46.68	36.48
Number of ribs per 30.48 cm (1 ft) =6		
12.43	72.03	59.54
32.43	60.37	46.96
52.43	52.27	38.58
102.43	46.62	35.54
152.43	42.22	34.19
Number of ribs per 30.48 cm (1 ft) =9		
12.43	70.38	58.45
32.43	63.34	47.13
52.43	57.67	41.75
102.43	51.24	36.70
152.43	49.04	35.53

Table 6-8. Continued.

Number of ribs per 30.48 cm (1 ft) =2		
Normal Pressure (kPa)	**Percentage of Influence on Shear Strength (%)-Peak**	**Percentage of Influence on Shear Strength (%)- Large Displacement**
12.43	25.25	26.18
32.43	47.49	59.15
52.43	47.51	41.97
102.43	34.99	42.04
152.43	49.51	40.75
Number of ribs per 30.48 cm (1 ft) =4		
12.43	44.17	45.96
32.43	59.19	61.33
52.43	55.57	50.75
102.43	35.25	45.70
152.43	47.29	54.50
Number of ribs per 30.48 cm (1 ft) =6		
12.43	30.27	28.70
32.43	56.09	66.02
52.43	51.94	54.14
102.43	52.28	59.64
152.43	35.28	44.59
Number of ribs per 30.48 cm (1 ft) =9		
12.43	56.67	40.37
32.43	60.53	59.15
52.43	53.22	50.08
102.43	42.86	47.74
152.43	47.68	50.60

Pullout Test: To evaluate the effect of the ribs spacing on the pullout force obtained from tests in a full box, the pullout force versus displacement is shown in Figure 6-18. The pullout force increasing with increasing the number of ribs per 30.48 cm. Table 6-9 describes the effect of the number of ribs on pullout force in terms of percentage of ribbed steel strip reinforcement pullout force over smooth steel strip reinforcement pullout force. The peak pullout force for 1-rib, 2-rib, and RECO standard configuration of steel strip reinforcement enhances the pullout force by 4.8%, 12%, and 32%, respectively.

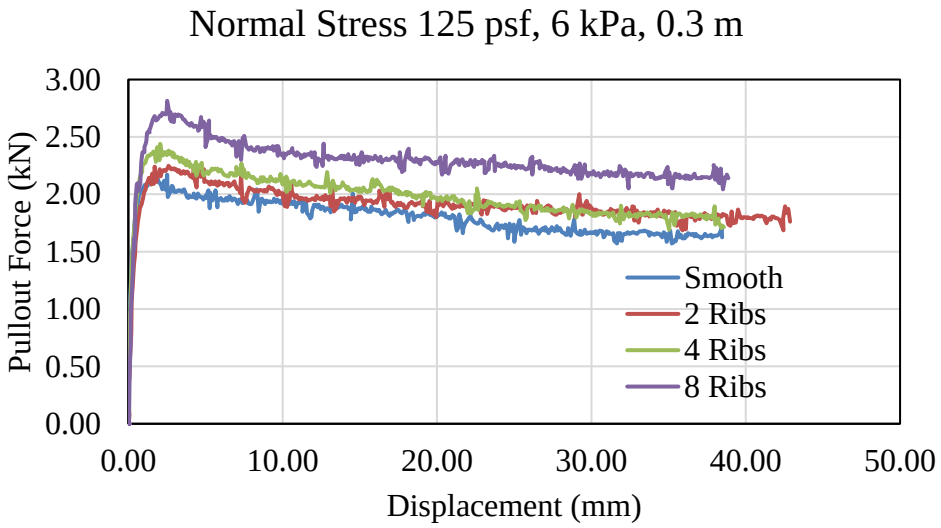

(a)

Figure 6-18. Effect of the Ribs Spacing on Pullout Force at Various Depth of Soil, Full Box, Dense Sand, (a) 0.3 m, (b) 1.5 m, (c) 3 m, (d) 4.5 m, (e) 6 m

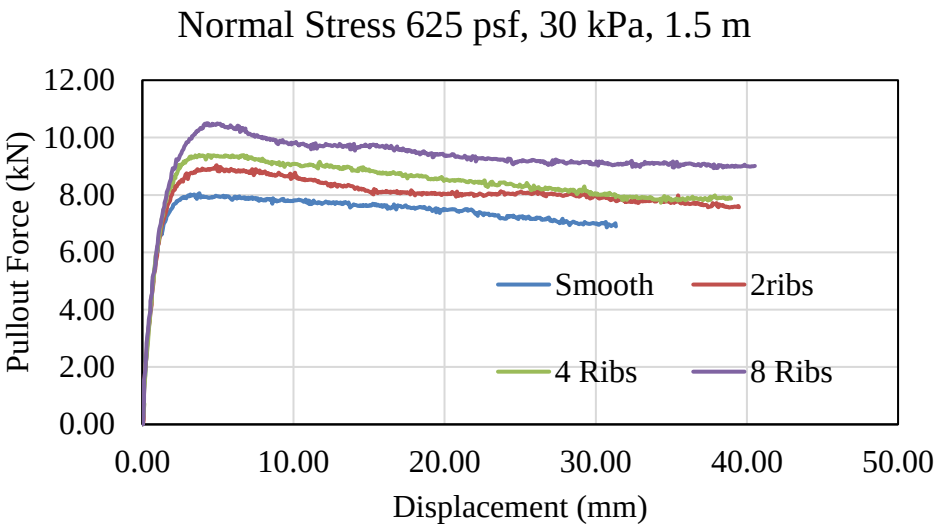

(b)

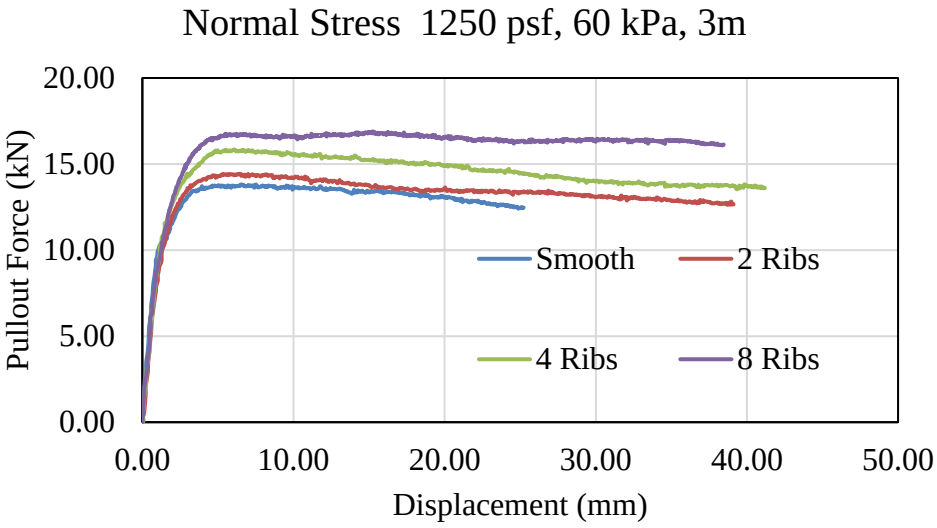

(c)

Figure 6-18. Continued.

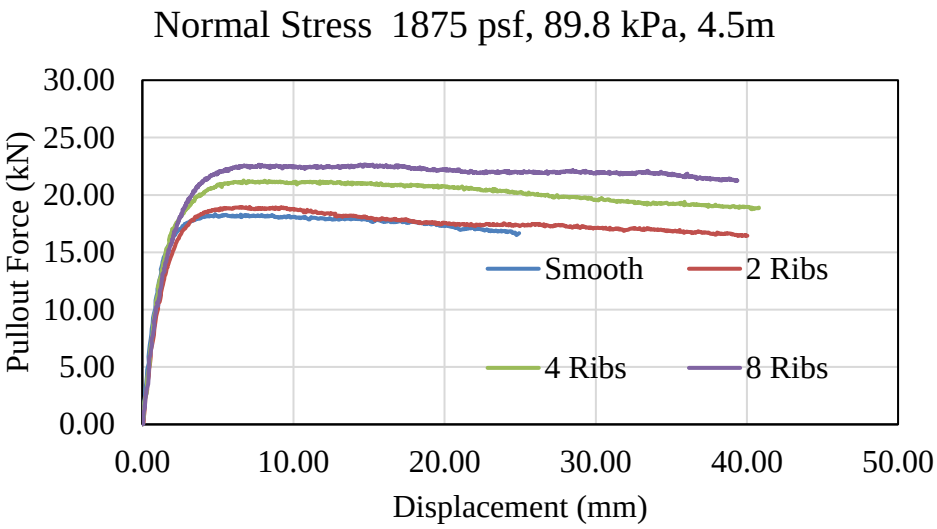

(d)

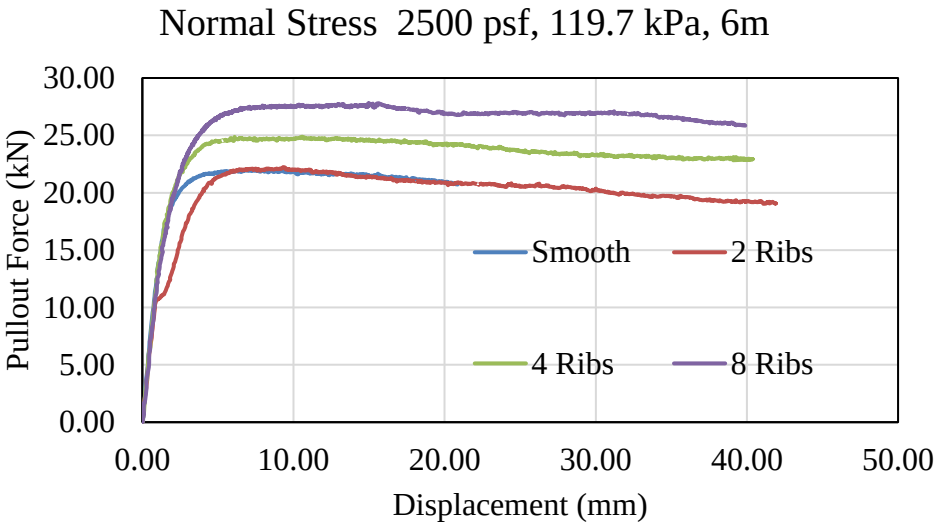

(e)

Figure 6-18. Continued.

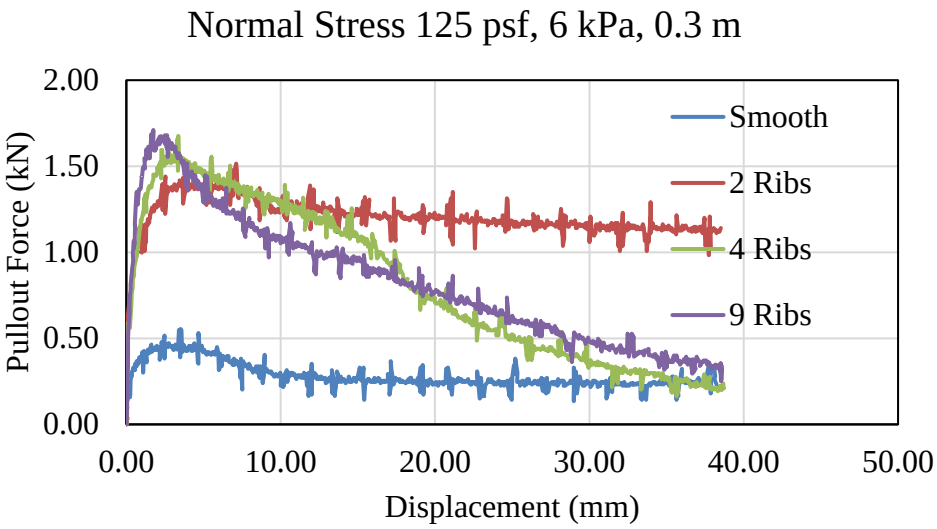

(a)

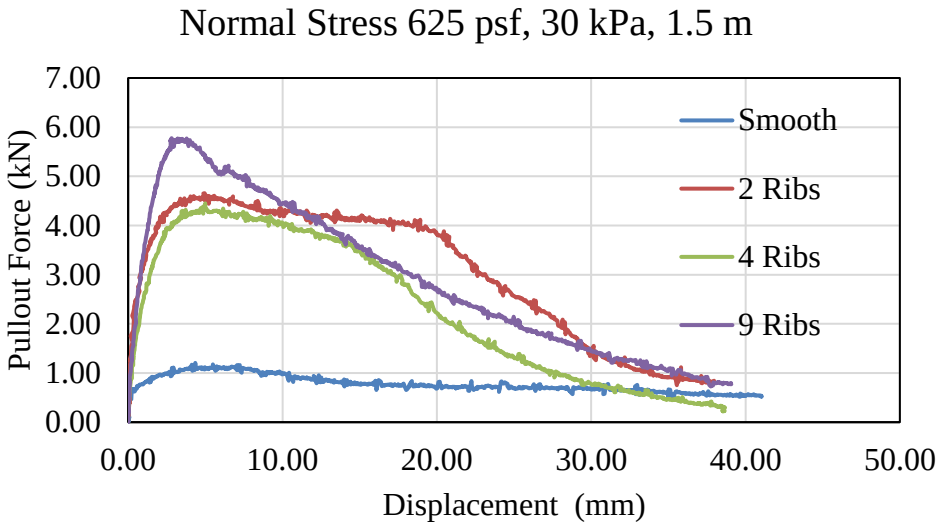

(b)

Figure 6-19. Effect of the Ribs Spacing on Pullout Force at Various Depth of Soil, Half Box, Dense Sand, (a) 0.3 m, (b) 1.5 m, (c) 3 m, (d) 4.5 m, (e) 6 m

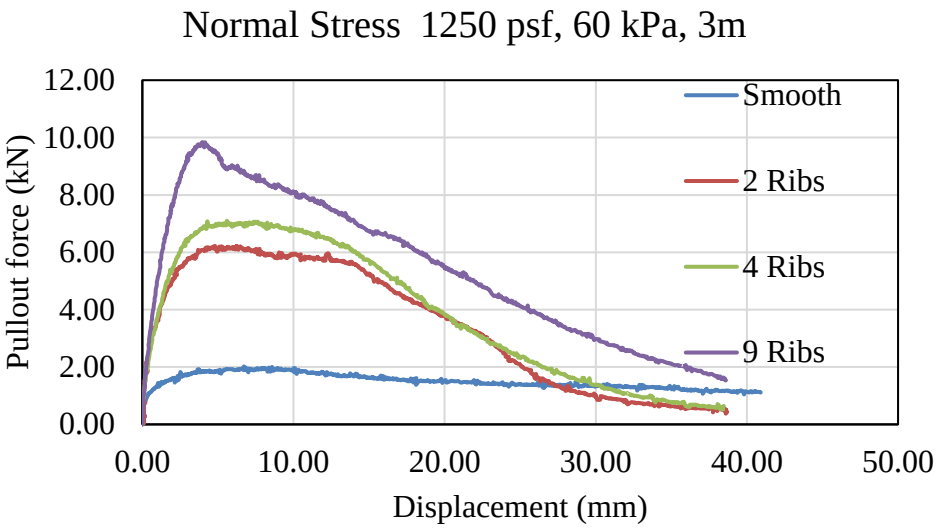

(c)

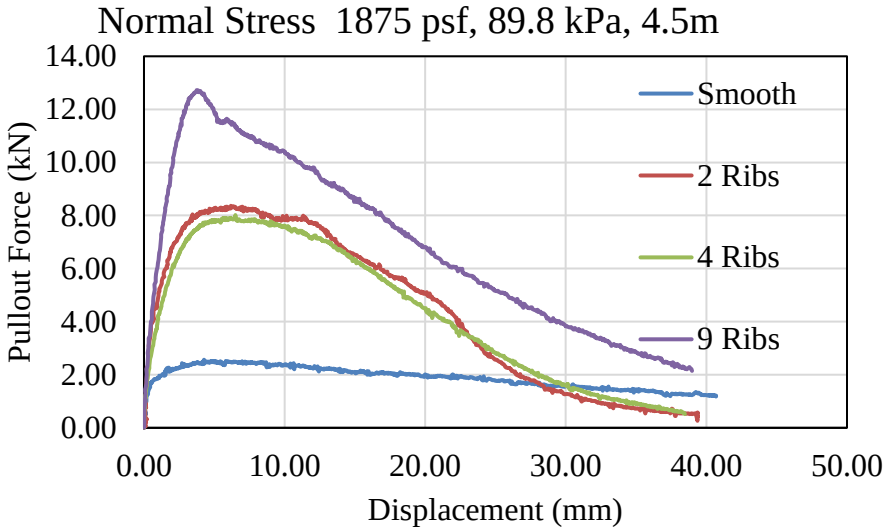

(d)

Figure 6-19. Continued.

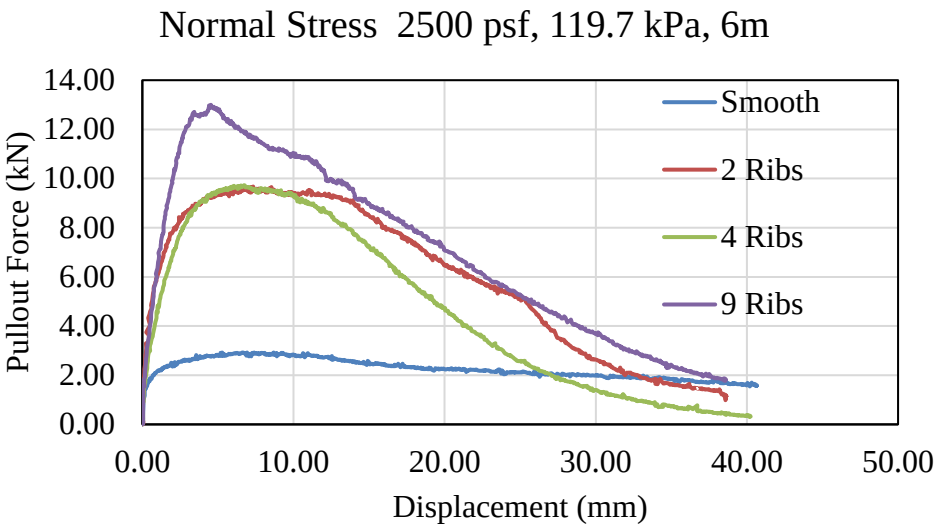

(e)

Figure 6-19. Continued.

Table 6-9. Effect of the Number of Ribs per 30.48 cm on Pullout Force, (a) Loose Sand, (b) Dense Sand, (c) Crushed Limestone with Fines

Number of ribs per side per 30.48 cm (1 ft) = 1 (Ribs Spacing = 259.6 mm)		
Normal Pressure (kPa)	**Percentage of Influence on Pullout Force (%)-Peak**	**Percentage of Influence on Pullout Force (%)- Large Displacement**
6.00	4.82	4.29
30.00	10.81	6.91
60.00	4.28	3.37
89.80	3.33	0.70
119.70	1.20	-0.86
Number of ribs per side per 30.48 cm (1 ft) = 2 (Ribs Spacing = 129.8 mm)		
6.00	11.92	17.10
30.00	14.23	12.30
60.00	12.78	13.48
89.80	13.80	15.73
119.70	11.70	13.22
Number of ribs per side per 30.48 cm (1 ft) = 4 (Ribs Spacing = 9.9 mm, 104.9 mm)		
6.00	32.46	31.75
30.00	23.25	20.49
60.00	18.25	21.69
89.80	19.06	21.07
119.70	20.98	22.07

The obtained F* value from pullout test in Full box and direct shear test is summarized in Figure 6-20 and Figure 6-21, respectively. The F* value obtained from pullout tests in full box increases with increasing the number of ribs per side per 30.48 cm (1 ft) from 0 to 4 ribs. The F* value obtained from maximum pullout force is in the range

of 1.7-3.1 for the smooth plate and is 2.1-4.5 for RECO steel strip reinforcement under normal stress of 120 kPa and 6 kPa, respectively. The F* value obtained from pullout force at large displacement is in the range of 1.6-2.6 for the smooth plate and is 2.1-3.6 for RECO steel strip reinforcement under normal stress of 120 kPa and 6 kPa, respectively. Comparing RECO steel strip reinforcement and smooth steel strip reinforcement, the F* value enhances by the amount of 1.4 at depth of 0.3 m and 0.5 at depth of 6m. At large displacement, comparing RECO steel strip reinforcement and smooth steel strip reinforcement, the F* value enhances by the amount of 1 at depth of 0.3 m and 0.5 at depth of 6m. Therefore, the effect of the ribs is greater at a lower depth of the soil and at small displacements corresponding to the peak pullout force.

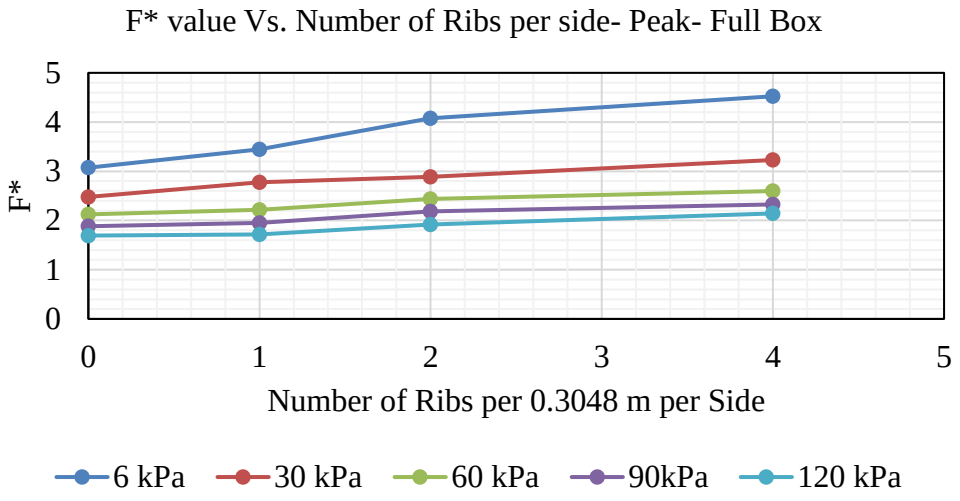

(a)

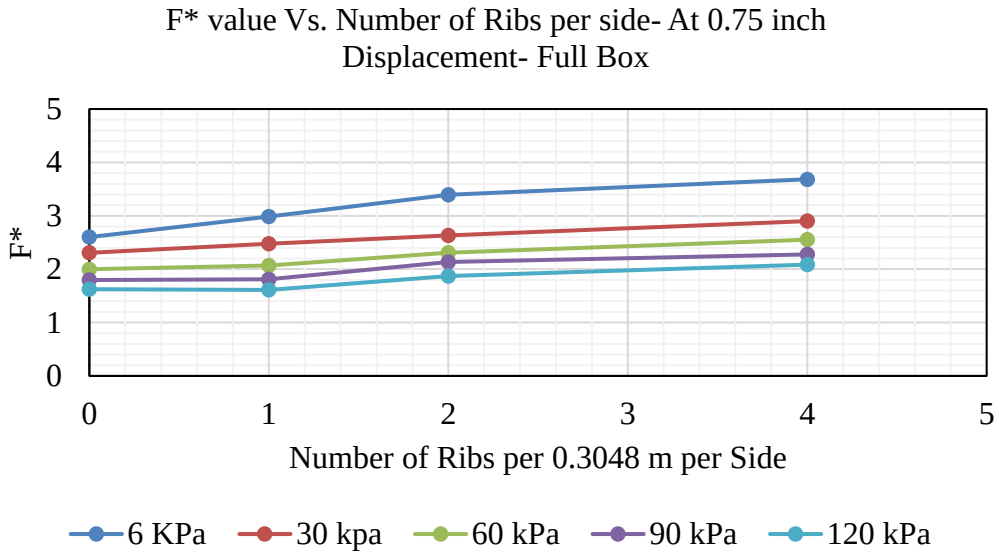

(b)

Figure 6-20. F* value vs. Number of Ribs per 0.3048 m (1 ft.) per side, Full Box, (a) Maximum, (b) Large-Displacement (0.75 inches)

To evaluate the influence of the ribs spacing on the F* value obtained from interface direct shear test between smooth/ribbed plates and three different type of soil, the obtained F* value versus a number of ribs per 30.48 cm is provided in Figure 6-21. Figure 6-21 (a) shows that the maximum F* value obtained from smooth/ribbed plates and loose sand occurs at 9 ribs (ribs spacing = 25.4 mm). On the other hand, as Figure 6-21 (b) shows, that the maximum F* value obtained from smooth/ribbed plates and dense sand occurs at 4, 6, and 9 ribs depend on the confining pressure (depth of embedment). Figure 6-21 (c) illustrates that there is not a pattern for the maximum F* value calculated from crushed limestone and the ribbed reinforcements. Figure 6-22 shows the Ci value versus the number of ribs on a plate. As shown in this figure, the Ci value of ribbed plates is greater at lower normal stresses than a higher one. The maximum Ci value is observed for 6-rib plate under 10 kPa normal stress, and the one is obtained for 9-rib plate under 30, 50, 100, and 150 kPa normal stress for both loose and dense sand.

The figure shows that for both loose and dense sand, the plate should have at least 4 ribs to obtain the shear strength more than internal soil shear strength. The Ci value reaches 1.5 for 9-rib plate-dense sand, 1.25 for 9-rib plate-loose sand, and 1 for 9-rib plate-crushed limestone. Therefore, it is more effective for dense to increase the ribs for better performance.

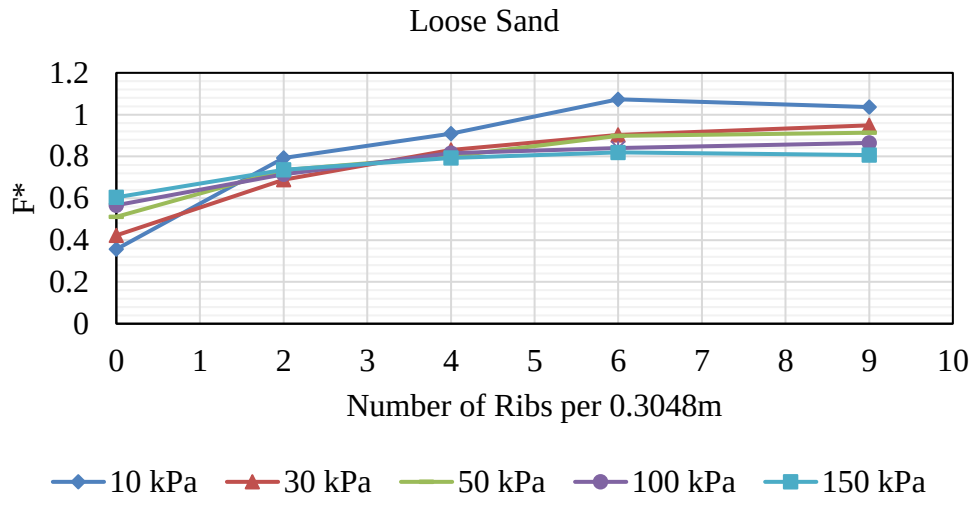

(a)

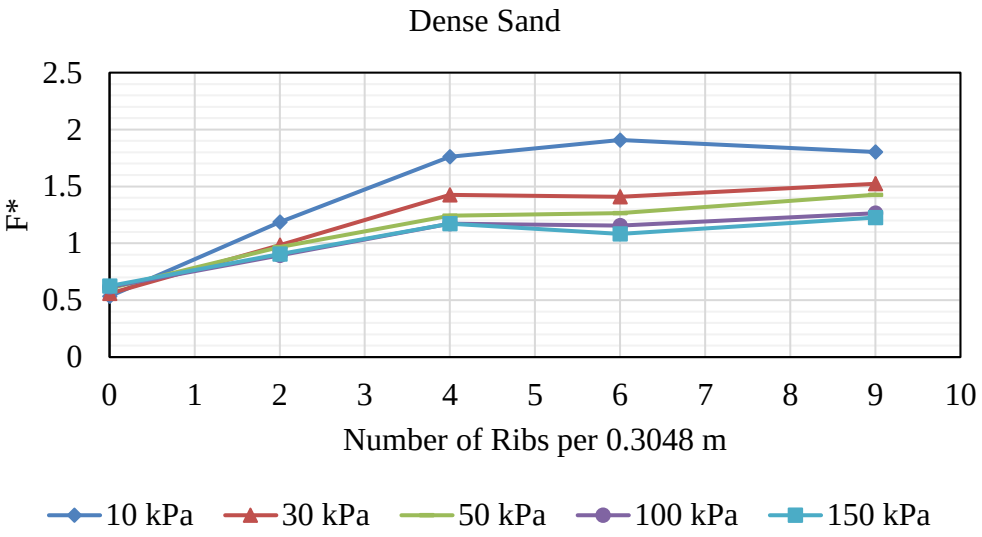

(b)

Figure 6-21. F* value vs. Number of Ribs per 0.3048 m (1 ft.), IDST, (a) Loose Sand, (b) Dense Sand, (c) Crushed Limestone with Fines

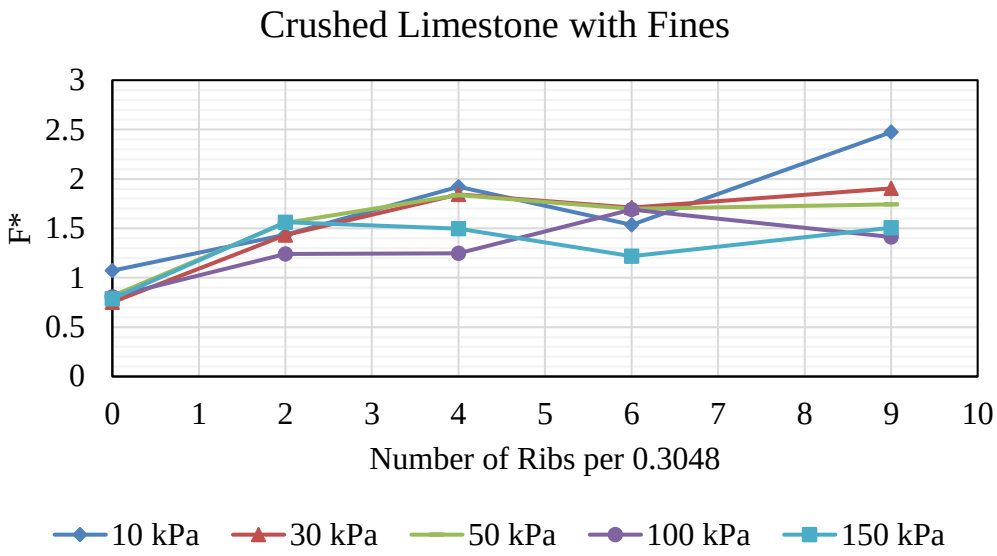

(c)

Figure 6-21. Continued.

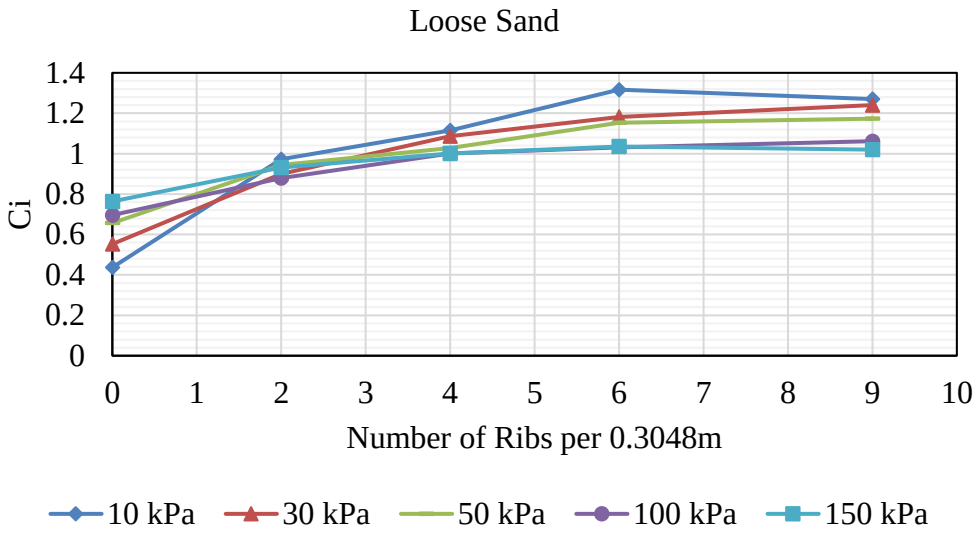

(a)

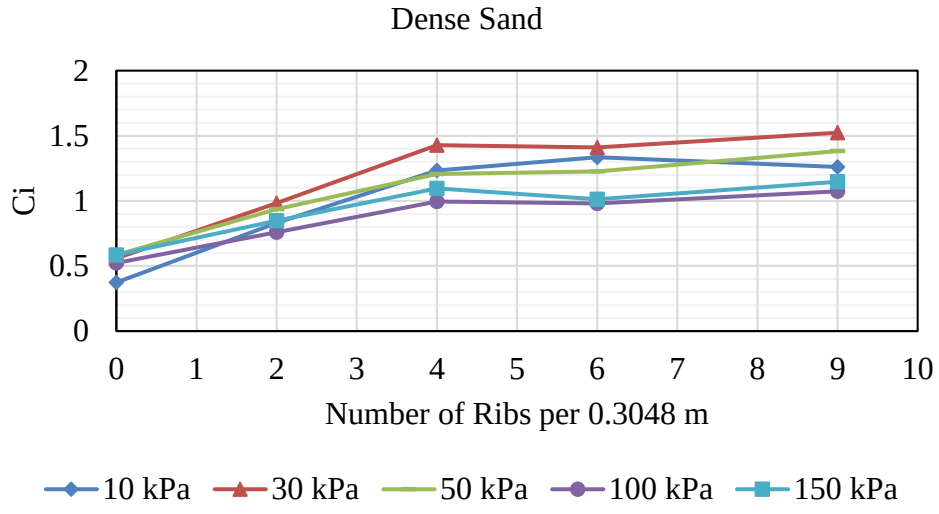

(b)

Figure 6-22. F* value vs. Number of Ribs per 0.3048 m (1 ft.), IDST, (a) Loose Sand, (b) Dense Sand, (c) Crushed Limestone with Fines

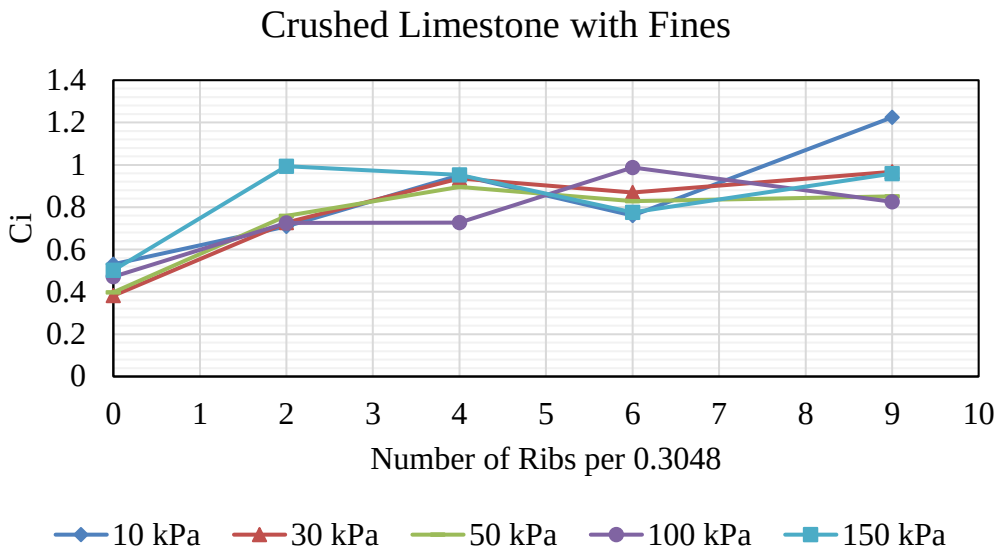

(c)

Figure 6-22. Continued.

6.5 Contribution of Passive Resistance and Frictional Resistance

Direct Shear Mode: The contribution of ribs of the plates on the shear strength obtained from the direct shear test is calculated for each reinforcement under various normal stresses and presented in Figure 6-23. As shown in Figure 6-23 (a), with increasing the number of the ribs per 30.48 cm (1 ft.), the contribution of ribs is also increasing. It is observed from Figure 6-23 (a) that the contribution of ribs is higher for specimens under 10 kPa (low normal stress) and decrease with increasing the normal stresses to 150 kPa (higher normal stress). The same behavior is observed for the results of the interface direct shear test of ribbed plate-dense sand. However, the influence of normal stress on the contribution of shear strength is slightly lower for dense sand compared to the loose sand.

On the other hand, the percentage of contribution of ribs in total interface shear strength between ribbed plates and crushed limestone with fines indicates that the results do not follow a pattern. The average percentage of influence is in the range of 30%-60% depending on the confining pressure.

In conclusion, the percentage of contribution of ribs in the interface shear strength depends on the soil characteristics (grain size and density) and confining pressure. For loose sand, the average contribution of ribs in the shear strength of 2-rib plate, 4-rib plate, 6-rib plate, the 9-rib plate is in the range of 20%-55%, 24%-60%, 26%-66%, 25%-66%, respectively. For dense sand, the average contribution of ribs in the shear strength of 2-rib plate, 4-rib plate, 6-rib plate, and the 9-rib plate is in the range of 32%-65%, 40%-70%, 42%-72%, and 49%-70%, respectively. Therefore, increasing the density of the soil enhances the influence of the ribs in the shear strength.

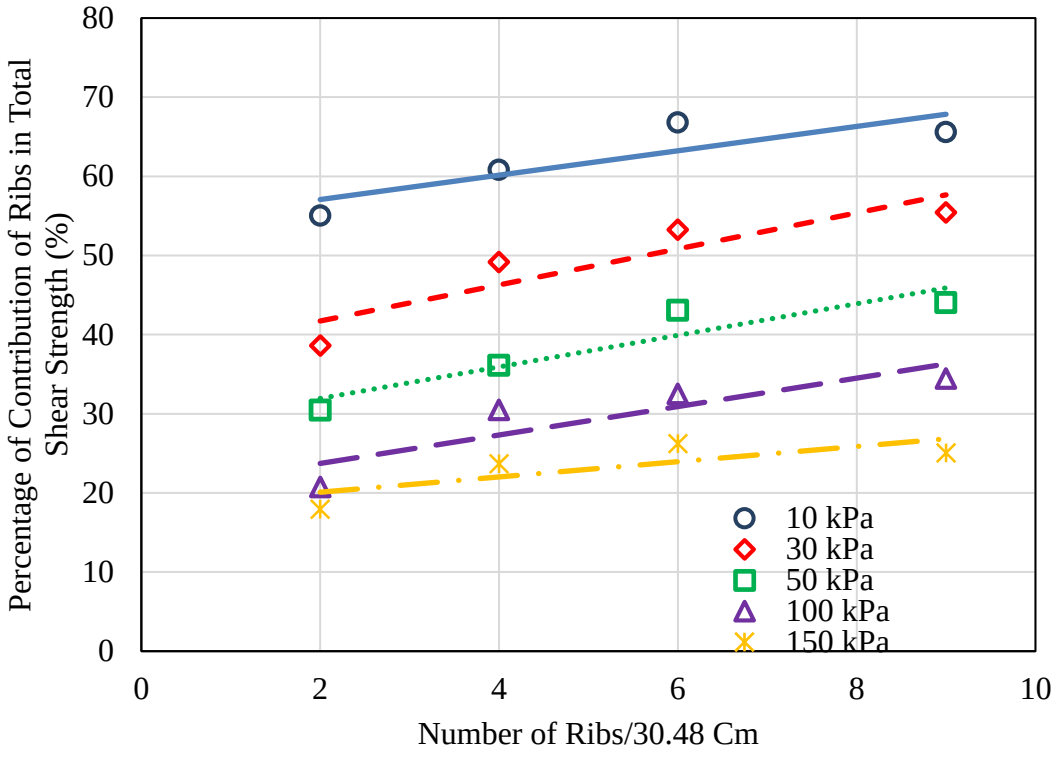

(a)

Figure 6-23. The contribution of Ribs in Total Shear Strength

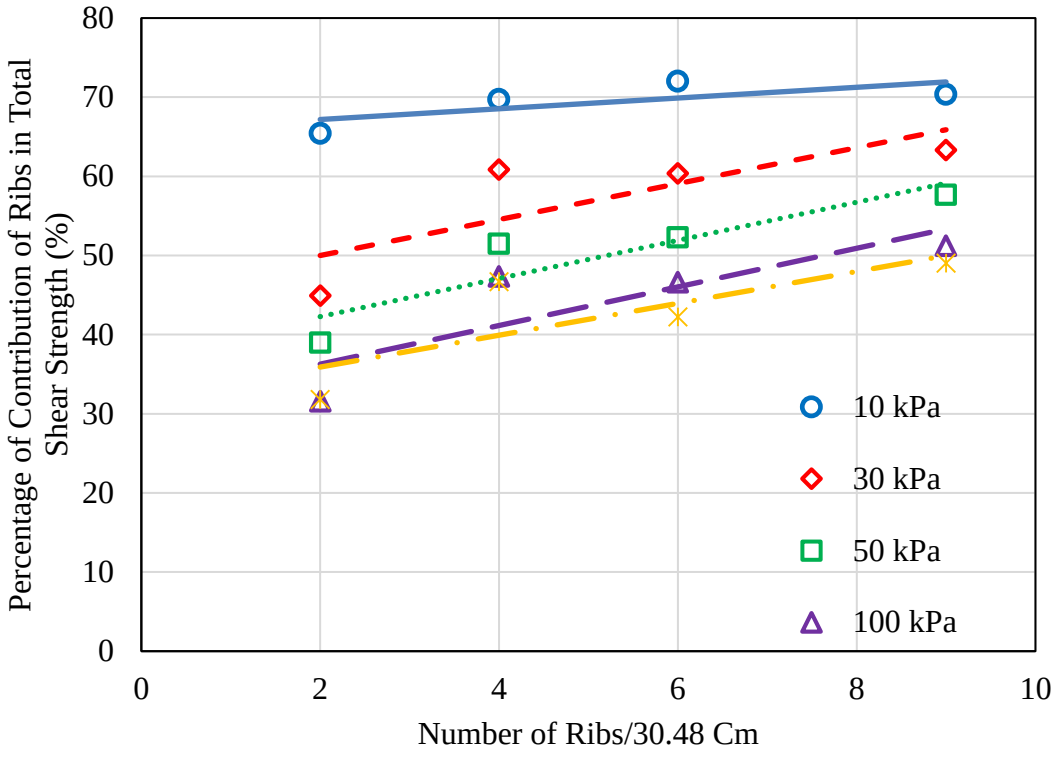

(b)

Figure 6-23. Continued.

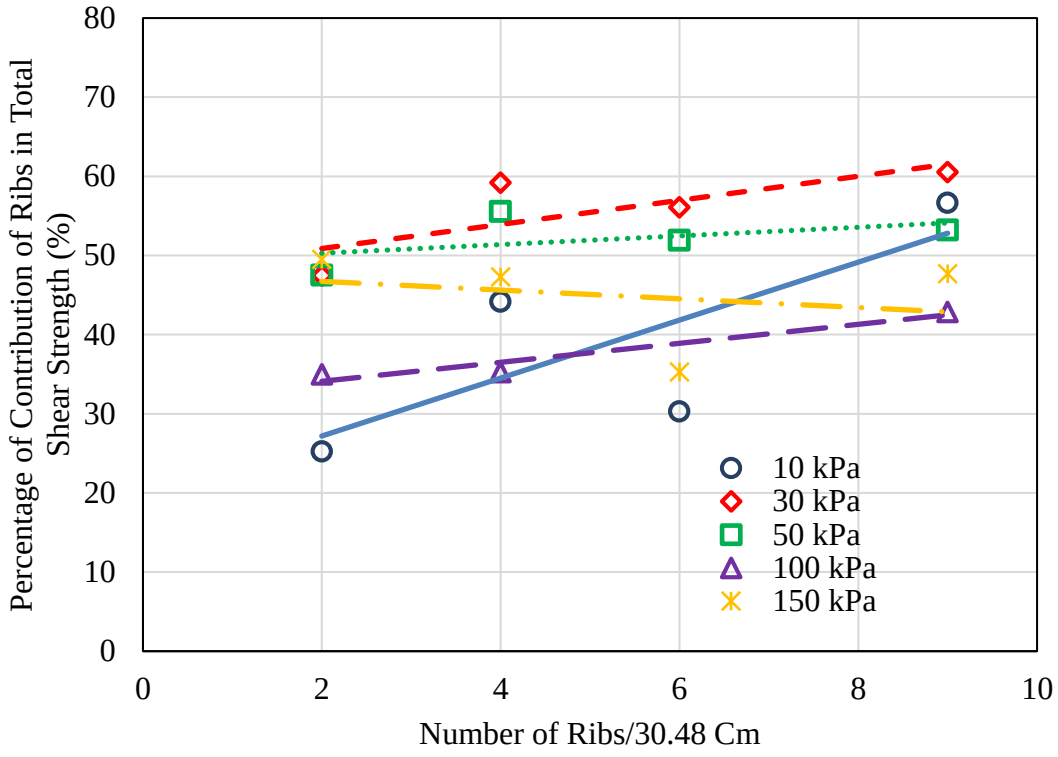

(c)

Figure 6-23. Continued.

Pullout Mode: The influence of various ribs spacing is illustrated in Figure 6-24 where the contribution of the ribs in the peak pullout force is illustrated versus the number of ribs per 30.48 cm (1 ft.). With increasing the number of ribs, the percentage of contribution of ribs increases too. The contribution of the rib(s) of 1-rib, 2-rib, and 4-rib steel strip reinforcements in pullout force are in the range of 1.2%-10.8%, 10%-15.8%, 18%-28%, respectively.

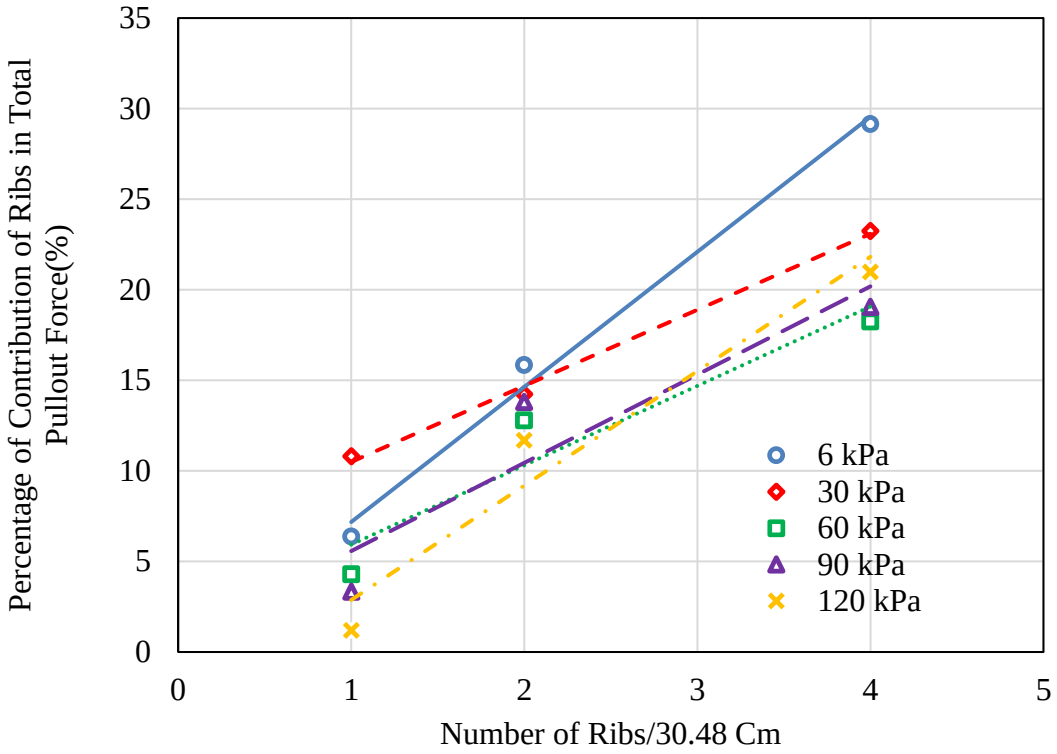

Figure 6-24. The Contribution of Ribs in the Pullout Force

The total pullout force consists of two components of frictional force and bearing force (passive resistance):

$$F_t = F_f + F_b$$

Where, F_f is a frictional force can be obtained using Mothe hr-Coulomb criterion as bellow:

$$F_f = \tau_f \times 2A = (C_a + \sigma_n \tan \delta_a) \times 2A$$

Where, τ_f is the actual frictional resistance,

C_a is the actual adhesion between the reinforcement and soil,

σ_n is the normal stress at the level of reinforcement,

δ_a is the friction angle between the reinforcement and soil,

A is the embedded area of the reinforcement

For the case of smooth strip reinforcement, the bearing force is zero, and the total pullout force is equal to the frictional force. Therefore, the frictional resistance can be calculated as follow:

$$\tau_f = \frac{F_f}{2A} = \frac{F_t}{2A}$$

As an example, the shear resistance is calculated for smooth strip reinforcement under 6 kPa and 120 kPa. The peak pullout force obtained from the pullout test on the smooth strip under 6 kPa and 120 kPa is 2 kN and 21.97 kN, respectively. Therefore, considering the embedded length (1.07 m) and embedded width (0.0508) of the reinforcement, the frictional resistance calculated as 18.4 kPa and 202.09 kPa, respectively. This agrees with the shear resistance obtained from the numerical simulation as shown in Figure 6-25.

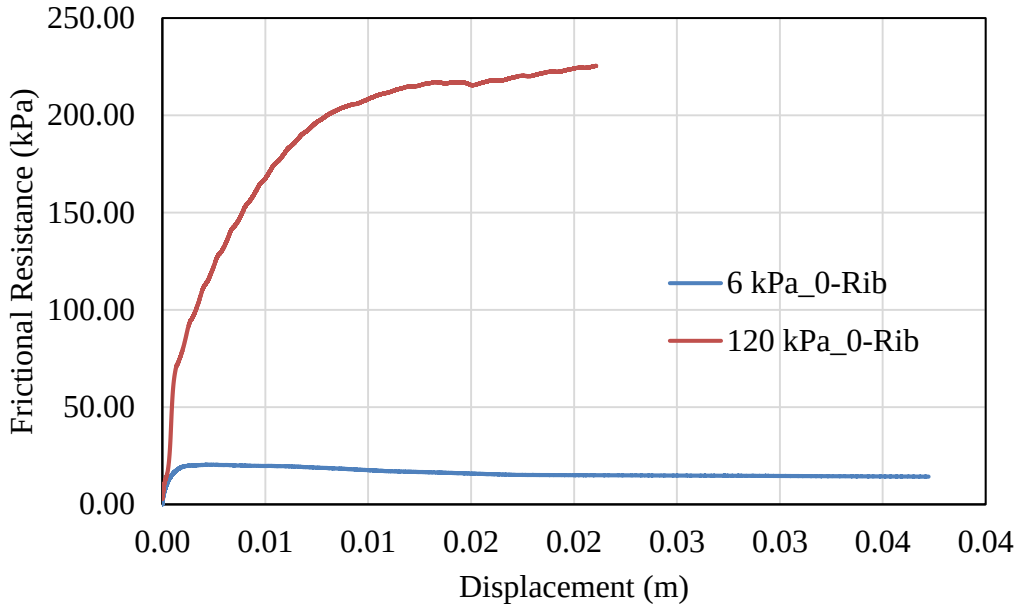

Figure 6-25. Frictional Resistance of the Smooth Strip Reinforcement in Pullout Test

For the case of ribbed steel strip reinforcements, the total pullout force consists of frictional force and the bearing force due to the passive resistance of ribs. There are two methods to calculate the frictional force and the bearing force:

1- obtain the bearing capacity using the numerical simulation and then back-calculate the frictional force from the following equation:

$$F_t = F_f + F_b$$

In this method, the bearing capacity of the ribs is obtained by measuring the force in front of each rib from a numerical simulation which is performed using FLAC3D and explained in chapter 5. Table 6-10 shows the average of passive resistance for each rib on

one side of a strip for specimens under 6 kPa and 120 kPa normal stresses. As shown in this table, for 2-rib steel strip reinforcement, the bearing resistance of first and second ribs are measured almost same. The contour of σ_{xx} in Figure 6-26(a) shows this observation. For 4-rib and RECO steel strip reinforcements, the bearing resistance of the front rib is greater than other ribs (almost two times greater than other ribs). This observation indicates the shadow effect of the first ribs over the ribs behind the first one (Figure 6-26 (b) and (c)). Table 6-10 shows that the RECO standard strip reinforcement illustrate that the bearing resistance of the first rib is almost 2 times more than other ribs.

Table 6-10. Bearing Resistance of Ribs for Steel Strip Reinforcements with Various Ribs Spacing

		Bearing Resistance (kPa)	
Reinforcement Type	**Rib**	**6 kPa**	**120 kPa**
2-Rib Steel Strip (1-Rib per Side per 30.48 cm)	1	93.87	1785.77
	2	89.73	1875.91
4-Rib Steel Strip (2-Rib per Side per 30.48 cm)	1	78.59	1450.22
	2	24.40	576.31
	3	36.08	608.51
	4	41.39	915.56

Table 6-10. Continued

		Bearing Resistance (kPa)	
Reinforcement Type	**Rib**	**6 kPa**	**120 kPa**
8-Rib Steel Strip (4-Rib per Side per 30.48 cm)	1	108.32	2023.48
	2	52.83	959.02
	3	49.62	992.15
	4	45.38	832.14
	5	61.40	1134.26
	6	53.48	979.11
	7	85.27	1414.24
	8	73.41	1036.90

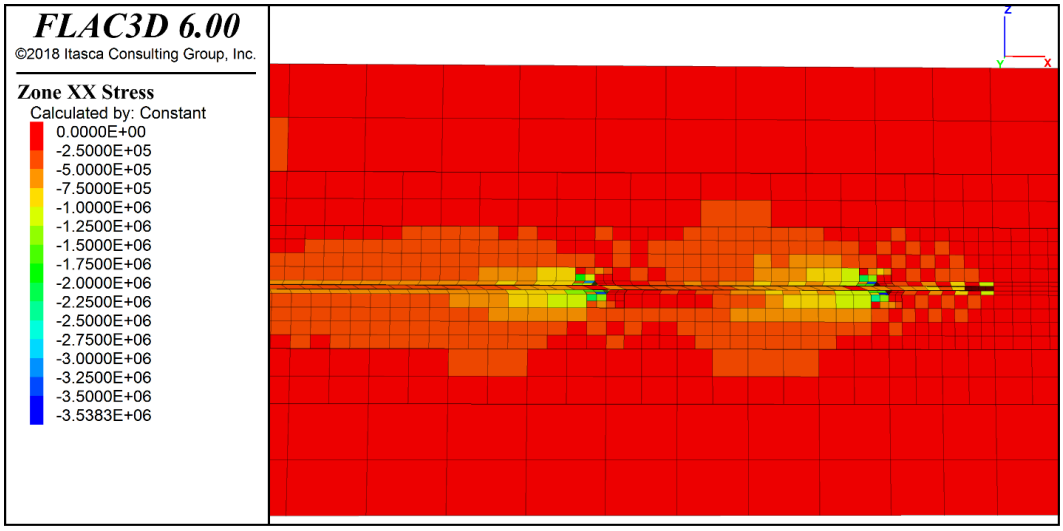

(a)

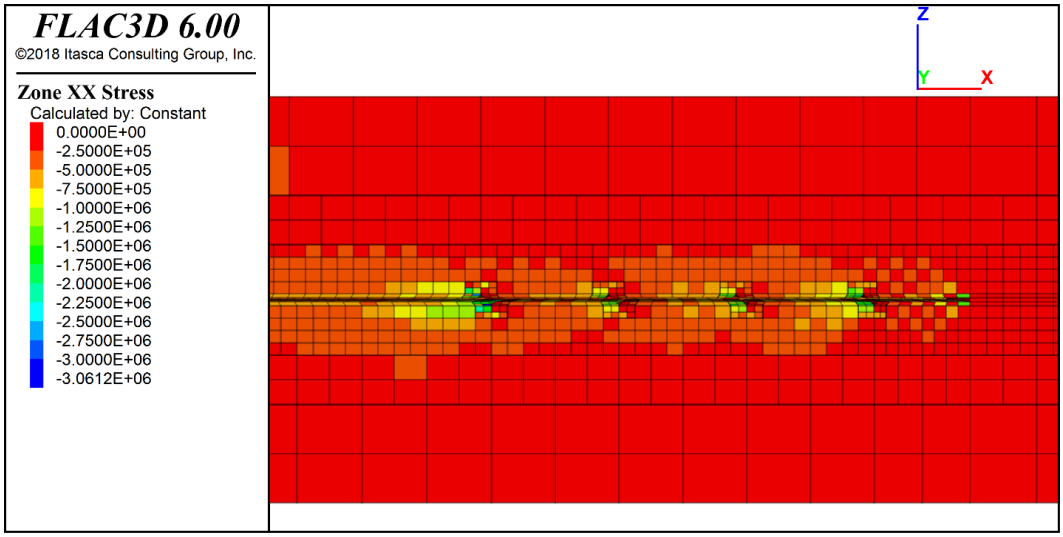

(b)

Figure 6-26. Contour of xx-Stress, 120 kPa Normal Stresses, (a), 2-Rib, (b) 4-Rib, (c) RECO Steel Strip Reinforcement

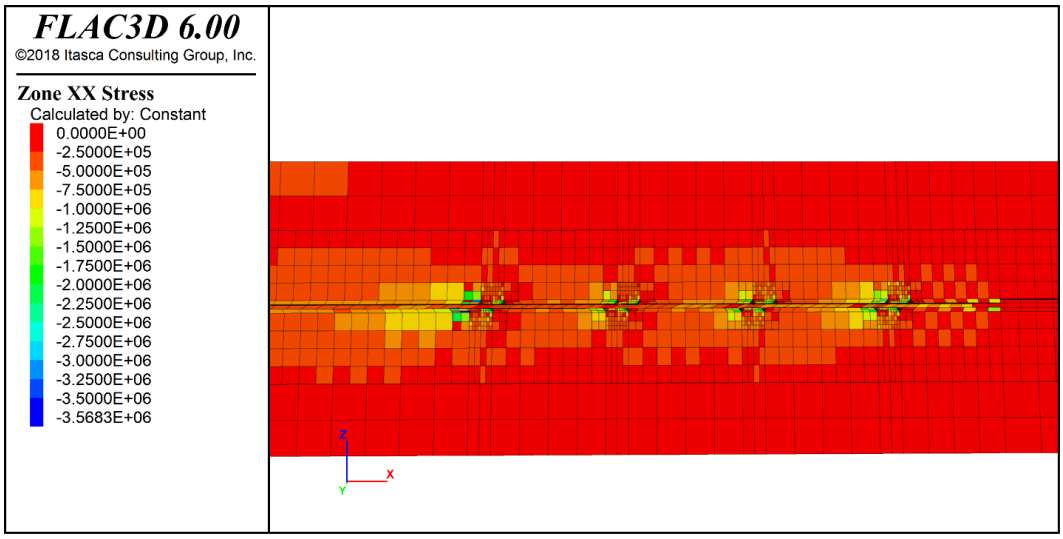

(c)

Figure 6-26. Continued.

The bearing force of all ribs per side is calculated for each steel strip reinforcements and reported in Table 6-11. Then the frictional force is calculated by taking out the bearing force from the total force. The calculations were performed for 2-rib, 4-rib, and RECO steel strip reinforcements under 6 and 120 kPa.

Table 6-11. Contribution of Passive Resistance and Frictional Resistance-Method 1

	2-Rib Steel Strip (1-Rib per Side per 30.48 cm)		4-Rib Steel Strip (2-Rib per Side per 30.48 cm)		8-Rib Steel Strip (4-Rib per Side per 30.48 cm)	
	6 kPa	**120 kPa**	**6 kPa**	**120 kPa**	**6 kPa**	**120 kPa**
Pullout force (kN)	2.24	22.24	2.44	24.88	2.94	27.80
Bearing Resistance per side (KPa)	183.60	3661.68	180.46	3550.60	529.71	9371.31
Bearing Force (kN)	0.06	1.12	0.06	1.08	0.16	2.86
Frictional Force(kN)	2.19	21.12	2.39	23.80	2.78	24.95

Calculate the frictional force from the experimental pullout results of smooth strip reinforcement embedded in dense sand. The frictional resistance per side of the smooth strip is calculated by dividing frictional force by 2 times the embedded area. The frictional force of the ribbed steel strip is calculated as follow:

$$F_{fr} = \tau_f \times 2 \times A_c$$

Where, A_c is aran ea of the embedded strip excluding the ribs.

Then the bearing force back calculated for a various number of ribs on the strip from total pullout force. Table 6-12 illustrates the results of the second method.

Table 6-12. Contribution of Passive Resistance and Frictional Resistance-Method 1

	Smooth Strip		2-Rib Steel Strip (1-Rib per Side per 30.48 cm)		4-Rib Steel Strip (2-Rib per Side per 30.48 cm)		8-Rib Steel Strip (4-Rib per Side per 30.48 cm)	
	6 kPa	**120 kPa**	**6 kPa**	**120 kPa**	**6 kPa**	**120 kPa**	**6 kPa**	**120 kPa**
Pullout force (kN)	2.00	21.97	2.24	22.24	2.44	24.88	2.94	27.80
Frictional Resistance per side (KPa)	18.40	202.10						
Frictional Force(kN)			1.98	21.70	1.95	21.44	1.90	20.90
Bearing Force (kN)			0.27	0.53	0.49	3.44	1.04	6.90

Comparing these two methods, the bearing and frictional forces are close to each other. As shown in these tables, the bearing resistance is almost 10 times more than frictional resistance. However, the area of frictional resistance is significantly greater than the area of ribs. Therefore, the frictional force is almost 20 times greater than bearing force. Figure 6-27 illustrates the frictional and bearing force for each strip reinforcement. As shown in this figure, the contribution of the frictional force is greater than bearing force due to the passive resistance of ribs. Also, it is observed that with increasing the number of ribs the bearing force is increasing, as expected.

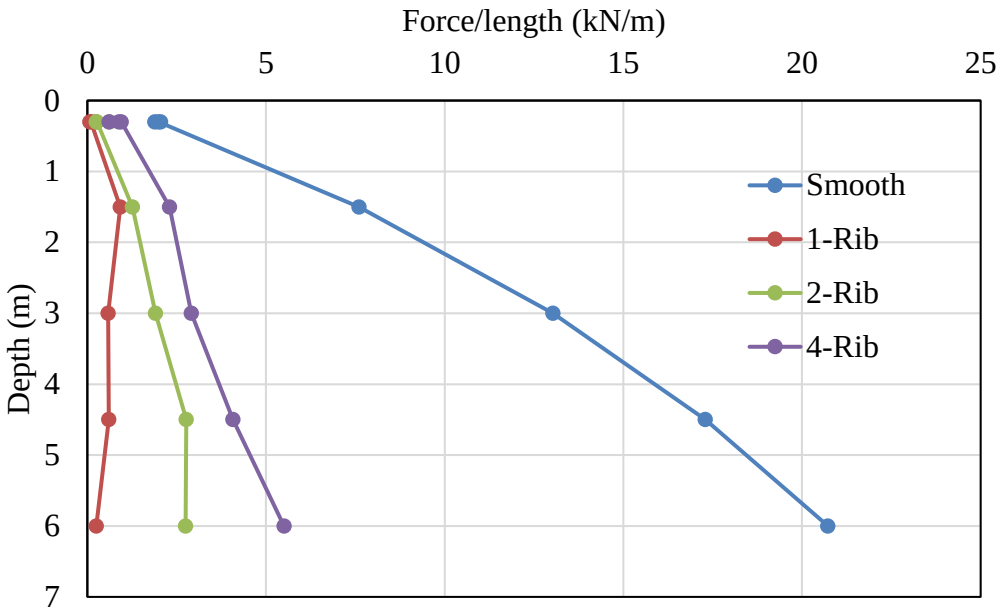

Figure 6-27. Contribution of Frictional Force and Passive Force

7 CONCLUSIONS AND RECOMMENDATIONS

7.1 Conclusions

This research presents the results of experimental and numerical work on the shear behavior of aggregates and of the interface properties of the soil-reinforcement using large-scale direct shear test, large-scale simple shear test, and pullout test. The main conclusions are summarized as follow:

- Both in the case of loose sand and dense sand, the shape of the curve is the same when testing with the small direct shear test (SDST) and the large direct shear tests (LDST). There is no scale effect for sand from the point of view of the shape of the curve.
- The measured peak friction angle of loose and dense sand with small and large direct shear test differed by no more than 3°. The friction angle of loose and dense sand at large displacement in LDST is 3.5° and 10° greater than the one in SDST, respectively. The difference is because during shearing at large displacements, the force concentration between the soil particles and the wall of the shear box increases the shear stress at large displacement and the dilation occurs at the front of the box, and the contraction happens at the back of the box. This phenomenon is greater for the LDST than for the SDST.
- The friction angle of loose sand, dense sand, and crushed limestone with fines obtained from LDST were measured to be 38°, 47°, and 56°, respectively. The

dilation angle of loose sand, dense sand, and crushed limestone with fines were measured to be 1°, 9°, and 1.5°, respectively.

- The simple shear test measurements are not sufficient to be able to draw the Mohr circle and thus the Mohr's Coulomb failure envelope because the stress field is not that of an element of soil. Assumptions must be made to obtain the friction angle.
- The measured fiction angle of loose sand, dense sand, and crushed limestone using two different assumptions (β-method and α-method) are different by the value of 5.5°, 7.5°, and 6°, respectively, and the friction angle obtained by the α-method are greater than the β-method.
- The interface friction angle between the smooth plate and the three types of soil tested are the same and equal to 33°. Therefore, the interface friction angle between a smooth aluminum plate and soil is independent of the soil density and grain size and controlled by the smooth plate.
- For all tested soil types, the interface shear strength increases with an increase in the number of ribs per unit length on an aluminum plate and with the normal stresses applied.
- For both loose and dense sand, the shear strength of the soil is higher than that of the interface between the smooth plate and the soil and that of a 2-rib per foot plate-soil interface. However, the peak and residual shear stress for 4-ribs/ft, 6-ribs/ft, and 9-ribs/ft aluminum plates are greater than the ones for the soil-soil internal shear strength.

- Unlike sand, the interface shear strength between smooth plates or ribbed plates and crushed limestone with fines (CLF) is always lower than the shear strength of the crushed limestone itself.
- In all shear tests on CLF, there is a significant fluctuation in the shear stress graphs because of the jagged nature of the movement of the large aggregates over each other and the breakage of the limestone aggregates under normal pressure.
- Measured vertical displacements during interface direct shear tests on smooth and ribbed plates reveal that, with an increasing number of ribs/ft on a plate, the dilation value of the specimen increases as the soil particles move over the ribs.
- The mobilize shear strength of geogrid-loose sand and geogrid-CLF is lower than for the loose sand and CLF internal shear strength, respectively while the peak shear strength of geogrid-dense sand is greater than the dense sand internal shear strength. Also, the stiffness of the geogrid-dense sand is greater than the dense sand stiffness.
- The friction angle of soil-geogrid is lower than soil-soil internal, different by 7° and 2.5° for loose and dense sand, respectively.
- Comparing DST on dense sand and IDST on ribbed plate-dense sand, the maximum dilation of dense sand occurs at the shear displacement corresponding to the peak shear strength while the maximum dilation values obtained from the interface direct shear test are observed at the end of the test.

- The maximum vertical displacement of the dense sand-geogrid happened at the shear displacement corresponding to the yield shear stress. On the other hand, the maximum vertical displacement of dense sand was observed at the horizontal displacement corresponding to the peak shear strength of the interface test.
- The F* value obtained from interface direct shear tests between the smooth strip and soil specimens (LS, DS, CLF) is higher than the AASHTO (2012) recommendation default F* values.
- The F* value obtained from IDT of the smooth plate and the loose sand, dense sand, and crushed limestone starts from 0.35, 0.53, and 1 at 10 kPa normal stress and increases slightly to 0.67, 0.63, and 0.78 at 150 kPa normal stresses, respectively.
- The measurements of IDST between all tested soil types and smooth plate as well as ribbed plates indicates that with increasing the number of ribs per foot on the plate, the F* and Ci value of reinforcements also increasing.
- The obtained interface properties of ribbed plate and soil showed that the influence of the number of the ribs on interface parameters (F*, F* ratio, Ci) is greater at low normal stresses than high normal stresses, and that the one is greater for the dense soil than loose soil under various normal stresses.
- Regardless of the type of the soil, particle size, and soil density, the Ci value (interface coefficient) is obtained around 0.5 for the interface between the smooth plate and three types of soil. In contrast to the smooth plate, in the case

of the ribbed plate, the particle size and soil density have an influence in the Ci value. For large aggregates with D80 more than the height of the rib (CLF), the Ci value is less than one for a various number of ribs. For soil specimens with D80 smaller than the height of the rib, the Ci value is more than one for ribs spacing less than 61 mm and increases with increasing the density of soil. Maximum Ci value was measured 1.2, 1.4, and 0.9 for loose sand, dense sand, and crushed limestone with fines, respectively.

- The results of interface direct shear test of the smooth plate or the ribbed plate and loose sand showed that as the number of ribs increases from 2 (ribs spacing = 101.6 mm) to 9 (ribs spacing = 25.4 mm), the interface shear strength improves 55% to 65% at 10 kPa normal stress and 18% to 25% improvement at 150 kPa normal stress, respectively.
- The results of interface direct shear test of the smooth plate and the ribbed plate and dense sand showed that as the number of ribs increases from 2 (ribs spacing = 101.6 mm) to 9 (ribs spacing = 25.4 mm), the interface shear strength improves 55% to 70% at 10 kPa normal stress and 31% to 50% improvement at 150 kPa normal stress, respectively.
- The peak pullout force for the steel strip with 1-rib/ft, 2-rib/ft, and RECO reinforcement enhances the pullout force by 4.8%, 12%, and 32% compare to the smooth steel strip reinforcement, respectively.
- The F* value obtained from the maximum pullout force of smooth strip and RECO steel strip reinforcement embedded in dense sand is 3.1 and 4.5 at 6

kPa normal stresses and decreases to 1.7 and 2.1 at 120 kPa normal stress, respectively.

- Pullout test results indicated that the effect of the ribs spacing on F* value is greater at a lower depth of embedment and at small pullout displacements.
- Pullout test results on smooth/ribbed steel strip reinforcements showed that the friction coefficient (F*), apparent friction coefficient ratio (F* ratio), and coefficient of direct sliding (Ci) increases with increasing the number of the ribs on the strip.
- The measured pullout resistance factor (F*) for smooth and ribbed steel strip reinforcement with a various number of ribs are greater than the AASHTO (2012) recommendation default F* values for smooth and ribbed steel strip reinforcement.
- The pullout test results showed that with increasing the number of ribs from smooth to the RECO steel strip (4 rib/ft), F* values are increasing in the range of 2.5- 4.8 at depth of 0.3 m and decreases to 1.7-2 at a depth of 6m, respectively.
- The results from the 3D finite difference analyses of the direct shear test, interface direct shear test between sand and smooth/ribbed plate, and the pullout test on smooth/ribbed steel strip reinforcement showed a good agreement with the results from the experimental tests of mentioned systems.
- The results of the numerical simulation of pullout test by FLAC3D illustrated that the optimum number of ribs is 4 ribs per side per 30.48 cm (RECO steel

strip reinforcement), and with increasing the number of ribs to 6 ribs per side per 30.48 cm, the pullout force improvement is insignificant. However, for a certain conclusion, conducting laboratory pullout force is recommended.

7.2 Contributions to New Knowledge

The major contribution to knowledge of the presented research is provided in the following points:

The shear properties of large aggregates obtained with large direct shear and simple shear test.

The soil- smooth/ribbed steel strip reinforcement interaction were explained in depth under shear and pullout mode.

The influence of rib spacing, soil density, grain size, and confining stress evaluated on interface shear and pullout force.

The percent contribution of the passive resistance and frictional resistance of ribs in the pullout force and shear resistance of the direct shear test were evaluated.

REFERENCES

1. Abu-Farsakh, M. Y., & Coronel, J. (2006). Characterization of Cohesive Soil-Geosynthetics Interactions from Large Direct Shear Tests. In *Transportation Research Board 85th Annual Meeting* (No. 06-0651).
2. Abu-Farsakh, M., Almohd, I., & Farrag, K. (2006). Comparison of field and laboratory pullout tests on geosynthetics in marginal soils. *Transportation Research Record: Journal of the Transportation Research Board*, (1975), 124-136.
3. ASTM, D.442 (2007). Standard test method for particle-size analysis of soils.
4. ASTM. (2012). Standard test method for determining the shear strength of soil-geosynthetic and geosynthetic-geosynthetic interfaces by direct shear. *D5321*.
5. ASTM D6243 / D6243M-16, Standard Test Method for Determining the Internal and Interface Shear Strength of Geosynthetic Clay Liner by the Direct Shear Method
6. ASTM. (2005). ASTM D4318, standard test method for liquid limit, plastic limit, and plasticity index of soils.
7. ASTM, D. 698.(2000). *Standard Test Method for Laboratory Compaction Characteristics of Soils ASTM International, West Conshohocken, PA, USA*.
8. Standard, A. S. T. M. D3080-04, 2004,". *Standard Test Method for Direct Shear Test of Soils under Consolidated Drained Conditions," Annual Book of ASTM Standards, ASTM International, West Conshohocken, PA*.
9. Awad, M. I., & Tanyu, B. F. (2014). Laboratory evaluation of governing mechanism of frictionally connected MSEW face and implications on design. Geotextiles and Geomembranes, 42(5), 468-478.
10. Bagherzadeh-Khalkhali, A., & Mirghasemi, A. A. (2009). Numerical and experimental direct shear tests for coarse-grained soils. Particuology, 7(1), 83-91.

11. Bakeer, R. M., Sayed, S. M., Cates, P., & Subramanian, R. (1998). Pullout and shear tests on geogrid reinforced lightweight aggregate. *Geotextiles and Geomembranes*, *16*(2), 119-133.
12. Bauer, G. E., & Zhao, Y. (1993). Evaluation of shear strength and dilatancy behavior of reinforced soil from direct shear tests. In *Geosynthetic Soil Reinforcement Testing Procedures*. ASTM International.
13. Baykal, G., & Dadasbilge, O. (2009). Experimental investigation of pullout resistance of uniaxial geogrids. *Geosynthetics in Civil and Environmental Engineering*, 174-178.
14. Bergado, D. T., Chai, J. C., Abiera, H. O., Alfaro, M. C., & Balasubramaniam, A. S. (1993). Interaction between cohesive-frictional soil and various grid reinforcements. Geotextiles and Geomembranes, 12(4), 327-349.
15. Bergado, D.T., Hardiyatimo, H.C., Cineros, C.B., Chun, C.J., Alfaro, M.C. Balasubramaniam, A.S., and Anderson, L.R. (1992). "Pull-out Resistance of Steel Geogrids with Weathered Clay as Backfill Material." *Geotechnical Testing Journal*, Vol. 15, No. 1., pp 33-46 (Mar).
16. Cancelli, A. (1992). Frictional characteristics of geogrids by means of direct shear and pullout tests. Earth Reinforcement Practice.
17. Cazzuffi, D., Picarelli, L., Ricciuti, A., & Rimoldi, P. (1993). Laboratory investigations on the shear strength of geogrid reinforced soils. In Geosynthetic Soil Reinforcement Testing Procedures. ASTM International.
18. Chang, J. C., Hannon, J. B., & Forsyth, R. A. (1977). *Pull resistance and interaction of earthwork reinforcement and soil* (No. 640).
19. Chu, L. M., & Yin, J. H. (2005). Comparison of interface shear strength of soil nails measured by both direct shear box tests and pullout tests. *Journal of geotechnical and geoenvironmental engineering*, *131*(9), 1097-1107.
20. Cowell, M.J., and Sprague, C.J. (1993). "Comparison of Pull-out Performance of Geogrids and Geotextiles." *Geosynthetics '93,* pp 579-592.

21. Dounias, G. T., & Potts, D. M. (1993). Numerical analysis of drained direct and simple shear tests. *Journal of Geotechnical Engineering*, *119*(12), 1870-1891.
22. El-Emam, M., Attom, M., & Khan, Z. (2012). Numerical prediction of plane strain properties of sandy soil from direct shear test. *International Journal of Geotechnical Engineering*, *6*(1), 79-90.
23. FHWA (2001). *Mechanically Stabilized Earth Walls and Reinforced Soil Slopes Design and Construction Guidelines.* Federal Highway Administration (FHWA), FHWA-NHI-00-043, Washington, D.C.
24. Frydman, S., & Operstein, V. (2001). Numerical simulation of direct shear of rootreinforced soil. *Proceedings of the Institution of Civil Engineers-Ground Improvement*, *5*(1), 41-48.
25. Geosynthetics and Soil-Tire Chip Mixtures." Journal of Geotechnical and Geoenvironmental
26. Geocomp Corporation 2015. Control and Report Software for Fully Automated Cyclic Direct Simple Shear Tests on ShearTrac-III DSS Systems using Windows®XP/Vista/7, Cyclic Direct Simple Shear- User's Manual.
27. Geocomp Corporation 2015. Control and Report Software for Fully Automated Direct Shear Tests on ShearTrac-III DSS Systems using Windows®XP/Vista/7, Cyclic Direct Simple Shear- User's Manual.
28. Härtl, J., & Ooi, J. Y. (2011). Numerical investigation of particle shape and particle friction on limiting bulk friction in direct shear tests and comparison with experiments. *Powder technology*, *212*(1), 231-239.
29. Holtz, R.D. (1977). "Laboratory Studies of Reinforced Earth Using a Woven Polyester Fabric." C.R. Coll. Int. Sols Textiles. Paris 1977, pp 149-154.
30. Jarret, P. M., & Bathurst, R. J. (1985). Frictional development at a gravel geosynthetic peat interface. In Proc., 2nd Canadian Symp. of Geotextiles and Geomembranes (pp. 1-6).
31. Jones, C. J. (2013). Earth reinforcement and soil structures. Elsevier.

32. Khemissa, M., Safer, S., & Aidjouli, S. (2015). Roughness's shapes comparative analysis of some reinforced earth elements under monotonous loading. *Alexandria Engineering Journal*, *54*(3), 577-582.
33. Khemissa, M., Safer, S., & Aidjouli, S. (2015). Roughness's shapes comparative analysis of some reinforced earth elements under monotonous loading. *Alexandria Engineering Journal*, *54*(3), 577-582.
34. Koutsourais, M., Sandri, D. and Swan, R. (1998). "Soil Interaction Characteristics of Geotextiles and Geogrids." *Geosynthetics* '98, pp 739-744.
35. Ladd, R. S. (1978). Preparing test specimens using under compaction. *Geotechnical Testing Journal*, *1*(1), 16-23.
36. Liu, C. N., Zornberg, J. G., Chen, T. C., Ho, Y. H., & Lin, B. H. (2009). Behavior of geogrid-sand interface in direct shear mode. Journal of geotechnical and geoenvironmental engineering, 135(12), 1863-1871.
37. Liu, S. H. (2006). Simulating a direct shear box test by DEM. Canadian Geotechnical Journal, 43(2), 155-168.
38. Liu, S. H. (2006). Simulating a direct shear box test by DEM. *Canadian Geotechnical Journal*, *43*(2), 155-168.
39. Liu, S.S., Liu, C.L., Liu, J.C. and Kuo, S.H. (1996). "Short Term Pull-out Tests of Geogrid in a Compacted Lateritic Soil." *Journal of Geotechnical Engineering*, ASCE, pp 543-559.
40. Lobo-Guerrero, S., & Vallejo, L. E. (2005). Discrete element method evaluation of granular crushing under direct shear test conditions. Journal of Geotechnical and Geoenvironmental Engineering, 131(10), 1295-1300.
41. Lobo-Guerrero, S., & Vallejo, L. E. (2005). Discrete element method evaluation of granular crushing under direct shear test conditions. *Journal of Geotechnical and Geoenvironmental Engineering*, *131*(10), 1295-1300.
42. Lopes, M. L. (2002). Soil-geosynthetic interaction. Thomas Telford, London.

43. Lopes, M. L., & Silvano, R. (2010). Soil/geotextile interface behaviour in direct shear and pullout movements. *Geotechnical and geological engineering*, *28*(6), 791-804.
44. Melton, J. S., & Morgan, T. (1996). Evaluation of tests for recycled material aggregates for use in unbound application. *Final Report of RMRC Project*, *6*, 18.
45. Mitchell, J. K., & Villet, W. C. (1987). Reinforcement of earth slopes and embankments. NCHRP Report, (290).
46. Moayed, R. Z., Tamassoki, S., & Izadi, E. (2012). Numerical modeling of direct shear tests on sandy clay. *World Academy of Science, Engineering and Technology*, *61*, 1093-1097.
47. Ochiai, H., Otani, J., Hayashic, S. and Hirai T. (1996). "The Pull-out Resistance of Geogrids in Reinforced Soil." Geotextiles and Geomembranes, Vol. 14, pp 19-42.
48. Peterson, L. M. (1980). *Pullout resistance of welded wire mesh embedded in soil* (Doctoral dissertation, Utah State University. Department of Civil and Environmental Engineering).
49. Peterson, L.M. and Anderson, L.R. (1980). "Pull-out Resistance of Welded Wire Mats Embedded in Soil," *Master of Science thesis*, Utah State University, Logan, UT.
50. Potts, D. M., Dounias, G. T., & Vaughan, P. R. (1987). Finite element analysis of the direct shear box test. Geotechnique, 37(1), 11-23.
51. Rowe, R.K., Ho, S.K. and Fisher, D.G. (1985). "Determination of Soil-Geotextile Interface Strength Properties." Second Canadian Symposium on Geotextiles and Geomembranes, pp 25-34 (Sept).
52. Saada, A. S., & Townsend, F. C. (1981). State of the art: laboratory strength testing of soils. In Laboratory shear strength of soil. ASTM International.
53. Strahler, A. W., Walters, J. J., & Stuedlein, A. W. (2016). Frictional Resistance of Closely Spaced Steel Reinforcement Strips Used in MSE Walls. Journal of Geotechnical and Geoenvironmental Engineering, 04016030.

54. Tatlisoz, N., Edil, T. B., & Benson, C. H. (1998). Interaction between reinforcing geosynthetics and soil-tire chip mixtures. *Journal of Geotechnical and Geoenvironmental Engineering*, *124*(11), 1109-1119.
55. Taylor, P., T. (2018). F*ramework for determining the pullout resistance of inextensible 2-wire soil-reinforcing elements embedded in sand* (Doctoral dissertation, University of Texas at Arlington) .
56. Weldu, M. T. (2015). *Pullout Resistance of MSE Wall Steel Strip Reinforcement in Uniform Aggregate* (Doctoral dissertation, University of Kansas).
57. Xiao, Z. Y., Xu, W., Deng, Y. S., & Tu, F. (2012). Numerical Simulation of Interface Softening for Large Size Direct Shear Test. In *Advanced Materials Research* (Vol. 368, pp. 3230-3235). Trans Tech Publications.
58. Zehtab, K. H., Fei, X., Hubler, J., Athanasopoulos-Zekkos, A., Zekkos, D., & Marr, W. A. (2018). Development of a Large-Size Cyclic Direct Simple Shear Device for Characterization of Ground Materials with Oversized Particles. *Geotechnical Testing Journal*, *41*(2).
59. Zekkos, D., Athanasopoulos-Zekkos, A., Hubler, J., Fei, X., Zehtab, K., and Marr, W. (2017). Development of a Large-Size Cyclic Direct Simple Shear Device for Characterization of Ground Materials with Oversized Particles, *Geotechnical Testing Journa.*
60. Zhang, L., & Thornton, C. (2007). A numerical examination of the direct shear test. Geotechnique, 57(4), 343-354.